NIRS-R-52

「4次元CTの研究開発」報告集

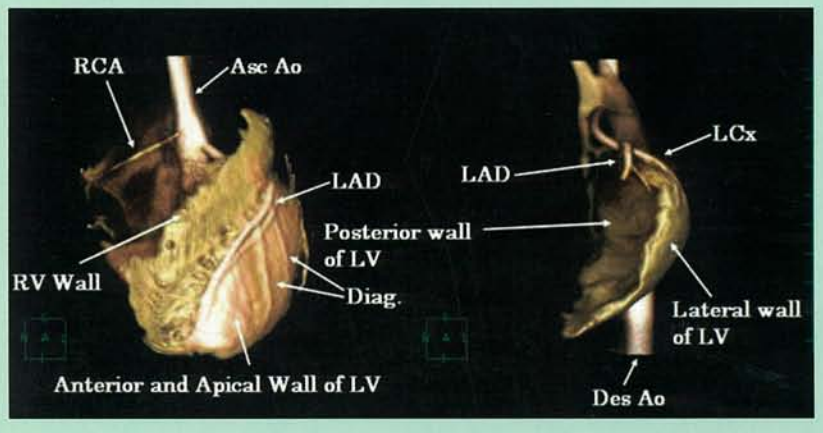

LAD Injection　　LCx Injection

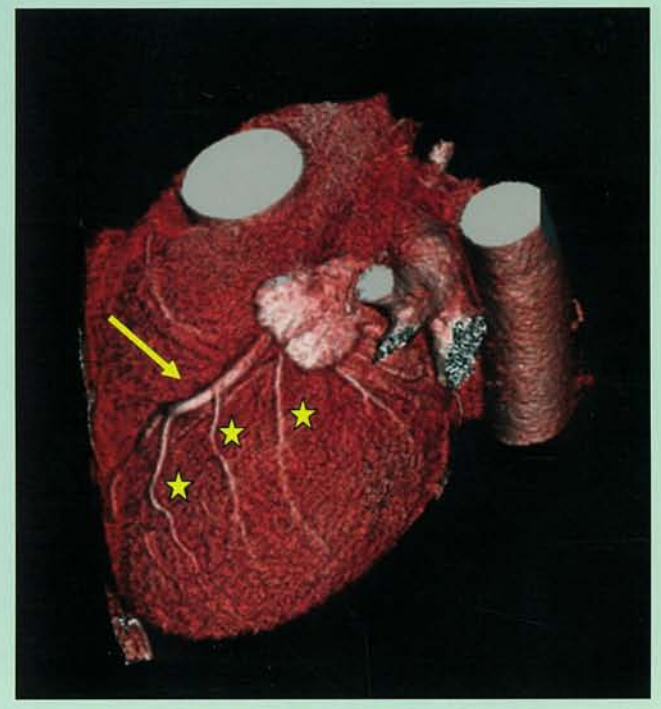

編集：放射線医学総合研究所　遠藤真広
2006年2月発行

NIRS-R-52

「４次元ＣＴの研究開発」報告集

編集：放射線医学総合研究所　遠藤真広

2006 年 2 月発行

目　次

表紙の説明

左上の図：ブタの冠状動脈の選択的造影。造影剤を注入した血管により支配領域の心筋のみが造影されている。選択的造影により、冠状動脈の主要血管の支配領域を同定できることが示唆された。(文献 11)

左下の図：４次元 CT 装置の外観

右下の図：健常ボランティアの心臓の造影。心電図非同期の径静脈的造影により、冠状動脈が描出されている。(矢印：左前下行枝、星印：対角枝)

序　文

CT（コンピュータ断層法）が臨床に使用されるようになったのは、1972 年のことである。その臨床試験の結果は 1973 年の British Journal of Radiology に Ambrose などにより報告された。その論文はまさに衝撃的であり、それまで外部からは視ることのできなかった脳内の病巣が鮮明に描出されていた。CT が医療に与えた影響はきわめて大きく、このことは、1979 年のノーベル医学生理学賞が CT の開発者である Hounsfield と先駆的な研究を行った Cormack に与えられたことからもわかる。

CT の登場のころから、一部の研究者の間には、この方法で拍動する心臓を画像化したいという夢が語られていた。1980 年代の前半に米国の Mayo Clinic において行われた Dynamic Spatial Reconstructor (DSR)の開発は、まさにこの夢を実現しようというものであった。DSR は、28 対の X 線テレビシステムを用いることにより 1 秒間に 20 ボリュームの撮像をめざすという極めて野心的な装置であったが、当時の X 線検出技術やコンピュータを中心とするデジタル信号処理技術ではその要求を満足することができなかったため、壮大な失敗に終わった。

DSR の失敗を挟みながらも CT 技術は着実に進歩し、1990 年代の初頭にはヘリカル CT を生み出した。これは X 線管－検出器系の連続回転と寝台の連続移動を組み合わせ、X 線管を被写体から見てらせん（ヘリカル）軌道を描かせることにより 3 次元（ボリューム）データの収集を容易にしたものであった。ヘリカル CT の登場により、3 次元画像の応用は急速に進み、CT は 2 次元の横断画像を撮るだけの装置から、3 次元画像の取得も可能な装置へと変貌した。

3 次元データを取得する方式には、ヘリカル CT のほかにコーンビーム CT という方法がある。この方法は、X 線管と 2 次元検出器を被写体の周りに回転させるものであり、1 回転で 3 次元データの取得が可能である。コーンビーム CT については、以前から放射線医学総合研究所（放医研）において検討を進めてきた。コーンビーム CT は、3 次元画像を得るという点で、原理的にはヘリカル CT よりも優れた点が多い。しかし、1990 年代の末ころまでは、CT に必要な仕様を満足する 2 次元検出器が得られず、コーンビーム CT はその原理的な優越性を十分に発揮できなかった。

この事情は２１世紀に入り大きく変化した。２１世紀に入り半導体加工技術の進歩に伴い、CT に必要な 2 次元検出器が開発されるようになった。その一つは FPD（フラットパネル検出器）と呼ばれる検出器であり、この検出器の導入により、放射線治療の際の精密位置決めや血管の 3 次元撮影にコーンビーム CT が利用されるようになった。しかし、FPD では CT 検出器のスピードとダイナミックレンジの達成は困難であった。

他の一つは CT 検出器の多列化であり、スキャンに要する時間の短縮を主な目的に、1998 年頃に 4 列のマルチスライス CT が開発された。放医研では、この検出器の可能性に着目し、4 列を 256 列に大幅に拡張することにより 2 次元検出器を開発し、それを搭載した CT 装置を

開発することとした。この装置では、1回転で3次元画像が得られ、連続回転することにより、ダイナミック（時間変化する）3次元画像の撮像が可能となる。放医研では、この装置に3次元画像に時間の次元を加えるという意味で4次元CTと名付けた。

放医研は2001年度より独立行政法人に移行したが、4次元CT開発計画は中期計画において認められ、5年間で256列マルチスライスCTを開発して、臨床試験を行うことが計画された。計画スタート当時、臨床に使用されていたのが、4列のマルチスライスのみであったので、その64倍の検出器を搭載するCTを5年間で開発することは、大変に挑戦的であった。

関係者の努力により、開発計画は順調に進捗し、2001年度には256列検出器の試作、それを搭載した機能試験機の開発などを行った。また、2002年度には256列検出器と並ぶキーテクノロジーである超高速再構成装置の試作を行い、2003年度には4次元ビューアーの試作を行った。これら要素技術の開発を背景に4次元CT装置の開発を2004年度に終了し、2005年度にはこの装置で臨床試験を行った。

この装置の仕様は、以下に採録した論文に詳述されているので詳しくは述べないが、0.5秒で1回転し、体軸方向で128mmの視野を持つ。したがって、ハーフ再構成法を用いるならば0.25秒の時間分解能でボリュームを撮像できる。当然、心臓のダイナミック撮影も可能であり、この装置によりCT開発以来の究極の夢が実現できたといえる。

この開発に際して、多くの論文が発表された。本報告集は、中期計画の終わりにあたり、それらの中から解説2編と原著論文のすべて（15編）を採録し、開発の成果をまとめたものである。機器開発のプロジェクトでは、後になるほど論文が増加することが多いが、本研究もその例にもれず現在、投稿中または準備中の論文が多数ある。これらについては、論文掲載が一段落したときに補遺として出版することを考えている。

この研究を遂行するにあたり、多くの方の協力を得た。佐々木康人放医研理事長、村田啓、辻井博彦重粒子医科学センター長には、この研究の遂行をお認めいただき、さまざまなご指導をいただいた。企画室や総務部などの事務方のスタッフには予算の獲得や執行などでお世話になった。多くの研究者と共同で作業を行ったが、この中で医学物理部のテクニカルスタッフである森慎一郎氏の活躍は特筆に価する。彼がいなければ、この報告集は存在しなかったと思う。放医研の研究者だけではなく、多くの方に4次元CT研究班員として参画をお願いし、また装置開発にはソニー（株）と東芝メディカルシステムズ（株）の協力を得た。4次元CT研究班員、ソニー（株）と東芝メディカルシステムズ（株）の主だった協力者の氏名を付録に示す。最後に、ここに示した方の協力とプロジェクト成功に向けた真摯な努力に深く感謝したい。

放射線医学総合研究所
遠藤　真広

1．研究業績目録

4次元CT研究業績目録（2001-2005年）

◆原著

1) Endo M, Tsunoo T, Nakamori N, Yoshida K: Effect of scattered radiation on image noise in cone beam CT. *Medical Physics* **28**: 469-474, 2001

2) Endo M, Tsunoo T, Kandatsu S, Tanada S, Aradate H, Saito Y: Four dimensional computed tomography (4D CT) – Concepts and preliminary development. *Radiation Medicine* **21**: 17-22, 2003

3) Endo M, Mori S, Tsunoo T, Kandatsu S, Tanada S, Aradate H, Saito Y, Miyazaki H, Satoh K, Matsusita S, Kusakabe M: Development and performance evaluation of the first model of 4-D CT-scanner. *IEEE Trans on Nuclear Science* **NS-50**: 1667-1671, 2003

4) Mori S, Endo M., Tsunoo T, Kandatsu S, Tanada S, Aradate H, Saito Y, Miyazaki H, Sato K, Matsushita S, Kusakabe M: Physical performance evaluation of a 256-slice CT-scanner for 4-dimensional imaging. *Medical Physics* **31**: 1348-1356, 2004

5) 中土裕樹、渡辺直行、中土幸男、但野　茂、小林道明、森泉哲治：骨梁構造を組み込んだヒト大腿骨近位部の有限要素解析．日本臨床バイオメカニクス学会誌　**25**: 267-272, 2004

6) Mori S, Kondo C, Suzuki N, Yamashita H, Kusakabe M, Endo M: Volumetric cine imaging for cardiovascular circulation using prototype 256-detector row computed tomography scanner (4-dimensional computed tomography) - A preliminary study with a porcine model. *J Comput Assist Tomogr* **29**: 26-30, 2005

7) Mori S, Endo M, Obata T, Murase K, Fujiwara H, Kandatsu S, Tanada S: Clinical potentials of the prototype 256-detector row CT-Scanner. *Academic Radiology* **12**: 148-154, 2005

8) Mori S, Endo M, Nishizawa K, Tsunoo T, Aoyama T, Fujiwara H, Murase K: Enlarged longitudinal dose profiles in cone-beam CT and the need for modified dosimetry. *Medical Physics* 32: 1061-1069, 2005

9) Mori S, Obata T, Kishimoto R, Kato H, Murase K, Fujiwara H, Kandatsu S, Tanada S, Tsujii H, Endo M: Clinical potentials for dynamic contrast-enhanced hepatic volumetric cine imaging with the prototype 256-MDCT scanner, *American J Roentogenology* **185**: 253-256, 2005

10) Funabashi N, Yoshida K, Tadokoro H, Nakagawa K, Komiyama N, Odaka K, Tsunoo T, Mori S, Endo M, Tanada S, Komuro I: Cardiovascular circulation and hepatic perfusion of pigs in 4-dimensional films evaluated by 256-slice cone-beam computed tomography. *Circulation J* **69**: 585-589, 2005

11) Funabashi N, Yoshida K, Tadokoro H, Nakagawa K, Komiyama N, Odaka K, Tsunoo T, Mori S, Endo M, Tanada S, Komuro I: Three dimensional segmented myocardial perfusion images by selective intracoronary injection of contrast using 256 slice cone beam computed tomography. *Heart* 91: 1349-1351, 2005

12) Kondo C, Mori S, Endo M, Kusakabe K, Suzuki N, Hattori A, Kusakabe M: Real-time volumetric imaging of human heart without electrocardiographic gating by 256-detector row computed tomography- Initial experience. *J Comput Assist Tomogr* **29**: 694-698, 2005

13) Mori S, Obata T, Nakajima N, Ichihara N, Endo M: Volumetric perfusion CT using prototype 256-detector row computed tomographic scanner: Preliminary study with healthy porcine model. *Am J Neuroradiol* **26**: 2536-2541, 2005

14) Mori S, Endo M, Nishizawa K, Ohno M, Miyazaki H, Tsujita K, Saito Y: Prototype heel effect compensation filter for cone-beam CT. *Phys Med Biol* **50**: N359-N370, 2005

15) Mori S, Kohno R, Nishio T, Mizuno H, Yamashita H, Abe Y, Ikeda T, Ishihara T, Asakura H, Endo M: Physical evaluation of multidetector-row computed tomography (MDCT) scan methods and conditions for improvement of carbon beam distribution, 日本放射線技術学会雑誌 **61**: 1609-1615, 2005

16) Funabashi N, Yoshida K, Tadokoro H, Odaka K, Tsunoo T, Mori S, Endo M, Tanada S, Komuro I: Time series of volumetric measurement of porcine three dimensional segmented myocardial perfusion by selective contrast injection using 256-slice cone beam computed tomography. *Int J of Cardiology* (in press)

17) Mori S, Endo M, Nishizawa K, Murase K, Fujiwara H, Tanada S: Comparison of patient doses in 256-slice CT and 16-slice CT scanners. *Brit J Radiol.* (in press)

18) Mori S, Kondo C, Suzuki N, Hattori A, Kusakabe M, Endo M: Volumetric coronary angiography using the 256-detector row CT-scanner: Comparison in vivo and in vitro with porcine models. *Acta Radiologica* (in press)

19) Mori S, Kanematsu N, Mizuno H, Sunaoka M, Endo M: Physical evaluation of CT scan methods for radiation therapy planning: Comparison of fast, slow and gating scan using the 256-detector row CT scanner. *Phys Med Biol* (in press)

20) Mori S, Baba M, Yashiro T, Komatsu S, Kandatsu S, Endo M: Volumetric cine imaging for four-dimensional radiation therapy planning using the second model of the 256-detector row CT-scanner: Initial experience in lung cancer. *European J of Radiology* (in press)

◆プロシーディングス

1) Endo M, Tsunoo T, Satoh K, Matsusita S, Kusakabe M, Fukuda Y: Performance of cone beam CT using a flat-panel imager. *Proc. of SPIE* **4320**: 815-821, 2001

2) 遠藤真広、角尾卓紀、神立　進、棚田修二、荒舘　博、斎藤泰男：４次元 CT－その概念と設計．第８１回日本医学物理学会報文集、pp.56-57、2001

3) 角尾卓紀、遠藤真広、佐藤一雅：コーンビーム CT における散乱線除去．第８１回日本医学物理学会報文集、pp.56-57、2001

4) Nakamori N, Yang YQ, Yoshida Y, Tsunoo T, Endo M, Satoh K: Monte Carlo analysis of relation between patient dose and noise characteristics of flat-panel detector for

cone-beam CT. *Proc of SPIE* **4682**: 724-731, 2002

5) Endo M, Tsunoo T, Kandatsu S, Tanada S, Aradate H, Saito Y: 4-dimensional computed tomography (4D CT) – Its concepts and preliminary development. *2001IEEE NSS Conf Record*, M7-6, 2002

6) Endo M, Tsunoo T, Kandatsu S, Tanada S, Aradate H, Saito Y, Kusakabe M, Satoh K, Matsusita S: Development and performance evaluation of the first model of 4D CT-scanner. *Proc. of CARS2002,* pp.372-376, 2002

7) 中森伸行、楊　義強、吉田靖夫、角尾卓紀、遠藤真広、佐藤一雅：コーンビーム型 CT 画像のノイズ除去と被曝線量の低減．第８３回日本医学物理学会報文集、pp.156-159, 2002

8) 遠藤真広、角尾卓紀、森　慎一郎、神立　進、棚田修二、荒舘　博、斎藤泰男、日下部　正宏、佐藤一雅、松下　聡：４次元 CT 試験機の開発と性能評価．第２１回日本医用画像工学会大会報文集、OP8-37, 2002

9) Endo M, Mori S, Tsunoo T, Kandatsu S, Tanada S, Aradate H, Saito Y, Miyazaki H, Satoh K, Matsusita S, Kusakabe M: Development and performance evaluation of the first model of 4D CT-scanner. *Proc of KJMP2002*, pp.373-375, 2002

10) Mori S, Endo M, Tsunoo T, Kandatsu S, Tanada S, Aradate H, Saito Y, Miyazaki H, Satoh K, Matsusita S, Kusakabe M: Basic performance evaluation of the first model of 4-dimensional CT-scanner. *Proc of KJMP2002*, pp. 376-378, 2002

11) Mori S, Endo M, Tsunoo T, Kandatsu S, Tanada S, Aradate H, Saito Y, Miyazaki H, Satoh K, Matsusita S, Kusakabe M: Basic performance evaluation of the first model of 4-dimensional CT-scanner. *Proc of SPIE* **5030**: 702-710, 2003

12) Endo M, Mori S, Tsunoo T, Kandatsu S, Tanada S, Aradate H, Saito Y, Miyazaki H, Satoh K, Matsusita S, Kusakabe M: Performance evaluation of the first model of 4D CT-scanner. *Proc of CARS2003*, pp.19-25, 2003

13) 松本政雄、末兼浩司、角尾卓紀、遠藤真広：４次元 CT 装置の高速平面検出器の物理特性とスペクトル．第８５回日本医学物理学会報文集、pp.148-150, 2003

14) 森　慎一郎、遠藤真広、角尾卓紀：４D CT における散乱線の画質への影響．第８５回日本医学物理学会報文集、pp.151-153, 2003

15) 森　慎一郎、遠藤真広、西澤かな枝、青山隆彦、角尾卓紀：４次元 CT における線量分布の精確な測定．第８６回日本医学物理学会報文集、pp.200-203, 2003

16) 松本政雄、末兼浩司、角尾卓紀、遠藤真広：４次元 CT 用高速２次元検出器の画像特性の評価について．２００４年度日本写真学会秋季大会・研究発表会講演要旨集、pp.76-77, 2004

17) Endo M, Mori S, Tsunoo T, Nishizawa K, Aoyama T.: Dose profile measurement of a four-dimensional CT (4D-CT). *Proc of SPIE* **5368**: 596-609, 2004

18) 中土裕樹、渡辺直行、中土幸男、但野　茂、森　慎一郎、遠藤真広：コーンビーム型３次元 CT 画像より構築したヒト大腿骨近位部の有限要素モデル．第１６回バイオエンジニアリング講演会報文集、pp.155-156, 2004

19) Nakatsuchi H, Watanabe N, Nakatsuchi Y, Tadano S, Moriizumi T, Mori S, Endo M: Biomechanical role of trabecula networks in the human proximal femur under static

loading, *Proc of IMECE2004-60100* (CD-ROM), 2004

20) 森　慎一郎、遠藤真広、西澤かな枝、角尾卓紀：４次元 CT における散乱線を考慮に入れた線量分布測定：16 列マルチディテクタ CT との線量比較．第８８回日本医学物理学会報文集、pp. 192-193, 2004

21) Mori S, Endo M, Tsunoo T, Kandastu S, Tanada S, Funabashi N, Suzuki M: Performance evaluation of the first model 4D CT. *Proc of the Japan-France Workshop on Radiobiology and Isotopic Imaging*, pp. 153-158, 2004

22) Mori S, Endo M, Tsunoo T, Murase K, Fujiwara H: Evaluation of weighted FDK algorithms applied to four-dimensional CT (4D-CT). *2004IEEE NSS/MIC Conf Record*, M5-450, 2005

23) Mori S, Endo M, Kohno R, Minohara S, Kohno K, Asakura H, Fujiwara H, Murase K: Respiratory-gated segment reconstruction for radiation treatment planning using 256-slice CT-scanner during free breathing. *Proc of SPIE* **5745**: 711-721, 2005

24) 森　慎一郎、河野良介、遠藤真広、池田　恢、池田　剛、榎戸義浩、高橋　豊、遠山尚紀、成田　雄一郎、西尾禎治、羽生祐二、水野秀之：呼吸性移動を考慮した治療計画ＣＴ画像の物理的評価．第８９回日本医学物理学会報文集、pp. 192-193, 2005

25) Asakura H, Mori S, Endo M: A study of (3+1)-dimensional charged particle therapy by using 4D CT-Scanner. *Proc of KJMP2005,* pp. 192-193, 2005

26) Mori S, Asakura H, Endo M: Improved respiratory-gated CT scan method for four-dimensional radiation therapy planning. *Proc of KJMP2005*, pp. 155-158, 2005

27) Oono M, Mori S, Endo M, Akahane K, Iwai K, Nishizawa K: Patient doses under 4D-CT examination. *Proc of KJMP2005*, pp. 310-311, 2005

28) Endo M, Mori S, Kandatsu S, Tanada S, Sugihara N, Saito Y, Adachi A, Miyazaki H: Development of real 4D CT with real-time reconstruction and display. *2005IEEE NSS/MIC Conf Record*, M11-252 (in press)

◆総説・その他

1) 遠藤真広：４次元 CT 装置の開発とこれからの展開．新医療、pp.98-101, 2002(12)

2) 遠藤真広、角尾卓紀、森　慎一郎、神立　進、棚田修二、荒舘　博、斎藤泰男、宮崎博明、佐藤一雅、松下　聡、日下部　正宏：４次元 CT 装置の開発．映像情報メディカル **34**:1400-1403, 2002

3) 遠藤真広、角尾卓紀、森　慎一郎、神立　進、棚田修二、荒舘　博、斉藤泰男、宮崎博明、佐藤一雅、松下　聡、日下部　正宏：四次元 CT の開発の現状．日獨医報 **48**: 248-255, 2003

4) 遠藤真広：４次元 CT の研究開発－その基礎的側面－．医学物理 **23**(Sup.4): 13-28, 2003

5) 遠藤真広：４次元 CT の開発とその応用．RADIOISOTOPES **52**: 705-711, 2003

6) 船橋伸禎、遠藤真広、棚田修二：立体 CT の可能性を探る．Medical Tribune Circulation Today 2004 12/23 循環器疾患版

7) 船橋伸禎、遠藤真広：四次元立体 CT―心大血管、脳、肝、腎への新しい画像診断の応用

Four-dimensional computed tomography. 医学のあゆみ **210**: 701-702, 2004
8) 片田和廣：画像診断法の過去・現在・未来－CT 領域. 日獨医報 **50**: 30-39, 2005
9) 遠藤真広、森　慎一郎：４次元 CT の開発と臨床利用の展望. MEDICAL IMAGING TECHNOLOGY **23**: 69-76, 2005
10) 片田和廣：高速マルチスライス CT の開発と臨床応用. 最新医学 **60**: 965-973, 2005
11) 森　慎一郎：4 次元診断から４次元治療へ. 放射線科学 **48**: 145-154, 2005
12) 森　慎一郎、遠藤真広、近藤千里：256 列 CT が可能とする医療. 新医療、pp. 50-53; 2005(10)
13) 遠藤真広、森　慎一郎、神立　進、棚田修二、近藤千里：４次元 CT 装置－画質評価と臨床応用. 映像情報メディカル **37**: 1372-1377, 2005

◆特許

1) 遠藤真広、森　慎一郎：ファントムおよびファントム集合体、特許願 2003-427312、2003 年 12 月 24 日出願
2) 遠藤真広、森　慎一郎：ヒール効果補正フィルタおよびＸ線照射装置並びにＸ線ＣＴ装置、特許願2003-427312、2004年3月29日出願
3) 森慎一郎、鈴木昌彦：駆動装置、動態撮影システム及び動態撮影方法、特許願2004-341290、2004年11月25日出願
4) 森慎一郎、遠藤真広：運動部分のCT撮影方法及び装置、特許願2005-127123、2005年4月25日出願
5) 森慎一郎、遠藤真広：CT 投影データの差分画像再構成法及び装置、特許願 2005-375659、2005 年 12 月 27 日出願

2. 解　　説

特集 CT技術のブレイクスルー

4次元CT装置の開発

放射線医学総合研究所重粒子医科学センター[*1]／東芝・医用システム社[*3]
ソニー・コーポレートテクノロジー部[*3]／福井大学工学部[*4]
遠藤真広[*1]／角尾卓紀[*1]／森慎一郎[*1]／神立進[*1]／棚田修二[*1]／荒舘博[*2]
斎藤泰男[*2]／宮崎博明[*2]／佐藤一雅[*3]／松下聡[*3]／日下部正宏[*4]

はじめに

1973年のCTの登場以来、動く臓器のダイナミック・ボリュームイメージングはこの分野の究極の夢と考えられてきた。早くも1980年代の前半に米国のメーヨークリニックにおいて、心臓のダイナミック・ボリュームイメージングを目的として、Dynamic Spatial Reconstructor (DSR) の開発が試みられている[1]。DSRは1秒間に20ボリュームの撮像をめざすという極めて野心的な装置であったが、当時のX線検出技術やコンピュータを中心とするデジタル信号処理技術ではその要求を満足することができなかったため、壮大な失敗に終わった。

しかし、その後のCT技術の進歩によりDSRの夢を実現することは不可能ではなくなってきた。ダイナミック・ボリュームイメージングを行うCT装置の開発により、診断だけではなくインターベンション治療にも新たな応用が切り開かられると予想される。放射線医学総合研究所では、このような装置を3次元画像に時間の次元を加えるという意味で4次元CTと名付け、数年前から東芝やソニーと共同でその開発を進めてきた。最近ようやくその試験機を完成させたが、この稿では著者らの行ってきた4次元CTの開発の現状について述べることにする。

4次元CTの原理とその実現法

4次元CTを行うためには短時間かつ連続的にボリュームデータ (3次元データ) を取得せねばならない。現在、ヘリカルCTが大変に発展し、ボリュームデータの取得は容易となったが、寝台の移動を伴うヘリカルCTでは、ボリュームデータの連続的収集は原理的に困難である。したがって、4次元CTの実現には寝台を動かさずにボリュームデータの取得が可能なコーンビームCTの採用が必要である。コーンビームCTでは、**図1**に示すようにコーンビームを連続回転することにより、ダイナミック・ボリュームデータ (4次元データ) を得ることができる。

コーンビームCTは既にDSRでも採用された方法であり、その後もボリュームデータを得る方法として、著者らを含めていくつかのグループで研究されてきた[2~5]。コーンビームCTを行う上での大きな問題は、2次元検出器に何を用いるかということである。数年前まではコーンビームCTに使用可能なサイズと空間分解能を有する検出器はX線テレビしかなかった。しかし、X線テレビでは検出可能な信号のダイナミックレンジは高々10ビットであり、CT検出器に要求される16～18ビットには足りない。このためこの方式のCTは、肺、骨、造影血管など高コントラストな被写体のボリュームデータの取得には威力を発揮したが、

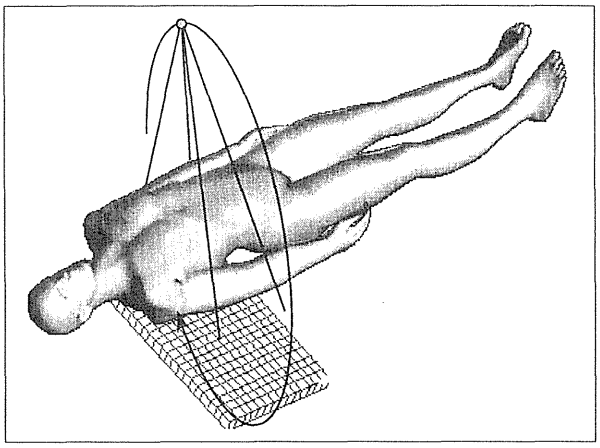

図1　コーンビームCTの原理
コーンビームを1回転することによりボリュームデータが取得でき、連続回転することによりダイナミック・ボリュームイメージングを行うことができる。

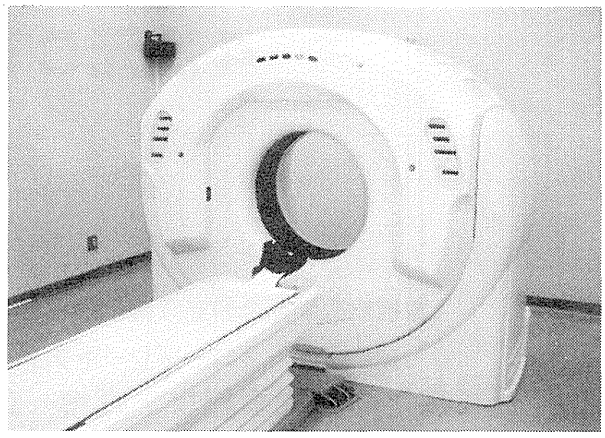

図2　4次元CT試験機の外観写真

CTが主な対象とする低コントラスト被写体の描出は困難であった。

最近、X線の2次元検出器我々として、フラットパネル検出器(FPD)が開発され、臨床に使用されるようになった。FPDはデジタル的にX線画像を取得できる方法であり、透視装置として用いた場合、従来のX線テレビよりもダイナミックレンジが広い(12～14ビットといわれている)。したがって、FPDをコーンビームCTの検出器として用いれば、従来のX線テレビを用いる方法より低コントラスト認識能が向上することが予想される。このためFPDを用いた研究開発が現在盛んに行われている。

しかし、以下の2つの理由によりFPDでも4次元CTに用いるには十分とはいえない。すなわち、①FPDのデータ収集速度が30～60フレーム／秒であり、現在のCTと同等のレートでボリューム撮像するのに必要な900～1800フレーム(ビュー)／秒に比べてはるかに遅い。したがって、短い間隔でのダイナミックな撮影は困難である。②散乱線の除去が困難なためCT値の定量性は期待できない。

著者らは上記の理由によりFPDを4次元CTに用いることは断念し、現在のCT検出器の技術にもとづき新しい2次元検出器を製作した[6]。そして、最新の商用CTのガントリーに取り付けることで4次元CTの機能試験機(図2)を完成させた。以下にその概要を紹介したい。

4次元CT試験機の概要

ガントリーの回転機構には、最新の商用装置である(株)東芝製アクイリオンの機構を利用し、その上に、X線発生装置および検出機構を取り付けた。回転機構は0.5秒/回転の速度で回転する能力を持つが、取り付けた装置の設計が必ずしも対応していないため、本試験機においては1秒/回転に制限して使用している。また、広いコーン角で一様な強度を得るため、X線管は回転軸に対して少し傾けて取り付けてある。

2次元検出器は、ピクセル毎に独立の検出素子を持ついわゆる離散型ピクセル検出器である。この検出器はマルチスライスCT用検出器技術を発展させて製作したものであり、シンチレータとフォトダイオードにより構成される。検出素子数は912(チャンネル)×256(セグメント)であり、検出素子のサイズは約1mm×1mmである。データ収集速度は900ビュー(フレーム)/秒、A/Dコンバータのダイナミックレンジは16ビットである。シンチレータは素子毎に独立していて、通常のCTと同じ材質からできている。フォトダイオードはマルチスライスCTと同じように単結晶シリコン上に形成される。

利用可能な単結晶シリコンウェファーの大きさに制限があることにより、検出器はタイル貼り構造となっている。すなわち、1枚のウェファーから作られる検出素子のブロックは24(チャネル)×

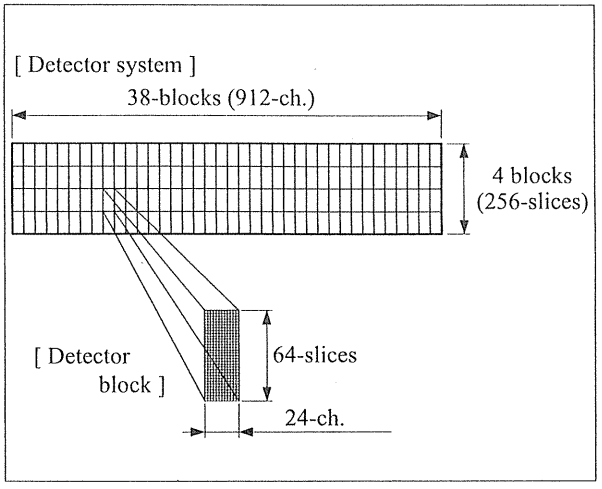

図3　検出器の構成
検出器は24チャネル×64セグメント(スライス)のブロック38×4個により構成される。

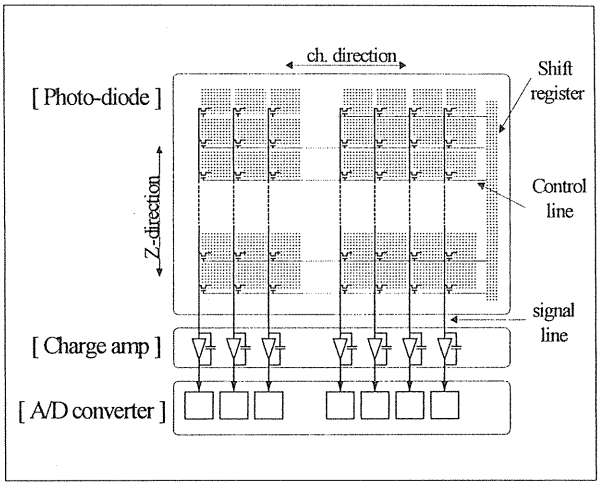

図4　データ収集システムのブロック・ダイヤグラム

64(セグメント)＝1536素子からできていて、検出器全体は38×4＝152ブロックで構成されている(**図3**)。

2次元検出器には、検出素子の間隔で薄いモリブデン平板を体軸と平行に配列したコリメータが取り付けられている。モリブデン平板の高さとコリメータ間隙の比であるコリメータ比は30：1である。

データ収集システムは通常のCT装置とは異なり、むしろフラットパネル検出器(FPD)と類似し、フォトダイオードに蓄積される電荷をチャンネル毎に読み出す方式を採用している(**図4**)。しかし、単結晶シリコンの利用と読み出し回路と1：1に接続することにより、FPDよりはるかに高速なデータ収集を可能としている。

連続回転するガントリーにおいては、収集されたデータは回転部分から静止部分に高速に伝送する必要があり、これは光通信の技術を応用して実現した。データ伝送システムに要求される伝送率は、正味の伝送率3.4Gbps(＝912×256×900×16)に誤り訂正符号や伝送制御符号などのオーバーヘッドを付加するとほぼ5Gbpsとなる。

この仕様を満たすため、それぞれが622Mbpsの伝送速度を持つレーザーダイオードーフォトダイオードを12対用いた。このシステムの伝送速度は、12×622Mbps＝7.4Gbpsとなり5Gbpsより大きいが、その差は伝送をスムーズに行うための設計余裕である。

ボリュームデータはFeldkamp－Davis－Kress(FDK)[7]アルゴリズムにより再構成される。再構成装置は128個のプロセッサを並列に使用することで、900ビューから512×512×256のボリュームを約6分で計算できる。

試験機での研究

現在、本試験機は放射線医学総合研究所に設置されていて、装置の調整と並行してファントムによる基礎的特性の評価や正常ボランティアの撮影を行っている。ファントム実験の結果、本試験機により取得された画像の空間分解能や画像ノイズのような画像特性は、従来のCT画像と同程度であることがわかった。また、FDKアルゴリズムは不完全再構成のため、それに由来するアーチファクトが発生するが、現在までの限られた経験では臨床画像においてはほとんど問題にならないとの感触を得ている。**図5**はボランティアの3次元画像を示すが、これは一連のダイナミック3次元画像(4次元画像)から切り出したものである。今後、4次元画像の可能性を検討するため、患者に対する臨床研究を行う予定である。

また、現在の装置は画像再構成に6分を要していて、インターベンション治療など新しい応用を行う際には、問題となることが予想される。これ

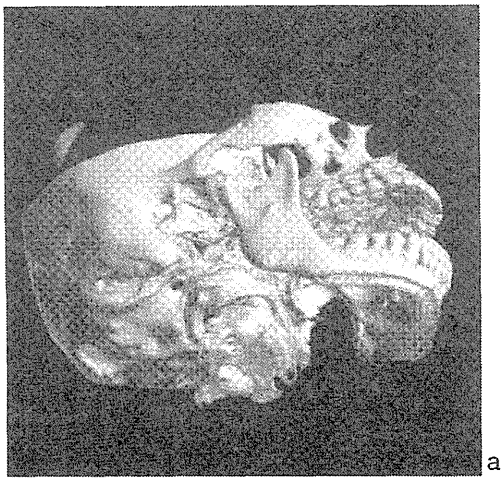
a

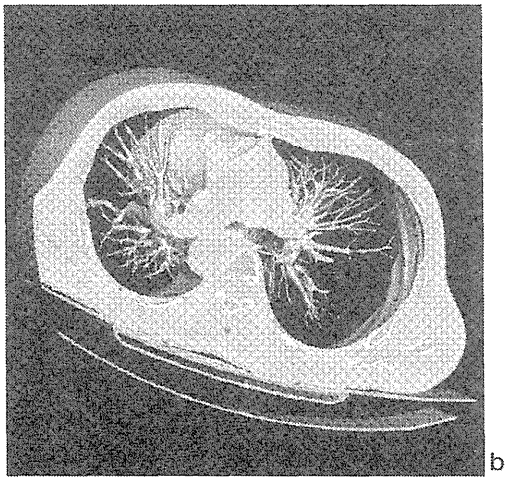
b

図5　4次元画像から切り出された3次元画像（実際には0.1秒間隔で30ボリュームが再構成され動画として表示されている）
a：頭部画像
b：胸部画像

表1　4次元CT1号機と2号機の比較

	1号機	2号機
スキャンモード	コーンビーム連続（4D）	コーンビーム連続（4D） ヘリカルコーンビーム（大視野3D）
検出器	912×256素子、1×1mm素子サイズ 16ビット、900ビュー/秒	左に同じ
スキャン速度	1秒/回転（最大30秒間連続）	0.5秒/回転（最大30秒間連続）
再構成マトリックス	512×512×256	512×512×512
コントラスト分解能	0.5%以下	左に同じ
再構成時間	512×512×256に対して6分	512×512×128に対して1秒以下

に対応するため、次世代のField Programmable Gate Array（FPGA）を用いた再構成装置を開発していて、2003年度中に完成する2号機に搭載することを計画している。**表1**は本報告の試験機（1号機）と2号機の仕様を比較したものである。表からわかるように第2号機はより本格的な装置であり、その仕様を決めるためにも第1号機で現在行っている研究の重要性は高い。

以上4次元CTの研究の概略を述べたが、著者らの研究が一つの契機となり、今後CTの研究は3次元から4次元へと進展していくと予想している。

謝辞

本研究は新エネルギー・産業技術開発機構（NEDO）の援助を受けて行われたことを明らかにするとともに、NEDOの関係者に対して深く感謝いたします。

文献

1) Robb RA : The dynamic spatial reconstructor: An x-ray video-fluoroscopic CT scanner for dynamic volume imaging of moving organs. IEEE Trans Med Imag 1 : 22-33, 1982
2) Saint-Felix et al : In vivo evaluation of a new system for computerized angiography. Phys Med Biol 39 : 585-595, 1994
3) Ning R et al : Image intensifier-based computed tomography volume scanner for angiography. Academic Radiology 3:344-350, 1996
4) 隈崎達夫ほか：I.I.検出型コーンビーム3D・CTの臨床応用. Medical Imaging Technology 15 : 387-388, 1997
5) Endo M et al : Development of a 3D CT-scanner using a cone beam and video-fluoroscopic system. Radiation Medicine 16: 7-12, 1998
6) Saito Y et al : Large area 2-dimensional detector for real-time 3-dimensional CT (4D-CT). Proc. of SPIE 4320 : 775-782, 2001
7) Feldkamp LA et al : Practical cone-beam algorithm. J Opt Soc Am A1 : 612-619, 1984

特集2 CT技術のブレイクスルー2006

4次元CT装置 ―画質評価と臨床応用―

放射線医学総合研究所重粒子医科学センター[*1]／東京女子医科大学放射線科核医学部[*2]
遠藤真広[*1]／森　慎一郎[*1]／神立　進[*1]／棚田修二[*1]／近藤千里[*2]

はじめに

1973年のCTの登場以来、動く臓器のダイナミック・ボリュームイメージングはこの分野の究極の夢と考えられてきた。早くも1980年代前半に米国のメーヨークリニックにおいて、心臓のダイナミック・ボリュームイメージングを目的として、Dynamic Spatial Reconstructor (DSR) の開発が試みられている[1]。DSRは1秒間に20ボリュームの撮像をめざすという極めて野心的な装置であったが、当時のX線検出技術やコンピュータを中心とするデジタル信号処理技術ではその要求を満足することができなかったため、壮大な失敗に終わった。

しかし、その後のCT技術の進歩によりDSRの夢を実現することは不可能ではなくなってきた。ダイナミック・ボリュームイメージングを行うCT装置の開発により、診断だけではなくインターベンション治療にも新たな応用が切り開かれると予想される。放射線医学総合研究所では、このような装置を3次元画像に時間の次元を加えるという意味で4次元CTと名付け、数年前から東芝やソニーと共同でその開発を進めてきた[2]。3年半前に試作1号機を完成させ[3]、ファントムによる画質評価、動物実験、臨床試験を行ってきた。また、本年3月には、大幅に機能を向上した試作2号機を完成させている。本誌においても2002年12月号で試作1号機の開発について報告したが[4]、この稿ではその後の研究の推移を、主にファントムによる画質評価と臨床応用について述べることにする。

4次元CT試験機の概要

4次元CT装置の原理や構成は前報[4]において詳述したので、この稿では仕様の概略を述べる。4次元CT装置は、912（チャンネル）×256（セグメント）の2次元検出器を持つコーンビームCT装置であり、256スライス（検出器列）CT装置ということもできる。

表1は試作1号機と2号機の仕様を示したものであり、表に示すように2号機においては、スキャン速度、検出器のダイナミックレンジ、再構成速度に大幅な改善がなされていることがわかる。また、ヘリカルコーンビーム収集、心電図同期再構成、プログラムスキャンなど臨床ソフトも充実し実用段階に入っているといえる。

2号機においては、3次元画像のリアルタイムビューアー（4次元ビューアー）も付属していて、取得した画像の観察の便宜をはかっている。**表2**は4次元ビューアーの仕様を示したものである。**図**

表1　4次元CT1号機と2号機の比較

	1号機	2号機
スキャンモード	コーンビーム連続（4次元）	コーンビーム連続（4次元） ヘリカルコーンビーム（大視野3次元） 心電図同期再構成
検出器	912×256素子、1×1mm素子サイズ、16ビット、900ビュー/秒	912×256素子、1×1mm素子サイズ、18ビット、900ビュー/秒
スキャン速度	1秒/回転（最大30秒間連続）	0.5秒/回転、1秒/回転（最大60秒間連続、プログラム可能）
再構成マトリックス	512×512×256	512×512×256
コントラスト分解能	0.5%以下	左に同じ
再構成時間	512×512×256に対して6分	512×512×128に対して1秒以下

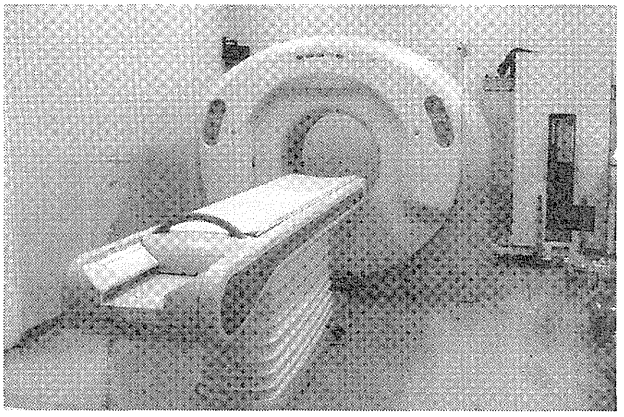

図1　試作2号機の外観写真

1は2号機の外観写真を示しているが、外観は1号機やこれらの元となった東芝メディカルシステムズ㈱のAquilion（アクイリオン）とほとんど変わらない。

ファントムによる画質評価

これらの試験機の静止画像の画質評価をファントムにより行った。ここでは、1号機の結果[5]を1～3節で述べ、2号機での改善点について4節でふれる。

1）均一性と画像ノイズ

均一性と画像ノイズを標準的な水ファントムにより評価した。直径200mm、長さ250mmの水ファントムを視野の中心に置き、X線管電圧120kV、管電流200mA、スキャン時間1秒で撮影し、0.468×0.468×0.500mm³のボクセルで再構成した。マトリックスサイズは512×512×256であり、体軸方向の有効視野は約100mmである。同じファントムを16スライスのMD CT（SOMATOM Volume Plus4）により、管電圧、管電流とスキャン時間の積などを同一条件で撮影し、結果を比較した。ただし、MD CTのボクセルサイズは、0.468×0.468×0.750mm³であった。**図2**および**図3**にその結果を示す。

表2　4次元ビューアーの仕様

リアルタイム3次元表示（ボリュームレンダリングおよび3断面MPR表示）	ボリュームサイズ：512×512×256 入力データレート：10ボリューム/秒 表示画像サイズ：512×512 画像生成レート：10フレーム/秒
シネレビュー3次元表示（ボリュームレンダリングおよび3断面MPR表示）	ボリュームサイズ、表示画像サイズ、画像生成レートはリアルタイム表示と同じ。入力データレートを0～10ボリューム/秒で可変とする。

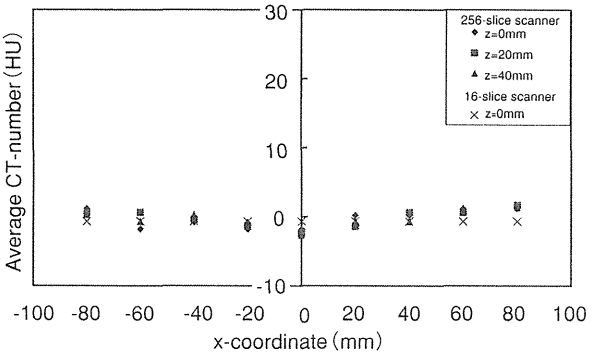

図2　CT値の一様性
平均CT値とROI位置の関係を示す[5]。

図2はCT値の均一性を評価するため、水ファントムの直径に沿って20mmおきに設定した10mm直径のROI（関心領域）内のCT値の平均値を求めたものである。図の横軸はROIの中心位置の座標を示す。図より4次元CT（256スライス）の均一性はz座標（体軸方向の座標を示す）に依存せず、またMD CT（16スライス）と同様であることがいえる。

また、**図3**は画像ノイズを評価するため、**図2**と同じROI内のCT値の標準偏差を求めたものである。図より4次元CTの画像ノイズはz座標に依存せず、MD CTとでほぼ同じ大きさであるこ

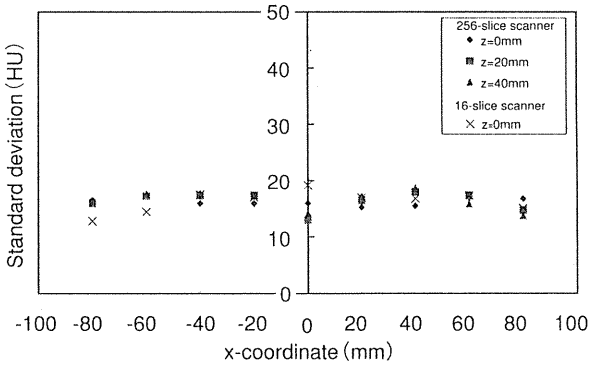

図3　画像ノイズの大きさ
CT値の標準偏差とROI位置の関係を示す[5]。

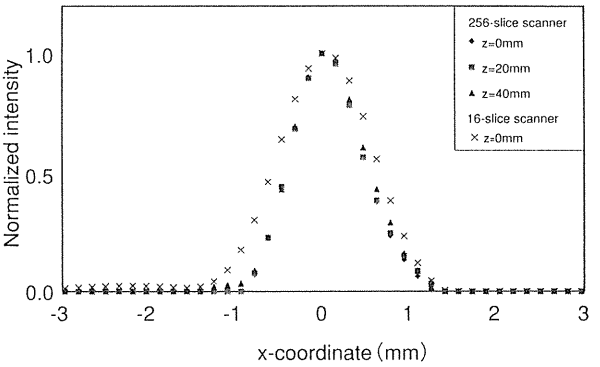

図4　横断面におけるCT値のプロフィール（点広がり関数）
4次元CT（256スライス）とMD CT（16スライス）について比較している[5]。

表3　4次元CT（256スライス）とMD CT（16スライス）の横断面内空間分解能の比較
点広がり関数のFWHMとFWTM（いずれもmm単位）を示す。括弧内は中心でのビームサイズ（256スライス0.58mm、16スライス0.75mm）に対する相対値[5]。

	256-slice scanner			16-slice scanner
	z=0mm	z=20mm	z=40mm	z=0mm
FWHM	0.94 (1.62)	0.95 (1.64)	0.98 (1.69)	1.26 (1.68)
FWTM	1.74 (3.00)	1.80 (3.10)	1.82 (3.13)	2.54 (3.39)

表4　4次元CT（256スライス）とMD CT（16スライス）のz方向空間分解能の比較
スライスプロフィールのFWHMとFWTM（いずれもmm単位）を示す。括弧内は中心でのビームサイズ（256スライス0.50mm、16スライス0.75mm）に対する相対値[5]。

	256-slice scanner			16-slice scanner
	z=0mm	z=20mm	z=40mm	z=0mm
FWHM	1.18 (2.36)	1.26 (2.52)	1.32 (2.64)	0.78 (1.04)
FWTM	1.85 (3.70)	2.03 (4.06)	2.07 (4.14)	1.37 (1.83)

とがいえる。

2）空間分解能

空間分解能は、Phantom Laboratory社製のCatphan 500を用いて測定した。このファントムには、0.288mm直径の炭化タングステン製の球が埋め込まれているが、球の部分を通る横断面と縦断面画像からCT値のプロフィールを求めた。撮影条件は、どちらのCTもX線管電圧120kV、管電流200mA、スキャン時間1秒とした。また、プロフィールの標本間隔を細かくするため、ズーム再構成を用いた。

図4は横断面におけるプロフィール（点広がり関数）を示している。図より、4次元CTの空間分解能の方がMD CTよりも良いことがわかる。**表3**は、**図4**よりそれぞれの曲線のFull Width at Half Maximum（FWHM）とFull Width at Tenth Maximum（FWTM）を求めたものである。いずれの値も4次元CTにおいてz座標依存性はほとんどなく、またMD CTよりも良いことがわかる。ただし、この空間分解能の差は、本質的なものではなく、両方のCTの検出器サイズによるものであり、それを補正することによりほとんど同じとなる（**表3**の括弧内の値）。

同様にして縦断面におけるz方向のプロフィールを求め、それから得たFWHMとFWTMを**表4**に示す。**表4**から、z方向の空間分解能は、MD CTの方が優れていることがわかる。また、4次元CTのz方向分解能はz方向の依存性があることもわかる。4次元CTのz方向の分解能が劣る理由は、z方向のX線強度分布の一様性を高めるため、X線管を少し傾けているが、これによりその実効焦点が大きくなることによる。また、z方向分解能のz方向の依存性は、実効焦点サイズの角度依存性で説明できる。

3）被ばく線量

被ばく線量はCT dose index（CTDI）により評価した。ここで、ビームのコリメータ幅が回転中

表5　被ばく線量（CTDI）の比較[5)]

Scanner	Nominal beam width (T)	Measured beam wifth (T')	CTDIcenter (mGy/100mAs)	CTDIperiphery (mGy/100mAs)	CTDIw (mGy/100mAs)
256-slice CT	128mm	140mm	21.4	22.9	22.4
16-slice CT	12mm	18mm	17.9	18.0	18.0

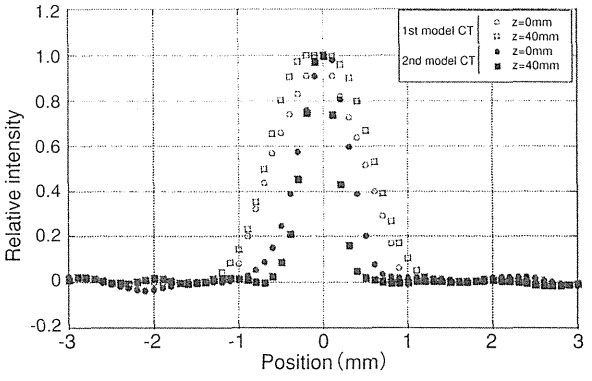

図5　1号機と2号機のz方向の空間分解能の比較
スライスプロフィールを示す[7)]。

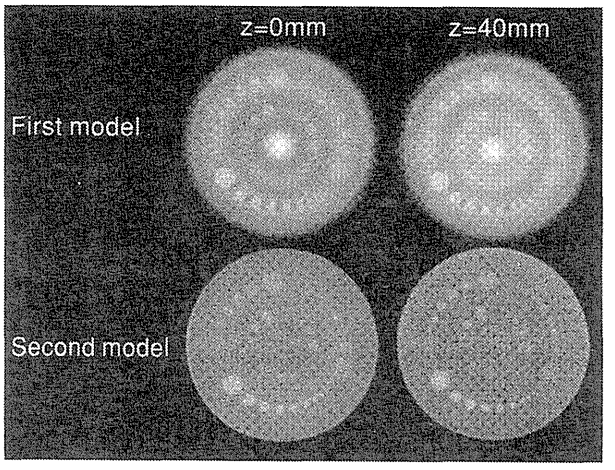

図6　低コントラストファントムの画像の比較
CT値の差は、1.5%、1.0%、0.5%。上が1号機、下が2号機の画像。低コントラストの認識能は著明に改善されている[7)]。

心で約128mmと大きいため、通常の2倍の長さとなる300mmのファントムを用いた。なお、ファントム直径は160mmである。CTDI測定用の線量計の有感領域の長さが100mmであるので、ファントムの長軸方向のすべての位置での線量を積算するため、ファントム内で100mmずつ移動して3回測定を行った。CTDIはこの3回の測定値から以下の式で計算した。

$$CTDI=\frac{1}{T}\sum_{i=1}^{3}IC_i$$

ここで、Tは名目的なビーム幅（=128mm）であり、IC_iは電離箱の出力である。

表5に測定結果を示す。表のT'は実測されたビーム幅であり、名目幅Tよりやや大きい。これは、MD CTやその延長である4次元CTでは、半影部分が検出器に入らないように、その分ビーム幅を広げていることによる。$CTDI_W$とは、中心の$CTDI_{center}$と周辺の$CTDI_{periphery}$から次式により計算した平均的な$CTDI$である。

$$CTDI_w=(\frac{1}{3}CTDI_{center}+\frac{2}{3}CTDI_{periphery})$$

表よりCTDIは、4次元CT（256スライス）の方がやや大きいが、これは横断面の空間分解能が良いことの代償ともいえ、総合的に判断する必要がある。なお、4次元CTを含んでMD CTでは、従来のCTDIの考え方では、被ばく線量評価のために十分ではないところがある。これについては、著者らの論文を見られたい[6)]。

4）試作2号機における改善

以上をまとめると、試作1号機においては、画像ノイズや一様性は、4次元CTは商用のMD CT並みであり、横断面の空間分解能は4次元CTが優れているが、これは被ばく線量と合わせて総合的に評価する必要がある。また、4次元CTはz方向の空間分解能においては劣ることが確認された。また、ここでは比較を示していないが、低コントラスト認識能においても4次元CTは劣っていた。これは、1号機の画像処理ソフトウェアが検出器特性に対して最適化されていないことによると考えられる。

2号機においては、これらのすべてが改善された[7)]。雑音と被ばく線量は、同じ撮影条件に対して1、2割改善された。横断面内の空間分解能は1

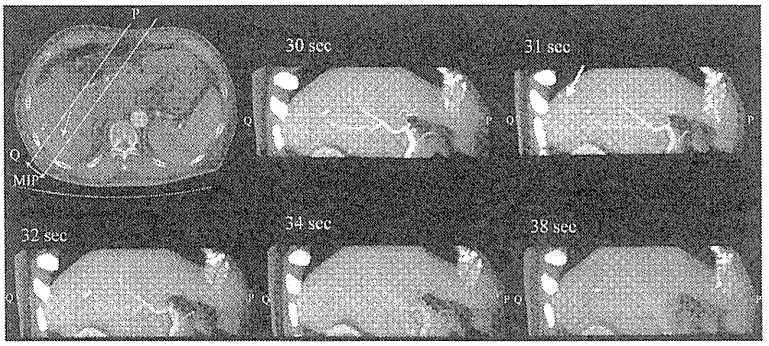

図7a | 図7b | 図7c
図7d | 図7e | 図7f

図7　肝細胞がんの造影検査
aに示すオブリーク面に対して時間変化を追跡している。動脈からの流出（bからe）、静脈への流入（dからf）が観測され、腫瘍（cの矢印）との位置関係、腫瘍の濃染される時期がわかる[13]。

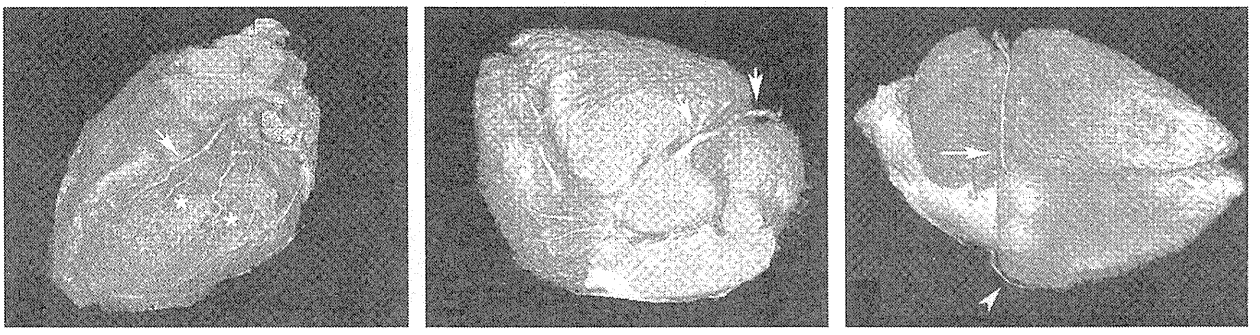

図8　正常人の心臓造影画像（3次元画像）
心電図には同期していない。a：左前下行枝（矢印）や対角枝（星印）が描出されている。
右冠状動脈の根幹（b）から辺縁（c）が描出されている[14]。

図8a | 図8b | 図8c

号機とほとんど同じであったが、z方向の空間分解能は**図5**に示すように劇的に改善された。これは、z方向の強度分布が一様でかつ焦点サイズの小さいX線管を開発して使用したことによる。また、**図6**に示すように低コントラスト認識能も大幅に改善された。以上のように、試作2号機では特に1号機で商用装置に比べて劣っている点が大幅に改善され、これにより商用装置の最高性能のものと肩を並べるか、またはそれをも凌駕する段階に達したと考えられる。

臨床応用

これらの試作機を用いて行った臨床試験について若干の結果を述べる。試作1号機においては、ブタを用いた動物実験も精力的に行ったが、それについては著者らの文献[8～12]を参照されたい。

1）肝腫瘍の造影

肝腫瘍の造影CTにおいては、比較的に広い範囲の造影剤の動態を追跡する必要があり、4次元CTの良い適用と考えられる。

これを確かめるため、試作1号機により肝腫瘍の患者3人に対して、経静脈的な造影検査を行った。90mlのヨウ素造影剤（Iopamiron 370）を3.5ml/sの速度で末梢静脈より注入した。注入開始から30秒後から10秒間の連続スキャンにより4次元画像を得た。**図7**はこのようにして得られた4次元画像からオブリーク断面を作成し、その経時的な変化を見たものである。図より動脈からの流出（bからe）と静脈への流入（dからf）が観測され、腫瘍との位置関係や腫瘍が濃染される時期との関係もわかる[13]。

2）冠状動脈の造影

良く知られているように、MD CTの登場により冠状動脈疾患へのCTの応用が著しく進んだ。特に心電図同期ヘリカルCTにより、経静脈法により冠状動脈撮影ができるようになったことは、心臓疾患の検査法を大きく変えたといい得る。そして、MD CTのスライス数が、4、16、64と増大するにつれて、冠状動脈撮影がより容易になってきている。この極限は、より多列のCTを用いて寝台移動を伴わないスキャンで心臓撮影を行う

ことであると容易に想像できる。

我々は、このような寝台移動を伴わないスキャンで心臓撮影を行うべく、4次元CT装置を用いて研究を行ってきた。その結果、**図8**に示すように冠状動脈を心電図非同期のハーフスキャンにより撮影できることがわかった。この図は試作1号機により得られたもので、1秒/回転のため時間分解能は約500ミリ秒であるが、冠動脈の主な分枝は鮮明に描出されている[11]。試作2号機の0.5秒/回転による撮影も既に行っていて、さらに良い結果を得ているが、これについては進行中の研究であるので割愛したい。

試作2号機においては上記以外、肺がんの呼吸移動の解析と4次元治療計画への応用、COPD(慢性閉塞性肺疾患)における運動性の解析などを行っていて、今後、順次公表する予定である。

おわりに

以上述べたように我々が開発してきた4次元CT装置は、臨床ソフトウェアが充実し、画質的にも従来の商用装置と肩を並べるかそれを凌駕するほどになり、ほぼ実用段階に達したものと考えられる。今後、遠くない時期に商品化が行われると考えるが、そのときには、ここで述べた循環器診断や4次元放射線治療への応用がさまざまな形で行われるとともに、さらに、インターベンション治療への応用も行われよう。これによりCTは、また新たな時代に突入すると期待される。

謝辞

本研究は放射線医学総合研究所の関係者、4次元CT研究班、東芝メディカルシステムズ㈱との協力により行われたものである。関係各位に深く感謝いたします。

参考文献

1) Robb RA : The dynamic spatial reconstructor: An x-ray video-fluoroscopic CT scanner for dynamic volume imaging of moving organs. IEEE Trans Med Imag 1: 22-33, 1982
2) Endo M et al: Four-dimensional computed tomography (4D CT) - Concepts and preliminary development. Radiation Medicine 21: 17-22, 2003
3) Endo M et al: Development and performance evaluation of the first model of 4D CT-scanner. IEEE Trans Nuclear Science 50: 1667-1671, 2003
4) 遠藤真広ほか：4次元CT装置の開発. 映像情報メディカル 34 (15)：1400-1403, 2002
5) Mori S et al: Physical performance evaluation of a 256-slice CT-scanner for four-dimensional imaging. Med Phys 31: 1348-1356, 2004
6) Mori S et al: Enlarged longitudinal dose profiles in cone-beam CT and the need for modified dosimetry. Med Phys 32: 1061-1069, 2005
7) Endo M et al: Development of real 4D CT with real-time reconstruction and display. Conf Record of 2005 IEEE NSS/MIC M11-252 (in press)
8) Mori S et al: Volumetric cine imaging for cardiovascular circulation using prototype 256-detector row computed tomography scanner (4-dimensional computed tomography) A preliminary study with a porcine model. J Comput Assist Tomogr 29 : 26-30, 2005
9) Funabashi N et al: Three-dimensional segmented myocardial perfusion images by selective intracoronary injection of contrast using 256-slice cone-beam computed tomography. Heart 91:1349-1351, 2005
10) Funabashi N et al: Cardiovascular circulation and hepatic perfusion of pigs in four-dimensional films evaluated by 256-slice cone-beam computed tomography. Circ J 69 : 585-589, 2005
11) Funabashi N et al: Time series of volumetric measurement of porcine three dimensional segmented myocardial perfusion by selective contrast injection using 256 slice cone beam computed tomography. Int J of Cardiology (in press)
12) Mori S et al: Volumetric perfusion CT using prototype 256MDCTscanner: Preliminary study with healthy porcine mode. American J of Neuroradiology (in press)
13) Mori S et al: Clinical potentials for dynamic contrast-enhanced hepatic volumetric cine imaging with the prototype 256-detector row CT-scanner. American J of Roentogenology 185:253-256, 2005
14) Kondo C et al: Real-time volumetric imaging of human heart without electrocardiographic gating by 256-detector row computed tomography- Initial experience. J Comput Assist Tomogr 29 : 694-698, 2005

3. 原　著

Effect of scattered radiation on image noise in cone beam CT

Masahiro Endo[a] and Takanori Tsunoo
National Institute of Radiological Sciences, 9-1 Anagawa 4-Chome, Inage-ku, Chiba, 263-8555, Japan

Nobuyuki Nakamori
Kyoto Institute of Technology, Matsugasaki, Sakyo-ku, Kyoto, 606-8585 Japan

Katsuya Yoshida
Chiba University School of Medicine, 1-8 Inohana 1-Chome, Chuo-ku, Chiba, 260-8677 Japan

(Received 7 June 2000; accepted for publication 23 January 2001)

Cone beam CT has a capability for the 3-dimensional imaging of large volumes with isotropic resolution, and has a potentiality for 4-dimensional imaging (dynamic volume imaging), because cone beam CT acquires data of a large volume with one rotation of an x-ray tube-detector pair. However, one of the potential drawbacks of cone beam CT is a larger amount of scattered x-rays, which may enhance the noise in reconstructed images, and thus affect the low-contrast detectablity. Our aim in this work was to estimate the scatter fractions and effects of scatter on image noise, and to seek methods of improving image quality in cone beam CT. First we derived a relationship between the noise in a reconstructed image and in an x-ray intensity measurement. Then we estimated the scatter to primary ratios in x-ray measurements using a Monte-Carlo simulation. From these we estimated the image noise under relevant clinical conditions. The results showed that the scattered radiation made a substantial contribution to the image noise. However, focused collimators could improve it by decreasing the scattered radiation drastically while keeping the primary radiation at nearly the same level. A conventional grid also improved the image noise, though the improvement was less than that of focused collimators. © *2001 American Association of Physicists in Medicine.* [DOI: 10.1118/1.1357457]

Key words: Cone beam CT, scattered radiation, flat-panel imager, image noise

I. INTRODUCTION

Since the pioneer work of the Dynamic Spatial Reconstructor (DSR) in the early 80's, cone beam CT has been studied by several groups.[1–5] They demonstrated isotropic resolutions in 3-dimensional imaging of large volumes, and suggested the possibilities of 4-dimensional imaging (dynamic volume imaging), because cone beam CT acquires data of a large volume with one rotation of the x-ray tube-detector pair. However, their efforts have not resulted in routine clinical CT except for the imaging of high-contrast objects, such as lung or blood vessels enhanced by a contrast agent. This was because all groups only showed much poorer image quality for low-contrast objects than conventional CT due to the narrow dynamic range of the x-ray video fluoroscopic system employed as 2-dimensional detectors.

Figure 1 shows a sagittal section of a normal head taken by our prototype scanner.[4] This image demonstrated isotropic resolutions in the sagittal section, and clearly differed from conventional sagittal images, which were reformatted from a stack of transaxial images. However, Fig. 1 failed to show low-contrast structures, such as ventricles in the brain, which could be delineated by conventional CT.

Recently, a so-called flat-panel imager has been introduced to clinical radiology. It is a digital x-ray imaging device based on the solid-state technologies developed for active-matrix, flat-panel displays, and is capable of high-sensitivity, high-speed imaging with a wide dynamic range.[6] It is expected that low-contrast detectablity of cone beam CT could be improved if a solid-state detector, such as a flat-panel imager, is employed instead of an x-ray video fluoroscopic system, because the former shows a wider dynamic range than the latter. The other candidate of a solid-state detector is an extension of a multiple-row detector array equipped in a multi-slice CT.[7]

Another potential drawback of cone beam CT is a larger amount of scattered x-rays. These x-rays may enhance the noise in reconstructed images, and thus affect low-contrast detectablity. Our aim in this work was to estimate scatter fractions and the effects of scatter on image noise, and to seek methods of improving the image quality in cone beam CT with solid-state detectors.

II. MATERIALS AND METHODS

A. Image noise formulation

The noise in a reconstructed image has a relationship with the noise in x-ray intensity measurements. The noise-to-signal-ratio in a reconstructed image is defined as σ/μ, where μ is the true value of the attenuation coefficient at a point, and σ is the variance in a set of measurements of the attenuation at that point. Chesler *et al.* proposed a formula of σ/μ for a convolution algorithms in a parallel beam geometry.[8] Because the Feldkamp algorithm,[9] which is typically used in cone beam reconstruction, is an extension of the convolution algorithm, Chesler's formula is a good approxi-

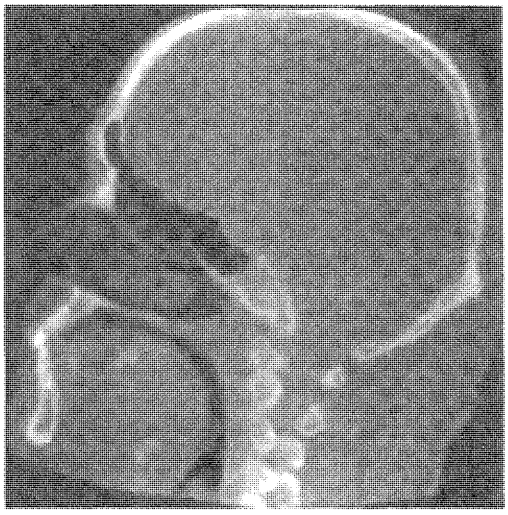

FIG. 1. Sagittal section of a normal head taken by a prototype cone beam CT-scanner.

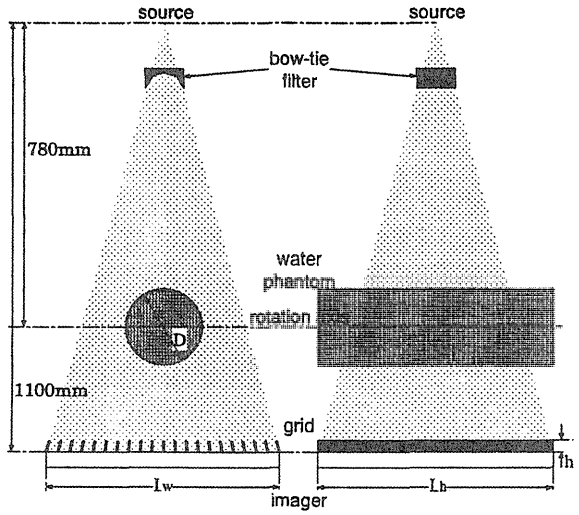

FIG. 2. Geometry of the cone beam system used in the simulation. A patient was modeled as a water cylinder of diameter D ($D=200$ or 300 mm) and of infinite length. The size of the irradiation field was $L_w \times L_h = 440$ mm $\times 440$ mm at the detector. A compensating bow-tie filter was inserted between the source and the patient. Collimators or a grid, which were focused and one-directional, were inserted before the detector to reject scattered radiation.

mation of the noise-to-signal-ratio of a reconstructed image in cone beam CT if the cone-angle is not sufficiently large. It follows that

$$\left(\frac{\sigma}{\mu}\right)^2 = \frac{\pi^2 \sigma_{\mathrm{PRO}}^2 a}{\mu^2 n} \int_{-\infty}^{\infty} |G(k)|^2 dk, \tag{1}$$

where n is the number of views, a the linear sampling distance and σ_{PRO} the standard deviation of projections, that is,

$$\sigma_{\mathrm{PRO}} = \left| \frac{d}{dI}\left(\ln \frac{I_0}{I}\right)\sigma_I \right| = \frac{\sigma_I}{I}, \tag{2}$$

where I_0 and I are the incident and transmitted x-ray intensities, respectively, and σ_I is the standard deviation of the transmitted x-ray intensity. Equation (1) shows that σ_{PRO} equals the noise-to-signal-ratio of x-ray intensity measurements. $G(k)$ is a correction function in k-space (Fourier domain). For the Shepp and Logan correction function,[10]

$$G(k) = \begin{cases} \dfrac{1}{\pi a}|\sin(\pi k a)| & (|k| \leq 1/(2a)), \\ 0 & (|k| \geq 1/(2a)). \end{cases} \tag{3}$$

If we substitute Eqs. (2) and (3) to Eq. (1),

$$\left(\frac{\sigma}{\mu}\right)^2 = K^2 \left(\frac{\sigma_I}{I}\right)^2, \tag{4}$$

where

$$K^2 = \frac{1}{2\mu^2 a^2 n}. \tag{5}$$

B. Noise in intensity measurement

As derived in Appendix A, the noise-to-signal-ratio of x-ray intensity measurements is approximately given by

$$\left(\frac{\sigma_I}{I}\right)^2 = \frac{N_P \langle E^2\rangle_P + N_S \langle E^2\rangle_S + (N_{\mathrm{add}}\langle E\rangle_P)^2}{(N_P \langle E\rangle_P)^2}, \tag{6}$$

where N_P and N_S are the numbers of primary and scattered x-ray photons absorbed in a detector element per view, respectively. N_{add} is the additive electronic noise in a detector that includes read-out electronics, and is converted to x-ray photon numbers of energy $\langle E\rangle_P$. $\langle E\rangle_P$, $\langle E^2\rangle_P$ and $\langle E^2\rangle_S$ are defined as follows:

$$\langle E\rangle_P = \int_0^{E\,\max} E\,\eta(E)\Phi_P(E)dE, \tag{7}$$

$$\langle E^2\rangle_P = \int_0^{E\,\max} E^2\,\eta(E)\Phi_P(E)dE, \tag{8}$$

$$\langle E^2\rangle_S = \int_0^{E\,\max} E^2\,\eta(E)\Phi_S(E)dE, \tag{9}$$

where $\Phi_P(E)$ and $\Phi_S(E)$ are the primary and scattered x-ray spectra incident on the detector, respectively, and $\eta(E)$ is the x-ray absorption efficiency of energy E at the detector. $E_{\max}$ is the maximum x-ray energy.

C. Parameters in noise estimation

Using the above formulations, we estimated the image noise under relevant clinical conditions. The geometry of cone beam system is shown in Fig. 2. A patient was modeled as a water cylinder having a diameter of D ($D=200$ or 300 mm) and of infinite length. The source to rotation axis distance was 780 mm, and the source to detector distance was 1100 mm. The size of the irradiation field was $L_w \times L_h = 440\,\mathrm{mm} \times 440\,\mathrm{mm}$ at the detector. In the simulation the x-ray tube was assumed to be 120 kV of the tube voltage, with a tungsten target and 5.4 mm Al total filtration. A bow-tie filter, that compensated the attenuation of x-rays in the objects and flattened the x-ray intensity incident to the

TABLE I. Specifications of collimators and a grid used in the simulation. Spacing and width were defined at the detector plane, whose distance from the source was 1100 mm.

	Material	Spacing	Width	Height h	Grid ratio	Density
Collimator 1	Pb/Air	1.0 mm	0.2 mm	10 mm	12.5	10 lines/cm
2	Pb/Air	1.0	0.2	20	25	10
Grid	Pb/Al	250 μm	50 μm	2.5	12.5	40

detector,[11] was inserted between the source and the patient. Collimators or a grid, which were focused to the x-ray source and one-directional, were inserted before the detector to reject scattered radiations. Table I gives their specifications. Though a focused and cross collimator or grid might be more effective to reject scatter, it was not considered in the present study because the heat expansion during operation would cause focal spot to move in the longitudinal direction.

The spectra of primary and scattered x-ray were estimated using a self-made Monte-Carlo code. We examined photoelectric effects, elastic and in-elastic scattering of x-ray photons more than 5 keV of energy. Escape of characteristics x-ray from Pb in the grids was also examined. The x-ray spectrum emitted from the tube was estimated using the Birch and Marshall formula.[12] Cross sections of the above interactions and angular distributions of scattering were employed from the references.[13,14] The 2×10^8 incident photons were traced in the estimation of each spectrum.

$\eta(E)$ was assumed to be 0.6, independent of x-ray photon energy for a flat-panel imager. This may be reasonable because the calculation by Siewerdsen *et al.* showed that the mean absorption efficiency of a Lanex Fast-B rare earth screen was 0.67 for 90 kVp x-ray.[15] We also examined the noise characteristics of an ideal detector whose efficiency, $\eta(E)$ is 1 and independent of the x-ray energy. N_{add} was assumed to be 70 x-ray photons per detector element for the flat-panel imager (See Appendix B) and 0 for the ideal detector. The size of the detector element was assumed to be $1.0\times1.0\,mm^2$, and the x-ray exposure was assumed to be 1.0 mAs per view, that corresponded to 5.7×10^6 photons incident to each detector element per view in the absence of the bow-tie filter and the phantom. The number of views was assumed to be 360 per scan. The scanner geometry and x-ray conditions were based on our prototype scanner.[4] The signal in reconstruction was assumed to be $0.2\,cm^{-1}$, which produced K of approximately 1.86 in Eq. (4) for the Shepp and Logan correction function. These parameters are summarized in Table II.

TABLE II. Summary of the parameters used in a noise estimation.

Phantom diameter D	200/300 mm
Source to detector distance	1100 mm
Source to isocenter distance	780 mm
Detector size $L_w\times L_h$	440 mm×440 mm
Element size a	1.0 mm
X-ray absorption	$\eta=0.6$ (flat-panel)
Efficiency η	$\eta=1.0$ (ideal)
Additive noise N_{add}	$N_{add}=70$ (flat-panel)
	$N_{add}=0$ (ideal)
X-ray tube voltage	120 KV_P
X-ray current	1.0 mAs per view
Photon numbers incident to a detector element in the absence of bow-tie filter and phantom	5.7×10^6 photons per view
Number of views	360
Signal in reconstruction μ	$0.200\,cm^{-1}$
K for Shepp and Logan	1.86

III. RESULTS

Figure 3 shows the estimated spectra used in this simulation. Table III summarizes the estimated results of image noise for the flat-panel imager. Figure 4 shows the relative image noises (noise-to-signal-ratios) for phantoms having diameters of $D=200$ mm and 300 mm. Curve 3 shows the relative noise due only to primary radiation for the ideal detector, as well as the ultimate values if all scatters are removed. Figure 5 shows the relative noise of a flat-panel imager with separated noise components for the phantoms having diameters of $D=200$ mm and 300 mm.

These results show that scattered radiation contributed substantially to the image noise in cone beam CT without any scatter rejection. However, focused collimators could improve it, because they decreased the scatter radiation drastically (less than one twentieth in our geometry) while keeping the primary radiation at nearly the same level. A conventional grid also improved the image noise, though the improvement was less than that of focused collimators. The detector noise was also substantial for a cylinder with $D=300$ mm.

IV. DISCUSSIONS

In this paper we derived the relationship between the noise in a reconstructed image and in an x-ray intensity mea-

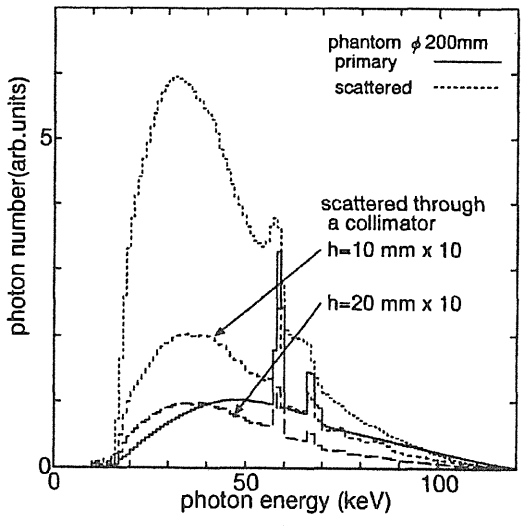

FIG. 3. Estimated spectra used in the simulation. The solid line shows the spectrum of primary radiation after a phantom of diameter 200 mm, while the dotted line shows a spectrum of scattered radiation. The broken lines show the spectra of scattered radiation through a collimator of height h ($h=10$ or 20 mm). The ordinate is enlarged 10 times for these lines.

TABLE III. Estimated results of image noise for a flat-panel imager. $\langle E\rangle_P$ in keV. $\langle E^2\rangle_P$ and $\langle E^2\rangle_S$ in $(\text{keV})^2$.

D	Grid/Collimator	N_P	N_S	N_{add}	$\langle E\rangle_P$	$\langle E^2\rangle_P$	$\langle E^2\rangle_S$	σ_I/I	σ/μ
	None	3.6×10^4	13.2×10^4	70	58.0	3803	2213	1.01%	1.89%
200 mm	Collimator 1	2.9	0.56	70	58.0	3803	2471	0.71	1.32
	Collimator 2	2.9	0.26	70	58.0	3803	2652	0.69	1.28
	Grid	2.2	0.64	70	61.8	4215	3597	0.89	1.66
	None	4.8×10^3	53.5×10^3	70	64.8	4628	2093	4.00	7.49
300 mm	Collimator 1	3.8	2.5	70	64.8	4628	2422	2.70	5.02
	Collimator 2	3.8	1.2	70	64.8	4628	2425	2.60	4.84
	Grid	3.0	2.4	70	67.6	4949	3587	3.34	6.21

surement, and then estimated the scatter to the primary ratio in the measured x-ray intensity, using a Monte-Carlo simulation. From these we estimated the magnitudes of the image noises for the geometry and x-ray conditions of our prototype scanner.[4] x-ray detectors were assumed to be a flat-panel imager. Ideal detectors with 100% detection efficiency and no additive noise were also employed to examine the limitation of image quality forced by photon statistics.

The results showed that the scattered radiation made a substantial contribution to the image noise, though focused collimators improved it because they decreased the scattered radiation drastically while keeping the primary radiation at nearly the same level. A conventional grid also improved the image noise, though the improvement was less than that of focused collimators. The image noise was mainly limited by detected x-ray photon statistics, except for a larger size object with the flat-panel imager, in which case the additive detector noise could be substantial.

With regard to comparison between conventional CT and cone beam CT, the conventional CT is believed to implement an almost ideal detector of approximately 100% efficiency with negligible additive noise. The estimated amount of scattered radiation is very small in conventional CT,[11] because a collimator similar to the present study is applied and because the only narrow slice in the axial direction is irradiated.

Therefore the relative noise (σ/μ) of conventional CT would correspond to curve 3 (ideal detector without scattered radiation) in Figs. 4 and 5 if the other conditions (such as the detector element size, etc.) are assumed to be the same. In

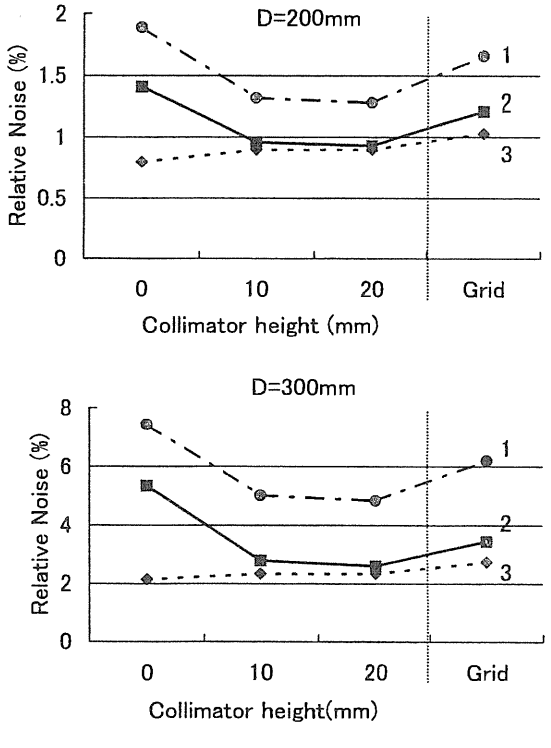

FIG. 4. Relative image noises (noise-to-signal-ratios) for phantoms of diameter $D=200$ mm and 300 mm. Curve 1 (●) shows the relative noise of a flat-panel imager, while curve 2 (■) shows the relative noise of an ideal detector. Curve 3 (◆) shows the relative noise due only to primary radiation for an ideal detector, as well as the ultimate values if all scatters are removed.

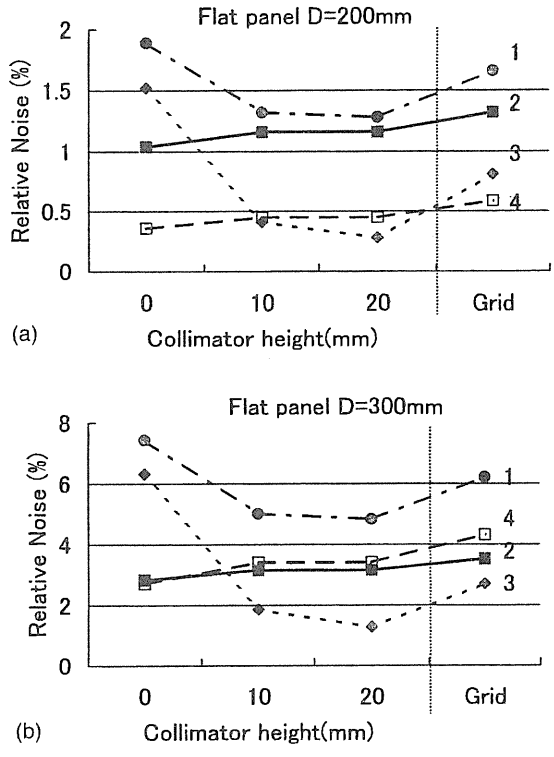

FIG. 5. Relative image noise (noise-to-signal-ratios) of a flat-panel imager with separated noise components for the phantoms of diameter $D=200$ mm and 300 mm. Curve 1 (●) shows the total noise, while curves 2 (■), 3 (◆) and 4 (□) show the noise from primary and scattered radiations, and additive electronic noise, respectively.

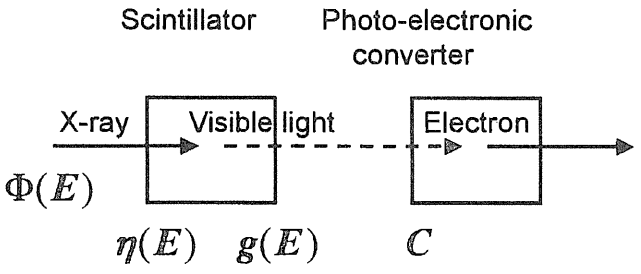

FIG. 6. X-ray detector model. In this model x-rays are converted to visible light at a scintillator, which is converted to electrons at a photo-electronic converter. $\Phi(E)$ is the spectrum of x-ray photons, and $\eta(E)$ is the x-ray absorption efficiency of energy E. $g(E)$ is the gain factor from x-ray photons to light photons. C is the opticalcoupling efficiency.

this assumption the relative noise of conventional CT are 0.90% ($D=200$ mm) and 2.40% ($D=300$ mm), while the relative noise of cone beam CT using the flat-panel imager and the collimator of 20 mm height are 1.28% ($D=200$ mm) and 4.83% ($D=300$ mm). The ratio of relative noise of cone beam CT to the conventional one is 1.4 ($D=200$ mm) and 2.0 ($D=300$ mm).

In our experience cone beam CT using a video-fluoroscopic system showed much larger (approximately 10 times larger) relative noise than conventional CT, though imaging conditions were different from each other.[5] Consequently the relative noise of 1.4–2.0 times larger than conventional CT would be a substantial improvement.

From the above discussions we might conclude that we could develop a cone beam CT with much better detectablity for low-contrast objects than the present ones if a flat-panel imager with a focused collimator is employed as the detector. This kind of cone beam CT would demonstrate clinical effectiveness in much wider fields due to improved detectablity for low-contrast objects as well as isotropic resolution inherent to cone beam CT, though the relative noise is estimated to be still larger than conventional CT.

The correctness of the conclusion depends on the assumptions made in this paper. They should be confirmed by an experimental study, which is being prepared. Nevertheless the framework presented here will be useful in a design study of cone beam CT of the new type mentioned in this paper.

ACKNOWLEDGMENTS

We thank Mrs. Masahiro Kusakabe, Kazumasa Satoh, and Satoru Matsusita of the Sony Frontier Science Laboratories for their kind collaborations.

APPENDIX A: NOISE FORMULATION IN X-RAY INTENSITY MEASUREMENT

To formulate the noise-to-signal-ratio of an x-ray intensity measurement σ_I/I, we assume a detector model as shown in Fig. 6. In the model, x-rays are converted to visible light at a scintillator, which is converted to electrons at a photo-electronic converter. In general, x-rays penetrating the scintillator will directly produce electrons at the photo-electronic converter. However the direct effects can be neglected for flat-panel imagers because the intrinsic layer of the photodiode is approximately 1 μm thick and much thinner than the scintillator.[6] In Fig. 6, $\Phi(E)$ is the spectrum of x-ray photons, and $\eta(E)$ is the x-ray absorption efficiency of energy E. $g(E)$ is a gain factor from x-ray photons to light photons, which means average light quanta emitted for each x-ray absorption of energy E, and is given by

$$g(E)=kE, \tag{A1}$$

where k is given by $\varepsilon/E_{\text{opt}}$. ε is an energy conversion efficiency for the scintillator, and E_{opt} is the mean energy of a light photon. C is an optical coupling efficiency, and is the mean probability that a light quanta emitted by the scintillator will generate an electron–hole pair in the converter.

In these notations signal I, which is the intensity of the primary x-rays, is given by

$$I=\int_0^{E\,\max} CN_P kE\,\eta(E)\Phi_P(E)dE, \tag{A2}$$

where $\Phi_P(E)$ is the spectrum of primary photons, and normalized as

$$\int_0^{E\,\max} \eta(E)\Phi_P(E)dE=1. \tag{A3}$$

N_P is the normalization factor corresponding to the photon number of a primary x-ray absorbed in a detector element per view.

The noise σ_I is given by

$$\sigma_I^2=\sigma_P^2+\sigma_S^2+\sigma_{\text{add}}^2, \tag{A4}$$

where σ_P is the statistical noise due to the primary x-rays, σ_S the statistical noise due to the scattered x-rays and σ_{add} is the additive noise due to the detector electronics. σ_P, σ_S and σ_{add} are given as follows, respectively:

$$\sigma_P^2=\int_0^{E\,\max} C^2N_P k^2E^2\,\eta(E)\Phi_P(E)dE, \tag{A5}$$

$$\sigma_S^2=\int_0^{E\,\max} C^2N_S k^2E^2\,\eta(E)\Phi_S(E)dE, \tag{A6}$$

$$\sigma_{\text{add}}^2=\left(\int_0^{E\,\max} CN_{\text{add}}kE\,\eta(E)\Phi_P(E)dE\right)^2, \tag{A7}$$

where $\Phi_S(E)$ is the spectrum of scattered photons, and normalized as

$$\int_0^{E\,\max} \eta(E)\Phi_S(E)dE=1. \tag{A8}$$

N_S is the normalization factor corresponding to the photon number of scattered x-rays absorbed in a detector element per view. N_{add} is the effective x-ray photon number of additive noise.

Therefore, the square of the noise-to-signal-ratio of an x-ray intensity measurement is given by

$$\left(\frac{\sigma_I}{I}\right)^2=\frac{\sigma_P^2+\sigma_S^2+\sigma_{\text{add}}^2}{I^2}$$

$$=\frac{N_P\langle E^2\rangle_P+N_S\langle E^2\rangle_S+(N_{\text{add}}\langle E\rangle_P)^2}{(N_P\langle E\rangle_P)^2}, \quad \text{(A9)}$$

where

$$\langle E\rangle_P=\int_0^{E\,\max} E\,\eta(E)\Phi_P(E)dE, \quad \text{(A10)}$$

$$\langle E^2\rangle_P=\int_0^{E\,\max} E^2\,\eta(E)\Phi_P(E)dE, \quad \text{(A11)}$$

$$\langle E^2\rangle_S=\int_0^{E\,\max} E^2\,\eta(E)\Phi_S(E)dE. \quad \text{(A12)}$$

APPENDIX B: ESTIMATION OF THE ADDITIVE ELECTRONIC NOISE, N_{add}

From Eq. (A7) in Appendix A,

$$N_{\text{add}}=\frac{\sigma_{\text{add}}}{Ck\int_0^{E\,\max}E\,\eta(E)\Phi_P(E)dE}. \quad \text{(B1)}$$

For a prototype flat-panel imager Siewerdsen *et al.*[12] reported that the electronic noise was 5000 electrons for a 127 μm$\times$127 μm pixel. If we add the signals from 8×8 pixels to obtain a detector of 1 mm element size, and assume no correlation between pixel noises, then

$$\sigma_{\text{add}}=\sqrt{8\times8}\times5000=40000.$$

k is the number of light photons per unit energy of x-ray, and given by $\varepsilon/E_{\text{opt}}$, where ε is the energy conversion efficiency, which was assumed to be 0.2 in the present study. E_{opt} is the mean energy of the light photons and is assumed to be 2 eV. C is the optical coupling efficiency, and is assumed to be 0.1 in the present study. $\int_0^{E\,\max}E\,\eta(E)\Phi_P(E)dE$ is the mean energy of the primary photon, and is assumed to be 60 keV. If we substitute these parameters into Eq. (B1),

$$N_{\text{add}}=40000/(0.1\times(0.2/2)\times60000)\approx70.$$

a)Electronic mail: endo@nirs.go.jp

[1] R. A. Robb, "The dynamic spatial reconstructor: An x-ray video-fluoroscopic CT scanner for dynamic volume imaging of moving organs," IEEE Trans. Med. Imaging **1**, 22–33 (1982).

[2] D. Saint-Felix, Y. Trousset, C. Picard, C. Ponchut, R. Romeas, and A. Rougee, "In vivo evaluation of a new system for computerized angiography," Phys. Med. Biol. **39**, 583–595 (1994).

[3] R. Ning and R. A. Kruger, "Image intensifier-based computed tomography volume scanner for angiography," Acad. Radiol. **3**, 344–350 (1996).

[4] M. Endo, K. Yoshida, N. Kamagata, K. Satoh, T. Okazaki, Y. Hattori, S. Kobayashi, M. Jimbo, M. Kusakabe, and Y. Tateno, "Development of a 3D CT-scanner using a cone beam and video-fluoroscopic system," Radiat. Med. **16**, 7–12 (1998).

[5] M. Endo, K. Nishizawa, K. Iwai, M. Matsumoto, K. Yoshida, K. Satoh, M. Matsusita, and M. Kusakabe, "Image characteristics and effective dose estimation of a cone beam CT using a video-fluoroscopic system," IEEE Trans. Nucl. Sci. **46**, 686–690 (1999).

[6] L. E. Antonuk, Y. El-Mohri, J. H. Siewerdsen, J. Yorkston, W. Huang, and V. E. Scarpine, "Empirical investigation of the signal performance of a high-resolution, indirect detection, active matrix flat-panel imager (AMFPI) for fluoroscopic and radiographic operation," Med. Phys. **24**, 51–70 (1997).

[7] K. Taguchi and H. Aradate, "Algorithm for image reconstruction in multi-slice CT," Med. Phys. **25**, 550–561 (1998).

[8] D. A. Chsler, S. J. Riederer, and N. J. Pelc, "Noise due to photon counting statistics in computed x-ray tomography," J. Comput. Assist. Tomogr. **1**, 64–74 (1977).

[9] L. A. Feldkamp, L. C. Davis, and J. W. Kress, "Practical cone-beam algorithm," J. Opt. Soc. Am. A **1**, 612–619 (1984).

[10] L. A. Shepp and B. F. Logan, "Fourier reconstruction of a head section," IEEE Trans. Nucl. Sci. **21**, 21–43 (1974).

[11] H. Kanamori, N. Nakamori, K. Inoue, and E. Takenaka, "Effect of scattered x-rays on CT images," Phys. Med. Biol. **30**, 239–249 (1985).

[12] R. Birch and M. Marshall, "Computation of bremsstrahlung x-ray spectra and comparison with spectra measured with a Ge(Li) detector," Phys. Med. Biol. **24**, 505–517 (1979).

[13] J. H. Hubbell, "Photon mass attenuation and energy absorption coefficients from 1 keV to 20 Mev," Int. J. Appl. Radiat. Isot. **33**, 1269–1290 (1982).

[14] J. H. Hubbell, W. J. Veigele, E. A. Briggs, R. T. Brown, D. T. Cromer, and R. J. Howerton, "Atomic form factors, incoherent scattering functions, and photon scattering cross sections," J. Phys. Chem. Ref. Data **4**, 471–538 (1975).

[15] J. H. Siewerdsen, L. E. Antonuk, Y. El-Mohri, J. Yorkston, W. Huang, and J. M. Boudry, "Empirical and theoretical investigation of the noise performance of indirect detection, active matrix flat-panel imagers (AMFPIs) for diagnostic radiology," Med. Phys. **24**, 71–89 (1997).

ORIGINAL ARTICLE

Radiation Medicine: Vol. 21 No. 1, 17–22 p.p., 2003

Four-dimensional Computed Tomography (4D CT)–Concepts and Preliminary Development

Masahiro Endo,* Takanori Tsunoo,* Susumu Kandatsu,* Shuji Tanada,* Hiroshi Aradate, and Yasuo Saito****

Four-dimensional computed tomography (4D CT) is a dynamic volume imaging system of moving organs with an image quality comparable to that of conventional CT. 4D CT will be realized by several technical breakthroughs for dynamic cone-beam CT: (1) a large-area two-dimensional (2D) detector; (2) high-speed data transfer system; (3) reconstruction algorithms; (4) ultra-high-speed reconstruction computer; and (5) high-speed, continuously rotating gantry. Among these, development of the 2D detector is one of the main tasks because it should have as wide a dynamic range and as high a data acquisition speed (view rate) as present CT detectors. We are now developing a 4D CT scanner together with the key components. It will take one volume image in 0.5 sec with a 3D matrix of 512×512×512. This paper describes the concepts and designs of the 4D CT system, as well as preliminary development of the 2D detector.

Key words: four-dimensional computed tomography (4D CT), dynamic volume imaging, two-dimensional (2D) discrete detector

Introduction

Since the advent of computed tomography (CT) in 1973, dynamic imaging of moving organs in a living person has been one of the main goals of this field. This concept is simply called four-dimensional (4D) CT because it takes three-dimensional (3D) images with the additional dimension of time. With 4D CT one could carry out not only new diagnoses but also provide new interventional therapy through real-time observation of its procedures. In the early 1980s researchers at the Mayo Clinic tried to develop a CT scanner for dynamic volume imaging called the Dynamic Spatial Reconstructor (DSR).[1] The project was ambitious and had as its goal the development of a CT scanner capable of taking up to 20 volume data per second. However, they did not achieve their goal, because the technologies used in the two-dimensional (2D) detector and digital signal processing were far from those required for 4D CT.

Continuous progress in CT technologies since the DSR project has increased the possibility of realizing 4D CT. Today's state-of-the-art CT scanners have the capability for high-speed rotation of the detector and X-ray tube pair (up to 0.5 sec/rotation), and the multi-row detector can be extended to a 2D detector with sufficient dynamic range and data acquisition speed. Algorithms for cone-beam reconstruction needed in 4D CT have been proposed by several authors, and their usefulness has been demonstrated in simulation and phantom experiments.[2,3] Therefore, it is likely that the 4D CT can be realized if a 2D detector and ultra-high-speed reconstruction processor, both of which are within reach of current technologies, are developed.

Materials and Methods

Specifications and necessary breakthroughs

Because volume data (3D data) can be acquired by cone-beam CT using rotation of the cone-beam,[4,5] continuous rotation of the cone-beam allows dynamic volume data

Received September 17, 2002; revision accepted November 13, 2002.

*Research Center of Charged Particle Therapy, National Institute of Radiological Sciences

**Medical System Company R&D Center, Toshiba Corporation

Reprint requests to Masahiro Endo, Ph.D., Research Center of Charged Particle Therapy, National Institute of Radiological Sciences, 9-1, Anagawa 4-chome, Inage-ku, Chiba 263-8555, JAPAN.

This work was supported in part by the NEDO (New Energy and Industrial Technology Development Organization).

(4D data) to be acquired. Although this idea is simple, several breakthroughs are necessary to realize it: (1) a large-area 2D detector with scatter rejection device; (2) high-speed data transfer system; (3) reconstruction algorithms; (4) ultra-high-speed reconstruction processor; and (5) high-speed, continuously rotating gantry.

Among these, the development of the 2D detector is one of the main tasks. The detector should have as wide a dynamic range and as high a data acquisition speed (view rate) as current CT detectors if temporal resolution and low-contrast detectability are to reach present levels. From this viewpoint, an image intensifier (II) and flat-panel detector (FPD) are both inadequate because their view (frame) rate is much lower than that required (more than or equal to 900 views/sec) and their dynamic range is narrower than would be needed (16 bits or more).[6,7] An entirely new 2D detector should be developed on the basis of current technology for CT detectors.

Table 1 summarizes the specifications of the prototype 4D CT detector. It is essentially a discrete pixel detector in which pixel data are measured by an independent detector element. The element of the detector consists of a scintillator and photodiode pair. Scattered radiation should be limited to negligible amounts with collimators to assure uniformity and linearity of the CT number and to reduce image noise.[8] The data transfer rate from the rotating part to the stationary part of the gantry should be at least 3.4 Gbps and roughly several tens of times higher than that of current CT scanners.

Table 1. Specifications of prototype 4D CT detector

Sampling rate	900 views/sec
Dynamic range of A/D converter	16 bits
Size	960×230 mm
Element size	1.03×0.94 mm
Number of elements	912×256
Material	Scintillator + photodiode
Data transfer rate	912×256×900×16≒3.4 Gbps
Scatter rejection	Collimators parallel to z-direction

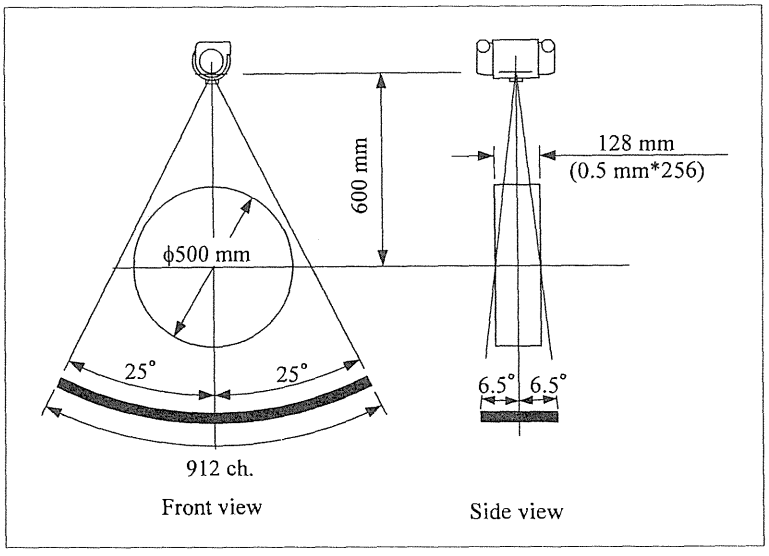

Fig. 1. Geometry of the prototype 4D CT scanner.

The detector and X-ray tube pair should be mounted on the gantry frame of a state-of-the-art CT scanner (e.g., Toshiba Corporation's Aquilion) to minimize design tasks. The scanning mechanism can ensure that the 4D CT scanner has a rotation speed of up to 0.5 sec/rotation, which means 0.3 sec/volume if half-scan algorithms are employed. Figure 1 shows the geometry of the prototype 4D CT scanner. The X-ray tube is slightly tilted to the rotation axis to cover a wide cone angle.

Volume data should be reconstructed in real time by the Feldkamp-Davis-Kress (FDK) algorithm or a more sophisticated one. To reconstruct the 512×512×128 matrix from 900 views (projections), $512\times512\times128\times900=3.0\times10^{10}$ unit operations (consisting of several multiplications and table-look-ups) should be done in the back-projection stage of the FDK algorithm. Because our goal of reconstruction time is less than 1 sec for a 512×512×128 matrix, more than 10 times 30 GOPS (giga-operations per second) is required. This could be fulfilled with the parallel use of several tens of field-programmable gate arrays (FPGA), each of which consists of 32 processor elements. Because a helical cone-beam mode should be employed to obtain 3D data from long objects such as the whole thorax or abdomen, the reconstructor should also be able to process helical cone-beam data. Table 2 summarizes the specifications of a prototype 4D CT scanner.

Design and preliminary development of key components

A test model of the prototype scanner with limited performance will be completed in 2002, with the support of New Energy and Industrial Technology Development Organization (NEDO). The prototype scanner itself will be completed in 2004. To this end we have done preliminary design and development work for several key components. Among them, those of a 2D detector and high-speed data transfer system are significant and are described here.

2D detector

The element of the detector consists of a scintillator and photodiode. The scintillator material is the same as that used for multi-slice CT detectors, and the photodiode is single-crystal silicon, the same as that used for multi-slice detectors. Because the size of a single-crystal silicon wafer is limited, the detector system has been realized by tiling detector blocks.[9] Figure 2 shows the construction of the detector. One detector block consists of 24 (in the channel direction) × 64 (in the slice direction) =1,536 elements, while one detector system consists of 38 (in the channel direction) × 4 (in the slice direction) = 152 blocks.

Figure 3 shows the first prototype model of the 2D detector (without anti-scatter collimator). Because it consists of 480 channels × 256 slices, we call it a half-channel detector. Figure 4 shows one detector block. The size of the detector block is approximately the same as that of the multi-slice detector.

The 2D detector has an anti-scatter collimator which is an assembly of thin molybdenum blades equally spaced. The pitch of the blade is the same as that of the detector element. The collimator ratio is the height of the sheet divided by the gap. We used a collimator with a ratio of approximately 30:1. The collimator blades are adjusted parallel to the z-axis (the rotational axis). Figure 5 shows the prototype model of the 2D detector with the anti-scatter collimator, which is covered with a protector of carbon-fiber plastics.

The newly developed data acquisition system (Fig. 6) is different from that of a conventional CT scanner, and is similar to that of a FPD. Charges are accumulated

Table 2. Specifications of prototype 4D CT scanner

Scan mode	Cone-beam continuous rotation (4D) Helical cone-beam (precise 3D)
Detector	912×256 elements, 1×1 mm element size, 16 bits, 900 views/sec
Scan time	0.5 sec/rotation (30 sec max)
Reconstruction matrix	512×512×512
Contrast resolution	Less than 0.5%
Reconstruction time	Less than 1 sec for 512×512×128
Reconstruction area	25-50 cm diameter × 10 cm length/rotation

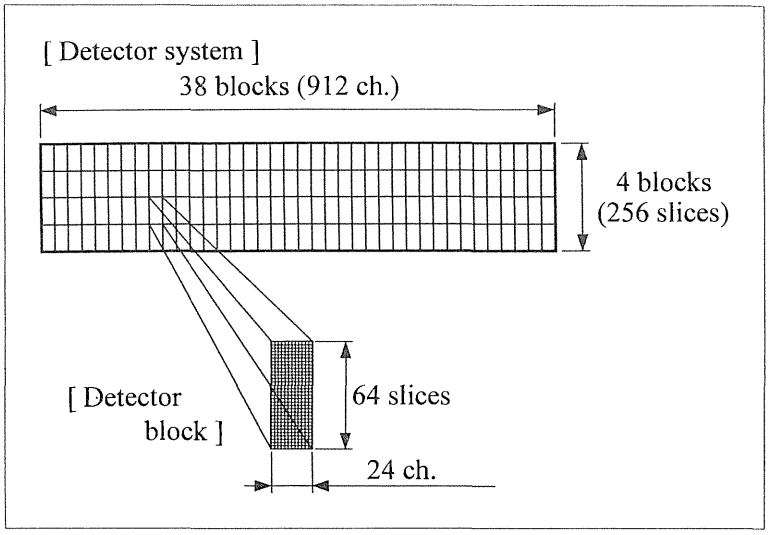

Fig. 2. Construction of the detector. One detector block consists of 24 (in the channel direction) × 64 (in the slice direction) = 1,536 elements, while one detector system consists of 38 (in the channel direction) × 4 (in the slice direction) = 152 blocks.

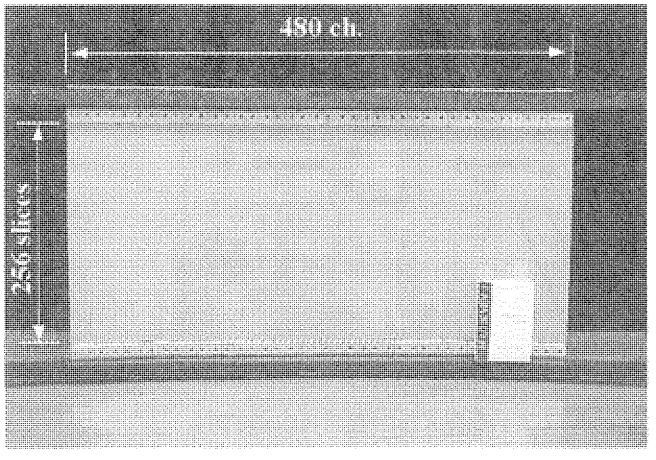

Fig. 3. The first prototype model of 2D detector without anti-scatter collimator. It consists of 480 channels × 256 slices.

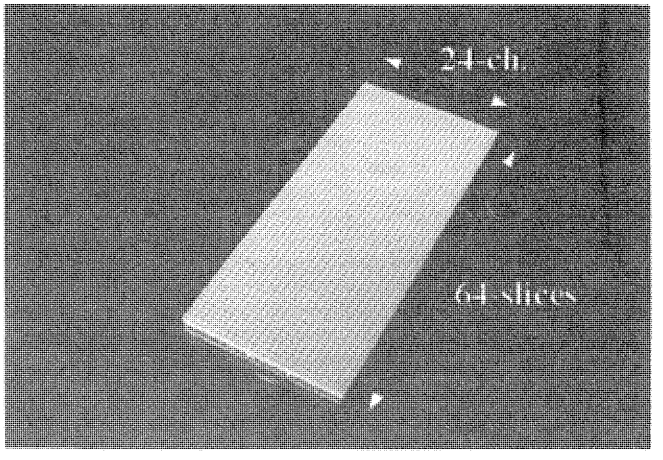

Fig. 4. Photograph of a detector block. Scintillator elements are shown in the upward surface, and photodiodes are hidden behind them.

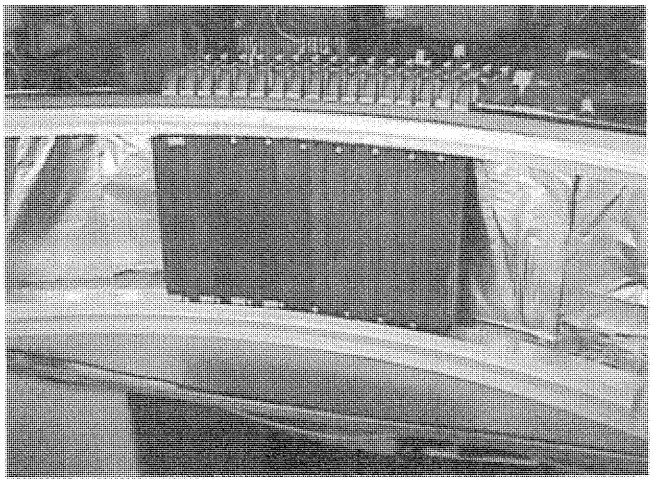

Fig. 5. Prototype model of 2D detector with anti-scatter collimator, covered with a protector of carbon-fiber plastics.

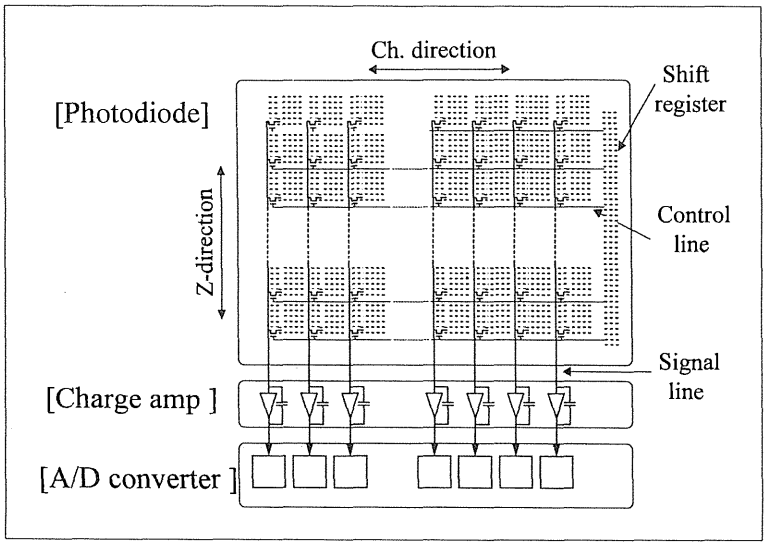

Fig. 6. Diagram of data acquisition system. Charges are accumulated in photodiodes and transferred to charge amplifiers in the order of slice position (z-coordinates).

in photodiodes and transferred to charge amplifiers in the order of slice position (z-coordinate) (Fig. 6). Since each channel has one charge amplifier and one analogue to digital (A/D) converter, there are 912 A/D converters in one system, while the resolution of each converter is 16 bits. Sampling rate (speed) is 900 views (frames) per second, and there are 256 elements in each channel. Therefore, data for one frame must be collected in 1 sec/900 = 1.1 msec, and one datum of each element must be sampled in 1.1 msec/256 = 4.3 micro-second by the charge amplifier and A/D converter.

High-speed data transfer system

In the 4D CT scanner, projection data should be transferred from the rotating part to the stationary part. Since the transfer rate is determined by multiplying a redundant factor of 1.3-1.4 by the required net rate of 3.4 Gbps, where the redundant factor is necessary for adding error correction codes, transfer control codes, and so on, it becomes approximately 5 Gbps.

We have realized this specification by the parallel use of 12 sets of a laser diode (LD)-photodiode (PD) pair, each of which has a transfer rate of 622 Mbps. Figure 7 shows a diagram of the data transfer system. In the figure a rotation interface encodes 912-channel data from the data acquisition system (DAS) to serial data, adds the error correction code, and divides these data into 12-channel data for transmitting by LD-PD pairs. A stationary interface decodes data and sends them to an image processing unit via a very-high-speed bus line. The

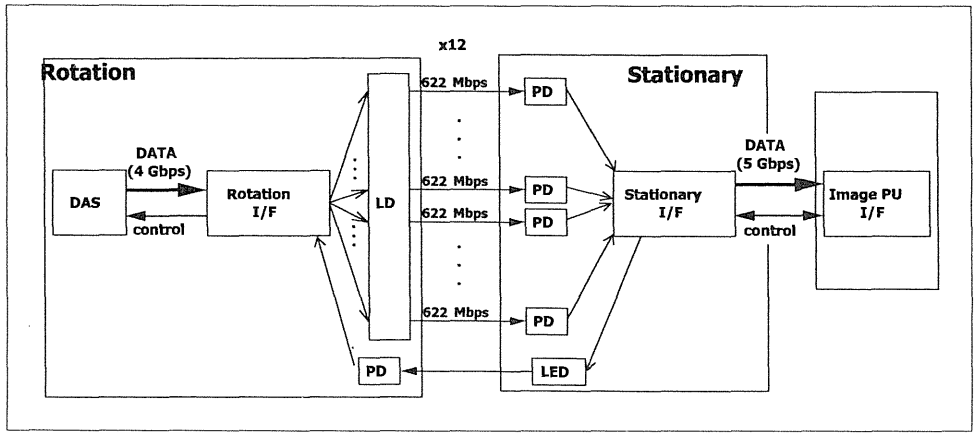

Fig. 7. Block-diagram of high-speed data transfer system. A rotation interface encodes 912-channel data from the DAS to serial data, adds the error correction code, and divides these data into 12-channel data for transmitting by LD-PD pairs. A stationary interface decodes data and sends them to the image processing unit via a very-high-speed bus line.
DAS: data acquisition system, PD: photodiode, LD: laser diode, Image PU: image processing unit.

difference between the required 5 Gbps and maximum transfer rate of 7.4 Gbps (= 622 Mbps × 12) is a design margin that accounts for dead time of the data transfer system caused by gaps between light-concentrating devices for the photodiodes.

Experiment with the half-channel detector

In one preliminary test, we acquired projection data for a moving object using the half-channel detector and a turntable (Fig. 8), and reconstructed the images. In the experimental geometry, the rotating axis (z-axis) was vertical, while the plane including the X-ray source and detector was horizontal. The rotation speed of the turntable was up to one rotation per second. The output signal from the A/D converter was connected directly to the computer for data acquisition and control.

The temporal response of the detector was evaluated using a falling shield block made of lead. X-rays were intercepted by the shadow of the lead block. Falling speed was approximately 2.4 meters per second, and the data sampling rate was 900 views per second. Figure 9 shows the results. Both falling response and rising response were within a few milliseconds, the same as for the multi-slice detector.

A magic hand driven by motor was selected as a moving object. The fingers were folded and then extended in a cycle time of approximately 6 seconds. In a reconstruction experiment, 900 projections of 912×256 pixels were collected for each rotation (one rotation per second), and data collection was continued during six rotations, covering one cycle of the magic hand's motion. Effective data were 480×256 out of 912×256 pixels because we employed the half-channel detector. Other data were dummy, and were abandoned after data collection. Five volumes were reconstructed for each rotation, and 30 volumes were obtained for six rotations. Image reconstruction was done using the FDK algorithms. Figure 10a shows 3D-rendered images of the magic hand during approximately one half cycle of its motion, while Fig. 10b shows 3D-rendered images at another angle with partial cutting. Figure 10c shows sagittal sections of the magic hand.

Discussion

In this report we have described the concepts and preliminary development work of a 4D CT system. A 2D detector of an entirely new type and a high-speed data transfer system were designed and tested to examine their feasibility.

To confirm the performance of these components in a real situation, we are now developing a test model of the prototype scanner that uses the 2D detector and a high-speed data transfer system on the gantry of Toshiba Corporation's Aquilion. This work is supported by NEDO. The test model will be completed in 2002, and clinical evaluation is planned to explore the possibilities of 4D CT, although the specifications listed in Table 2 will not be fulfilled.

We are now studying reconstruction algorithms for cone-beam and helical cone-beam geometries and

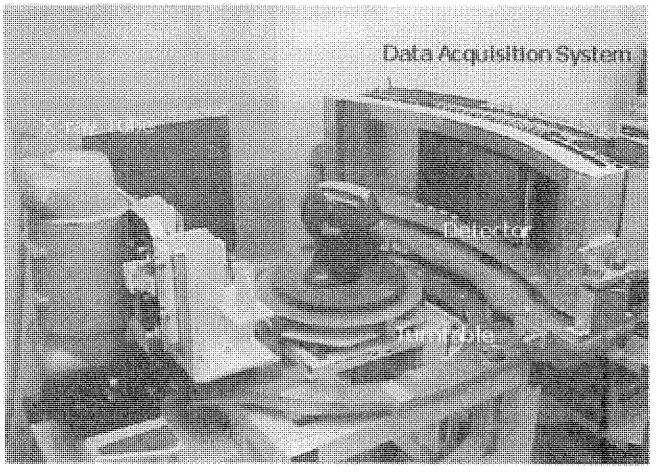

Fig. 8. Set-up of preliminary test of half-channel detector. A phantom on the turntable is rotated around a vertical axis with the rotation speed of up to one rotation/sec, while X-rays are irradiated from an X-ray tube and transmitted X-rays are detected.

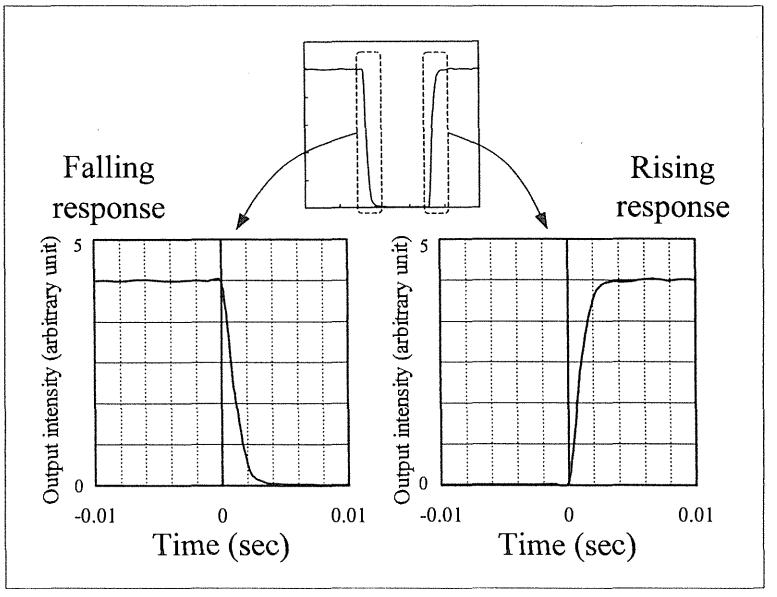

Fig. 9. Temporal response of detector evaluated with a falling shield block made of lead. X-rays were intercepted by the shadow of the lead block. Both falling response and rising response were within a few milliseconds.

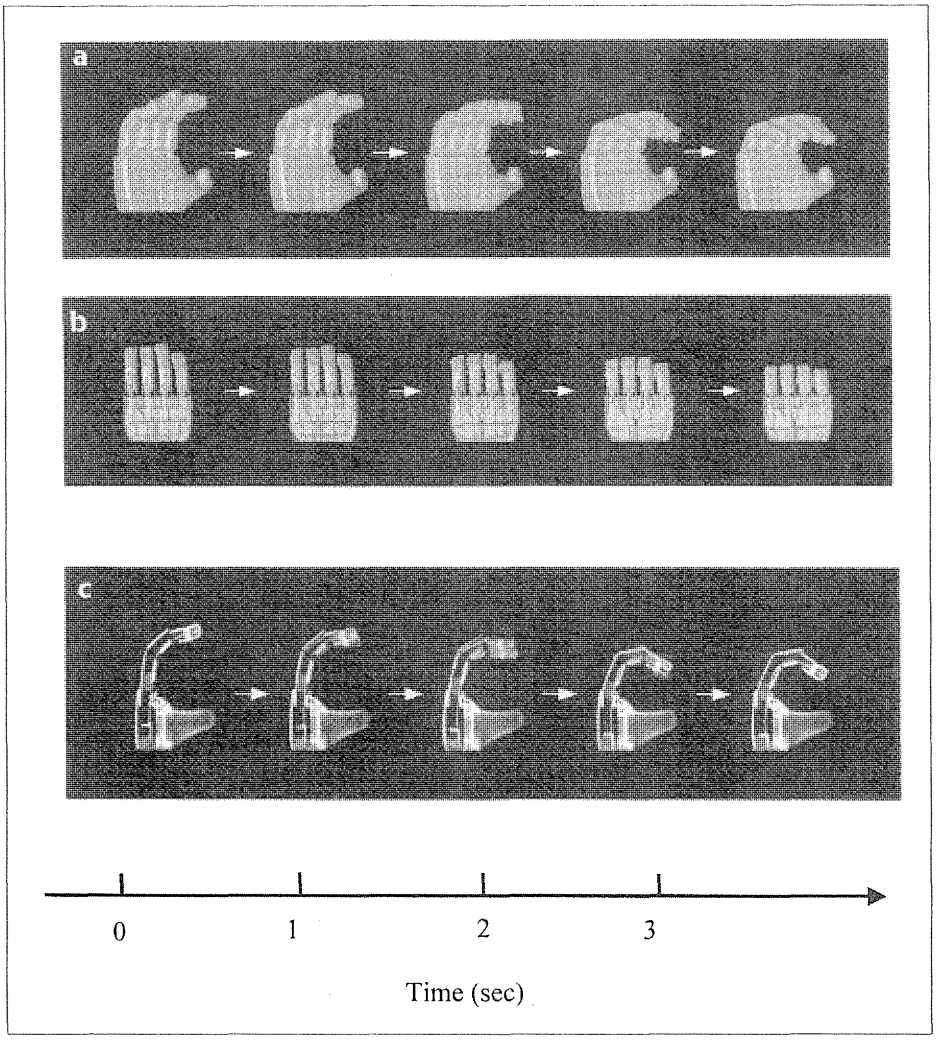

Fig. 10. Results of reconstruction experiment of moving phantom. a: 3D-rendered images of the magic hand during approximately one-half cycle of its motion, b: 3D-rendered images at another angle with partial cutting, c: sagittal sections of the magic hand.

designing an ultra-high-speed reconstruction processor. A test model of the processor will be produced and examined in 2003. After these preparatory studies we will complete in 2004 a prototype 4D CT scanner that has the desired specifications listed in Table 2, and we will evaluate its clinical usefulness not only in diagnosis but also in interventional therapy.

References

1) Robb RA. The dynamic spatial reconstructor: An X-ray video-fluoroscopic CT scanner for dynamic volume imaging of moving organs. *IEEE Trans Med Imaging,* 1: 22–33, 1982.
2) Feldkamp LA, Davis LC, Kress JW. Practical cone-beam algorithm. *J Opt Soc Am,* A1: 612–619, 1984.
3) Kudo H, Saito T. Derivation and implementation of a cone-beam reconstruction algorithm for nonplanar orbits. *IEEE Trans Med Imaging,* 13: 196–211, 1994.
4) Saint-Felix D, Trousset Y, Picard C, Ponchut C, Romeas R, Rougee A. *In vivo* evaluation of a new system for computerized angiography. *Phys Med Biol,* 39: 585–595, 1994.
5) Endo M, Yoshida K, Kamagata N, *et al.* Development of a 3D CT-scanner using a cone beam and video-fluoroscopic system. *Radiat Med,* 16: 7–12, 1998.
6) Colbeth RE, Boyce S, Fong R, *et al.* 40×30 cm flat panel imager for angiography, R&F and cone-beam CT applications. *Proc SPIE,* 4320: 94–102, 2001.
7) Ross W, Basu S, Edic P, *et al.* Design and image quality results from volumetric CT with a flat panel imager. *Proc SPIE,* 4320: 783–791, 2001.
8) Endo M, Tsunoo T, Nakamori N, Yoshida K. Effect of scattered radiation on image noise in cone beam CT. *Med Phys,* 28: 469–474, 2001.
9) Saito Y, Aradate H, Miyazaki H, Igarashi K, Ide H. Large area 2-dimensional detector for real-time 3-dimensional CT (3D-CT). *Proc SPIE,* 4320: 775–782, 2001.

Development and Performance Evaluation of the First Model of 4-D CT-Scanner

M. Endo, S. Mori, T. Tsunoo, S. Kandatsu, S. Tanada, H. Aradate, Y. Saito, H. Miyazaki, K. Satoh, S. Matsusita, and M. Kusakabe

Abstract—**Four-dimensional (4-D) computed tomography (CT) is a dynamic volume imaging system of moving organs with an image quality comparable to conventional CT and it is realized by continuous and high-speed cone-beam CT. We have developed a novel two-dimensional (2-D) detector for 4-D CT, which is based on the present CT technology, and mounted it on the gantry frame of the state-of-the-art CT-scanner. In the present paper, we describe the design and the performance evaluation results of the first model of the 4-D CT-scanner. The X-ray detector for the 4-D CT-scanner is a discrete pixel detector in which pixel data are measured from independent detector elements. The numbers of elements are 912 (channels) × 256 (segments) and the element size is approximately 1 mm × 1 mm. Data sampling rate is 900 views (frames)/s and the dynamic range of the A/D converter is 16 bits. The rotation speed of the gantry is 1.0 s/rotation. The data transfer system between rotating and stationary parts in the gantry consists of laser diode and photodiode pairs and it achieves a net transfer speed of 5 Gbps. Volume data of 512 × 512 × 256 voxels are reconstructed with an Feldkamp–Davis–Kress (FDK) algorithm by parallel use of microprocessors. The image characteristics such as noise, uniformity, and spatial resolution were evaluated with stationary phantoms in a single rotation. Exposure dose to an object was measured with an extension of the standard measurement method of CT dose index (CTDI). Several volunteers were scanned to explore clinical potentials. For the 4-D CT-scanner, the image characteristics of stationary objects were almost the same as that of conventional CT, while CTDI of the 4-D CT was slightly higher than that of conventional CT. Isotropic resolving power of less than 0.5 mm was achieved for the stationary object.**

Index Terms—**Dynamic volume imaging, four-dimensional computed tomography (4-D CT), phantom study.**

I. Introduction

SINCE the advent of computed tomography (CT) in 1973, dynamic imaging of moving organs in a living person has been one of the biggest dreams in this field [1]. The concept is simply called 4-D CT because it takes a three-dimensional (3-D) image with the additional dimension of time. With four-dimensional (4-D) CT, physicians could carry out not only new diagnoses, but also provide new interventional therapy by real-time observation of its procedures. Because volume data (3-D data) can be acquired by cone-beam CT using a rotation of the cone-beam [2], [3], continuous rotation of the cone-beam allows dynamic volume data (4-D data) to be acquired. In order to realize 4-D CT, we have developed a novel two-dimensional (2-D) detector based on the present CT technology [4], and mounted it on the gantry frame of the state-of-the-art CT-scanner (Toshiba Corp. Aquillion) [5], [6]. In the present report we describe the design and performance evaluation results of the first model of the 4-D CT-scanner.

Manuscript received April 1, 2003; revised April 10, 2003. This work was supported in part by the New Energy and Industrial Technology Development Organization (NEDO).

M. Endo, S. Mori, T. Tsunoo, S. Kandatsu, and S. Tanada are with the National Institute of Radiological Sciences, Chiba 263-8555, Japan (e-mail: endo@nirs.go.jp).

H. Aradate, Y. Saito, and H. Miyazaki are with the Toshiba Corporation Medical System Company, Otawara 324-8550, Japan.

K. Satoh and S. Matsusita are with the Sony Corp. Corporate Technology Department, Tokyo 141-0001, Japan.

M. Kusakabe is with the Fukui University Faculty of Engineering, Fukui 910-8507, Japan.

Digital Object Identifier 10.1109/TNS.2003.817407

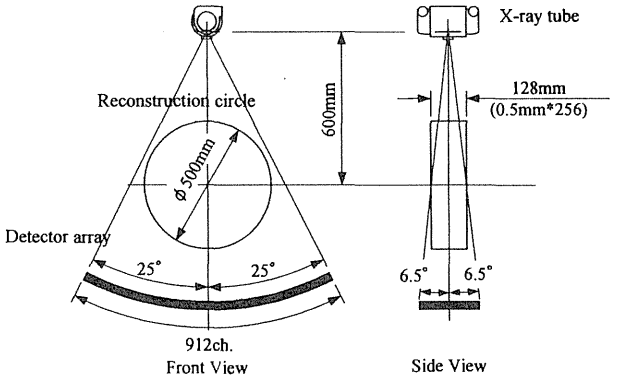

Fig. 1. Geometry of the scanner.

II. Description of Scanner System

A. Gantry

The detector and X-ray tube pair are mounted on the gantry frame of the state-of-the-art CT-scanner. Fig. 1 shows the geometry of the scanner, and Fig. 2 shows a photograph of the gantry under development. The scanning mechanism can assure a rotation speed of up to 0.5 s/rotation. However the first model employs 1.0 s/rotation as the maximum speed due to the acceleration limit of the X-ray tube that covers a wide cone-angle; this tube is slightly tilted to the rotation axis.

B. Detector

The detector is a discrete pixel detector in which pixel data are measured from independent detector elements. The numbers of elements are 912 (channels) × 256 (segments), and the element size is approximately 1 mm × 1 mm. Data sampling rate is 900 views (frames)/s, and the dynamic range of the A/D converter is 16 bits. The detector element consists of a scintillator and photodiode. The scintillator is Gd_2O_2S ceramic, and the photodiode is made of single-crystal silicon, the same as for

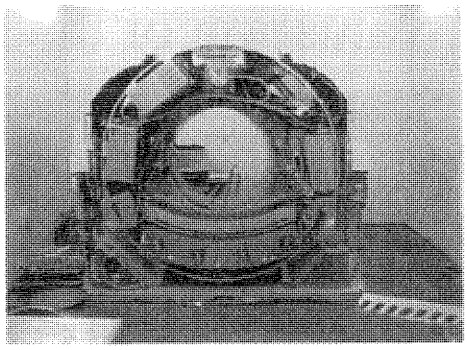

Fig. 2. Photograph of the gantry under development.

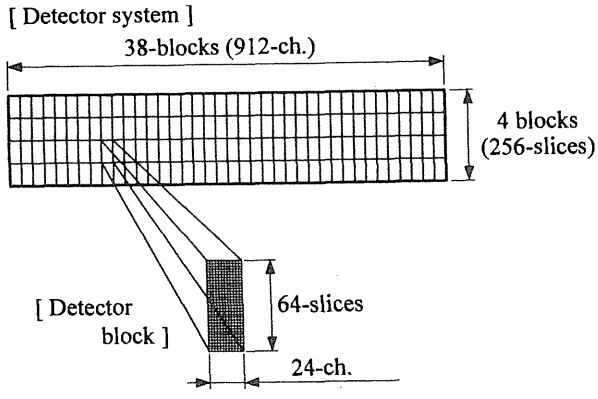

Fig. 3. Construction of the detector.

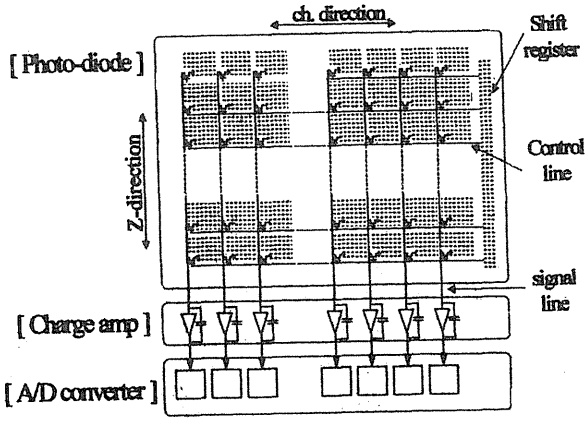

Fig. 4. Diagram of data acquisition system.

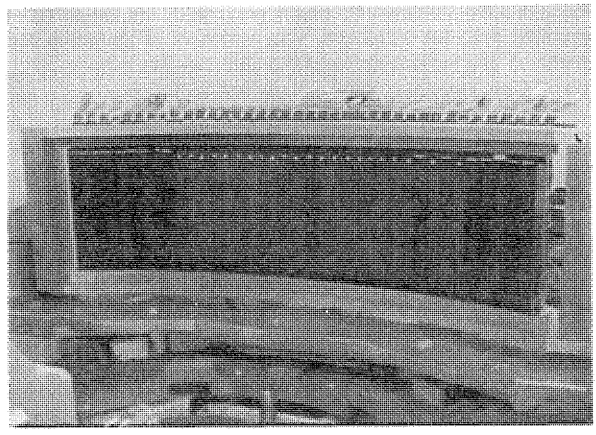

Fig. 5. Photograph of the detector system.

those of a multidetector (MD) CT detector. Because the size of a single-crystal silicon wafer is limited, the detector system has been realized by tiling detector blocks. One detector block consists of 24 (channels) $\times$ 64 (segments) $=$ 1,536 elements, while one detector system consists of 38 $\times$ 4 $=$ 152 blocks. Fig. 3 shows the construction of the detector.

The 2-D detector has an anti-scatter collimator that is an assembly of thin equally spaced molybdenum septa. The collimator blades are adjusted parallel to the rotation axis, and the pitch of the blade is identical to the detector element pitch. The collimator ratio is approximately 30:1, which is the height of the blades divided by the length of the gap.

The data acquisition system is different than that of the conventional CT-scanner, and is rather similar to that of a flat panel detector (FPD) as shown in Fig. 4. However much faster readout-speed than that of the FPD is achieved for two reasons; the circuits on the single-crystal silicon shows much lower resistance than a thin-film transistor (TFT) and one-to-one bonding of each data line to readout electronics. Fig. 5 shows a photograph of the detector system.

C. High-Speed Data Transfer System

In the present system projection data should be transferred from the rotating part to the stationary part. Since the transfer rate is determined by multiplying the required net rate of 3.4 Gbps ($=$ 912 $\times$ 256 $\times$ 900 $\times$ 16) by a redundant factor of 1.3–1.4, where the redundant factor is necessary for adding error correction codes, transfer control codes etc, it becomes approximately 5 Gbps. This value is realized by parallel use of 12 sets of a laser diode—photodiode pair, each of which has a transfer rate of 622 Mbps. Fig. 6 shows a block-diagram of high-speed data transfer system. At the rotation interface, a view data of 912 $\times$ 256 $\times$ 16 bits are divided to 12 channels, added error correction codes and transfer control codes, and then transferred as bit streams. At the stationary interface the view data are decoded from the bit streams with the inverse process at the rotation interface. The difference between the required 5 Gbps and the maximum transfer rate of 7.4 Gbps ($=$ 622 Mbps $\times$ 12) is the design margin that accounts for the dead time of the data transfer system caused by gaps between light-concentrating devices for the photodiodes.

D. Image Reconstruction Computer

Volume (3-D) data are reconstructed with an Feldkamp–Davis–Kress (FDK) algorithm [7] from 360 degree full rotation data after preprocessing that consists of offset subtraction, correction of nonuniformities of detector response and logarithmic conversion.

The image reconstruction computer consists of 128 microprocessors, each of which has the maximum computation speed of 400 MFLOPS. Reconstruction time is less than 6 min for 512 $\times$ 512 $\times$ 256 from 900 views.

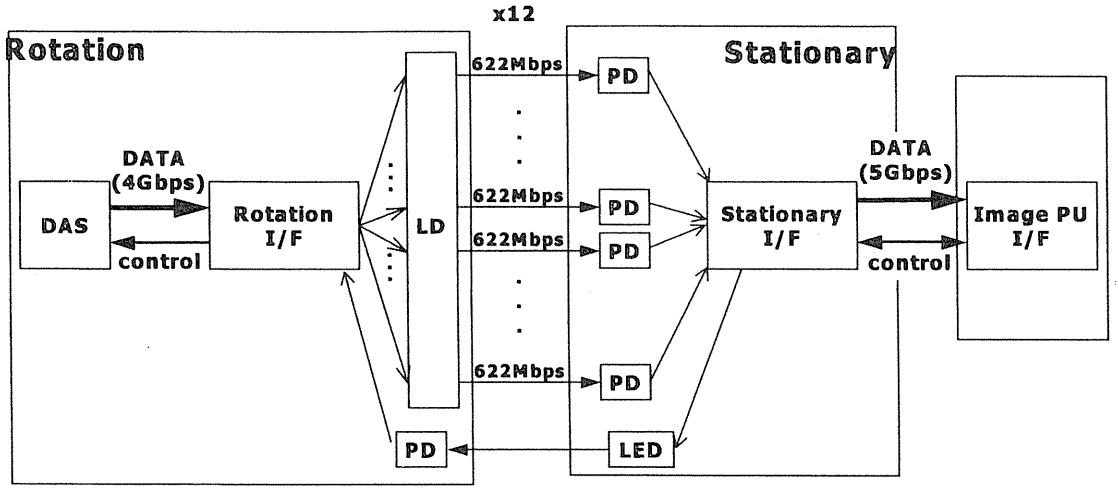

Fig. 6. Block-diagram of high-speed data transfer system. DAS: data acquisition system; PD: photodiode; LD: laser diode; Image PU: Image processing unit; I/F: interface.

III. Experiments

A. Image Characteristics

The image characteristics such as noise, uniformity and spatial resolution were evaluated with stationary phantoms in a single rotation.

The noise and uniformity were evaluated with a water-filled phantom of 200 mm diameter and 250 mm height. The phantom wall was made of 10 mm thick lucite. The voxel size was a 0.5 mm cube. The X-ray tube voltage and current were 120 KV and 120 mA, respectively. The same phantom was scanned with a state-of-the-art MD CT-scanner (Siemens SOMATOM Volume Plus4). The same scan conditions were selected except that the MD CT-scanner was operated with a slice width of 5 mm.

For 4-D CT, ten contiguous transverse images around the mid-plane on which an X-ray source was rotated were obtained from 3-D data of the water-filled phantom. They were then averaged to supply a transverse image of 5 mm slice thickness. On the transverse images of 5 mm slice thickness obtained from the 4-D CT and MD CT, means and standard deviations of CT-numbers were calculated in regions of interest (ROIs) of 10 mm diameter aligned along the x-axis. We examined uniformity and noise with the mean and standard deviations of CT-numbers in ROIs, respectively.

The spatial resolution was evaluated with a specially designed rod phantom consisting of five sets of high contrast rods (Fig. 7) [8]. Each set consisted of three rods with the same diameter and material. The diameters were 0.5, 1.0, 1.6, 2.0, and 3.0 mm, respectively. The four larger rods were made of aluminum, and the smallest 0.5 mm rod was made of steel. The rod phantom was inserted to the center of a lucite cylinder of 200 mm diameter and the same height. The voxel size was 0.5 mm cube with the rod phantom placed in the center of the imaging volume. The CT data were acquired at X-ray 120 KVp and 200 mA.

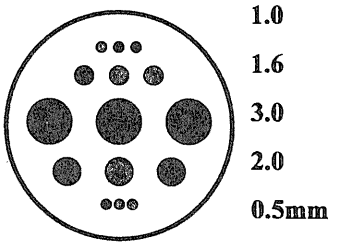

Fig. 7. Cross section of the rod phantom.

B. Radiation Dose

Radiation dose to an object was measured with an extension of the standard measurement method of CT dose index (CTDI). A lucite cylinder of 320 mm diameter was used in this measurement. The phantom was 300 mm long, which was twice the length of the standard phantom to accommodate the longitudinal field of view (collimator aperture) was 128 mm along the rotational axis in the present scanner. Because the effective length of the standard chamber was 100 mm, exposure dose was measured at three contiguous positions separated by intervals of 100 mm. CTDI was obtained by the following:

$$CTDI = \frac{1}{d}\sum_{i=1}^{3} IC_i \tag{1}$$

where d was a nominal slice thickness (128 mm), and IC_i was output of the ion chamber at each position.

C. Volunteer Study

Several volunteers were scanned to explore clinical potentials. The study protocol was approved by the ethics committee of the National Institute of Radiological Sciences, and each subject gave written informed consent prior to participating in the study. While most were scanned in a 3-D mode using a

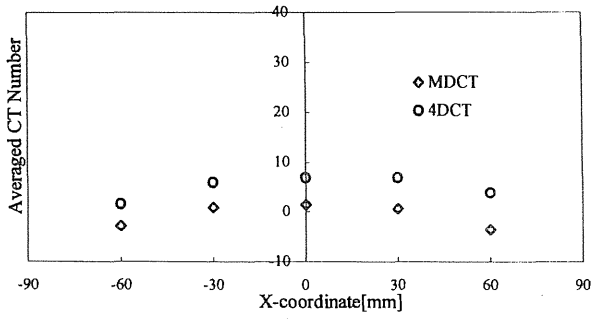

Fig. 8. Averaged CT-numbers in ROIs aligned along the x-axis.

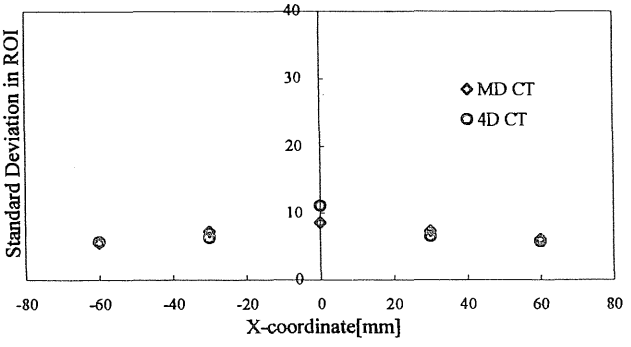

Fig. 9. Standard deviations of CT-numbers in ROIs aligned along the x-axis.

"step-and-shoot" acquisition, two were scanned in a 4-D mode in which scanner was performed with multiple rotations. Total exposure dose for each volunteer was limited to 600 mAs, which corresponds to 10 mSv for effective dose or 100 mGy for skin dose at the maximum in the 4-D mode.

IV. Results and Discussion

A. Image Characteristics

Fig. 8 shows uniformity measurement results. Though the CT-numbers of 4-D CT were slightly higher than 0 due to their insufficient calibrations, 4-D CT had a relative uniformity which was almost the same as that of MD CT. Fig. 9 shows noise measurement results and standard deviations of CT-numbers in the ROIs aligned along the x-axis. Standard deviations indicating magnitudes of image noises were almost identical for both CT, except at the center region where a slight ring artifact was observed in 4-D CT.

Fig. 10 shows spatial resolution measurement results. These images were obtained from 3-D data of the spatial resolution rod phantom. Because the voxel size was a 0.5 mm cube, pixel size was 0.5 mm and slice thickness was 0.5 mm in both figures. In the left figure rods are inserted perpendicularly to the transverse plane, while in the right figure rods are parallel to the transverse plane and rods of the same diameter are aligned to the z-direction. All sets of rods down to 0.5 mm diameter were separable in both figures, which meant an isotropic resolving power of less than 0.5 mm was achieved.

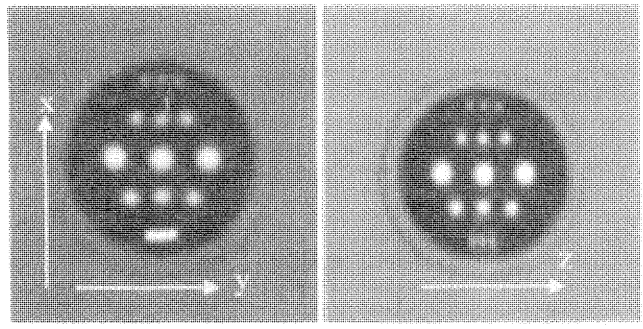

Fig. 10. Transverse (left) and longitudinal (right) images of resolution phantom.

TABLE I
CTDI of 4-D CT

	Center	Peripheral
4D CT	10.2	16.7
MD CT	6.0	14.9

Unit: mGy/100mAs, MD CT: Toshiba Corp. Aquillion

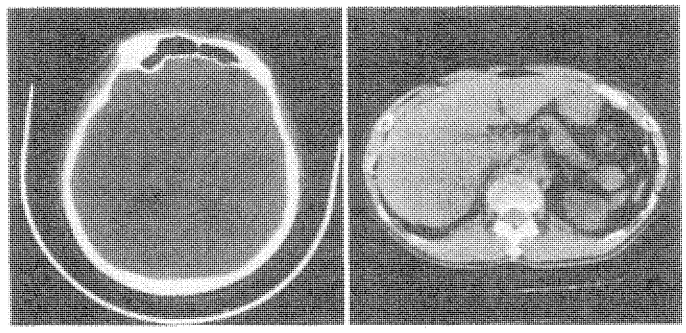

Fig. 11. Transverse images of volunteers (left: head; right: liver).

B. Radiation Dose

Table I shows results of radiation dose measurements. The CTDI of over 300 mm length was measured in this report, and was a little higher than the standard CTDI of an ordinary CT-scanner (Toshiba Corp. Aquillion) [9], especially in the center region. This result might be attributed to larger amounts of scattered X-rays in the cone-beam geometry though further study will be necessary to confirm this.

C. Volunteer Study

Figs. 11 and 12 show examples of volunteer results. Fig. 11 shows transverse images of volunteers. These images were obtained from 3-D data of volunteers. Voxel sizes were 0.5 mm for head, and 0.6 mm for liver, respectively. Because slice thickness was the same as the voxel size for each case, image noises were more significant than ordinary images which are usually taken with thicker slices. These noises may be decreased by z-direction smoothing.

Fig. 12 shows dynamic 3-D rendered images (4-D image) of a volunteer during intended motion of his jaws. These images were examples of thirty 3-D images reconstructed with a

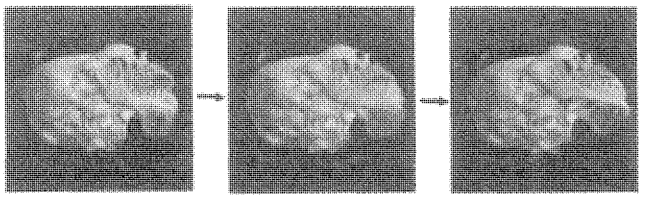

Fig. 12. Dynamic 3-D rendered images (4-D image) of a volunteer during intended motion of his jaws.

TABLE II
SPECIFICATION OF THE FIRST AND SECOND MODEL

	First model	Second model
Scan mode	Cone-beam continuous rotation (4D)	Cone-beam continuous rotation (4D) Helical cone-beam (large 3D)
Detector	912x256	The same as the first
Scan time	1sec/rot (14sec max)	0.5sec/rot (30sec max)
Reconstruction matrix	512x512x256	512x512x512
Contrast resolution	Less than 0.5%	The same as the first
Reconstruction time	6min for 512x512x256	Less than 1sec
End of construction	March 2002	March 2004

0.1 s interval. Clinical studies as well as animal experiments are planned to explore the possibilities of 4-D CT.

D. Future Development

Since in the first model, the reconstruction time is 6 min for the full size matrix and much slower than the scan time, it may be an obstacle to clinical applications, especially for interventional therapy. We are now constructing a second model that had a much faster reconstruction computer composed of next generation field programmable gate arrays (FPGA). This model will be completed by the end of fiscal year 2003. Table II summarizes specifications of the two models.

REFERENCES

[1] R. A. Robb, "The spatial reconstructor: an X-ray video-fluoroscopic CT scanner for dynamic volume imaging of moving organs," *IEEE Trans. Med. Imaging*, vol. MI-1, pp. 22–33, July 1982.
[2] D. Saint-Felix, Y. Trousset, C. Picard, C. Ponchut, R. Romeas, and A. Rougee, "In vivo evaluation of a new system for computerized angiography," *Phys. Med. Biol.*, vol. 39, pp. 585–595, 1994.
[3] M. Endo, K. Yoshida, N. Kamagata, K. Satoh, T. Okazaki, and Y. Hattori *et al.*, "Development of a 3D CT-scanner using a cone beam and video-fluoroscopic system," *Radiat. Med.*, vol. 16, pp. 7–12, 1998.
[4] Y. Saito, H. Aradate, H. Miyazaki, K. Igarashi, and H. Ide, "Large area 2-dimensional detector for real-time 3-dimensional CT (4D-CT)," *Proc. SPIE*, vol. 4320, pp. 775–782, 2001.
[5] M. Endo, T. Tsunoo, S. Kandatsu, S. Tanada, H. Aradate, and Y. Saito, "4-dimensional computed tomography (4D CT)—its concepts and preliminary development," in *Proc. M7-6 2001 IEEE NSS Conf. Record*, San Diego, CA, Nov. 2001.
[6] M. Endo, T. Tsunoo, S. Kandatsu, S. Tanada, H. Aradate, and Y. Saito, "4-dimensional computed tomography (4D CT)—its concepts and preliminary development," *Radiat. Med.*, vol. 21, pp. 17–22, 2003.
[7] L. A. Feldkamp, L. C. Davis, and J. W. Kress, "Practical cone-beam algorithm," *J. Opt. Soc. Amer.*, vol. A1, pp. 612–619, 1984.
[8] M. Endo, K. Nishizawa, K. Iwai, M. Matsumoto, K. Yoshida, and K. Satoh *et al.*, "Image characteristics and effective dose estimation of a cone beam CT using a video-fluoroscopic system," *IEEE Trans. Nucl. Sci.*, vol. 46, pp. 686–690, June 1999.
[9] Y. Saito, "private communication," unpublished.

Physical performance evaluation of a 256-slice CT-scanner for four-dimensional imaging

Shinichiro Mori, Masahiro Endo,[a] Takanori Tsunoo, Susumu Kandatsu, and Shuji Tanada
National Institute of Radiological Sciences, Chiba 263-8555, Japan

Hiroshi Aradate, Yasuo Saito, and Hiroaki Miyazaki
Toshiba Medical Systems, Otawara 324-8550, Japan

Kazumasa Satoh and Satoshi Matsushita
Sony Corporation, Tokyo 141-0001, Japan

Masahiro Kusakabe
Fukui University Faculty of Engineering, Fukui 910-8507, Japan

(Received 29 May 2003; revised 5 March 2004; accepted for publication 29 March 2004; published 17 May 2004)

We have developed a prototype 256-slice CT-scanner for four-dimensional (4D) imaging that employs continuous rotations of a cone-beam. Since a cone-beam scan along a circular orbit does not collect a complete set of data to make an exact reconstruction of a volume [three-dimensional (3D) image], it might cause disadvantages or artifacts. To examine effects of the cone-beam data collection on image quality, we have evaluated physical performance of the prototype 256-slice CT-scanner with 0.5 mm slices and compared it to that of a 16-slice CT-scanner with 0.75 mm slices. As a result, we found that image noise, uniformity, and high contrast detectability were independent of z coordinate. A Feldkamp artifact was observed in distortion measurements. Full width at half maximum (FWHM) of slice sensitivity profiles (SSP) increased with z coordinate though it seemed to be caused by other reasons than incompleteness of data. With regard to low contrast detectability, smaller objects were detected more clearly at the midplane ($z=0$ mm) than at $z=40$ mm, though circular-band like artifacts affected detection. The comparison between the 16-slice and the 256-slice scanners showed better performance for the 16-slice scanner regarding the SSP, low contrast detectability, and distortion. The inferiorities of the 256-slice scanner in other than distortion measurement (Feldkamp artifact) seemed to be partly caused by the prototype nature of the scanner and should be improved in the future scanner. The image noise, uniformity, and high contrast detectability were almost identical for both CTs. The 256-slice scanner was superior to the 16-slice scanner regarding the PSF, though it was caused by the smaller transverse beam width of the 256-slice scanner. In order to compare both scanners comprehensively in terms of exposure dose, noise, slice thickness, and transverse spatial resolution, $K=D\sigma^2ha^3$ was calculated, where D was exposure dose (CT dose index), σ was magnitude of noise, h was slice thickness (FWHM of SSP), and a was transverse spatial resolution (FWHM of PSF). The results showed that the K value was 25% larger for the 16-slice scanner, and that the 256-slice scanner was 1.25 times more effective than the 16-slice scanner at the midplane. The superiority in K value for the 256-slice scanner might be partly caused by decrease of wasted exposure with a wide-angle cone-beam scan. In spite of the several problems of the 256-slice scanner, it took a volume data approximately 1.0 mm (transverse) $\times$ 1.3 mm (longitudinal) resolution for a wide field of view (approximately 100 mm long) along the z axis in a 1 s scan if resolution was defined by the FWHM of the PSF or the SSP, which should be very useful to take dynamic 3D (4D) images of moving organs. © *2004 American Association of Physicists in Medicine.* [DOI: 10.1118/1.1747758]

Key words: CT technology, cone-beam CT, CT image quality, CT exposure dose

I. INTRODUCTION

Since Hounsfield and Ambrose installed a prototype of the EMI-scanner at Atkinson Morley Hospital in 1971, continuous and remarkable developments have been made in CT technology. As a result of such developments, we can take 32 to 40 slices per second with a state-of-the-art CT-scanner. This is several thousand times faster than the original EMI-scanner that could take only two slices in $4\frac{1}{2}$ min. The developments of CT technology have allowed applications of three-dimensional (3D) images in clinical fields such as diagnosis, surgical simulation, planning of radiation therapy, and monitoring of interventional therapy. Moreover, the latest 16-slice scanner developed has made dynamic 3D imaging possible, this could be called four-dimensional (4D) im-

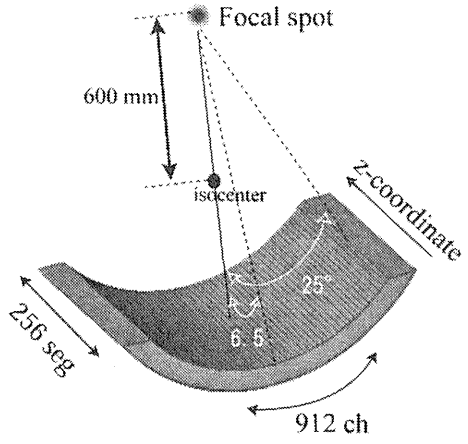

FIG. 1. Illustration of the detector and the geometry used in 256-slice scanner.

aging. However, the axial field of view of the 16-slice scanner is 32 mm at the maximum, which imposes a limit on application of 4D imaging. In order to take 4D images of a wider field of view, we have developed a prototype 256-slice CT-scanner by mounting a novel wide-area two-dimensional (2D) detector on a gantry frame of a state-of-the-art CT-scanner[1] (Toshiba Aquilion: Toshiba Medical Systems, Japan). Because of its mechanical simplicity, the prototype uses continuous rotations of a cone-beam to take 4D images. Since a cone-beam scan along a circular orbit does not collect a complete set of data to make an exact reconstruction of a volume (3D image), disadvantages or artifacts might occur if cone angle is substantially wide.[2] To examine effects of the cone-beam data collection on image quality, we have evaluated physical performance of the prototype and compared it to that of a state-of-the-art 16-slice CT-scanner.

II. MATERIALS AND METHODS

A. Prototype 256-slice CT-scanner

A wide-area 2D detector was designed on the basis of the present CT technology[3] and mounted on the gantry frame of the state-of-the-art CT-scanner. The number of elements was 912 channels×256 segments; element size was approximately 1.02 mm×0.90 mm, which corresponds to 0.58 mm (transverse)×0.50 mm (longitudinal) beam width at the center of rotation (Fig. 1). Scanning time was 1.0 s/rotation. The scanner could scan a field of view approximately 100 mm long in the z direction with 1 s scan. Data sampling rate was 900 views (frames)/s, and dynamic range of the A/D converter was 16 bits. The detector element consisted of a scintillator and photodiode. The scintillator was Gd_2O_2S ceramic with thickness of approximately 2 mm; both material and thickness were the same as for the scintillator of a multi-detector CT-scanner (Toshiba Aquilion). The 2D detector had a blade collimator that was an assembly of thin equally spaced molybdenum septa, which were adjusted parallel to the rotation axis, and the pitch of the blade was identical to the detector element pitch. The collimator ratio was approximately 30:1, which was the height of the blades divided by the length of the gap. A Feldkamp–Davis–Kress (FDK)[2] algorithm was used for reconstruction. It took about 10 min to reconstruct volume data of 512×512×256 voxels by parallel use of 128 microprocessors.

B. Evaluation methods and scan conditions

We measured the following items with stationary phantoms designed for the 256-slice scanner by the same method as that of conventional CT: (i) point spread function (PSF), (ii) slice sensitivity profile (SSP), (iii) image noise and uniformity, (iv) high contrast and low contrast detectabilities, (v) distortion, and (vi) exposure dose. We compared them with the evaluation results of a 16-slice CT-scanner routinely used at our institute (SOMATOM Sensation 16, Siemens AG.). Scan conditions for the 256-slice scanner were 120 kV, 200 mA, 1.0 s exposure, 1.0 s gantry rotation time, 0.5 mm slice thickness, and 256×0.5 mm slice collimation. Those for the 16-slice scanner were 120 kV, 200 mA, 1.0 s exposure, 1.0 s gantry rotation time, 0.75 mm slice thickness, and 16×0.75 mm slice collimation. The beam width for the 16-slice scanner was 0.75 mm×0.75 mm at the rotation center. Scan conditions for almost all items were the same for each scanner and they were chosen to approximate clinical CT imaging. Reconstruction parameters for the 256-slice scanner were a voxel size of 0.468×0.468×0.500 mm^3 with 0.500 mm reconstruction increment along z axis and matrix size of 512×512×256, and those for the 16-slice scanner were a voxel size of 0.468×0.468×0.750 mm^3 with 0.750 mm reconstruction increment along the z axis and matrix size of 512×512×16. Convolution kernels were standard body kernels; FC10 for the 256-slice scanner and B40s for the 16-slice scanner. Scans under other conditions are noted as necessary. Table I shows details of scan conditions.

1. Point spread function (PSF)

A PSF was assessed using a commercially available CT image quality phantom (Catphan 500 with module CTP528, Phantom Laboratory, Salem, NY) which contained a 0.288 mm tungsten carbide bead positioned 38 mm up from the center of the phantom. We employed zoomed reconstruction for both CTs, in which voxel sizes were 0.146×0.146 ×0.500 mm^3 for the 256-slice scanner and 0.146×0.146 ×0.750 mm^3 for the 16-slice scanner. PSFs were obtained as normalized CT-number profiles along the center of the bead at the midplane ($z=0$ mm) for both CTs, and $z=20$ mm and $z=40$ mm for the 256-slice scanner. Full width at half maximums (FWHMs) and full width at tenth maximums (FWTMs) were evaluated by interpolating PSFs.

2. Slice sensitivity profile (SSP)

The same phantom as for the PSF was used to evaluate a SSP by making a coronal reconstruction through the bead. Reconstruction increment along the z axis was 0.1 mm for the 256-slice scanner. For the 16-slice scanner reconstruction increment was 0.75 mm. In order to make finer sampling intervals, the phantom was scanned at three contiguous positions with 0.5 mm interval, which effectively made the

TABLE I. Scan conditions for 256-slice scanner and 16-slice scanner.

	Evaluation items	Scanner	Section	Voltage (kV)	Current (mA)	Scan time (s)	Slice collimation	Slice thickness (mm)	Scan mode
1	PSF	256-slice CT	Transverse	120	200	1.0	256×0.5 mm	0.5	Axial
		16-slice CT					16×0.75 mm	0.75	
2	SSP	256-slice CT	longitudinal	120	200	1.0	256×0.5 mm	0.5	Axial
		16-slice CT					16×0.75 mm	0.75	
3	Image noise, uniformity	256-slice CT	Transverse	120	200	1.0	256×0.5 mm	0.5	Axial
		16-slice CT					16×0.75 mm	0.75	
4	High contrast	256-slice CT	Transverse	120	200	1.0	256×0.5 mm	0.5	Axial
		16-slice CT					16×0.75 mm	0.75	
5	Low contrast	256-slice CT	Transverse	120	400	1.0	256×0.5 mm	12.0	Axial
		16-slice CT					16×0.75 mm		
6	Distortion	256-slice CT	Longitudinal	120	200	1.0	256×0.5 mm	0.5	Axial
		16-slice CT		120	200	8.3	16×0.75 mm	0.75	Helical (pitch: 1.25)
7	Exposure dose	256-slice CT		120	200	1.0	256×0.5 mm		Axial
		16-slice CT					16×0.75 mm		

sampling interval of 0.25 mm. SSPs were obtained as normalized CT-number profiles along the center of the bead at $z=0$ mm for both CTs, and $z=20$ mm and $z=40$ mm for the 256-slice scanner. FWHMs and FWTMs were evaluated by interpolating SSPs.

3. Image noise and uniformity

Image noise was measured with a 200-mm-diam and 250-mm-high acrylic cylinder filled with water. Standard deviations (SDs) of CT-number were calculated in nine regions of interest (ROIs) of 10 mm diameter aligned every 20 mm along the diameter of the phantom in the transverse section (Fig. 2). For the 256-slice scanner, calculations were made at $z=0$ mm, $z=20$ mm, and $z=40$ mm. The same phantom and ROIs were used for the uniformity measurement as for the noise measurement, and averages of CT-number were calculated in these ROIs.

4. High contrast and low contrast detectabilities

High contrast and low contrast detectabilities were assessed with commercially available CT phantoms for CT performance evaluation (high contrast: Kyoto Kagaku Co., Ltd., Japan, low contrast: Catphan 500 with module CTP515). Figure 3 shows schematic drawings of the two phantoms. The phantom for high contrast detectability included six sets of spheres and two sets of cylinders. Each set consisted of spheres (or cylinders) of 2, 3, 5, 7, and 10 mm diameter, and their CT-numbers were +50 HU (Hounsfield Unit), while that of the background was approximately −650 HU. The results were evaluated by observing images and by obtaining the relationships between the CT-number difference and the diameter of the cylinder. This CT-number difference was obtained by subtracting the CT-number of the background from that of the cylinder. For the 256-slice scanner, evaluations were made at $z=0$ mm, $z=20$ mm, and $z=40$ mm.

The low contrast phantom included three supra-slice and sub-slice sets of cylinders. The sub-slice targets have z axis lengths of 3, 5, and 7 mm and diameters of 3, 5, 7, and 9 mm. These supra-slice sets consisted of cylinders of 2, 3, 4, 5, 6, 7, 8, 9, and 15 mm diameter, and contrasts of three sets of cylinders from background were 0.3%, 0.5%, and 1.0%. A

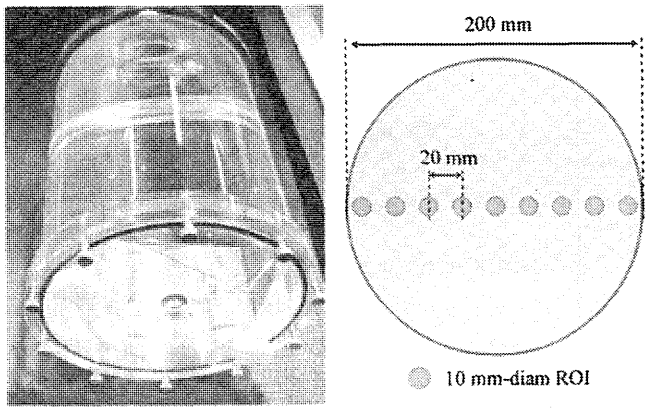

FIG. 2. Photograph of the water phantom for the evaluation of image noise and uniformity. Nine ROIs of 10 mm diameter were aligned every 20 mm along the diameter of the phantom.

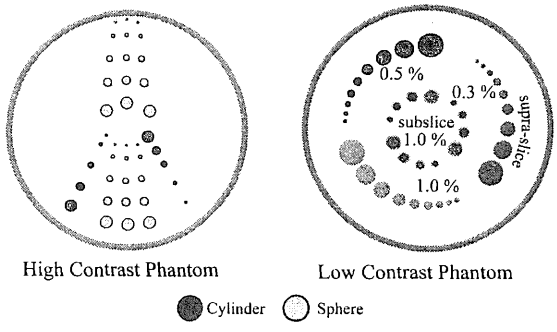

FIG. 3. Schematic drawing of the phantoms for high and low contrast detectabilities. The CT-numbers for the high contrast phantom were +50 HU, and that of the background was approximately −650 HU. The phantom included sets of spheres (or cylinders) of 2, 3, 5, 7, and 10 mm diameter. For the low contrast phantom, contrasts of three sets of cylinders except subslice sets from the background were 0.3%, 0.5%, and 1.0%. The phantom included sets of cylinders of 2, 3, 4, 5, 6, 7, 8, 9, and 15 mm diameter.

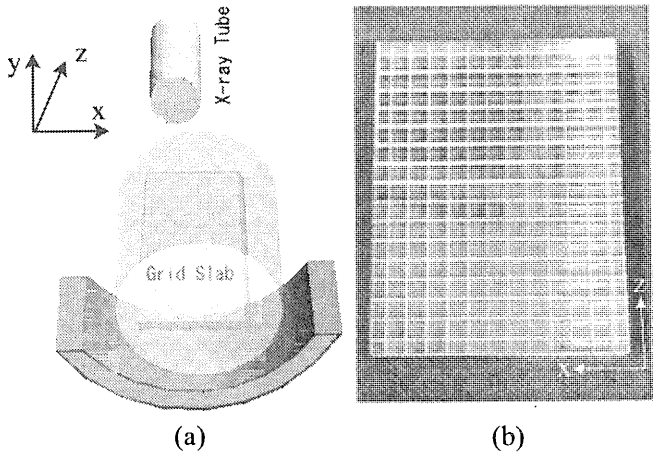

FIG. 4. Distortion phantom. (a) Schematic drawing of scanned geometry. (b) Photograph.

1.0% contrast means that the mean CT-number of the object differs from its background by 10 HU. Slice thickness was 12.0 mm for both CTs. It was given by the average of twenty-four 0.5 mm slices for the 256-slice scanner, and given by the average of sixteen 0.75 mm slices for the 16-slice scanner. The results were evaluated by observing images with supra-slice targets to avoid any volume-averaging errors. For the 256-slice scanner, evaluations were made at $z=0$ mm and $z=40$ mm.

5. Distortion

The distortion phantom was an acrylic slab on which straight grooves of 1.0 mm width, 10 mm depth, and 15 mm spacing were machined to form a grid (Fig. 4). It was inserted into an acrylic cylinder perpendicularly to the transverse plane to evaluate the distortions in the longitudinal section. We evaluated distortions to make a profile through the phantom along the longitudinal direction and to measure spacing of grids. For the 16-slice scanner we evaluated a multi-planar reformat (MPR) image of 0.50 mm pixel size in the longitudinal section using 8.3 s exposure and helical pitch of 1.25.[4]

6. Exposure dose

Exposure dose to an object was measured with an extension of the standard measurement method of CT dose index (CTDI). The dose measurements were performed with a pencil-shaped ionization chamber connected to an electrometer (AE-132a, 2902210, Oyogiken, Japan). The active length of the chamber (CT-10, Oyogiken) was 100 mm. We used an acrylic phantom[5] of 160 mm diameter and 300 mm length. The length of the phantom was twice the standard one because the longitudinal field of view (beam collimation) was 128 mm along the rotation axis for the 256-slice scanner. The phantom was placed on the patient table and its center was aligned at the scan isocenter. The ionization chamber was inserted into either the central or one of the peripheral cavities of the phantom (other cavities being filled with perspex rods). Because the active length of the ionization chamber was 100 mm, exposure dose was measured at three contiguous positions with 100 mm interval. The nominal tube current for both CTs was 200 mA (200 mAs). The standard CTDI was measured using 256×0.5 mm beam collimation for the 256-slice scanner and 16×0.75 mm beam collimation for the 16-slice scanner. CTDI was obtained by the following:

$$\mathrm{CTDI}=\frac{1}{T}\sum_{i=1}^{3}\mathrm{IC}_i,$$

where T (mm) was the beam collimation width at the rotation center (128 mm for the 256-slice scanner and 12 mm for the 16-slice scanner), and IC_i (mGy mm) was output of the ionization chamber at each position. Weighted CTDI (CTDI_w)[5,6] was calculated from CTDIs measured at the center and peripheries of the phantom as follows:

$$\mathrm{CTDI}_w=(\tfrac{1}{3}\mathrm{CTDI}_{\mathrm{center}}+\tfrac{2}{3}\mathrm{CTDI}_{\mathrm{periphery}}),$$

where $\mathrm{CTDI}_{\mathrm{center}}$ means the CTDI measured at the center, and $\mathrm{CTDI}_{\mathrm{periphery}}$ means the average CTDIs measured on the periphery.

To compare with the nominal beam width (beam collimation width mentioned above), actual beam width T' was measured for the both scanners. A film (Kodak X-Omat V non-screen therapy verification film) was placed at the rotation center and exposed without gantry rotation. FWHM of density profile of the exposed film along the z axis was obtained as the actual beam width.

7. Figure of merit

Because magnitude of noise, transverse spatial resolution, slice thickness, and exposure dose are related to one another in the CT performance evaluation, individual comparisons of each item are not sufficient. A figure of merit K as follows was compared in this study,

$$K=D\sigma^2ha^3,$$

where D is exposure dose (weighted CTDI), σ is magnitude of noise, h is slice thickness (FWHM of SSP), and a is transverse spatial resolution (FWHM of PSF).[7,8] For each

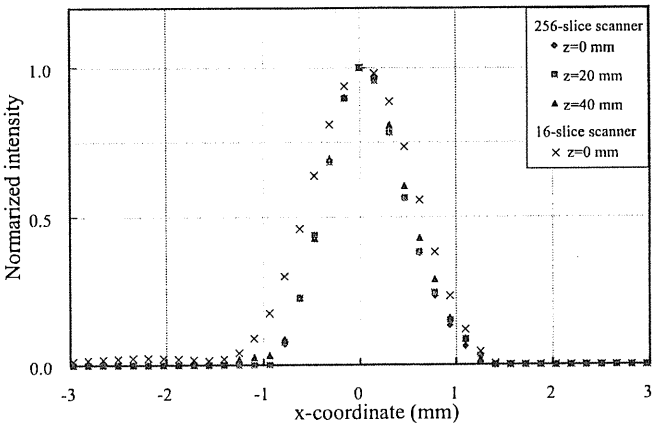

FIG. 5. Point spread functions (PSFs) for 256-slice scanner and 16-slice scanner.

TABLE II. Full width at half maximum (FWHM) and full width at tenth maximum (FWTM) of point spread function. Relative values to transverse beam width (0.58 mm for 256-slice scanner and 0.75 mm for 16-slice scanner) are given in parentheses.

	256-slice scanner			16-slice scanner
	$z=0$ mm	$z=20$ mm	$z=40$ mm	$z=0$ mm
FWHM	0.94	0.95	0.98	1.26
	(1.62)	(1.64)	(1.69)	(1.68)
FWTM	1.74	1.80	1.82	2.54
	(3.00)	(3.10)	(3.13)	(3.39)

TABLE III. Full width at half maximum (FWHM) and full width at tenth maximum (FWTM) of slice sensitivity profiles. Relative values to longitudinal beam width (0.50 mm for 256-slice scanner and 0.75 mm for 16-slice scanner) are given in parentheses.

	256-slice scanner			16-slice scanner
	$z=0$ mm	$z=20$ mm	$z=40$ mm	$z=0$ mm
FWHM	1.18	1.26	1.32	0.78
	(2.36)	(2.52)	(2.64)	(1.04)
FWTM	1.85	2.03	2.07	1.37
	(3.70)	(4.06)	(4.14)	(1.83)

model of the CT-scanners, K remains constant if the phantom and x-ray effective energy are the same. From the equation it might be suggested that a CT-scanner with smaller K value could take CT images of the same σ, h, and a with lower exposure dose. In the present study we employed three phantoms to measure the above-mentioned items D, σ, h, and a. However, the above-presented equation was approximately correct because attenuation characteristics of the phantoms were similar to one another.

III. RESULTS

A. Point spread function

PSFs for the 256-slice scanner and the 16-slice scanner are shown in Fig. 5, and FWHMs and FWTMs of PSF are listed in Table II. In the table, relative values to transverse beam widths are given as well as the absolute ones. The FWHM for the 256-slice scanner showed slight dependence on z coordinate as being 0.94 mm at $z=0$ mm, 0.95 mm at 20 mm, and 0.98 mm at $z=40$ mm. The FWHM for the 16-slice scanner was 1.26 mm. Although the absolute FWHMs for the 256-slice scanner were smaller than that for the 16-slice scanner, the relative values were approximately 1.6–1.7 and similar for both CTs.

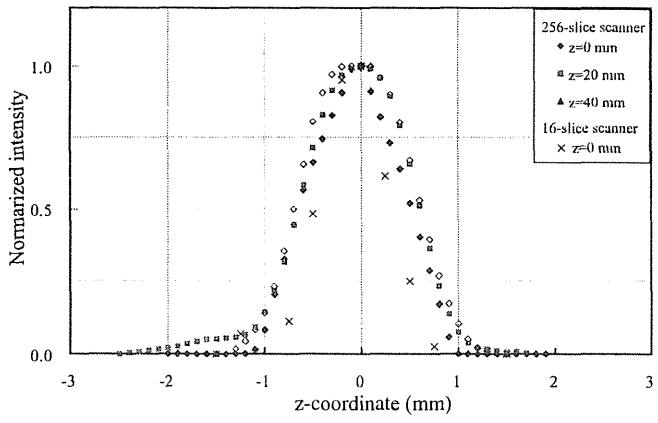

FIG. 6. Slice sensitivity profiles (SSPs) of axial scan for 256-slice scanner and 16-slice scanner.

B. Slice sensitivity profile

SSPs for the 256-slice scanner and the 16-slice scanner are shown in Fig. 6, and FWHMs and FWTMs of SSPs are listed in Table III. In the table, relative values to the longitudinal beam width are given as well as the absolute ones. The FWHM for the 256-slice scanner showed z coordinate dependence as being 1.18 mm at $z=0$ mm, 1.26 mm at 20 mm, and 1.32 mm at $z=40$ mm. The FWHM for the 16-slice scanner was 0.78 mm, better than for the 256-slice scanner, and this nearly coincided with the longitudinal beam width. The relative values of FWHM for the 256-slice scanner were much larger than that for the 16-slice scanner.

C. Image noise and uniformity

The magnitude of image noise was obtained from the standard deviations of CT-number in the nine ROIs in a transverse section (see Fig. 2). Figure 7 shows the relationship between the standard deviation and the position along the x axis for both scanners. Since average standard deviations of nine ROIs were 16.2 HU at $z=0$ mm, 17.0 HU at $z=20$ mm, and 16.7 HU at $z=40$ mm for the 256-slice scanner, the magnitude of noise was independent of z coordinates for it. As average standard deviation of nine ROIs for the

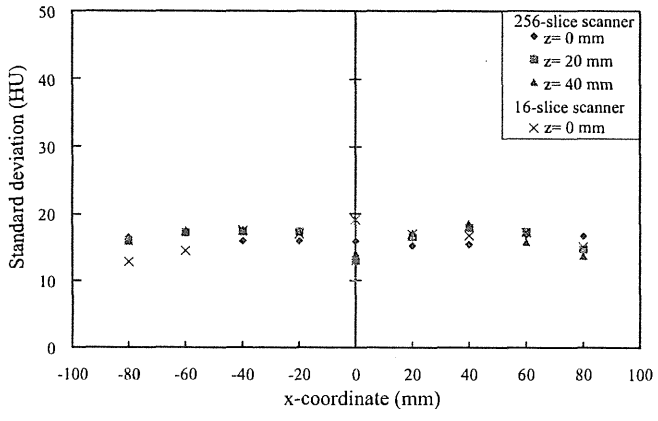

FIG. 7. Relationship between the standard deviation (s.d.) of CT-number and the x coordinate in the transverse section. The average standard deviations of nine ROIs were 16.2 HU (256-slice scanner $z=0$ mm), 17.0 HU (256-slice scanner $z=20$ mm), 16.7 HU (256-slice scanner $z=40$ mm), and 16.0 HU (16-slice scanner $z=0$ mm).

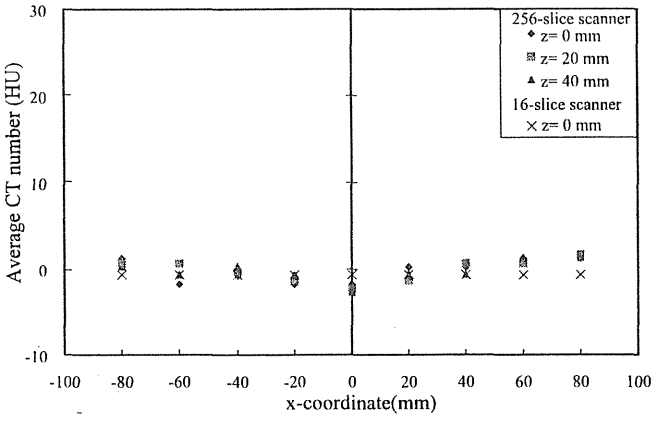

FIG. 8. Relationship between the average of CT-number and the x coordinate in the transverse section. Standard deviations of nine ROIs were 1.3 HU (256-slice scanner $z=0$ mm), 1.3 HU (256-slice scanner $z=20$ mm), 1.2 HU (256-slice scanner $z=40$ mm), and 0.0 HU (16-slice scanner $z=0$ mm).

16-slice scanner was 16.0 HU, the magnitude of noise for the 256-slice scanner was approximately the same as that for the 16-slice scanner.

For the uniformity measurement, we calculated averages of CT-number in ROIs in the transverse section (see Fig. 2). Figure 8 shows the relationship between the average and the position along the x axis for both scanners. The standard deviations of the average were 1.3 HU at $z=0$ mm, 1.3 HU at $z=20$ mm, and 1.2 HU at $z=40$ mm for the 256-slice scanner and 0.0 HU for the 16-slice scanner. From these uniformity measurements, we noted the 256-slice scanner showed nearly the same performance as the 16-slice scanner, and no dependence on z coordinate was observed for the 256-slice scanner.

D. High contrast and low contrast detectabilities

With regard to high contrast detectability we could observe objects down to 2 mm for the 256-slice scanner in all sections ($z=0$, 20, and 40 mm) [Figs. 9(a)–9(c)]. Also for the 16-slice scanner, objects down to 2 mm could be observed [Fig. 9(d)]. Figure 10 shows relationships between the CT-number difference and the cylinder diameter. The CT-number difference gradually decreased as the cylinder diameter decreased with nearly identical response for both CTs. For the 256-slice scanner the response was nearly identical at all sections. Therefore, in high contrast detectability, the 256-slice scanner showed nearly equivalent performance to that of the 16-slice scanner, and no dependence on z coordinate was observed for the 256-slice scanner.

Figure 11 shows images of the low contrast phantom for the 256-slice scanner and the 16-slice scanner. Table IV lists the minimum diameters of detected cylinders. From the table, we noted performance of the 16-slice scanner was significantly better than that of the 256-slice scanner at $z=0$ mm. Performance of the 256-slice scanner at $z=40$ mm was worse than at $z=0$ mm. Circular-band like artifacts might affect the results for the 256-slice scanner.

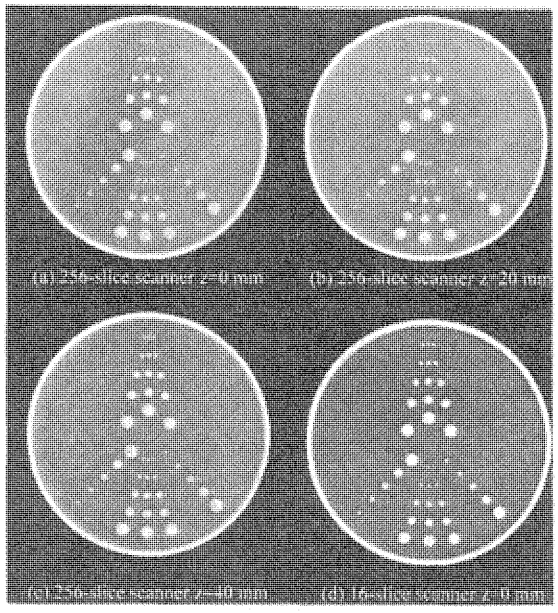

FIG. 9. High contrast phantom images in the transverse sections. (WL: −400, WW: 1200).

E. Distortion

Figure 12 shows images of the distortion phantom in the longitudinal section for both CTs. In the 256-slice scanner

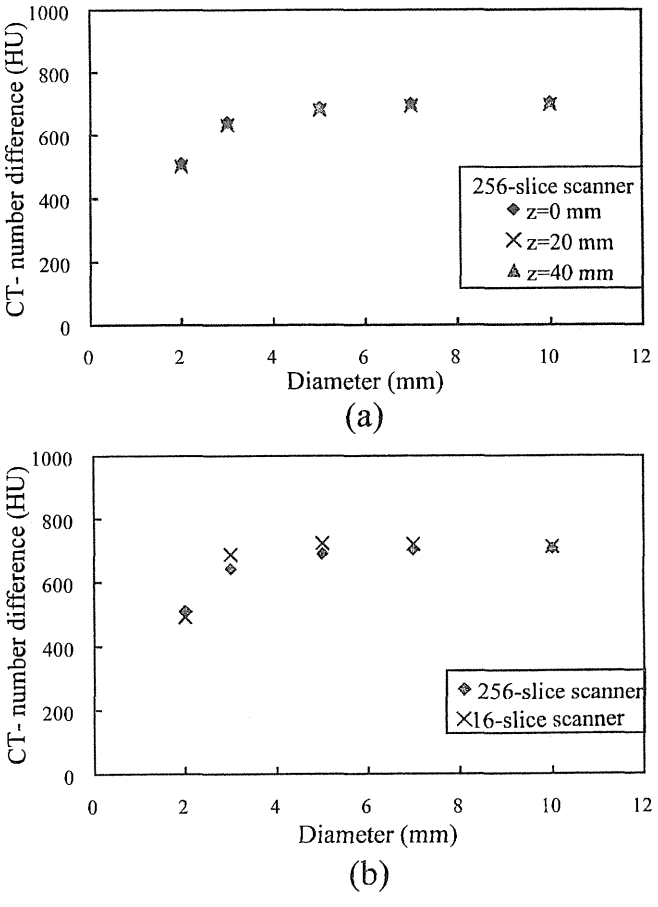

FIG. 10. Relationships between the CT-number difference and the diameter of cylinder.

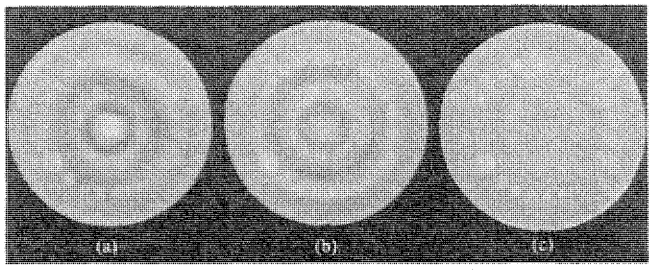

FIG. 11. Low contrast phantom images in the transverse section. (a) 256-slice scanner, $z=0$ mm. (b) 256-slice scanner, $z=40$ mm. (c) 16-slice scanner, $z=0$ mm.

image, grooves of the grid became slightly wider on leaving the center of the phantom in the longitudinal direction. Figure 13 reproduces a profile of CT-number along the z axis for both CTs. In this profile, the depth of the valley became shallower and its width became wider on leaving the center. This artifact could be attributed to a Feldkamp artifact which is caused by incompleteness of data obtained in cone-beam geometry and that occurs when x-ray attenuation is changed rapidly along z axis. From the figure, valley-to-valley distance was calculated to obtain grid spacing. The results were 15.5 mm (31 pixels×0.500 mm) at the center and 15.0 mm (30 pixels×0.500 mm) at other points. The difference between them was one pixel and within truncation errors. This fact indicated that the Feldkamp artifact had a little effect on the geometrical accuracy. For the 16-slice scanner, the MPR image [Fig. 12(b)] was clear and the shapes of valley were essentially the same in the profile measurement [Fig. 13(b)].

F. Exposure dose

Table V shows the results of CTDI measurements for both scanners. CTDIs were given with normalization to 100 mAs[9] in Table V. The $CTDI_w$ for the 256-slice scanner was approximately 24% larger than that for the 16-slice scanner. Measured beam widths T' were larger than nominal values T for both scanners.

G. Figure of merit

Table VI summarizes K value calculation for both scanners. For the 256-slice scanner, K values increased gradually on leaving from the midplane mainly because FWHM of SSP h increased. The K value of the 16-slice scanner was larger than the K value of the 256-slice scanner at $z=0$ mm, but smaller than the one at $z=40$ mm.

TABLE IV. Minimum diameter of detected cylinders (mm).

Scanner	Position (mm)	Contrast (%)		
		1.0%	0.5%	0.3%
256-slice CT	$z=0$ mm	4	5	8–9
	$z=40$ mm	4	5–6	9
16-slice CT	$z=0$ mm	3	4	6–7

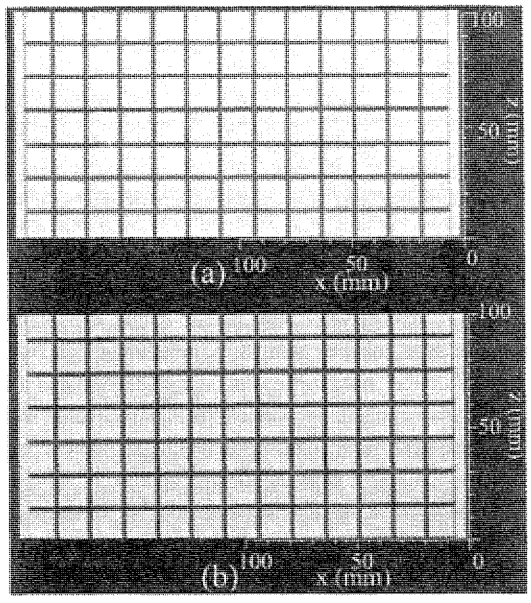

FIG. 12. Distortion phantom images in the longitudinal section. (a) 256-slice scanner, (b) 16-slice scanner.

IV. DISCUSSION

We have developed a prototype 256-slice scanner that employs continuous rotations of the cone-beam. To examine effects of incompleteness which is inevitable for cone-beam

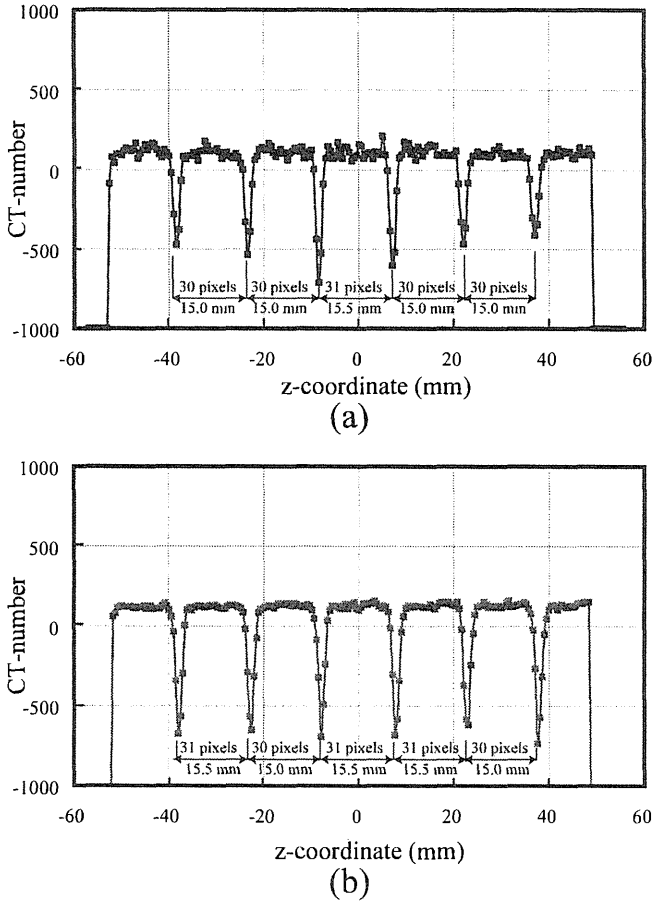

FIG. 13. Profiles through the distortion phantom along the z axis. (a) 256-slice scanner, (b) 16-slice scanner.

TABLE V. Exposure dose.

Scanner	Nominal beam width (T)	Measured beam width (T′)	$CTDI_{center}$ (mGy/100 mAs)	$CTDI_{periphery}$ (mGy/100 mA/s)	$CTDI_{w}$ (mGy/100 mAs)
256-slice CT	128 mm	140 mm	21.4	22.9	22.4
16-slice CT	12 mm	18 mm	17.9	18.0	18.0

data collection, we evaluated physical performance of the prototype. As a result, we found image noise, uniformity, and high contrast detectability were independent of z coordinate.

In the distortion measurement, we observed a Feldkamp artifact that was caused by incompleteness of data collected in cone-beam geometry, and that occurred when x-ray attenuation was changed rapidly along the z axis. This type of artifact was shown in simulation studies.[10,11] In these studies, the authors used thin dense disks equally spaced and aligned perpendicular to the z axis, and they showed that the disk density lowered as it was leaving from the midplane. This was thought to be the similar artifact as we observed in the present experiment. Clinical meanings of this artifact should be carefully examined in a future study, because the phantoms used in these studies including ours were not likely to resemble patient anatomy.

With regard to SSP, FWHMs of SSP increased with z coordinate. However, its cause does not seem incompleteness of data, but it might be caused by an increase of effective focal spot size due to variation of the angle between target surface and x-ray path, though careful studies will be necessary to prove it. With regard to PSF, FWHMs of PSF showed a slight dependence on z coordinate. Because change of FWHM was very little (4%), further study will be necessary to confirm it.

With regard to low contrast detectability, smaller objects were detected at $z=0$ mm more clearly than at $z=40$ mm. However, this result might be affected by the circular-band like artifact that was caused by a slight sensitivity difference of the detector blocks. We are now producing correction software for this artifact, and its correction may change the present results.

We have compared the above-mentioned items and exposure dose between the 256-slice scanner and the 16-slice scanner. The comparison showed better performance for the 16-slice scanner regarding the SSP, low contrast detectability, and distortion. The inferiority of the 256-slice scanner regarding the SSP might be attributed to the x-ray focal spot size being larger in the z direction than for usual CT-scanners, because the x-ray tube was slightly tilted to cover a wider field of view and this tilting enlarged the effective focal spot size in z direction. Although the magnitudes of noise were almost the same for both scanners, the 256-slice scanner was significantly inferior to the 16-slice scanner regarding the low contrast detectability. This might be attributed to band-like artifacts and/or increased scatter in cone-beam geometry that would lower image contrast. Prematurity in image processing for the 256-scanner might also be included in reasons. Further studies are necessary to improve image quality before constructing a practical model.

The 256-slice scanner was superior to the 16-slice scanner with regard to PSF, though it was caused by the smaller transverse beam width of the 256-slice scanner. A figure of merit K was calculated to compare both scanners comprehensively in terms of magnitude of noise, transverse spatial resolution, slice thickness, and exposure dose. With regard to the K value, the 256-slice scanner was superior to the 16-slice scanner at $z=0$ mm, but inferior to it at $z=40$ mm. The K value of the 256-slice scanner at $z=0$ mm was 5764, while the K value of the 16-slice scanner was 7233. This result showed that the 256-slice scanner at the midplane was approximately 1.25 ($=7233/5764$) times more effective than the 16-slice scanner in terms of K value and it suggested that the former might take images of the same quality with 1/1.25 the exposure dose of the latter. The superiority of the 256-slice scanner in K value at least in the midplane might be partly caused by CTDI definition that takes into account all exposure dose whether it is effective to form image or not. From Table V, ratios of the measured beam width to the nominal one are 1.50 for the 16-slice scanner and 1.09 for the 256-slice scanner. As the ratio approaches unity, ratio of wasted exposure and K value decreases. Because measured beam width should be set by adding a certain margin to nominal one to cover penumbra and mechanical errors, ratio of both beam width and wasted exposure tends to decrease as beam width increases.

We examined physical performances of the 256-slice scanner with phantom experiments. As the results, we observed several problems such as the Feldkamp artifact in the distortion measurement, z coordinate dependence of SSP and

TABLE VI. List of K-value calculation.

Scanner	Position (mm)	K value	Dose D (mGy/100 mAs)	Image noise σ (HU)	SPS h (mm)	PSF a (mm)
256-slice CT	$z=0$	5764	22.41	16.20	1.18	0.94
	$z=20$	7029	22.41	17.04	1.26	0.95
	$z=40$	7774	22.41	16.71	1.32	0.98
16-slice CT	$z=0$	7233	18.04	16.03	0.78	1.26

inferiority of low contrast detectability to the-state-of-art multi-detector CT-scanner. These problems other than the Feldkamp artifact seemed to be partly caused by the prototype nature of the 256-slice scanner and should be improved in the future scanners. Concerning CTDI and K value, we found that wide-angle cone-beam scan might be advantageous to decrease wasted exposure due to decrease of penumbra ratio.

Although the 256-slice scanner showed several problems mentioned earlier, it took volume data approximately 1.0 mm (transverse) $\times$ 1.3 mm (longitudinal) resolution for a wide field of view (approximately 100 mm long) along the z axis in 1 s scan if resolution was defined by FWHM of PSF or SSP. This should be very useful to take dynamic 3D images of moving organs. Clinical studies as well as animal experiments are under way to investigate application possibilities of the 256-slice scanner to 4D imaging.

ACKNOWLEDGMENT

This work is supported in part by the NEDO (New Energy and Industrial Technology Development Organization), Japan.

[a]Corresponding author. Department of Medical Physics, National Institute of Radiological Sciences, 9-1 Anagawa 4-chome, Inage-ku, Chiba 263-8555, Japan. Electronic mail: endo@nirs.go.jp

[1] M. Endo, S. Mori, T. Tsunoo, S. Kandatsu, S. Tanada, H. Aradate, Y. Saito, H. Miyazaki, K. Satoh, S. Matsusita, and M. Kusakabe, "Development and performance evaluation of the first model of 4D CT-scanner," IEEE Trans. Nucl. Sci. **50**, 1667–1671 (2003).

[2] L. A. Feldkamp, L. C. Davis, and J. W. Kress, "Practical cone-beam algorithm," J. Opt. Soc. Am. A **1**, 612–619 (1984).

[3] Y. Saito, H. Aradate, K. Igarashi, and H. Ide, "Large area 2-dimensional detector for real-time 3-dimensional CT (4D CT)," Proc. SPIE **4320**, 775–782 (2001).

[4] International Electrotechnical Commission, "Evaluation and routine testing in medical imaging departments: part 2-6 constancy test-x-ray equipment for computed tomography," Pub. IEC 1223-2-6 (1994).

[5] T. B. Shope, R. M. Gagne, and G. C. A. Johnson, "Method for describing the doses delivered by transmission x-ray computed tomography," Med. Phys. **8**, 488–495 (1981).

[6] P. C. Shimptom, K. A. Jessen, J. Geleijns, W. Panzer, and G. Tosi, "Reference doses in computed tomography," Radiat. Prot. Dosim. **80**, 55–59 (1998).

[7] R. A. Brooks and G. D. Chiro, "Principles of computer assisted tomography (CAT) in radiologic and radioisotope imaging," Phys. Med. Biol. **21**, 689–732 (1976).

[8] H. H. Barrett and R. S. Hershel, "Statistical limitations in transaxial tomography," Comput. Biol. Med. **6**, 307–323 (1976).

[9] W. Leitz, B. Axelsson, and G. Szendrö, "Computed tomography dose assessment—A practical approach," Radiat. Prot. Dosim. **57**, 377–380 (1995).

[10] H. Kudo and T. Saito, "Derivation and implementation of a cone-beam reconstruction algorithm for nonplanar orbits," IEEE Trans. Med. Imaging **13**, 196–211 (1994).

[11] H. Hu, "A new cone beam reconstruction algorithm and its application to circular orbits," Proc. SPIE **2163**, 223–234 (1994).

骨梁構造を組み込んだヒト大腿骨近位部の有限要素解析

中土　裕樹[※1]　渡辺　直行[※2]　中土　幸男[※3]　但野　茂[※1]
小林　道明[※4]　森泉　哲次[※5]

Finite element analysis of the human proximal femur incorporating the trabecular architecture of cancellous bone.

Hiroki NAKATSUCHI, Naoyuki WATANABE, Yukio NAKATSUCHI, Shigeru TADANO, Michiaki KOBAYASHI, Tetsuji MORIIZUMI

Abstract

The purpose of this study was to construct a new type of finite element model of the human femur and to clarify the fracture mechanism of the femoral neck in osteoporosis by knowing the biomechanical role of the cancellous bone. There are new points in making the finite element model of human femur : first, to reconstruct a geometrical model directly from three-dimensional imaging data obtained from a cone beam CT machine ; second, to distinguish the cortical and cancellous bones in the finite element model. Two kinds of the FE model were made, one model into which the trabecular structure was incorporated, and the other model which consisted of only cortical bone shell without any trabecular bone inside. Static analysis was carried out on the assumption of one-legged support standing. The results of our study revealed that the concentration of tensile and compressive stress became remarkably increased in the femoral neck by removing the cancellous bone. That change of the stress distribution between the two models means that the trabecular bone would make a contribution to dispersing the concentration of tensile and compressive stress in the femoral neck. The results of the present study also suggest that the stress concentration increases in the femoral neck even in a static condition such as in one-legged standing as osteoporosis advances. Consequently, that phenomenon would account for the increased risk of a femoral neck fracture in osteoporosis.

Key words : Finite element analysis, Human proximal femur, Trabecular architecture, Cancellous bone, Three-dimensional cone beam CT system.

※1　北海道大学大学院　工学研究科機械科学専攻
〒060-8628　札幌市北区北13条西８丁目

※2　東京都立科学技術大学　航空宇宙システム工学科
〒191-0065　東京都日野市旭が丘6-6
※3　国立病院機構長野病院　整形外科
〒386-8610　上田市緑が丘1-27-21
※4　北見工業大学　機械システム工学科
〒090-8507　北見市公園町165
※5　信州大学　医学部第二解剖学
〒390-8621　松本市旭3-1-1

Corresponding Author : Hiroki NAKATSUCHI
Department of Mechanical Science, Hokkaido University
Kita 13, Nishi 8, Kita-ku, Sapporo, 060-8628, Japan
Tel : 011-706-6406　　Fax : 011-706-6406
E-mail address : nakatuchi@mech-me.eng.hokudai. ac.jp

はじめに

骨粗鬆症に基因する大腿骨頚部骨折（以下頚部骨折）の発生機序を研究する上で有限要素（以下FE）解析は有用な手段である．これまで大腿骨近位のFEモデルには外面形状の皮質骨のみで髄腔内の海綿骨を組み込んだものは少なかった．海綿骨を考慮している場合でも骨梁構造としてではなく領域として定義している報告がほとんどであった[6]．しかし，骨粗鬆症においては，皮質骨のみならず骨髄内の海綿骨骨梁の減少や消失が顕著となる．そのため，骨粗鬆症の進展による頚部骨折発生機序をFEモデル上で解析する場合には，海綿骨を領域としてではなく骨梁そのものをモデル化していく必要がある．

今回我々は高解像度の3次元CTデータの取得とボクセルをベースとしたモデル構築技法を組み合わせることで骨梁を組み込んだFEモデルを作成し，片脚起立を想定した静解析を行った．Sighnの分類にみられるような骨粗鬆症の進行に伴う大腿骨近位部の主要な骨梁走行パターンの減少がどのような応力分布の変化を呈するかを知ることを本研究の最終的な目的にしている．その第一段階として骨梁構造を取り除いた極度の骨粗鬆症モデルを解析し，骨髄内の海綿骨骨梁の機能について考察した．

材料および方法

材料は63歳女性（体重62kg，死因急性呼吸不全）の解剖実習用死体標本より摘出した大腿骨を使用した．骨粗鬆症の程度はレントゲン像上でSighn分類ではGrade Ⅲであった．本大腿骨のCT撮影を行った．CT装置は放射線医学総合研究所に設置されているコーンビーム型3次元装置“Athena”[1]を用いた（撮影条件：X線管電圧120kv，管電流200mA，スキャン時間1秒）．CTデータの解像度を0.35mmに設定し，その場合，1回のスキャンで約90mmの範囲の3次元データが取得できる．このため5回のスキャンで全長41cmを撮影した．得られたスキャンデータは配列サイズが512×512×256で，1辺が0.35mmのボクセルデータで再構成した．

大腿骨近位部のCTデータを3次元骨梁構造解析ソフトTRI/3DBON（ラトックシステムエンジニアリング社製）を用いてワークステーションXW5000（ヒューレット・パッカード社製）で読み込み，3次元形状モデルを構築した．皮質骨と海綿骨骨梁は各CT断面図の画素数と

CT値の正規分布から背景（髄腔）と抽出領域（皮質骨と骨梁）の２つの極大値を算出し，その中間点を分離点と定め抽出した．細かい形状の修正はCT画像をもとに手作業で行った．その後，ボクセルを１要素としてFEモデルを構築した．図１-(a)と(b)はそれぞれCT画像とモデルのAxial断面図を示している．解析には骨髄内の海綿骨骨梁構造を組み込んだモデルと，それを取り除き皮質骨のみにしたモデルの２種類のモデルを用いた．一辺0.35mmの要素サイズでは要素数と節点数が100万を超え，計算機の容量制限を上回るため，一辺0.7mmの８節点正六面体要素を用いた．図２-(a)は骨梁構造を組み込んだFEモデルのcoronal断面図である．白い部分が皮質骨で灰色の部分が海綿骨骨梁を示している．総要素数132,674個，総節点数221,350個となった．一方，図２-(b)は骨梁構造を取り除き，皮質骨のみにしたモデルのcoronal断面図である．総要素数87,191個，総節点数125,763個となった．両モデルの要素数の差が骨梁の要素数に相当し，全体に占める骨梁の割合は約34%であった．

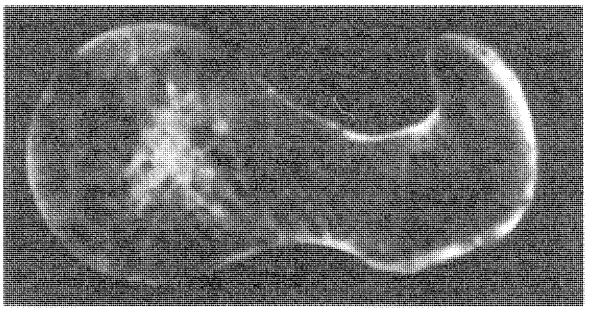

(a)

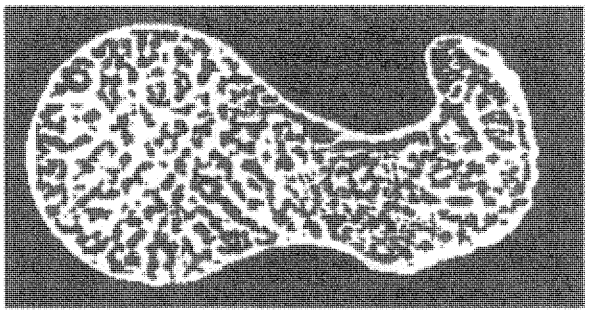

(b)

図１．An axial CT image sectioned at the femoral head and neck acquired by the cone beam 3D-CT system (a) and the FE model reconstructed from the CT data at the same area (b).

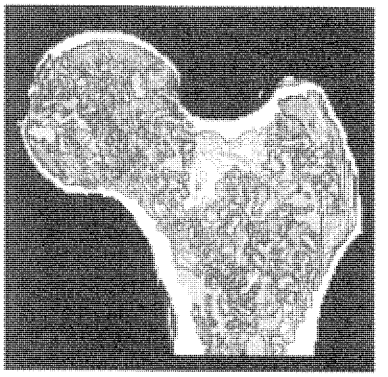

(a)

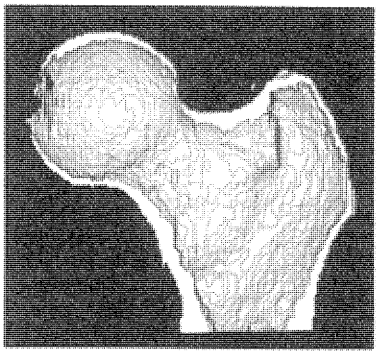

(b)

図２．A FE model of the human proximal femur coronal section image.
a：The model incorporating the trabecular architecture of intramedullary cancellous bone.
b：The model composed only cortical bone after removing the trabecular architecture of cancellous bone.

解析条件は片脚起立を想定した．その際の荷重条件はInmanら[2]の報告による外転筋の筋力および作用方向と，Williams and Lissnerら[4]のX線写真からアーム長を求め，力とモーメントの釣り合いから導出した．この計算結果から大腿骨頭にかかる力は骨幹軸に対し22.4°外側方向に下向きに1379［N］，外転筋による力は大転子上端から骨幹軸に対し27°側方向に上向きに906［N］とそれぞれなった．今回の解析は大腿骨頚部の応力分布に注目しているので，モデル下端は簡単化のため完全拘束とした．皮質骨と海綿骨骨梁の材料特性は中土ら[5]による超音波顕微鏡の計測データを参考にし，皮質骨，

骨梁ともヤング率25［GPa］，ポアソン比0.36とした．解析には有限要素解析ソフトANSYS ver. 7.0（ANSYS，Co. Ltd.）を用いた．

結　　果

図3は前面から見た大腿骨近位部の皮質骨表面の応力分布を示している．表示されている応力分布は頚部軸方向の応力を示している．単位はMPaで，aとbの両図とも同じスケールで表されている．図3-(a)は骨梁構造を組み込んだモデルの応力分布を，図3-(b)は内部の骨梁構造を取り除き外部の皮質骨だけにしたモデルの応力分布をそれぞれ示している．両図の応力分布を比較すると，図3-(a)では大腿骨頚部外側上面に引張応力が，頚部内側下面に圧縮応力が分布していた．図3-(b)ではそれらの応力集中の範囲と程度が増大していた．すなわち，骨梁を組み込んだ場合には頚部外側上面の引張応力が10～34［MPa］，頚部内側下面の圧縮応力が－30～－20［MPa］で分布しているのに対し，骨梁を取り除き皮質骨のみにした場合には頚部外側上面の引張応力が20～57［MPa］，頚部内側下面の圧縮応力が－53～－30［MPa］となった．引張，圧縮とも平均で約40%応力値が増加した．

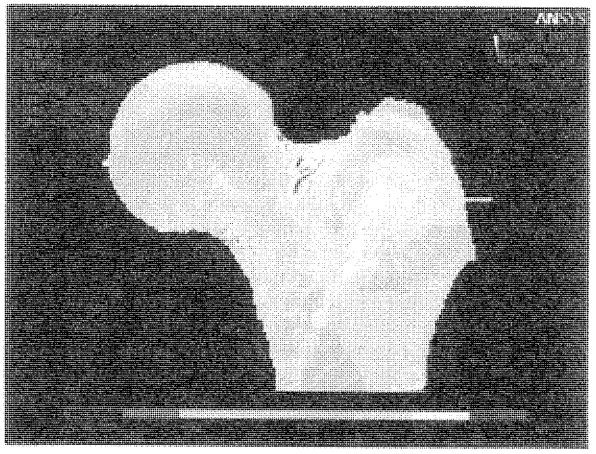

(a)

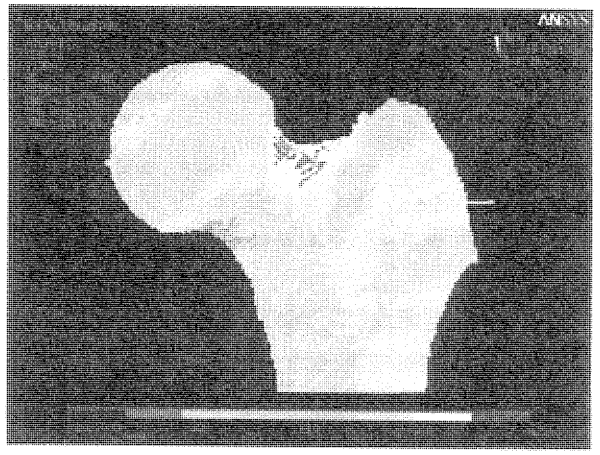

(b)

図3．Stress distributions in the cortical bone on anterior surface of the proximal femur in the model. Stress of tension and compression was illustrated.
a：The stress distribution when the trabecular structure of cancellous bone was incorporated into the model.
b：The stress distribution when the trabecular structure of medullary cancellous bone inside was removed and consequently the model was made up of the outer cortical shell.

考　　察

片脚起立を想定した今回の静解析の結果から，骨梁構造を取り除くと，大腿骨頚部の骨頭に近い部分を中心に引張，圧縮とも平均で約40%の応力集中の増大が見られた．このことから，海綿骨骨梁は静荷重下において大腿骨頚部に集中する引張および圧縮応力を分散させる働きがあると考えられる．吉田ら[7]は大腿骨に衝撃を加えた際に生じる振動特性に注目し，そのうちのねじれ振動モードにおける大腿骨近位での応力分布をFEモデルを用いて調べた．それによると，ねじれ振動モードで最大変形時の頚部軸方向の応力分布は，頚部の前下方には圧縮，後上方には引張の応力集中が見られたとしている．この結果は今回片脚起立を想定した我々の静解析の結果とよく一致した．中土ら[5]は骨粗鬆症の大腿骨近位部の皮質骨を超音波顕微鏡を用いて観察し，マイクロクラックが小転子に比べ大転子に圧倒的に多くみられたとしている．これらのことから衝撃荷重負荷時および静荷重負荷時に大腿骨近位の外側部に引張応力が，内側部には圧縮応力が作用していると考えられる．骨の粗鬆化が大腿骨近位部に及ぶと，

このような応力集中が増大し，同部で骨折を起すものと推定される．すなわち，片脚起立を想定した静解析においても，あるいは衝撃によるねじれ振動の影響を受けた場合でも，大腿骨頚部について注目すると頚部上面に引張，頚部下面に圧縮の応力集中を起す頚部前下方への曲げが頚部骨折を引き起こす要因となっていると推察できる．一方，臨床的には転子部骨折の方が頚部内側骨折よりも骨粗鬆症の影響を受けやすくなるとの報告が多い．今回，大転子部よりは頚部の外側部に引張応力の集中がみられ，臨床的な観察とやや部位的にずれた結果となった．その理由として，今回は解析条件を動的な転倒ではなく，静的な片脚起立を想定したためであると考えられる．今後，骨脆弱性骨折の解析を発展させるには転倒時あるいは転倒直前の防御動作時に生じる衝撃荷重量やその作用方向による大腿骨近位部の動的解析を行っていく必要がある．

Lengsfeldら[3]によるとボクセル要素によるFEモデル構築法はCTデータから直ちにモデル構築を行うことができるため，迅速化および自動化に繋がるとし，FE解析の臨床応用への期待を述べている．一方で，ボクセル要素は同じ大きさの六面体要素の積み重ねで構成されているため，要素間の凹凸が局所的な応力集中を引き起こし解析精度に影響を及ぼすともしている．今回の我々の解析においては厳密な応力値での評価ができなかった．この原因は1要素のサイズが一辺0.7mmの立方体ボクセルであること，すなわち今回のCTの解像度にあると考える．このボクセルサイズでは厚さ1mmにも満たない薄い皮質骨部分やさらに微小な骨梁構造において1要素の有無が形状や解析に与える影響が大きいと言える．また，皮質骨と骨梁の明確な分離抽出にも同様の問題点がある．将来，臨床的に骨粗鬆症による頚部骨折のリスク診断などにFE解析を用いようとする際には，X線被曝と解像度との相反する問題が常に存在する．このため本法の臨床応用を考える際にはCTデータの解像度と被検者の被爆量とを考慮しながら目的に合った最適なモデル構築法について検討する必要がある．

骨粗鬆症の進展により消失していく骨梁の力学的な影響を考慮していくには従来のように海綿骨を領域として定義し均質な材料特性を与えるモデルでは難しく，骨梁そのものをモデル化したFEモデルが必要である．今回の研究によって骨梁構造を組み込んだ大腿骨近位部のモデル構築が可能となった．今後，臨床における骨粗鬆症の診断にFE解析を組み込んだ生体力学的な機能的診断法を導入したいと考えている．

結　　語

コーンビーム型3次元CT装置による高解像度のCTデータからボクセル要素でのモデルを構築し，骨髄内の骨梁構造を組み込んだ大腿骨近位部の有限要素モデルを作成した．構築したモデルで片脚起立を想定した静解析を行ったところ，大腿骨頚部外側に引張，内側に圧縮の応力集中がみられた．さらに，このモデル上で骨梁構造を取り除くことにより，それぞれの応力範囲が拡大し，平均で約40％の応力値の増加が見られた．このことから海綿骨骨梁は静荷重下で大腿骨頚部に集中する引張および圧縮応力を分散する役割をしている可能性が示唆された．

＜謝　　辞＞

本研究の一部は平成13－15年度厚生労働科学研究費補助金（効果的医療技術の確立推進臨床研究事業費）（課題番号：H13－痴呆・骨折－013）によって行われたことを付記し，謝意を表する．有限要素解析ソフトANSYSの使用に際し，ご指導とご協力を頂きました長野県工業試験場工藤誠一氏に感謝いたします．CT撮影に際し，ご協力頂きました放射線医学総合研究所重粒子医科センター医学物理部部長遠藤真広先生および同研究所森慎一郎先生，福井大学工学部知能システム工学科日下部正宏先生に感謝いたします．

文　　献

1）遠藤真広，角尾卓紀 他：四次元CTの開発の現

状. 日獨医報 48：248-255, 2003.
2）Inman VT : Functional aspects of the abductor muscles of the hip. J Bone Joint Surg. 29 : 607-619, 1947.
3）Lengsfeld M, Schmitt J et al. : Comparison of geometry-based and CT voxel-based finite element modeling and experimental validation. Medical Engineering and Physics 20 : 515-522, 1998.
4）LeVeau BF, Williams M et al. : Biomechanics of human motion (2nd/ed.), Saunders, 1977.
5）中土幸男, 立岩裕 他：超音波顕微鏡によるヒト大腿骨頚部におけるマイクロクラックの観察. 日本臨床バイオメカニクス学会誌 22：269-274, 2001.
6）Taylor W. R, Roland E et al. : Determination of orthotropic bone elastic constants using FEA and model analysis. Journal of Biomechanics 35 : 767-773, 2002.
7）吉田郁夫, 中土幸男 他：振動解析用大腿骨有限要素モデルの作成と骨の力学的特性評価への応用. 医用電子と生体工学 37-3：285-292, 1999.

Volumetric Cine Imaging for Cardiovascular Circulation Using Prototype 256–Detector Row Computed Tomography Scanner (4-Dimensional Computed Tomography)

A Preliminary Study With A Porcine Model

Shinichiro Mori, MS, Chisato Kondo, MD,† Naoki Suzuki, PhD,‡ Hiroyo Yamashita, RT,* Asaki Hattori, PhD,‡ Masahiro Kusakabe, PhD,§ and Masahiro Endo, PhD**

Summary: This is a preliminary demonstration of volumetric cine imaging of cardiovascular circulation in domestic pigs using a prototype 256–detector row computed tomography (CT) scanner. The scan range is approximately 120 mm in the craniocaudal direction, with a 0.5-mm slice thickness. The thin sections can be used to create cine loops in multiple planes. Thus, the 256–detector row CT scanner overcomes some of the limitations of present helical CT methods.

Key Words: 4-dimensional, volume data, cone beam, circulation, cine imaging

(*J Comput Assist Tomogr* 2005;29:26–30)

Developments in computed tomography (CT) technology have allowed applications of 3-dimensional (3D) images in clinical fields such as diagnosis, surgical simulation, planning of radiation therapy, and monitoring of interventional therapy. The development of the latest multidetector CT (MDCT) scanner has made dynamic 3D imaging possible. The craniocaudal coverage of the MDCT scanner without gantry movement is typically only 20–40 mm, however, which imposes a limit on cine imaging (the table remains stationary), that is, the capturing of images continuously (approximately 1 or more images per second) during and immediately after completion of the injection of contrast material.

To achieve cine imaging with a wider coverage in the craniocaudal direction (volumetric cine imaging), a prototype 256–detector row CT (4-dimensional [4D] CT) scanner was developed at the National Institute of Radiologic Sciences. The concept is simply called 4DCT, because it takes a 3D image with the additional dimension of time. The craniocaudal coverage of the 4DCT is a length of approximately 100 mm with 1 rotation. Because volume data (3D data) can be acquired by cone-beam CT using a rotation of the cone beam,[1,2] continuous rotation of the cone beam allows dynamic volume data (4D data) to be acquired. Volume data are acquired from many images taken at the same phase of the cardiac motion from 1 slice to another.

This study provides a preliminary demonstration of volumetric cine imaging of cardiovascular circulation using 4 domestic pigs without the aid of an electrocardiographic signal.

MATERIALS AND METHODS

Prototype 256–Detector Row CT Scanner

The prototype 256–detector row CT (4DCT) scanner[3,4] used a wide-area cylindric 2-dimensional detector designed on the basis of present CT technology and mounted on the gantry frame of a 16–detector row CT scanner (Aquilion; Toshiba Medical Systems, Otawara, Japan) (Fig. 1).[5] The number of detectors was 912 (transverse) × 256 (craniocaudal), each with a size of approximately 0.5 mm × 0.5 mm at the center of rotation. The rotation time of the gantry was 1.0 seconds. Several collimation sets (eg, 1–256 × 0.5 mm, 1–128 × 1.0 mm, 1–64 × 2.0 mm) could be set up continuously to the 128-mm total beam width. The craniocaudal coverage of the 4DCT scanner was approximately 100 mm with 1 rotation. The data sampling rate was 900 views per second, and the dynamic range of the A–D converter was 16 bits. The detector element consisted of a scintillator and photodiode. The scintillator was Gd_2O_2S ceramic, and the photodiode was made of single-crystal silicon; these were the same as for an MDCT scanner.

A Feldkamp-Davis-Kress algorithm was used for reconstruction.[6] It took less than 1 second to reconstruct volume data of 512 × 512 × 256 voxels using a high-speed image processor with a field programmable gate array–based architecture. The physical performance of 4DCT had been previously identified as promising.[4]

Received for publication November 1, 2004; accepted November 9, 2004.
From the *Department of Medical Physics, National Institute of Radiological Sciences, Chiba, Japan; †Department of Radiology, Tokyo Women's Medical University, Tokyo, Japan; ‡Institute for High Dimensional Medical Imaging, Jikei University School of Medicine, Tokyo, Japan; and §Fukui University Faculty of Engineering, Fukui, Japan.
Reprints: Shinichiro Mori, Department of Medical Physics, National Institute of Radiological Sciences, Chiba, Japan, 4-9-1 Anagawa, Inage-ku, Chiba City, Chiba 263-8555, Japan (e-mail: shinshin@nirs.go.jp).

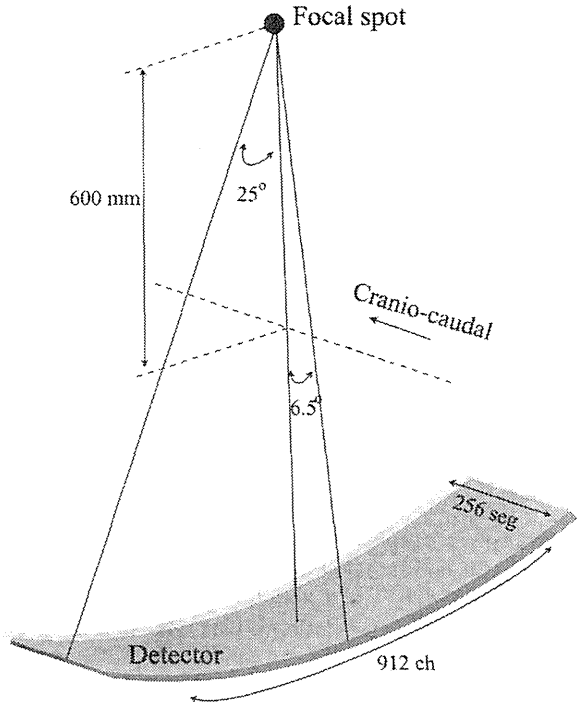

FIGURE 1. Geometry of the 4-dimensional computed tomography scanner.

Animal Experimentation

All animal procedures were approved by the Institutional Review Board. Four domestic pigs (20–25 kg each) were given an intramuscular injection of a mixture of 7 mg/kg ketamine hydrochloride (Sankyo Yell, Tokyo, Japan) and 7 mg/kg 2% xylazine (Bayer, Tokyo, Japan). All pigs were sedated and ventilated with isoflurane (2.0%–2.5%) using a respiratory pump. The heart rate was 103 beats per minute (bpm). A 5-French introducer was positioned in the superior vena cava via the external carotid artery.

Technique for Volumetric Cine Imaging

After undergoing an initial scout topogram of the chest, all pigs were scanned in a cine scan mode (table remains stationary), with the gantry centered over the heart. Scanning was begun after injection of 90 mL nonionic iodinated contrast material (Iopamiron 370; Nihon Schering, Osaka, Japan) using a power injector with a flow rate of 10.0 mL/s. The delay between the start of contrast material administration and CT scanning was 0 seconds. Scan parameters were 120 kV, 150 mA, 1.0-second rotation time, and 256-mm × 0.5-mm beam collimation. The entire scan time was 20 seconds. Effective dose was calculated as 42.0 mSv per 20 seconds. The ventilator was operated so that the breath of the pigs was held at end expiratory during scanning. A half-scan algorithm[7] was

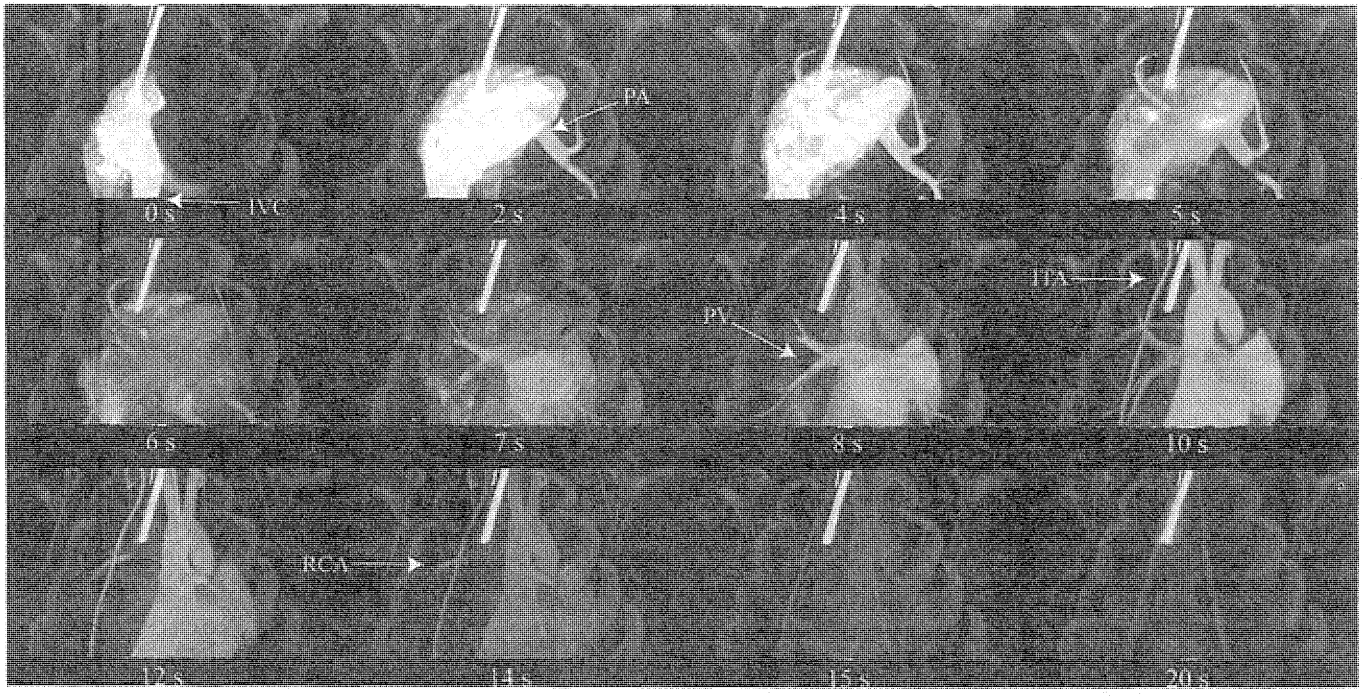

FIGURE 2. Contrast-enhanced volumetric cine images of chest using the 4-dimensional computed tomography scanner in pig 1. The data set, which was acquired within 20 seconds during suspended respiration, was reconstructed by use of the maximum intensity projection technique. At 8 seconds after injection of the contrast material, the right ventricle was weakly enhanced, and at 8–10 seconds, the aortic arch gradually appeared. At 10–15 seconds after injection, the right coronary artery (RCA) could be observed. ITA indicates internal thoracic artery; IVC, inferior vena cava; PA, pulmonary artery; PV, pulmonary vein.

applied, and the effective temporal acquisition window was 500 milliseconds.

The volume elements (voxels) were 0.47 mm × 0.47 mm × 0.47 mm in a 512 × 512 × 216 data matrix covering a 240-mm × 240-mm × 102-mm volume with a 0.1-second time interval. Images were transferred to a dedicated image postprocessing workstation for maximum intensity projection (MIP) (PV-WAVE; Visual Numerics, Alabama, CA) and volume rendering (Virtual Place Office; Azemoto, Tokyo, Japan).

RESULTS

The 4DCT scanning satisfactorily obtained continuous enhancement in the heart. Contrast enhancement could be observed in coronal planes with MIP postprocessing at 0–20 seconds after injection in Figure 2 (pig 1). The pulmonary artery was visualized in contrast enhancement 2 seconds after the start of contrast injection, and the pulmonary vein was visualized from 7 to 10 seconds after the start. The right coronary artery was observed after 10 seconds. Enhancement

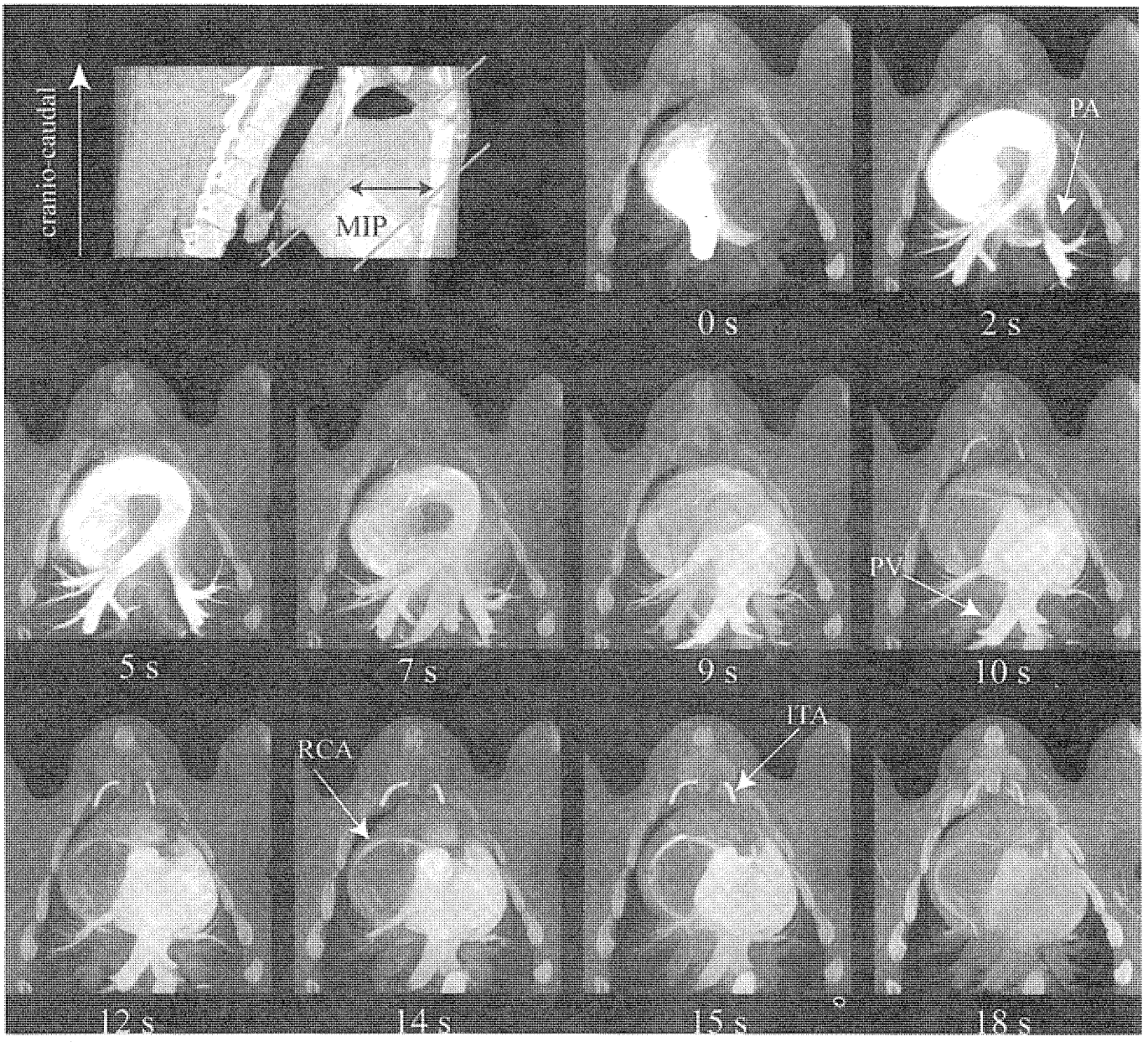

FIGURE 3. Maximum intensity projection (MIP) volumetric images of pig 2 using the 4-dimensional computed tomography scanner in an oblique section. The MIP slab thickness was 43.5 mm. The MIP slab position, oblique angle, and thickness were selected to avoid the thoracic vertebrae, and the introducer was positioned in the superior vena cava. The circulation of the pulmonary artery (PA) and pulmonary vein (PV) could be observed clearly. ITA indicates internal thoracic artery; RCA, right coronary artery.

of the ascending aorta and descending aorta was gradually visualized on the images obtained at 7 to 10 seconds, and they were weakly enhanced after 14 seconds. At 20 seconds, enhancement was completely lost and only internal thoracic arteries could be observed. Dynamic MIP postprocessing was generated in the oblique plane with an MIP slab thickness of 43.5 mm in Figure 3 (pig 2). The MIP slab position, oblique plane angle, and slab thickness were selected to avoid including the thoracic vertebrae and the introducer. The pulmonary artery and pulmonary vein were best visualized in the oblique plane rather than the coronal plane. The ascending aorta and descending aorta were not observed clearly in this plane, however. The well-enhanced right coronary artery was clearly visualized from 12 seconds onward after injection. Contrast enhancement could be observed in a posteroanterior direction with 3D volume rendering at 0–20 seconds after injection in Figure 4 (pig 3). The images of pig 4 were similar to those of pig 1.

DISCUSSION

We demonstrated multiphasic, contrast-enhanced, volumetric cine imaging for circulation in 4 pigs. Conventional MDCT performs cardiac imaging with electrocardiographic gating by the combination of fast gantry rotation, slow table movement, and the helical acquisition mode. The images obtained by MDCT have the same cardiac phase but a different time phase. With regard to the 4DCT, it was designed to allow volumetric cine imaging over a craniocaudal distance of approximately 120 mm in 1 rotation. The images that have been created have slice thickness less than 0.5 mm in the same time phase, resulting in isotropic voxels that can be used to create images and cine loops in multiple planes with any of several postprocessing techniques. This has not been possible previously with conventional MDCT. The prototype 4DCT scanner has the ability to provide useful information when examining 3D structures, as illustrated in this study (Fig. 4).

In this study, compared with a human adult, we examined a smaller sized heart found in pigs weighing 20–25 kg and with a high heart rate (103 bpm). In general, reasonably good image quality with a temporal resolution of 200 milliseconds can only be achieved with low heart rates (40–60 bpm).[8] If a clinical human study were to be conducted under good conditions, the 4DCT scanner could visualize the coronary artery more clearly than that of pigs without electrocardiographic gating.

With regard to the limitations of the 4DCT, the acceptable acquisition time should not be longer. Dose to patients should be of considerable concern, because the maximum nominal beam width is 128 mm, which is more than 3 times larger than the latest MDCT scanner. Additionally, the cine scan mode increases the effective dose in proportion to the scan time. Imaging results may vary considerably depending on differences in the circulation of the patients.[9] When radiologists make an effort to minimize the radiation dose (eg, test bolus), however, the radiation dose is essential to avoid imaging with an excessively high dose with the cine technique.

In conclusion, we have demonstrated the application of 4DCT for cardiac imaging by means of the volumetric cine scan. The coronary artery was more clearly observed with the

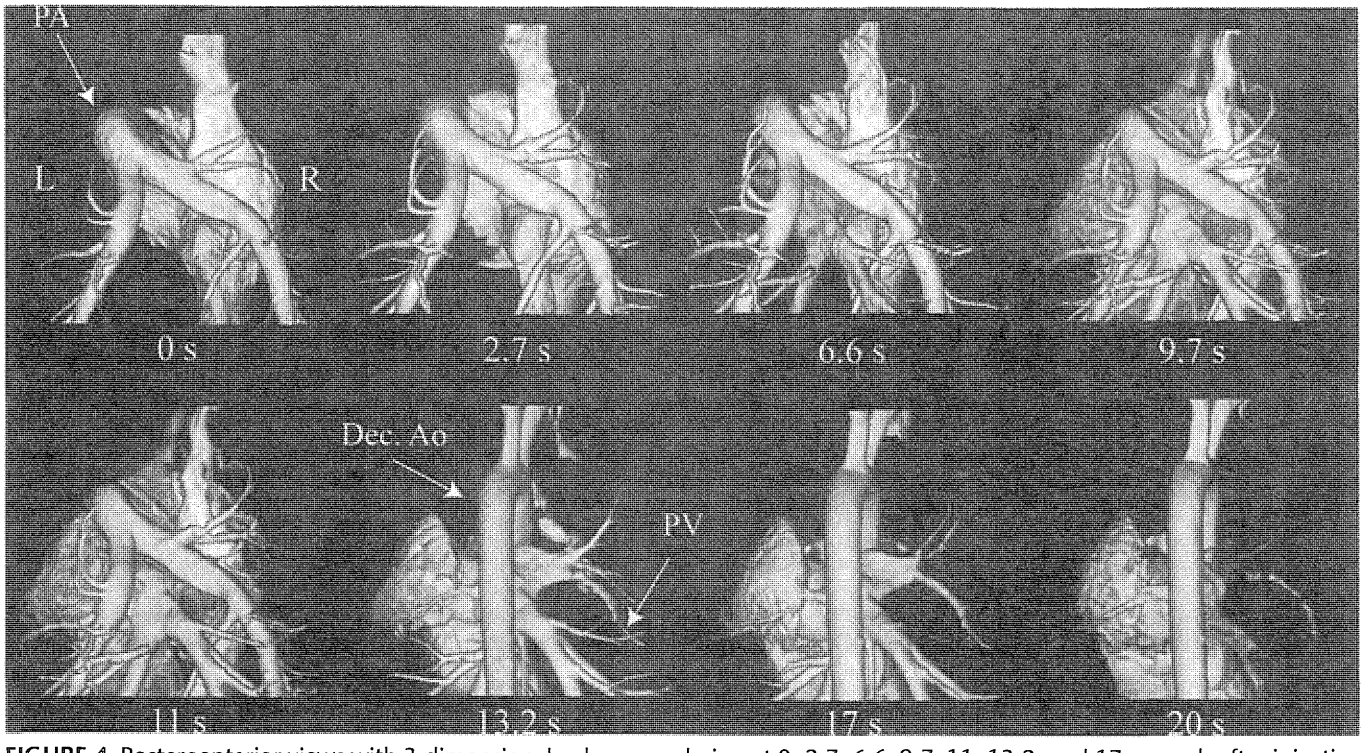

FIGURE 4. Posteroanterior views with 3-dimensional volume rendering at 0, 2.7, 6.6, 9.7, 11, 13.2, and 17 seconds after injection in pig 3. Dec. Ao indicates descending aorta; PA, pulmonary artery.

aid of an electrocardiographic signal. The volumetric cine imaging was useful for dynamic contrast enhancement such as that of the head, renal artery, and liver. It holds promise for the amount of diagnostic information that becomes available, and it overcomes some of the limitations of present helical CT methods. With volumetric cine imaging, physicians could not only carry out new diagnoses but could provide new interventional therapy with real-time observation of the procedure.

REFERENCES

1. Saint-Felix D, Trousset Y, Picard C, et al. In vivo evaluation of a new system for computerized angiography. *Phys Med Biol.* 1994;39:585–595.
2. Endo M, Yoshida K, Kamagata N, et al. Development of a 3D CT-scanner using a cone beam and video-fluoroscopic system. *Radiat Med.* 1998; 16:7–12.
3. Endo M, Mori S, Tsunoo T, et al. Development and performance evaluation of the first model of 4DCT-scanner. *IEEE Trans Nucl Sci.* 2003;50:1667–1671.
4. Mori S, Endo MS, Tsunoo T, et al. Physical performance evaluation of a 256-slice CT-scanner for 4-dimensional imaging. *Med Phys.* 2004; 31:1348–1356.
5. Saito Y, Aradate H, Igarashi K, et al. Large area 2-dimensional detector for real-time 3-dimensional CT (4DCT). *Proc SPIE.* 2001;4320:775–782.
6. Feldkamp LA, Davis LC, Kress JW. Practical cone-beam algorithm. *J Opt Soc Am.* 1984;1:612–661.
7. Parker DL. Optimal short scan convolution reconstruction for fanbeam CT. *Med Phys.* 1982;9:254–257.
8. Hong C, Becker CR, Huber A, et al. ECG-gated reconstructed multi-detector row CT coronary angiography: effect of varying trigger delay on image quality. *Radiology.* 2001;220:712–717.
9. Silverman PM, Roberts SC, Ducic I, et al. Assessment of a technology that permits individualized scan delays on helical hepatic CT: a technique to improve efficiency in use of contrast material. *AJR Am J Roentgenol.* 1996;167:79–84.

Clinical Potentials of the Prototype 256-Detector Row CT-Scanner[1]

Shinichiro Mori, MS, RT, Masahiro Endo, PhD, Takayuki Obata, MD, Kenya Murase, PhD, Hideaki Fujiwara, PhD, Kandatsu Susumu, MD, Shuji Tanada, MD

Rationale and Objectives. To evaluate clinical potentials of the 256-detector row computed tomography (CT) in healthy volunteers.

Materials and Methods. Eight healthy males (22–63 years) participated in the present study. They underwent a non-contrast-enhanced examination with a contiguous axial scan mode either for head, chest, abdomen, or pelvis. Dose was the same as routinely used for multislice CT examinations. Image quality was interpreted by three board-certified radiologists.

Results. With the 256-detector row CT, 0.5–0.8 mm isotropic volumetric data could be acquired in one rotation. Main promising findings are as follows. Three-dimensional structures were visualized clearly in the multiple planes without secondary reconstruction, whereas the axial images had nearly the same image quality as conventional CT. Shading or streak artifacts were observed at the edge of the scan region. The latter are also known as Feldkamp artifacts. Coronal chest images showed a motion artifact from the heart beating.

Conclusion. The 256-detector row CT promises to be useful in clinical applications with its ability to provide three-dimensional visualization of fine structures. The Feldkamp artifacts observed did not generally affect interpretation of images. Investigations are now continuing on image correction along the craniocaudal direction to improve the overall image quality.

Key Words. Computed tomography; cone-beam; image quality; four-dimensional.

Around 1980, it was general radiologic practice to examine one anatomical region only and to acquire no more than about 40 images in several minutes with the computed tomography (CT) scanner. With the advent of multidetector row CT (MDCT), it became common practice to examine two or more anatomical regions in one examination and to acquire more than 150 images within a single breath-hold period. As a result, multiplanar image reconstruction from CT datasets has been markedly improved. These developments of CT technology have provided more comfortable examinations for patients and allowed applications of three-dimensional (3D) images in many clinical fields such as diagnosis, surgical simulation, planning of radiation therapy, and monitoring of interventional therapy. Though the numbers of detectors usually used for MDCT are still in 4 to 16 segments (craniocaudal direction), for the latest MDCT at the selected institute it is 64 segments with a segment size of 0.5–0.625 mm at the center of rotation. The 64-detector row CT shows great improvements over the conventional MDCT, especially in cardiac imaging. The craniocaudal coverage without gantry movement is typically only 32–40 mm, which

Acad Radiol 2005; 12:148–154

[1] From the Department of Medical Physics (S.M., M.E.), Department of Medical Imaging (T.O., S.T.), and Research Center Hospital for Charged Particle Therapy (K.S.), National Institute of Radiological Sciences, Chiba 263-8555, Japan; School of Allied Health Sciences, Faculty of Medicine, Osaka University, Osaka 565-0871, Japan (S.M., K.M., H.F.). Received October 3, 2004; revised November 10, 2004; accepted November 10, 2004. **Address correspondence to** S.T. e-mail: tanada@nirs.go.jp

doi:10.1016/j.acra.2004.11.011

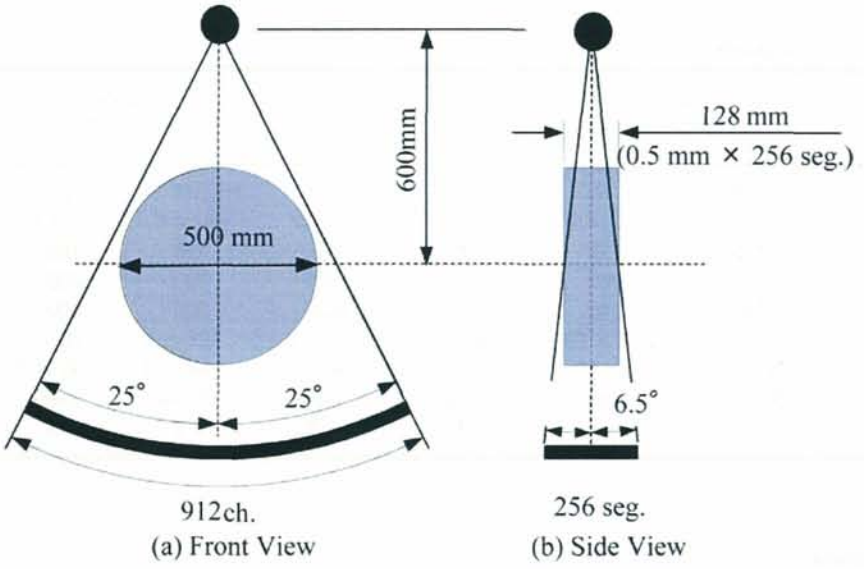

Figure 1. Geometry of the prototype 256-detector row computed tomography scan. (a) Front view and (b) side view. The scanner can scan a field of view approximately 100-mm long in the craniocaudal direction with one rotation.

imposes a limit on cine imaging with a wider coverage in the craniocaudal direction (volumetric cine imaging) (ie, the capturing of images continuously, approximately 1 or more images per second).

To achieve cine imaging with a wider coverage in the craniocaudal direction (volumetric cine imaging), we have developed a prototype 256-detector row CT (1,2). Because of its mechanical simplicity, the prototype uses continuous rotations of a cone beam to take volumetric cine images.

Our purpose in the present work was to obtain clinical images of healthy volunteers by using the 256-detector row CT to look at its clinical advantages.

MATERIALS AND METHODS

Prototype 256-Detector Row CT Scanner

The prototype 256-detector row CT used a wide-area cylindrical two-dimensional (2D) detector designed from present CT technology and mounted on the gantry frame of the 16-detector row CT (Aquilion, Toshiba Medical Systems, Otawara, Japan) (3). The number of detectors was 912 (transverse) × 256 (craniocaudal), each with a size of 0.58 mm × 0.50 mm at the center of rotation (Fig 1). In designing of this prototype, we preferred the wide coverage of x-rays in the craniocaudal direction and tilted x-ray tube at a few degrees. It cost us other tradeoffs, however, such as the heavy forces on the tube's bearing because of angular momentum conservation. The rotation time of the gantry was restricted 1 second to protect tube's bearing. Several collimation sets (eg, 1–256 × 0.5 mm, 1–128 × 1 mm, 1–64 × 2 mm) could be set up continuously to 128 mm total beam width. The craniocaudal coverage of the 256-detector row CT was approximately 100 mm long with one rotation (4,5). Data sampling rate was 900 views/second, and dynamic range of the A-D converter was 16 bits. The detector element consisted of a scintillator and photodiode. The scintillator was Gd_2O_2S ceramic, and the photodiode was made of single-crystal silicon; these were the same as for MDCT.

The 256-detector row CT had three scanning modes. The contiguous axial imaging mode was used to obtain a volume image having a craniocaudal coverage, which is larger than the detector height in a short scan time. The volumetric cine imaging mode was used to obtain dynamic volume data such as for breathing lungs or head CT angiography. The fluoroscopic imaging mode was used in interventional procedures such as needle biopsy, drainage, or ablation with a fixed detector. The helical scan mode was not installed at the time of study.

Image Processing

All data processing and interpretation were done with a high-speed image processor having a field-programmable gate array–based architecture. The Feldkamp-Davis-

Table 1
Subjects and Acquisition Parameters

	Head		Chest		Abdomen		Pelvis	
Examination	1	2	1	2	1	2	1	2
Age (y)	53	61	42	22	53	22	25	23
Total examination time (s)	4.9	4.9	6.7	6.7	4.8	4.8	4.6	4.6
Tube voltage (kV)	135	135	120	120	120	120	120	135
Tube current (mA)	200	200	150	150	300	200	300	200
Field of view (mm)	240	240	320	320	320	400	320	400
Slice collimation (mm)	256 × 0.5	256 × 0.5	256 × 0.5	256 × 0.5	128 × 1	128 × 1	128 × 1	128 × 1
Scan length (mm)	102 × 3	102 × 3	94 × 4	94 × 4	94 × 3	85 × 3	85 × 3	85 × 3
Focus	Small	Large	Large	Large	Small	Large	Large	Large
Overlap region (mm)	5	5	5	5	5	5	5	5

Table 2
Reconstruction Parameters

	Head		Chest		Abdomen		Pelvis	
Examination	1	2	1	2	1	2	1	2
Kernel	FC43	FC43	FC10	FC10	FC10	FC10	FC10	FC10
Matrix AP direction	512	512	512	512	512	512	512	512
LR direction	512	512	512	512	512	512	512	512
CC direction	205	205	145	145	145	111	145	111
Voxel size (mm^3)	0.47	0.47	0.63	0.63	0.63	0.78	0.63	0.78

AP: anteroposterior; LR: left-right; CC: craniocaudal.

Kress algorithm (4) was used for reconstruction, because the 256-slice CT has a wide cone angle and obtained only one rotation data. It took less than 1 second to reconstruct volume data of 512 × 512 × 256 matrix size. The 3D reconstructions were done with a volume-rendering algorithm on the software tool (Intage RV 1.3, Kubota Graphic Technology, Tokyo, Japan).

Subjects

We examined eight healthy male volunteers (mean age 37.6 years ± 8.2 [standard deviation]; age range 21–61 years). All studies were approved by the Institutional Review Board, and written informed consent was obtained from all subjects before beginning the study. An unenhanced examination with a contiguous axial imaging mode with 5 mm overlap region was done as follows: (1) head, (2) chest, (3) abdomen, and (4) pelvis for two subjects in each anatomical site. The subjects held their breath at peak inhalation for chest examination and peak exhalation for abdomen and pelvis examinations during scanning. All subjects underwent scanning in the supine position. No gating for physiologic signals was carried out during scanning.

Scan conditions we routinely used were 120 or 135 kV, 150–200 mA, 1 second exposure per scan, and 1 second rotation time. Slice collimation was 128 × 1 mm for abdomen and pelvis and 256 × 0.5 mm otherwise. The total examination time was approximately 4 seconds for three contiguous scans and 7 seconds for four contiguous scans, which included scan time and table translate time (1 second/100 mm). The examinations were performed according to the acquisition parameters in Table 1. With these protocols, we could acquire 0.5–0.8 mm isotropic volumetric data in one rotation. Therefore, coronal and sagittal images were obtained at sufficient spatial resolution without secondary reconstruction. Matrix size was 512 × 512 × 111 (0.78 × 0.78 × 0.78 mm^3) – 512 × 512 × 205 (0.47 ×0.47 × 0.47 mm^3), and the convolution kernel was the standard head kernel (FC43) for head examination and the standard body kernel (FC10) for the others (Table 2). The dose was the same as routinely used at our institute.

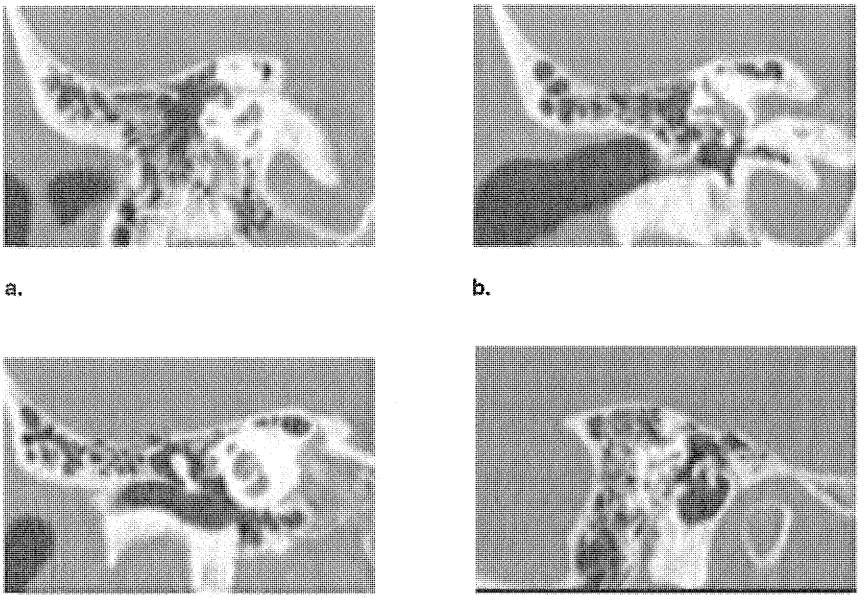

Figure 2. The isotropic normal anatomical images of temporal bone with 0.5-mm voxel size. (a–c) Coronal and (d) sagittal images were obtained without zooming reconstruction.

Image Quality Evaluation

Image quality and artifact were evaluated by three board-certified radiologists (S.T., S.K., and T.O.), who had more than 10 years' clinical experience. They compared quality of the images taken with the prototype scanner to their quality standard formed by experience. It took about 1.5 hours to read the images obtained in all eight cases in multiple planes.

RESULTS

We have shown coronal and sagittal images of the healthy volunteers. Temporal bone and paranasal sinuses are observed clearly with almost the same image quality as for the MDCT. In addition, the 256-detector row CT can cover a relatively wider area and motion artifacts may affect the images less. Fine structure of temporal bones such as the lateral semicircular canal, vestibule, and cochlea are observed without the zooming-reconstruction technique (Fig 2).

For chest examination, 3D visualization of the chest from four contiguous axial scans with 5-mm overlap is shown in Fig 3a. For cardiac examination, conventional MDCT implements continuous data sampling and retrospective volume reconstruction using simultaneous imaging; therefore, it does not have the same time phase in the image, but the 256-detector row CT can do an examination in the same time phase (Fig 3b). Motion artifact of the heart is shown in Fig 3b (marked by the arrow). An aorta, vena cava, and trachea are observed clearly (Fig 3a–d). An artifact that appears around the shoulders because of an inadequate number of x-ray photons affects the thoracic vertebra (third through fifth) area by the generation of large magnitude image noise (Fig 3d). Streak-shaped artifacts (marked by arrows in Fig 3c, d) over the aorta, which are called Feldkamp artifacts, can be seen. The artifacts are discussed later in the article.

For the abdominal examination, a coronal image of the abdomen from three contiguous axial scans with 5-mm overlap is shown in Fig 4a. Horizontal lines of the slightly higher CT number are due to the Feldkamp artifacts on the edges of the scan regions in Fig 4a, b (marked by arrows). Quality of the liver axial images is nearly the same as that of conventional MDCT image in Fig 4c with 2.6-mm slice thickness.

For the pelvic examination, a coronal image combined from three contiguous axial scans with 5-mm overlap shows fewer motion artifacts caused by bowel movement, particularly for the small intestine (Fig 5a). The 256-detector row CT achieves high spatial resolution with 0.78-

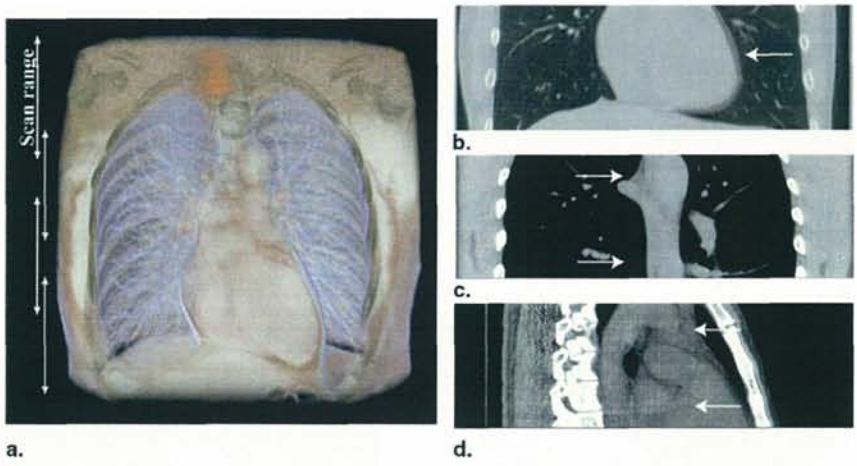

Figure 3. Normal chest images with 0.63-mm reconstruction increment. (a) Three-dimensional display of the chest with four contiguous scans. (b) Coronal image of heart (1-mm slice thickness). The arrow indicates a motion artifact of the heart. (c, d) Coronal and sagittal images (1-mm slice thickness). Arrows indicate Feldkamp artifacts.

mm isotropic volumetric data. Three-dimensional visualization of the pelvic bone (0.78-mm isotropic data) in three contiguous axial scans is shown in Fig 5b.

DISCUSSION

We obtained clinical images of healthy volunteers using the 256-detector row CT. The advantage of the 256-detector row CT is its ability to achieve an isotropic resolution of less than 0.5 mm for a wide craniocaudal coverage (approximately 100-mm long) in one rotation (1). High spatial resolution can help to achieve more accurate diagnosis (7). Additionally, it has the capability to provide useful information when examining 3D structures, as illustrated in this article. This advantage should be emphasized in examinations of the abdomen and chest because the major anatomical structures in these regions run longitudinally. The use of thin sections facilitates the de-

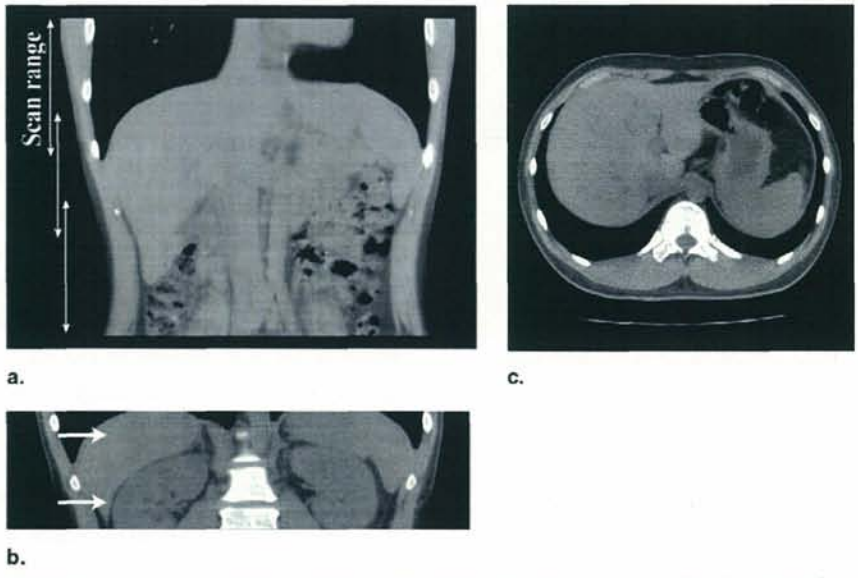

Figure 4. Normal anatomy images of abdomen (0.63-mm reconstruction increment). (a) Coronal and (b) sagittal images of liver (2.6-mm slice thickness). (c) Axial image of liver. Arrows indicate Feldkamp artifacts.

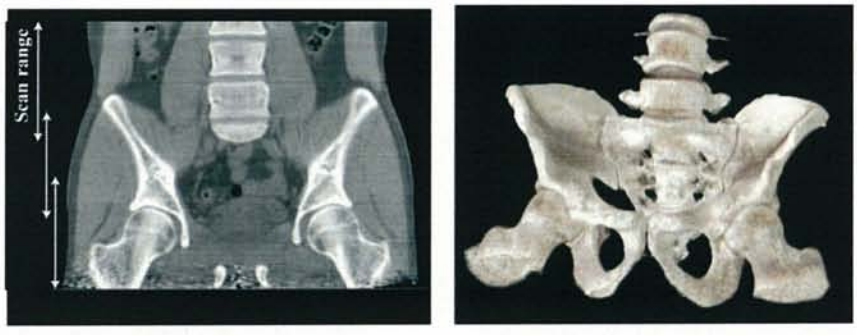

a. b.

Figure 5. Normal images of pelvis with 0.78- mm reconstruction increment. (a) Combination coronal image taken at three contiguous positions with 15-mm overlap (4-mm slice thickness). (b) Three-dimensional visualization of the pelvic bones with three contiguous scans.

tection of small lesions because relatively thick slices result in a partial volume artifact. Radiologists, therefore, may make more effective diagnoses using images in multiple planes from the volumetric data. The observation of the articulation sacroiliac and hip joint may enable us to diagnose disorders of these joints by 3D images.

In previous reports (1,2), we noted that inadequate image processing for the 256-detector row CT led to inferior image quality compared with conventional MDCT in the phantom study. However, in the present study, we applied a new data processing technique before backprojection to correct for ring artifacts and to suppress noise, therefore significantly raising the quality of clinical images, especially regarding low-contrast detectability. The quality of 2D images presented in the results section was evaluated by the three board-certified radiologists; their evaluation was that this new technique achieved at least the conventional level expected for CT, even if it did not achieve one of the highest levels. Effective dose in these studies was almost the same as routinely used. Although the dose in overlapped areas will be higher, overlapped areas are necessary to obtain volume data whose craniocaudal coverage is larger than the detector height.

One limitation for the 256-detector row CT we identified was that the craniocaudal image quality was inferior to that of MDCT. Generally, most reconstruction algorithms for helical interpolation in MDCT are based on estimating the optimum ray sum as a weighted average of measured ray sums (8). The helical scan with a small helical pitch value, therefore, provides satisfactory measurements and good image quality is acquired. On the other hand, we have not done any data processing in the craniocaudal direction for the 256-detector row CT. We are now investigating a technique for image correction along the craniocaudal direction to improve the image quality. Optimization of the image correction may provide radiologists with better images.

Another limitation we noted was the effect of the Feldkamp artifacts; they were specific to cone-beam CT. Because a cone-beam scan along a circular orbit does not collect a complete set of data in the 3D radon space to make an exact reconstruction of a volume, the Feldkamp artifacts will occur more often as the cone angle becomes wider (5). The artifacts occurred when x-ray attenuation was changed rapidly along the craniocaudal direction, and they appeared as shading or streaks in the soft-tissue region near either bony structures or air pockets. The CT number shift in the anatomical sites seems attributable to both the Feldkamp artifacts and a streak artifact caused by a bony structure, in which the latter might be induced by a protuberance at the edge of the vertebra. Because Feldkamp artifacts may lead to misdiagnosis, care must be taken when examining images in which these artifacts may appear.

As mentioned previously, the prototype did not install helical scan mode at the time of study. However, quite recently, we have added capability of helical cone-beam data collection to the prototype. Because the cone angle of the 256-detector row CT is three or four times wider than those of the MDCT, their helical reconstruction algorithm induced artifacts when they were adapted to the 256-detector row CT. Though some investigators (9–12) developed helical scan algorithm for cone-beam CT of wider cone angles, they still had several problems (eg, too complicated and time-consuming for exact algorithms, artifacts for approximate algorithms), and we have not decided which algorithm to adopt for the 256-detector row CT. We

are now comparing helical reconstruction algorithms for the 256-detector row CT; results will be reported later.

In conclusion, we showed advantages of the 256-detector row CT to clinical usage. The evaluation of the axial scan study will be helpful in evaluating the volumetric cine imaging. We are investigating volumetric cine imaging of moving organs, especially in multiphasic contrast examinations and functional studies for the head, liver, renal artery, and coronary artery (13,14). We are now constructing the second type 256-detector row CT, which can scan 0.5 seconds per rotation. Volumetric cine images with high temporal resolution will provide much more diagnostic information to radiologists.

REFERENCES

1. Endo M, Mori S, Tsunoo T, et al. Development and performance evaluation of the first model of 4D CT-scanner. IEEE Trans Nuc Sci 2003; 50:1667–1671.
2. Mori S, Endo M, Tsunoo T, et al. Physical performance evaluation of a 256-detector row CT-scanner for 4-dimensional imaging. Med Phys 2004; 31:1348–1356.
3. Saito Y, Aradate H, Igarashi K, et al. Large area 2-dimensional detector for real-time 3-dimensional CT (4D CT). Proc SPIE 2001; 4320:775–782.
4. Feldkamp LA, Davis LC, Kress JW. Practical cone-beam algorithm. J Opt Soc Am 1984; A1:612–619.
5. Jiang H. IEEE Medical Imaging Conference 2000: a practical cone beam artifact correction algorithm. IEEE Med Imag 2000; 15:71–74.
6. Mochizuki T, Murase K, Hosoi S, et al. The 256-detector-row cone-beam CT for 4D (2D/3D animation) cardiac imaging using CT applicable pulsating cardiac phantom (abstract). Radiology 2003 (suppl): 541.
7. Oliver JH III, Baron RL, Gederle MP, et al. Detecting hepatocellular carcinoma: value of unenhanced or arterial phase CT imaging or both used in conjunction with conventional portal venous phase contrast-enhanced CT imaging. Am J Roentgenol 1996; 167:71–77.
8. Kachelrieβ M, Schaller S, Kalendar WA. Advanced single-slice rebinning in cone-beam spiral CT. Med Phys 2000; 27:754–772.
9. Ye Y, Zhu J, Wang G. Geometric studies on variable radius spiral cone-beam scanning. Med Phys 2004; 31:1473–1480.
10. Katsevich A. Theoretically exact filtered backprojection-type inversion algorithm for spiral CT. J Appl Math 2002; 62:2012–2026.
11. Katsevich A. A general scheme for constructing inversion algorithms for cone beam CT. Int J Math Sci 2003; 21:1305–1321.
12. Kachelrieβ M, Knaup M, Kalender WA. Extended parallel back projection for standard three-dimensional and phase-correlated four-dimensional axial and spiral cone-beam CT with arbitrary pitch, arbitrary cone-angle, and 100% dose usage. Med Phys 2004; 31:1623–1641.
13. Funabashi N, Yoshida K, Nakagawa K, et al. Pulsating three-dimensional cardiac imagings; utility of four and five-dimensional diagnosis of cardiovascular disease using multislice CT and high-speed cone beam CT. J Cardiol. In press.
14. Mori S, Endo M, Tsunoo T, et al. Performance evaluation of the first model 4D CT. Proceedings of the fifth Japan-France Workshop on Radiobiology and Medical Imaging. Chiba, Japan: National Institute of Radiological Sciences. 2004; 153–158.

Enlarged longitudinal dose profiles in cone-beam CT and the need for modified dosimetry

Shinichiro Mori, Masahiro Endo,[a] Kanae Nishizawa, and Takanori Tsunoo
National Institute of Radiological Sciences, Chiba 263-8555, Japan

Takahiko Aoyama
School of Health Sciences, Nagoya University, Nagoya 461-8673, Japan

Hideaki Fujiwara and Kenya Murase
School of Allied Health Sciences, Faculty of Medicine, Osaka University, Osaka 565-0871, Japan

(Received 2 June 2004; revised 2 February 2005; accepted for publication 2 February 2005; published 25 March 2005)

In order to examine phantom length necessary to assess radiation dose delivered to patients in cone-beam CT with an enlarged beamwidth, we measured dose profiles in cylindrical phantoms of sufficient length using a prototype 256-slice CT-scanner developed at our institute. Dose profiles parallel to the rotation axis were measured at the central and peripheral positions in PMMA (polymethylmethacrylate) phantoms of 160 or 320 mm diameter and 900 mm length. For practical application, we joined unit cylinders (150 mm long) together to provide phantoms of 900 mm length. Dose profiles were measured with a pin photodiode sensor having a sensitive region of approximately 2.8×2.8 mm^2 and 2.7 mm thickness. Beamwidths of the scanner were varied from 20 to 138 mm. Dose profile integrals (DPI) were calculated using the measured dose profiles for various beamwidths and integration ranges. For the body phantom (320-mm-diam phantom), 76% of the DPI was represented for a 20 mm beamwidth and 60% was represented for a 138 mm beamwidth if dose profiles were integrated over a 100 mm range, while more than 90% of the DPI was represented for beamwidths between 20 and 138 mm if integration was carried out over a 300 mm range. The phantom length and integration range for dosimetry of cone-beam CT needed to be more than 300 mm to represent more than 90% of the DPI for the body phantom with the beamwidth of more than 20 mm. Although we reached this conclusion using the prototype 256-slice CT-scanner, it may be applied to other multislice CT-scanners as well. © *2005 American Association of Physicists in Medicine.* [DOI: 10.1118/1.1877852]

Key words: dose profile, dose profile integral (DPI), cone-beam CT, scattered radiation

I. INTRODUCTION

A prototype 256-slice CT has been developed at the National Institute of Radiological Sciences (NIRS) which employs continuous rotations of a cone-beam.[1,2] Radiation dose delivered to patients is of considerable concern, because the maximum beamwidth of the 256-slice CT is 138 mm and much larger than that of other CT scanners. Before the advent of multislice (MS) CT, the computed tomography dose index 100 ($CTDI_{100}$)[3] provided a good estimation of dose for narrow total beamwidth and its basic idea was generally accepted, because it expressed a reliable, approximate dose delivered to patients for clinical scan conditions. $CTDI_{100}$ was conveniently quantified by using a pencil ionization chamber with active length of 100 mm. To our knowledge, however, nothing is available in the literature on the reason for setting the integration range as 100 mm ($z = \pm 50$ mm) except for work on the ease of its practical use.[4,5] In cone-beam CT such as 256-slice CT, 100 mm is no longer an adequate integration range for wider irradiation fields, and phantoms should be longer to accurately measure dose including scattered radiation.

Recently Dixon[6] proposed a new method to measure a dose profile integral (DPI) in a cylindrical dosimetry phantom. It involved inserting a small chamber in the center of the phantom, and scanning the phantom with sufficient length to measure accumulated dose in the chamber. This method can be applied to wider beamwidths because it can measure DPI over any arbitrary range if sufficiently long phantoms are used. However Dixon[6] did not mention the necessary phantom length or integration range for individual cases. In the present study, we measured dose profiles in cylindrical phantoms using the 256-slice CT and examined the necessary phantom length and integration range for cone-beam CT with enlarged beamwidths.

II. MATERIALS AND METHODS

A. Prototype 256-slice CT scanner

Figure 1 shows a schematic drawing of the geometry of the prototype 256-slice CT. A wide-area two-dimensional (2D) detector was designed on the basis of the present CT technology[7] and mounted on the gantry frame of the state-of-the-art CT-scanner (Toshiba Aquilion; Toshiba Medical Systems). The number of elements was 912 channels $\times 256$ segments; element size was approximately 1.0 mm $\times 0.9$ mm corresponding to a 0.58 mm (transverse)

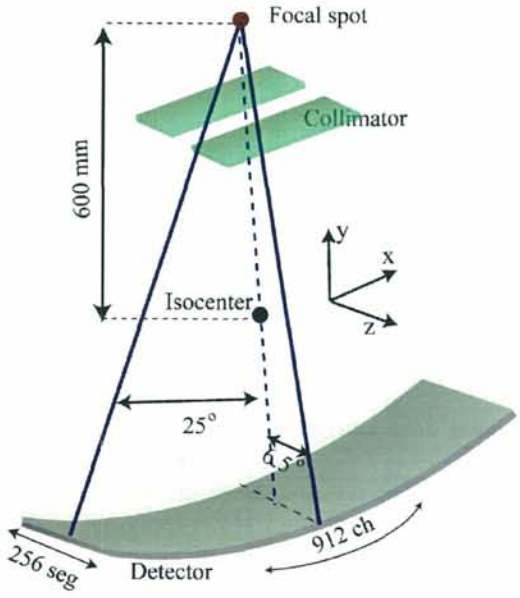

FIG. 1. Illustration of the detector and the geometry used in cone-beam CT-scanner.

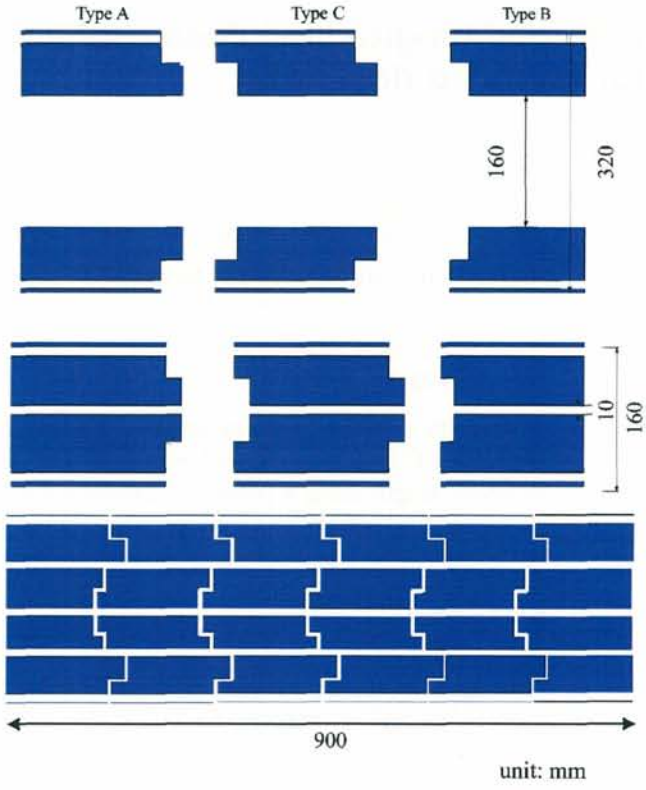

FIG. 2. Illustration of the CTDI body (upper) and head (middle) phantoms. Phantoms are combined together and extended to the necessary length.

$\times 0.50$ mm (longitudnal) beamwidth at the center of rotation. Rotation time was 1.0 s. The scanner could scan a field of view approximately 100 mm long at the maximum in the z direction with one rotation. Each detector element consisted of a scintillator and a photodiode, which was the same as for the MS CT. The beamwidth could be set continuously from 15 to 138 mm at the rotation center by moving the collimator jaws.

B. Phantom

The length of the FDA-recommended dosimetry phantom[8] is at least 140 mm. This conventional phantom contains holes just large enough to accept the pencil-shaped ionization chamber. For cone-beam CT dose measurement, the phantom length should be longer because of the wider beamwidth. In order to make a long, practical phantom, we joined unit cylinders together to provide phantoms of 900 mm length (Fig. 2). The unit cylinders were made of PMMA (polymethylmethacrylate) with diameters of 160 mm

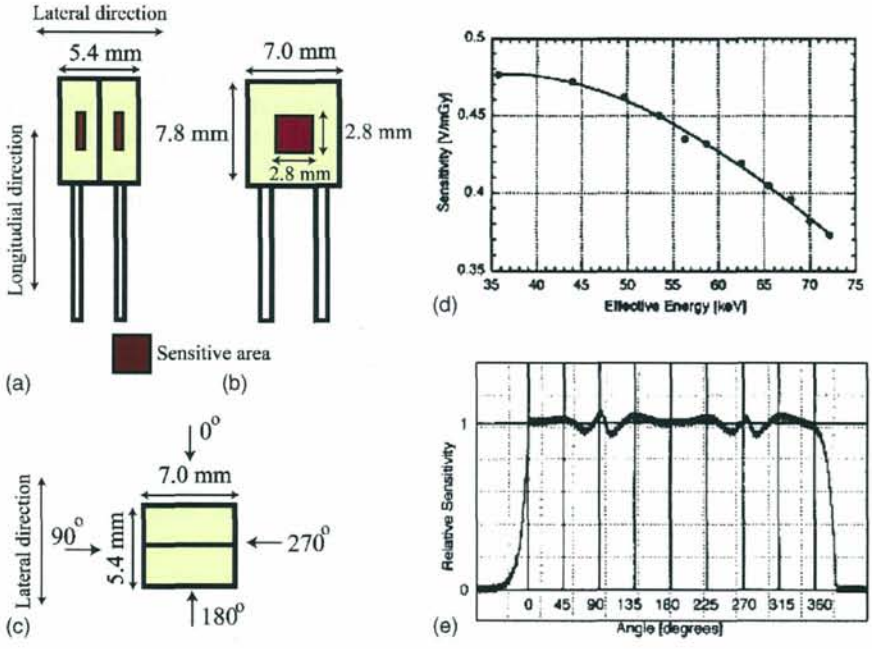

FIG. 3. Schematic drawing of the sensor formed by two *pin* silicon photodiodes (Hamamatsu S2506-04) and their specifications for directional and energy dependence. (a) Side view showing two photodiodes glued together. (b) Front view. (c) Top view. (d) X-ray energy dependence of the photodiode sensor for a higher effective energy region, where the sensitivity was measured with the higher sensitivity range. (Fig. 4(b) in ref. 9.) (e) Directional response of the photodiode sensor for lateral direction measured at a tube voltage of 120 kV, an effective energy of 52.5 keV. Incident angles of x rays for lateral directions are shown. (Fig. 6 in ref. 9.)

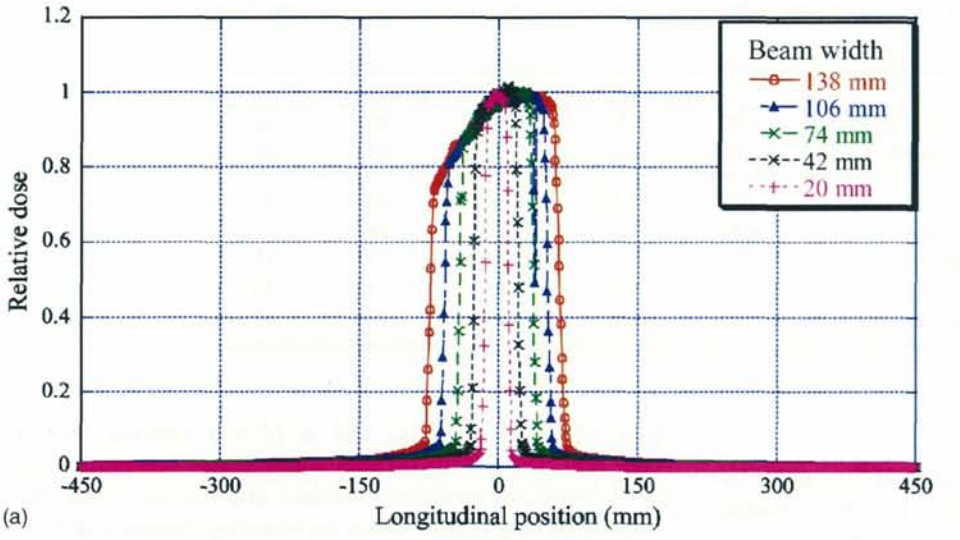

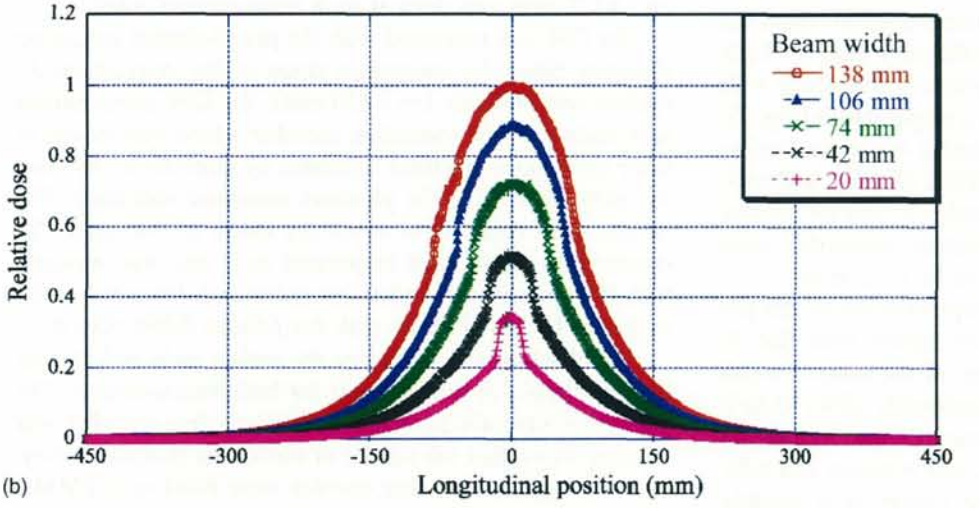

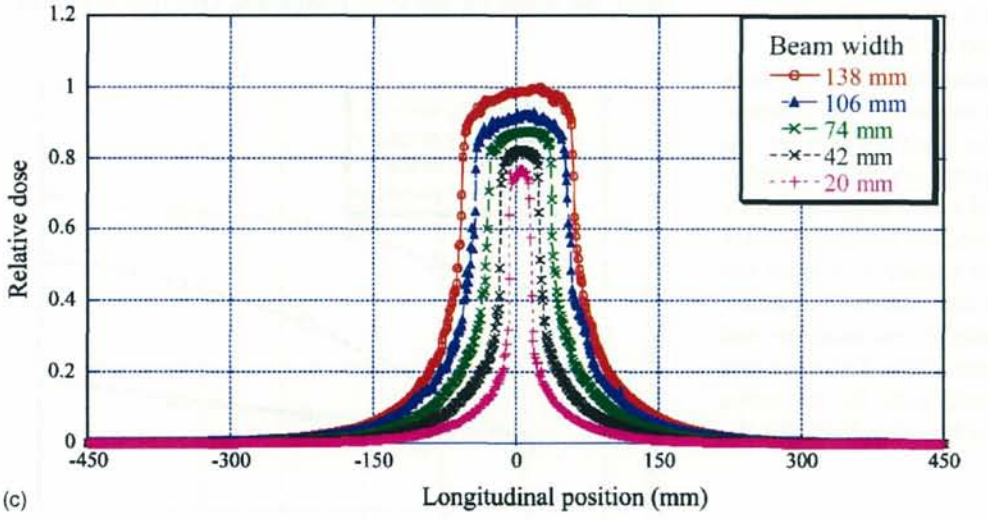

FIG. 4. Longitudinal dose profiles using the *pin* photodiode sensor with 20–138 mm beamwidths. (a) In free air. (b) In the body phantom at the center. (c) In the body phantom at the periphery.

for head examination and 320 mm for body examination. There were three types, type A for one end, type B for the other end, and type C for intermediate connections. Holes of 10 mm diameter were located parallel to the central axis of the cylinders, and the centers of the holes were located at the cylinder center and also 10 mm below the cylinder surface at 90° intervals. By inserting acrylic sticks through these holes, the cylinders were more tightly fixed to each other. Moreover, the connection portion of the phantoms was step-shaped so as not to allow direct passage of x rays through any gaps.

TABLE I. Full width at half maximum (FWHM) of the dose profile showing dependence of the beamwidth (both in mm).

		Width of dose profile (FWHM)				
	Nominal beamwidth	128	96	64	32	10
	Beamwidth	138	106	74	42	20
Air		138	110	76	46	24
Body	Center	159	139	118	94	67
	Periphery	139	110	74	42	23
Head	Center	143	115	85	53	30
	Periphery	138	106	75	43	23

C. Detectors

Two pin silicon photodiodes (S2506-04, Hamamatsu, Japan) were used as the x-ray sensor for dose profile measurements.[9] Each photodiode had a relatively large sensitive area of 2.8×2.8 mm^2 and 2.7 mm thickness. Since the incident side had a larger detection efficiency than the back side, two photodiodes were glued together back-to-back with epoxy cement, and they were used as a single sensor (Fig. 3). The pin photodiode sensor thus fabricated was connected to a dosemeter (Dual Counter 994, ORTEC, Illinois), and calibrated by a calibrated ionization chamber of 0.6 ml volume (C-110, Oyogiken, Japan). The minimum detectable dose with 25% uncertainty was estimated to be 0.02 mGy.

To clarify energy and direction dependencies of the pin photodiode sensor, we reproduced two figures from Ref. 9. Figure 3(d) shows energy dependence of the sensor, which decreased at a maximum rate of approximately 10%/10 keV by the increase of the effective energy. Figure 3(e) shows directional dependence of the sensor, and it shows that relative sensitivity is approximately flat though it is slightly waved around 90° and 270° (9 and 3 o'clock positions, respectively) with a maximum deviation of 8.5%.

A pencil-shaped ionization chamber (CT-30, Oyogiken, Japan) of active length 300 mm was connected to a dosemeter (AE-132, Oyogiken, Japan). This chamber was an extended type of the conventional pencil-shaped ionization chamber (CT-10, Oyogiken, Japan) of active length 100 mm, and used for measuring DPI. The dosemeter was calibrated at AIST (National Institute of Advanced Industrial Science and Technology, Japan) for the appropriate radiation qualities. The partial sensitivity of the long chamber was assessed, and the variations among the center part (100–200 mm) and both sides (0–100 or 200–300 mm), each for an active length of 100 mm, were shown to be less than 0.4% for the effective energy of 40–60 keV.

D. Dose profile and dose profile integral (DPI)

Dose profiles for the 900-mm-long phantoms were measured with the pin silicon photodiode sensor at every 1 mm interval within the full width at half maximum (FWHM) and a 2 mm or larger interval above the FWHM. For example, the dose profile for the 138 mm beamwidth was measured at a 1 mm interval up to $z=74$ mm, a 2 mm interval in the range from $z=74$ to 98 mm, a 4 mm interval in the range from $z=98$ to 189 mm, and a 10 mm interval over $z=189$ mm. The pin silicon photodiode sensor was placed facing anterior and posterior positions, and moved by the mechanical driving system while the phantom remained stationary. A CT scan was done at each measurement point.

The DPI was measured with the pencil-shaped ionization chamber. Since the integration range in the longitudinal direction was 900 mm ($z=\pm 450$ mm), the DPI measurement was made with the ionization chamber which was moved to three contiguous positions separated by intervals of 300 mm for each scan while the phantom remained stationary. The results were summed to cover the range of 900 mm. The exposure length-integral (expressed as R cm) was obtained with the ionization chamber dosemeter and converted to the values of DPI for PMMA with the f-factor 0.898 cGy/R.

The phantom was placed on the patient table and its center was aligned at the isocenter for both measurements. The pin silicon photodiode sensor or the ionization chamber was inserted into either the central or one of the peripheral cavities of the phantom (other cavities were filled with PMMA rods). All scans for the dose profile and DPI measurements

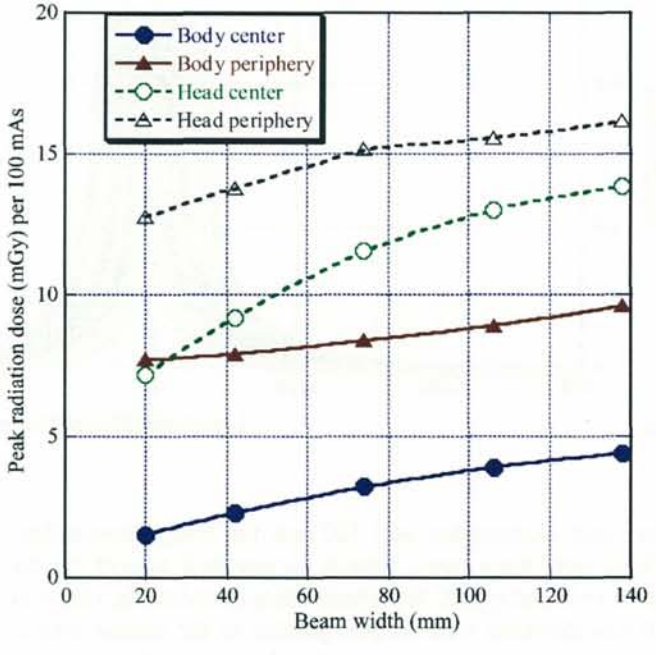

FIG. 5. Peak radiation dose per 100 mA s in the body phantom and head phantom for 20–138 mm beamwidths.

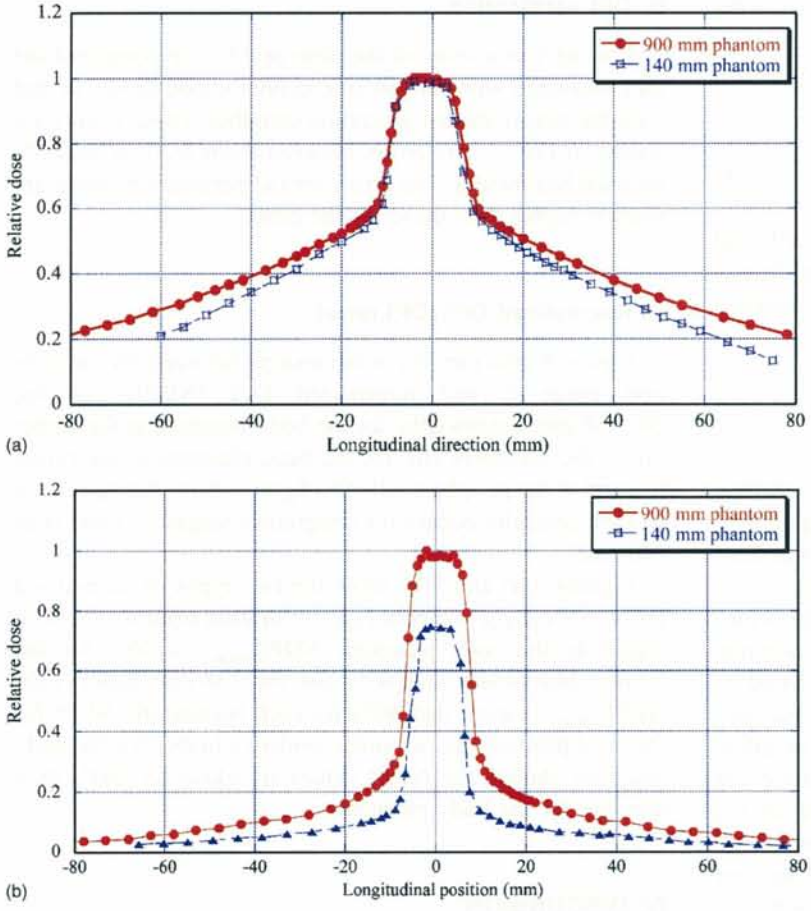

FIG. 6. Longitudinal dose profiles using the *pin* photodiode sensor with 15 mm beamwidths for the standard CTDI and 900-mm-long phantoms. The dose profiles are normalized against the PRD of the 900 mm phantom. (a) In the body phantom at the center. (b) In the body phantom at the periphery.

were made in the axial scan mode. Scan conditions for both measurements were 120 kV, 400 mA, 1.0 s exposure time, and 20, 42, 74, 106, and 138 mm beamwidths. In order to determine the beamwidth, we measured an intensity distribution of x rays with the built-in CT-detector array irradiated without any phantom (i.e., free-in-air). The beamwidth was defined as the FWHM of the longitudinal intensity profile at the rotation center.

To examine phantom dependency of the profile measurement we measured dose profiles with the 15 mm beamwidth (attainable minimum beamwidth) for the 900-mm-long body phantom and the standard CTDI body phantom (140 mm long). The measurement method for dose profiles was that using the pin silicon photodiode sensor with the same way as mentioned before except the measurement range was limited to ±70 mm.

E. DPI verification

The dose profile measurement was verified by comparison between the DPI measured with the pin silicon photodiode sensor and that with the pencil-shaped ionization chamber in both phantoms for a 900 mm range ($z=\pm 450$ mm). The former DPI is given as follows:

$$\mathrm{DPI}_{900}(b)=\sum_{z=-450}^{450} d_m(z,b)\times\Delta(z)\ [\mathrm{mGy\ mm}], \tag{1}$$

where $\mathrm{DPI}_{900}(b)$ is the DPI thus calculated, $d_m(z,b)$ is the dose profile measurement at location, $\Delta(z)$ is the interval of measurement at location, and b is the beamwidth.

F. Normalized DPI (DPI ratio)

To extend Eq. (1) equation, we calculate DPI for the integration range of L as follows:

$$\mathrm{DPI}_L(b)=\sum_{z=-L/2}^{L/2} d_m(z,b)\times\Delta(z)[\mathrm{mGy\ mm}]. \tag{2}$$

The weighted average of DPI for x, y coordinates is given by

$$\mathrm{DPI}_{\mathrm{ave}}=\tfrac{1}{3}\mathrm{DPI}_{\mathrm{center}}+\tfrac{2}{3}\mathrm{DPI}_{\mathrm{periphery}}\ [\mathrm{mGy\ mm}], \tag{3}$$

if we assume a linear decrease (or increase) of DPI in the radial direction,[10] where $\mathrm{DPI}_{\mathrm{center}}$ means DPI at the center and $\mathrm{DPI}_{\mathrm{periphery}}$ means average DPI on the peripheries. Since Eq. (3) is valid independently of L and b, we omit the suffix L and the variable b from the notation of DPI for simplification. We note volume integral dose in the phantom is given

by the product of DPI_{ave} and the phantom cross section in the transverse plane ($x-y$ plane).

Then we calculate the normalized DPI (DPI ratio) as follows:

$$NDPI_{L,ave} = \frac{DPI_{L,ave}}{DPI_{900,ave}}, \quad (4)$$

where $DPI_{L,ave}$ and $DPI_{900,ave}$ mean the averages of DPI_L and DPI_{900}, respectively. We omit variable b again from the notation of DPI. Using the above equations we calculated $NDPI_{100,ave}$ and $NDPI_{300,ave}$ for various beam sizes.

III. RESULTS

A. Dose profile measurement

The dose profiles in free air are plotted in Fig. 4(a), which shows angular distribution of the x-ray beam (heel effect). FWHM values of the dose profiles are listed in Table I. For the dose profile in free air, the difference between the beamwidth and FWHM is 2.8 mm on average. In Table I, nominal beamwidth (number of slice × slice collimation) is listed as well as the (actual) beamwidth determined from intensity profile on the built-in CT detector. The (actual) beamwidth is set to 10 mm larger than the nominal beamwidth to prevent any detector element from entering the penumbra of the x-ray beam and losing signals. However there is some room for reducing their difference, and this will be done in the next models. For the 900-mm-long body phantom, Figs. 4(b) and 4(c) show dose profiles at the center and the periphery, respectively. They are normalized against the peak radiation dose (PRD)[11] of the 138 mm beamwidth. The scattered tail falls off exponentially with distance from the primary beam sections.[12]

The magnitude of the scattered tail was evaluated as the range that gave a dose value of more than 1% of PRD. For the 138 mm beamwidth, we find $z=\pm 313$ mm at the center of the body phantom and $z=\pm 258$ mm at the center of the head phantom. For the 20 mm beamwidth, we find $z=\pm 270$ mm at the center of the body phantom and $z=\pm 186$ mm in the center of the head phantom. The range of the 1% PRD increases with increasing beamwidth. In spite of using irradiation with the same mA s value, the PRD increases with increasing beamwidth (Fig. 5). The results show that the scattered tail is detected in a wide range. The results of the dose profiles for the head phantom are similar to those of the body phantom.

Figure 6 shows the dose profiles with the 15 mm beamwidth at the center or periphery of the standard (140 mm) and 900-mm-long body phantoms, respectively. They are normalized against the PRD of the 900 mm phantom. In Fig. 6(b) the magnitude of the measured dose in the standard phantom is substantially smaller than that of the 900-mm-long phantom. The ratio of the former to the latter becomes smaller as leaving from 75% at $z=0$ mm to 50% at $z=50$ mm. In Fig. 6(a) the ratio is almost 100% at $z=0$ mm, but it again becomes smaller as leaving to 80% at $z=50$ mm.

B. DPI verification

For the verification of the dose profile, we compared the DPI measured with the pin silicon photodiode sensor to that with the pencil shaped ionization chamber. These results are shown in Fig. 7. The errors between them are less than 6% for each beamwidth. The errors for the periphery position are slightly higher than those for the center.

C. Normalized DPI (DPI ratio)

Figure 8 provides the relationships between the integration range L and normalized DPI (NDPI) for the 20–138 mm beamwidths for the body phantom at the center (a), at the periphery (b), for the head phantom at the center (c), and at the periphery (d). The figures show that saturation of DPI generally occurs for integration ranges of more than 300 mm.

Figures 9(a) and 9(b) show the two types of normalized DPI ($NDPI_{100,ave}$, and $NDPI_{300,ave}$) for each beamwidth. With regard to the body phantom, $NDPI_{100,ave}$ is 76% for the 20 mm beamwidth and 60% for the 138 mm beamwidth. $NDPI_{300,ave}$ is more than 90% for each beamwidth. NDPI for the head phantom has a similar tendency to that for the body phantom, though the NDPI values are closer to 100% than they are for the body phantom.

IV. DISCUSSION

In this paper, in order to examine the necessary phantom length and integration range in the dosimetry of cone-beam CT, we measured the dose profiles of the prototype 256-slice

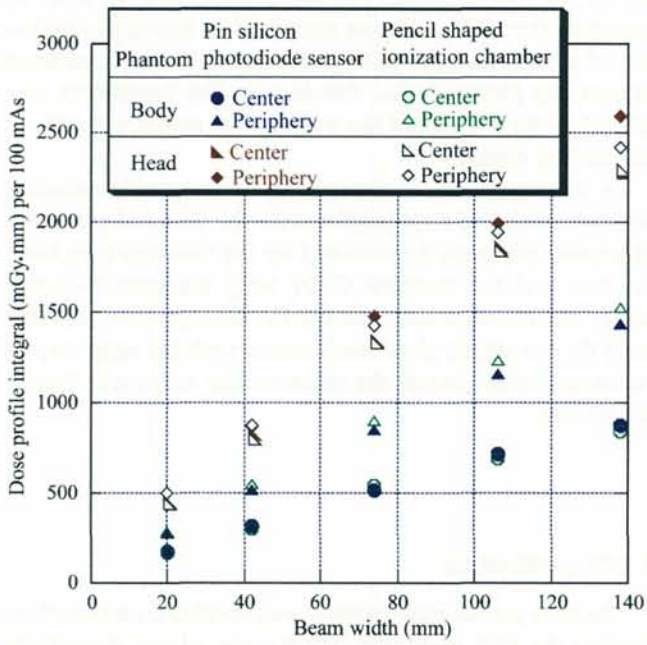

FIG. 7. DPI measured with the *pin* silicon photodiode sensor and DPI measured with the pencil shaped ionization chamber for 20–138 mm beamwidths.

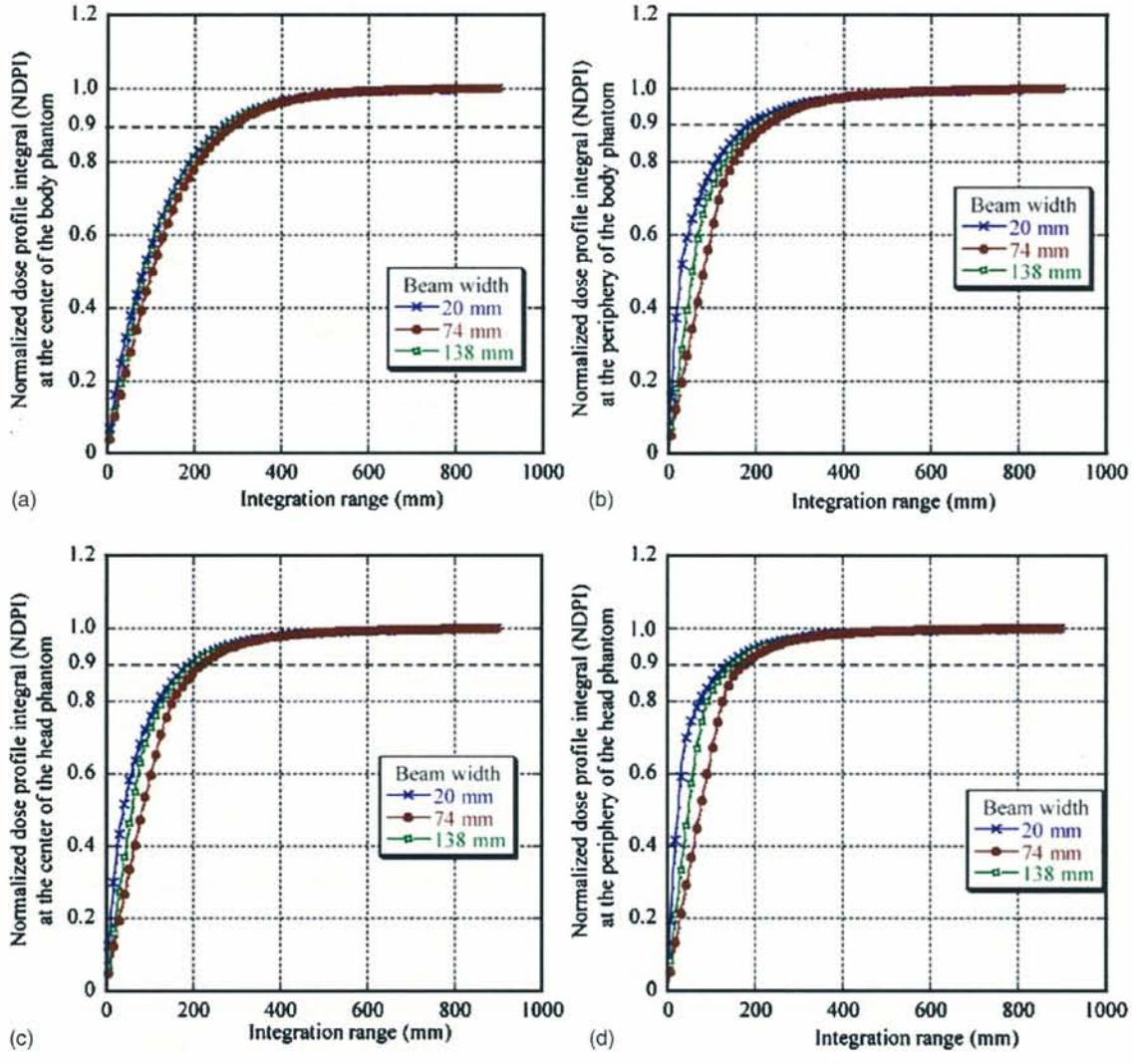

FIG. 8. Relationships between the normalized DPI (NDPI) of each beamwidth and the integration range for the 900-mm-long phantom. (a) Center of the body phantom. (b) Periphery of the body phantom. (c) Center of the head phantom. (d) Periphery of the head phantom.

CT in air and in the two phantoms. We first discuss possible errors of the dose profile measurement and validity of the present results.

The dose profiles measured in air had FWHM values slightly larger than the beamwidth. Though the difference between the beamwidth and the FWHM was 2.8 mm on average, which might be attributed to the size of detector used and experimental errors, it was negligibly small in comparison with the phantom length discussed here.

In the present study the dose profiles were measured with the pin silicon photodiode sensor; its sensitivity had some energy dependence across the diagnostic range of photon energies with a maximum rate of approximately 10%/10 keV [Fig. 3(d)]. In a water phantom of 300 mm diameter the effective energy of x rays in a beam would be varied by several kiloelectron volts mainly due to the selective attenuation of the low energy part of the spectrum. On the contrary, the effective energy of x rays at a distant point from the beam would be decreased by several kiloelectron volts since x rays incident on that point are solely those scattered in the phantom. Therefore, the effective energy variations in the body phantom of 300 mm diameter were thought to be within 10 keV, and the relative errors in dose profile measurements would be within 10%. The relative errors of the DPI could be less than those of profile measurements and we thought they were within several percent. Figure 7 shows that the differences between the measured and calculated DPIs were 6% at the maximum, which supported the above presented discussion. The figure shows that the differences for the periphery position were greater than those for the center, and that might be caused by the energy dependence of the detector sensitivity. Since NDPI is a ratio of two integrals of the same dose profile, its relative error is likely to be not more than that of DPI and within a few percent. To summarize the above presented discussion the energy dependence of the detector sensitivity was unlikely to affect the present result substantially.

The sensitivity of pin silicon photodiode had some angular dependence, and the relative sensitivity was slightly waved for the directions parallel to the glued plane though it was approximately flat for other directions [Fig. 3(e)]. How-

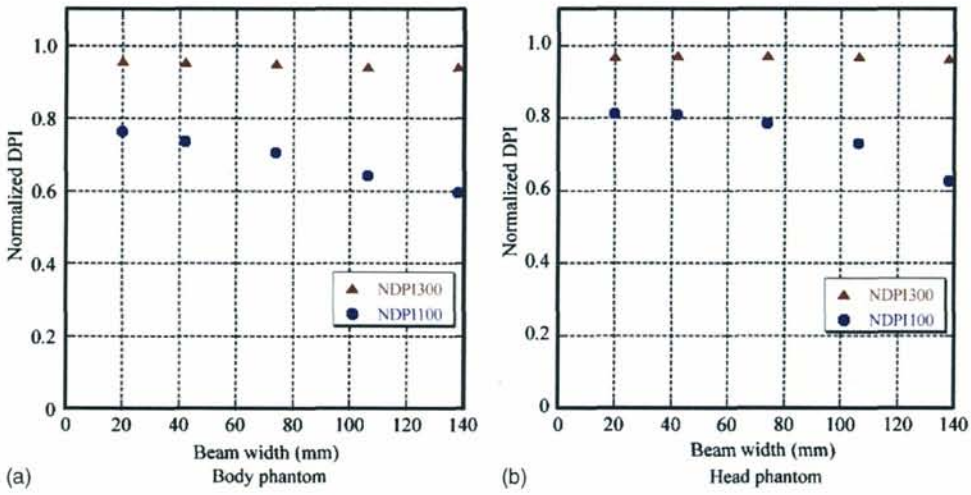

FIG. 9. Three types of normalized DPI ($NDPI_{100,ave}$ and $NDPI_{300,ave}$). (a) In the 900-mm-long body phantom. (b) In the 900-mm-long head phantom.

ever this would induce negligible error because the angular dependence was averaged in the measurement.

In this report so far we have not used CTDI, we used DPI as a dose index. As shown in the Appendix, $CTDI_L$ can be derived from DPI_L according to formula as follows:

$$CTDI_L = \frac{1}{N \cdot T} \cdot DPI_L, \tag{5}$$

where N(=256) is the number of slices and T(=0.5 mm) is the slice collimation.

Figure 10 shows reconstruction geometry of cone-beam CT. In the figure an x-ray source and a 2D detector rotate around the z axis. The volume that can be reconstructed with the Feldkamp algorithm is the region that is passed through during scanning by the tetra-angular pyramid whose apex and base are the x-ray source and the 2D detector, respectively. It is shown by the shaded region in the figure and is a double conical region within a cylinder of radius R_{max} that is determined by the detector size in the x direction and that shows the maximum field of view in the transverse plane.

Reconstruction is not made in the entire shaded region but in an inscribed cylinder of radius R (field of view radius). Since R shows a field of view and it varies with object size (for example R=120 mm for head and 200 mm for body in our 256-slice scanner), the height of the cylinder H is also varied with the object size (H=102 mm for head and 85 mm for body in our case). Other reconstruction algorithms than the full-scan Feldkamp may produce different coverage of the longitudinal direction.[13] The variations of reconstruction height H and its shortness in comparison with the nominal beamwidth $N \times T$ are characteristics of cone-beam CT with enlarged beamwidth, and should be taken into account with respect to radiation exposure of the patient.

Then we discuss necessary phantom length and integration range in the dosimetry of cone-beam CT. From Fig. 9(a) the values of $NDPI_{100,ave}$ were varied from 76% to 60% for the beamwidths between 20 and 138 mm, which suggested that the integration over 100 mm range does not produce the average of dose profile integral adequately. The results in Fig. 6 also suggested that the proper dose profile may not be measured with the standard phantom (140 mm long) for beamwidths of more than 15 mm due to escaped radiation. This results in further underestimation of DPI, for example $NDPI_{100,ave}$ for the 140-mm-long phantom was 84% of that for the 900-mm-long phantom if we calculated these values from the profiles in Fig. 6.

On the other hand, from Fig. 9(a) the values of $NDPI_{300,ave}$ were more than 90% for the beamwidth between 20 and 138 mm, which suggested that integration over the 300 mm range produces the average of DPI properly. Therefore the integration range of 300 mm is necessary to measure proper DPIs for our scanner. Moreover a similar integration range would be required for other MS CT-scanners with beamwidth of more than 20 mm, because scatter tails of their dose profiles are thought to be analogous to those for our prototype if the effective energies are close to each other. This discussion may be supported by a recent report by Nakonency *et al.*[14] They found that DPIs over a 250 mm range were approximately 25%–30% higher than those over a 100 mm range at the center of an ellipsoidal cylinder of 200 mm × 300 mm × 300 mm (length) for a MS CT.

The phantom length should at least cover the integration range. However, adding a certain margin to that length gives more reliable results to prevent deformation of dose profiles due to escaped radiation. Long phantoms can be conveniently obtained by combining unit cylinders as described in this paper. Dose profile integration can be carried out with the method proposed by Dixon,[6] which involved inserting a small chamber in the center of the phantom, and scanning the phantom from edge to edge to measure accumulated dose in the chamber. A long ionization chamber as used in the present study may be used as an alternative tool for any cone-beam CT-scanner that is unable to move its table in synchronization with rotations of an x-ray source and detector (for example, a certain type of C-arm CT).

Dosimetry phantoms of 320 mm diameter and more than 300 mm length are too bulky to use routinely in quality assurance (QA) checks even if they consist of the modular unit described in the present paper. In the QA checks the standard CTDI phantoms (140–200 mm long) and pencil ionization

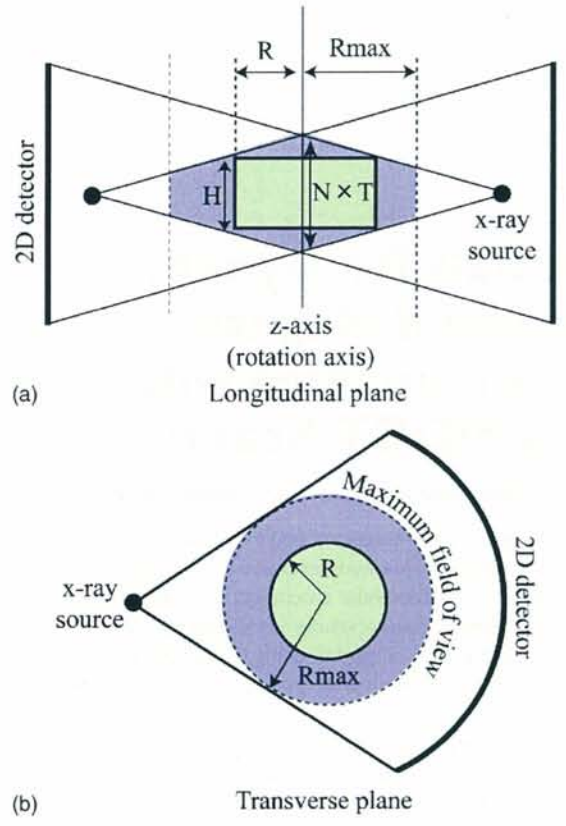

FIG. 10. Reconstruction geometry of cone-beam CT. An x-ray source and a 2D detector rotate around the z axis. The volume that can be reconstructed with the Feldkamp algorithm is shown by the shaded region and is a double conical region within a cylinder of radius R_{max} which is determined by the detector size in the x direction and shows the maximum field of view in the transverse plane. R and H show diameter and height, respectively, of a cylindrical reconstructed volume as it varied with an object. $N \times T$ show the nominal beamwidth where N is the number of slice and T is the slice collimation.

chamber (100 mm long) may be used if a set of correction factors that depend on the beamwidth and x-ray tube voltage is provided. Determination of such factors will be a practically important task to undertake as a next step.

In conclusion we examined the necessary phantom length and integration range in the dosimetry of cone-beam CT, and found that both had to be more than 300 mm to represent more than 90% of the DPI for the body phantom with the beamwidth of more than 20 mm. Although this conclusion was obtained with the prototype 256-slice CT scanner, it may be applied to other MS CT scanners.

APPENDIX

As mentioned in Sec. I CTDI is usually used for CT dosimetry and it is given as follows:[3,15]

$$\mathrm{CTDI}_L = \frac{1}{N \cdot T} \int_{-L/2}^{L/2} d(z)dz \quad [\mathrm{mGy}], \tag{A1}$$

where N is the number of slices, T is the slice collimation, and $d(z)$ is the dose profile for an axial scan. The subscript L indicates the integration range. The International Electrotechnical Commission (IEC) recommended the integration range of 100 mm.

If we redefine DPI in these notations, we obtain

$$\mathrm{DPI}_L = \int_{-L/2}^{L/2} d(z)dz \quad [\mathrm{mGy\ mm}]. \tag{A2}$$

From Eqs. (A1) and (A3),

$$\mathrm{CTDI}_L = \frac{1}{N \cdot T} \cdot \mathrm{DPI}_L. \tag{A3}$$

[a]Author to whom correspondence should be addressed; electronic mail: endo@nirs.go.jp

[1]M. Endo, S. Mori, T. Tsunoo, S. Kandatsu, S. Tanada, H. Aradate, Y. Saito, H. Miyazaki, K. Satoh, S. Matsusita, and M. Kusakabe, "Development and performance evaluation of the first model of cone-beam CT-scanner," IEEE Trans. Nucl. Sci. **50**, 1667–1671 (2003).

[2]S. Mori, M. Endo, T. Tsunoo, S. Kandatsu, S. Tanada, H. Aradate, Y. Saito, H. Miyazaki, K. Satoh, S. Matsusita, and M. Kusakabe, "Physical performance evaluation of a 256-slice CT-scanner for 4-dimensional imaging," Med. Phys. **31**, 1348–1356 (2004).

[3]International Electrotechnical Commission, "Evaluation and routine testing in medical imaging departments constancy tests - x-ray equipment for computed tomography," Publ. IEC, 1223-2-6 (1994).

[4]H. D. Nagel, in *Radiation Exposure in Computed Tomography*, 2nd ed. (Paul Hartung Druck, Hamburg, 2001).

[5]W. A. Kalender, *Computed Tomography* (Publicis MCD, Munich, 2000).

[6]R. L. Dixon, "A new look at CT dose measurement: Beyond CTDI," Med. Phys. **30**, 1272–1280 (2003).

[7]Y. Saito, H. Aradate, K. Igarashi, and H. Ide, "Large area 2-dimensional detector for real-time 3-dimensional CT (cone-beam CT)," Proc. SPIE **4320**, 775–782 (2001).

[8]U.S. FDA Code of Federal Regulations, "Diagnostic x-ray systems and their major components," 21CFR §1020.23, Govt. Printing Office, August 1984.

[9]T. Aoyama, S. Koyama, and C. Kawamura, "An in-phantom dosimetry system using pin silicon photodiode radiation sensors for measuring organ doses in x-ray CT and other diagnostic radiology," Med. Phys. **29**, 1504–1510 (2002).

[10]W. Leitz, B. Axelsson, and G. Szendro, "Computed tomography dose assessment – A practical approach," Radiat. Prot. Dosim. **57**, 377–380 (1995).

[11]R. L. Dixon and K. E. Ekstrand, "A film dosimetry system for use in computed tomography," Radiology **127**, 255–258 (1978).

[12]J. P. Felmlee, J. E. Gray, M. L. Leetzow, and J. C. Price, "Estimated fetal radiation dose from multislice CT studies," Am. J. Roentgenol. **154**, 185–190 (1990).

[13]M. Kachelrieß, M. Knaup, and W. Kalender, "Extended parallel backprojection for standard three-dimensional and phase-correlated four-dimensional axial and spiral cone-beam CT with arbitrary pitch, arbitrary cone-angle, and 100% dose usage," Med. Phys. **31**, 1623–1641 (2004).

[14]K. Nakonechny, G. Fallone, and S. Rathee, "Unreported scatter tails in CTDI and a new CT dose measurement method," Med. Phys. **31**, 1841 (2004).

[15]T. B. Shope, R. M. Gagne, and G. C. Johnson, "A method for describing the doses delivered by transmission x-ray computed tomography," Med. Phys. **8**, 448–495 (1981).

Clinical Potentials for Dynamic Contrast-Enhanced Hepatic Volumetric Cine Imaging with the Prototype 256-MDCT Scanner

Shinichiro Mori[1,2]
Takayuki Obata[3]
Riwa Kishimoto[4]
Hirotoshi Kato[4]
Kenya Murase[2]
Hideaki Fujiwara[2]
Susumu Kandatsu[4]
Shuji Tanada[3]
Hirohiko Tsujii[4]
Masahiro Endo[1]

OBJECTIVE. To achieve dynamic contrast-enhanced hepatic volumetric cine imaging, we developed a prototype 256-MDCT scanner. This study examined the feasibility of the technique for human hepatic imaging in three hepatocellular carcinoma patients.

CONCLUSION. Volumetric cine imaging successfully visualized dynamic contrast enhancement of the hepatocellular carcinoma. It is helpful to evaluate the phase of contrast enhancement or for functional studies of the head, renal artery, coronary artery, and liver.

Developments in CT technology have allowed applications of 3D images in clinical fields such as diagnosis, surgical simulation, planning of radiation therapy, and monitoring of interventional therapy. Multiphasic images provide important information for the diagnosis and characterization of liver neoplasms [1]. Arterial phase imaging is useful for the detection and characterization of hypervascular hepatic lesions. High spatial resolution can be helpful to achieve a more accurate diagnosis [1]. The development of the latest 16-MDCT has made dynamic 3D imaging possible. However, the craniocaudal coverage of the 16-MDCT scanner's detector, without gantry movement, is typically only 20–32 mm, which imposes a limit on cine imaging, that is, the capturing of images continuously (approximately 1 or more images per second) during and immediately after completion of contrast agent injection. To make cine imaging with a wider coverage in the craniocaudal direction (volumetric cine imaging), we developed a prototype 256-MDCT. The purpose of our study is to give a preliminary visualization of volumetric cine imaging during the arterial phase. For this we used the 256-MDCT to evaluate three hepatocellular carcinoma patients.

Subjects and Methods

Subjects

The subjects in this study were three male patients with hepatocellular carcinoma, ages 63, 70, and 74 years, who were selected at random among the hepatocellular carcinoma patients in our hospital. They gave their informed consent to be included in the study, which was conducted in accordance with the principles of the Declaration of Helsinki [2]. All were inpatients of the institute hospital and receiving radiation therapy with a carbon ion beam.

Prototype 256-MDCT

The prototype 256-MDCT used a wide-area cylindric 2D detector, designed on the basis of present CT technology and mounted on the gantry frame of the 16-MDCT (Aquilion, Toshiba Medical Systems) [3]. The number of detectors was 912 (transverse) × 256 (craniocaudal), each approximately 0.58 × 0.50 mm at the center of rotation, resulting in a total of 233,472 elements. The rotation time of the gantry was 1.0 sec. Several collimation sets (e.g., 1–256 × 0.5 mm, 1–128 × 1.0 mm, 1–64 × 2.0 mm) could be set continuously to a 128-mm total beam width. The craniocaudal coverage of the 256-MDCT was approximately 100 mm long with one rotation [4, 5]. The data sampling rate was 900 views/sec, and dynamic range of the analog–digital converter was 16 bits. The detector element consisted of a scintillator and photodiode. The scintillator was Gd_2O_2S ceramic, and the photodiode was made of single-crystal silicon; these were the same as for an MDCT.

Technique for Volumetric Cine Imaging

After we obtained an initial scout topogram of the abdomen, all patients were scanned in a cine fashion with the gantry centered over the upper abdomen after the onset of injection of 90 mL of nonionic iodinated contrast material (Iopamiron 370 [iopamidol], Nihon Schering) using a power injector with a flow rate of 3.5 mL/sec. The delay between the start of

Received July 16, 2004; accepted after revision October 15, 2004.

[1]Department of Medical Physics, National Institute of Radiological Sciences, Chiba, 4-9-1 Anagawa, Inage-ku, Chiba-shi, Chiba, 263-8555, Japan. Address correspondence to S. Mori (shinshin@nirs.go.jp).

[2]School of Allied Health Sciences, Faculty of Medicine, Osaka University, Osaka, Japan.

[3]Department of Medical Imaging, National Institute of Radiological Sciences, Chiba, Japan.

[4]Hospital, National Institute of Radiological Sciences, Chiba, Japan.

AJR 2005;185:253–256

0361–803X/05/1851–253

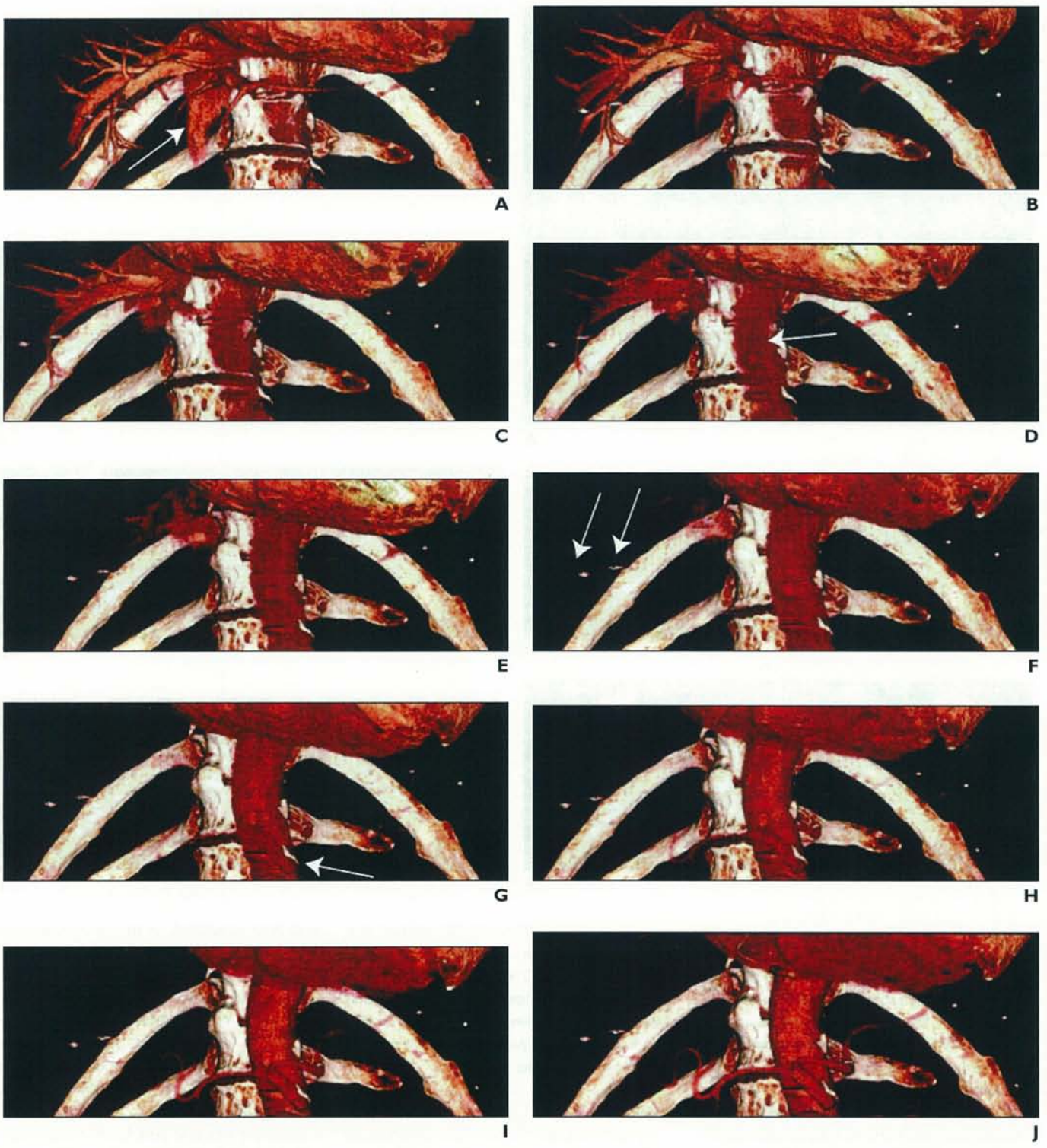

Fig. 1—74-year-old man with hepatocellular carcinoma.
A, Portal venous phase shows wash-out of contrast medium at inferior vena cava (*arrow*) 30 sec after injection.
B–J, Coronal views with 3D volume rendering every 1 sec after **A**. Note slightly enhanced abdominal aorta (*arrow*, **D**) 33 sec after injection. Two iridium beads (< 2 mm diameter) were implanted around hepatocellular carcinoma to verify patient positioning with fluoroscopy before each section of radi ation therapy. Two bright points (*arrows*, **F**) show iridium markers (also seen on other images). Slightly enhanced celiac artery (*arrow*, **G**) 36 sec after injection. Note markedly enhanced arterial systems (**J**) 39 sec after injection.

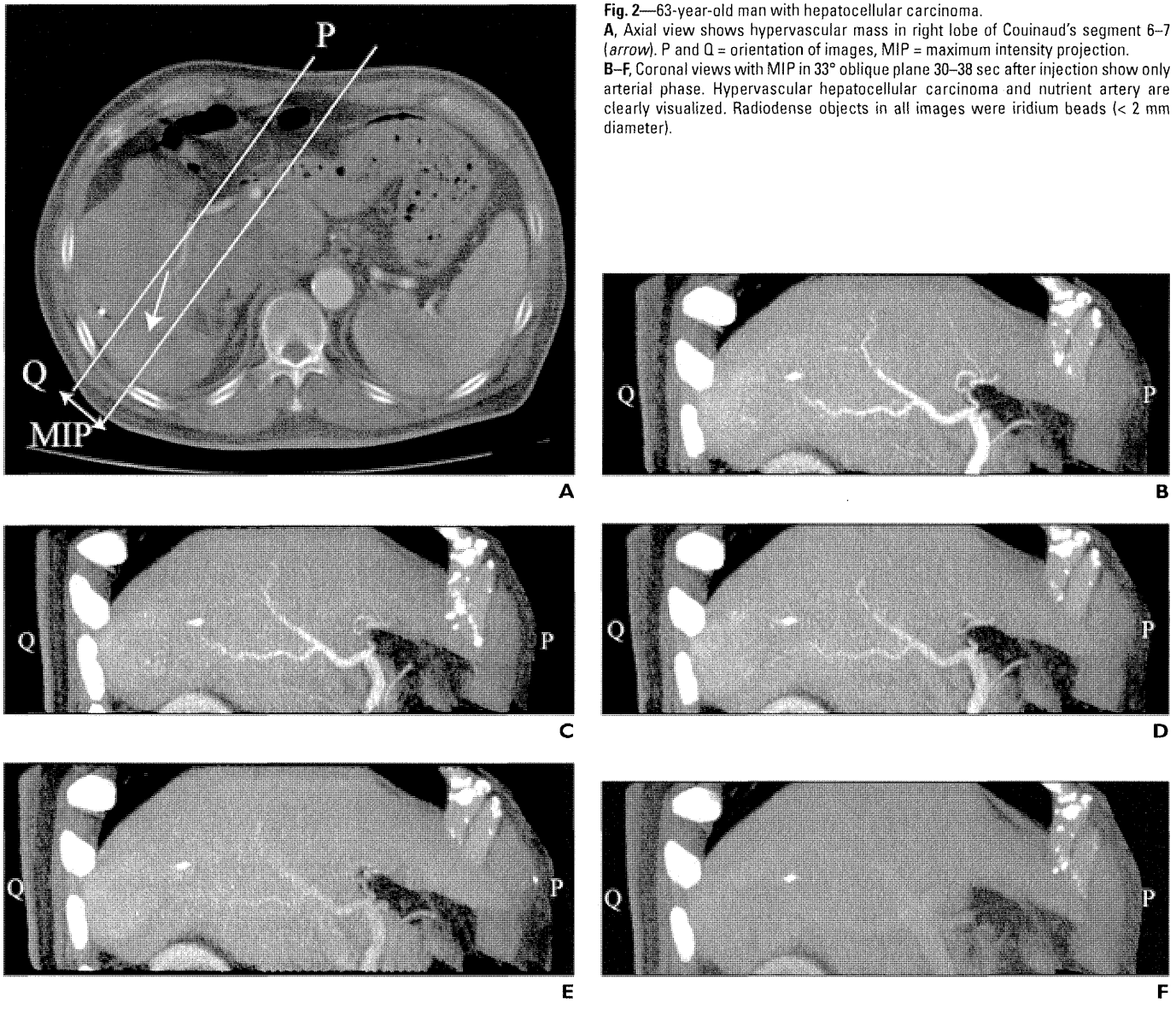

Fig. 2—63-year-old man with hepatocellular carcinoma.
A, Axial view shows hypervascular mass in right lobe of Couinaud's segment 6–7 (*arrow*). P and Q = orientation of images, MIP = maximum intensity projection.
B–F, Coronal views with MIP in 33° oblique plane 30–38 sec after injection show only arterial phase. Hypervascular hepatocellular carcinoma and nutrient artery are clearly visualized. Radiodense objects in all images were iridium beads (< 2 mm diameter).

contrast material administration and scanning was 30 sec. Scan parameters were 120 kV, 200 mA, 1 sec rotation time, 10 sec entire scanning time, and 256 × 0.5 mm beam collimation. Effective dose was 27.7 mSv/10 sec [6]. This dose was almost the same as we routinely used for the liver multiphasic protocol. The scanning time was conservatively limited to 10 sec less than the dose routinely used in the institute [6] because the 256-MDCT scans continuously at the same position and the dose increases in proportion to the scanning time. The patients held their breath at end-expiratory during scanning. A Feldkamp-Davis-Kress algorithm was used for reconstruction [7]. It took less than 1 sec to reconstruct volume data of 512 × 512 × 256 voxels by a high-speed image processor with a field programmable gate-array-based architecture. Its physical performance had been previously identified as promising [5]. The reconstruction increment was 0.62 mm with a 0.1 sec time interval and matrix size of 512 × 512 × 256. The reconstructed images were transferred to a workstation (Dell) and software routines were run within the PV-WAVE programming package (Visual Numerics) for image postprocessing.

Results

Dynamic hepatic CT satisfactorily obtained continuous enhancement in the arterial phase. Contrast enhancement could be observed in coronal views with 3D volume rendering 30 sec after injection (74-year-old man, Fig. 1A). This patient had heart failure, and the backflow of contrast material to the inferior vena cava (IVC) was clearly shown. The hepatic veins were best visualized on the images obtained approximately 30–34 sec after the start of contrast agent injection (Figs. 1A–1E). The IVC was visualized in contrast enhancement (*arrow*, Fig. 1A) and then enhancement was completely lost at 36 sec. After 34 sec, enhancement of the abdominal aorta increased gradually (Figs. 1D–1G). The renal artery enhanced gradually at 36 sec, and finally the arterial phase was best visualized on the images with high contrast in the celiac, splenic, and hepatic arteries (Figs. 1I–1J).

An example of dynamic maximum-intensity-projection-reconstructed contrast-enhanced CT from the arterial phase to the portal vein phase was obtained in the oblique plane (63-year-old man, Fig. 2). Hepatocellu-

lar carcinoma (50 × 40 mm) was observed in the right lobe of Couinaud's segment 6–7 (*arrow*, Fig. 2A). The hepatocellular carcinoma showed a typical early enhancement, and the well-enhanced hepatic artery supplying the hepatocellular carcinoma was clearly visualized at 30 sec after injection. At 31–34 sec, the hepatic arteries had less enhancement. At 38 sec, the hepatic arteries were not visualized at all, and only the hepatic portal veins were revealed (Fig. 2F).

Discussion

This 256-MDCT scanner was designed to allow cine imaging over a craniocaudal distance of approximately 10 cm. The images created had a 0.5 mm thickness, resulting in isotropic voxels that can be used to create images and cine loops, in any plane, with any of several postprocessing techniques. The scanner has the ability to provide useful information when examining 3D structures, as illustrated in this article. A significant advantage appears in examinations of the abdomen and chest since the major anatomic structures in these regions run longitudinally. High spatial resolution improves evaluation of the liver and its vascular system. The use of thin sections facilitates the detection of small lesions since relatively thick slices result in a partial volume artifact.

Cine images provide useful diagnostic information. In this study, the thin-slice cine images can also be used to create cine loops in multiple planes from the volumetric data acquired from a patient with hepatocellular carcinoma (Fig. 2). This was not possible before with conventional MDCT. Since imaging results can vary considerably depending on differences in patient circulation [8], appropriate timing of the scan after the start of contrast material injection is essential to avoid imaging for an excessively long period with the cine technique to reduce an excessively high dose or to eliminate the need for an excessively long breath-hold. Thus, a volumetric cine imaging with a test bolus is more useful for acquisition of the phase of contrast enhancement study.

In conclusion, the craniocaudal coverage of the 256-MDCT is limited for less than one whole organ such as the liver, and the effective dose is increased in proportion to the scanning time. However, cine imaging in the 256-MDCT is helpful to evaluate the phase of contrast enhancement or functional studies for the head, renal artery, coronary artery, and liver.

References

1. Oliver JH III, Baron RL, Gederle MP, Rockette HE Jr. Detecting hepatocellular carcinoma: value of unenhanced or arterial phase CT imaging or both used in conjunction with conventional portal venous phase contrast-enhanced CT imaging. *AJR* 1996; 167:71–77
2. World Medical Association. *Declaration of Helsinki: ethical principles for medical research involving human subjects, revised.* Edinburgh, Scotland: World Medical Association, 2000
3. Saito Y, Aradate H, Igarashi K, Ide H. Large area 2-dimensional detector for real-time 3-dimensional CT (4DCT). *Proc SPIE* 2001; 4320:775–782
4. Endo M, Mori S, Tsunoo T, et al. Development and performance evaluation of the first model of 4DCT-scanner. *IEEE Trans Nucl Sci* 2003; 50:1667–1671
5. Mori S, Endo M, Tsunoo T, et al. Physical performance evaluation of a 256-slice CT-scanner for 4-dimensional imaging. *Med Phys* 2004; 31:1348–1356
6. Mori S, Endo M, Nishizawa K, et al. Dose assessment for clinical approach including scattered radiation: comparison of exposure doses in 4DCT and 16-slice CT-scanners. *Br J Radiol* Manuscript submitted for publication
7. Feldkamp LA, Davis LC, Kress JW. Practical cone-beam algorithm. *J Opt Soc Am* 1984; 1:612–619
8. Silverman PM, Roberts SC, Ducic I, et al. Assessment of a technology that permits individualized scan delays on helical hepatic CT: a technique to improve efficiency in use of contrast material. *AJR* 1996; 167:79–84

Circ J 2005; **69:** 585–589

Cardiovascular Circulation and Hepatic Perfusion of Pigs in 4-Dimensional Films Evaluated by 256-Slice Cone-Beam Computed Tomography

Nobusada Funabashi, MD; Katsuya Yoshida, MD; Hiroyuki Tadokoro, MD*; Keiichi Nakagawa, MD; Nobuyuki Komiyama, MD; Kenichi Odaka, MD*; Takanori Tsunoo, PhD*; Shinichiro Mori, MSc*; Shuji Tanada, MD*; Masahiro Endo, PhD*; Issei Komuro, MD

Background In both cardiac and hepatic disorders it is desirable to accurately visualize the direction and scale of blood flow in the whole organ in pulsating 3-dimensional (D) images, which are known as 4-D images.
Methods and Results The present study used 256-slice cone-beam computed tomography (CT) (Athena, Sony-Toshiba) at one rotation per second and a section thickness of 0.5 mm to show the dynamics of cardiovascular circulation and hepatic perfusion by contrast injection in 4-D films of pigs. Four pigs (20 kg each) were anesthetized with isoflurane. The distal tips of the catheters were positioned in the inferior vena cava (IVC) (pigs 1–3) and in the proper hepatic artery (pig 4). Volumetric scanning and injection of contrast material were started simultaneously and continued for 25 s with image reconstruction at 1-s intervals. In pigs 1–3, 4-D filming revealed the dynamics of cardiovascular circulation, first in the IVC, followed by the right ventricle and pulmonary artery, then the left ventricle, left atrium, pulmonary vein, and finally, the right heart disappeared and only the left heart and aorta remained visible. In pig 4, the hepatic arterial trees, followed by the venous trees, could be easily visualized in turn on the 4-D images.
Conclusions This technology successfully demonstrated cardiovascular circulation and hepatic perfusion in 4-D and will have clinical applicability. (*Circ J* 2005; **69:** 585–589)

Key Words: 4-D perfusion cardiovascular circulation; Hepatic perfusion; 256-slice cone beam computed tomography

In cardiovascular medicine, many subjects present with circulatory disorders, such as shunt flow in subjects with congenital shunt disease[1] or disorders of blood inflow into the left atrial appendage (LAA) in subjects with chronic atrial fibrillation[2,3] or left ventricular (LV) aneurysm seen in those with extensive anterior myocardial infarction[4] which may lead to thrombi in the LAA or LV aneurysm. Therefore, it is desirable to accurately visualize the direction and scale of the shunt flow or disorders of blood flow in the whole heart in pulsating 3-dimensional (D) images, which are known as 4-D images.

Similarly, in hepatic medicine, many subjects present with perfusion disorders such as liver cirrhosis or hepatocellular carcinomas and perfusion studies are performed to characterize the blood flow[5–7] Again, in such cases it is desirable to continuously visualize all the hepatic arterial, capillary and venous trees in 4-D images.

In the studies using a prototype high-speed cone-beam computed tomography (CT) apparatus employing 256-detector rows (Athena, Sony-Toshiba), an entire volume of the thoracic part or liver can be imaged within a single gantry rotation (1 second per rotation) and a section thickness of 0.5 mm[8–10] Furthermore, maximum continuous 25 s scanning enables 4-D analysis. Although this CT technique does not involve electorcardiogram (ECG)-gated acquisition, the combination of its synchrony with volumetric data and reconstruction technique in which 1 scanning period is divided into a maximum of 100 phases, facilitates selection of the most static images and allows entire heart data acquisition without cardiac motion artifacts. In the present study we investigated the ability of this new technology to capture cardiovascular circulation and hepatic perfusion on 4-D dynamic volumetric images of pigs.

Methods

Four domestic pigs, weighing 20 kg each, were mechanically ventilated under isoflurane anesthesia. The distal tips of the catheters were positioned in the inferior vena cava (IVC) for the cardiovascular system (pigs 1–3) and in the proper hepatic artery (pig 4) for obtaining images of the hepatic perfusion. The heart rate of the pigs ranged from 70–80 beats/min. The experiments were approved by the Animal Welfare Committee of the Institute, and were performed in compliance with the guidelines for the care and use of laboratory animals as described by the National Institutes of Health.

Scan conditions for the 256-slice cone-beam CT were: 120 kV, 200 mA, 1.0 s exposure, 1.0 s gantry rotation time,

(Received November 30, 2004; revised manuscript received January 24, 2005; accepted February 7, 2005)
*Department of Cardiovascular Science and Medicine, Chiba University Graduate School of Medicine, *National Institute of Radiological Sciences, Chiba, Japan*
Mailing address: Nobusada Funabashi, MD, Department of Cardiovascular Science and Medicine, Chiba University Graduate School of Medicine, 1-8-1 Inohana, Chuo-ku, Chiba 260-8670, Japan. E-mail: nobusada@ma.kcom.ne.jp

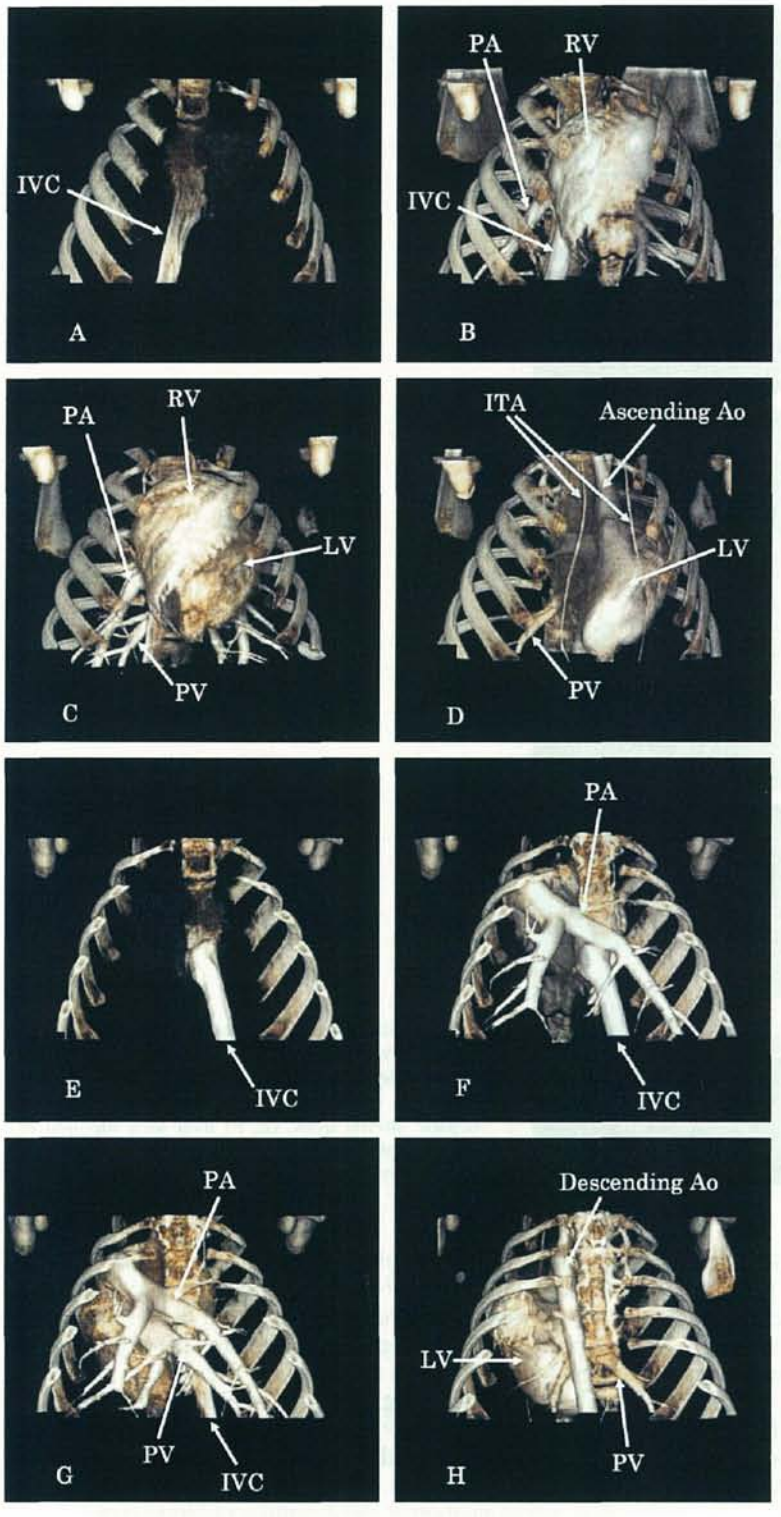

Fig 1. Volume-rendered reconstruction images of a porcine heart using 256-slice cone beam computed tomography represent the vessel lumens and the heart cavity filled with contrast material, with the surrounding ribcage observed from the anterior view (A–D) and posterior view (E–H), acquired after injection of contrast at 2 s (A, E), 5 s (B, F) 12 s (C, G), and 17 s (D, H). At 2 s after injection of the contrast material, only the inferior vena cava (IVC) could be observed (A, E); at 5 s, the right ventricle (RV), pulmonary artery (PA) and IVC could be observed (B, F); at 12 s, in addition to the RV and PA, the left ventricle (LV) and pulmonary vein (PV) could be observed (C, G); but at 17 s, the right heart disappeared and only the LV, PV, ascending aorta (Ao) and the right and the left internal thoracic arteries (ITA) could be observed (D, H).

0.5 mm slice thickness, and 256×0.5 mm slice collimation.

To begin, 10 ml of the iodinated contrast material (300 mgI/ml) was diluted with 40 ml of saline and injected at a rate of 3 ml/s at the same time as scanning of the entire heart was begun. Scanning continued for 25 s and in that time the radiation dose was 100 mSV[11]

The temporal resolution of this new CT is 1 s and the spatial resolution is approximately 1.0 mm (transverse) and 1.3 mm (longitudinal). Image reconstruction was performed at every 0.1-s interval and we selected the most static images around every 1-s interval after injection of contrast resulting in 25-phase volume data which were transferred to a workstation (Virtual Place Advance Plus, AZE, Japan).

Results

In pigs 1–3, at 2 s after injection, the volume-rendered images showed only the IVC (Fig 1A,E); at 5 s, the right

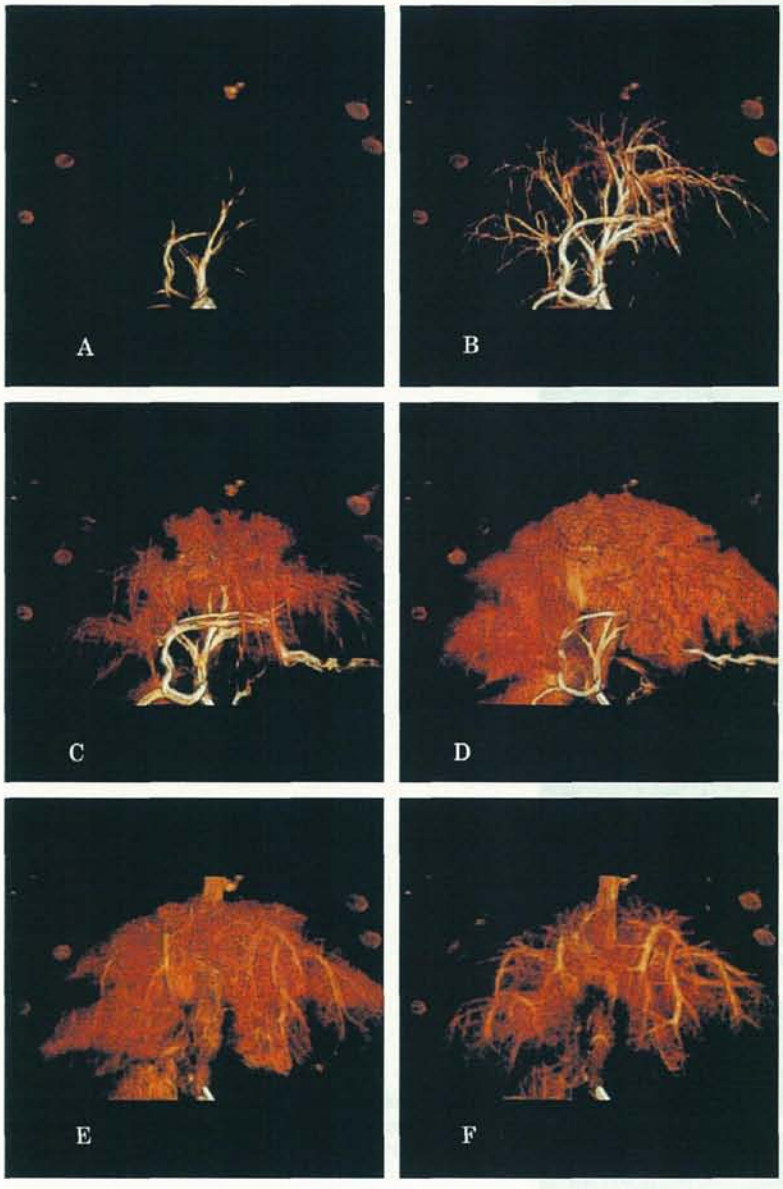

Fig 2. Volume-rendered reconstruction images of a porcine liver using 256-slice cone-beam computed tomography. (A, B) Hepatic arterial trees; (C, D) liver area supplied by blood capillaries within the hepatic arterial trees; (E, F) liver area supplied by blood capillaries beginning to disappear and the hepatic venous trees appearing.

heart, including the right ventricle, the pulmonary artery, and the IVC could be seen (Fig 1B,F); at 12 s, the LV, left atria (LA), including the LAA, and pulmonary vein (PV) could also be observed (Fig 1C,G). At 17 s, the right heart had disappeared and only the LV, LA and PV, ascending and descending aorta, and the right and left internal thoracic arteries were visible (Fig 1D,H). Finally the LAA images disappeared completely, followed by those of the LV and the dynamics of the cardiovascular circulation could be observed in 4-D filming (data not shown).

In pig 4, at 3 s after injection, the volume-rendered images revealed only the hepatic arterial tree (Fig 2B); at 8 s, the area supplied by capillaries could be observed (Fig 2D); at 15 s, the hepatic arterial tree disappeared and the hepatic venous tree appeared (Fig 2F). These sequences could be visualized in 4-D filming, which allowed the hepatic perfusion to be easily observed (data not shown).

Discussion

Echocardiography,[12,13] a flow pattern study of magnetic resonance imaging,[14] electron-beam CT,[15,16] conventional left ventriculography[17,18] and aortography have all been used to evaluate of cardiovascular blood flow, but they all use pulsating 2-D images only, which make it difficult to observe the 3-D spatial relationships circulation.

The 3-D images using ECG-gated multislice CT (MSCT)[19] or electron-beam CT[20–23] are constructed by building up data from the same cardiac phase (R-to-R interval) but with a different cardiac beat. However, these 3-D images do not allow any evaluation of the dynamics of blood flow.

The new 256-slice cone-beam CT with its combination of reconstruction techniques can successfully demonstrate the dynamics of the cardiovascular circulation system on 4-D films in which the configuration of the heart continued to the through plane without any gaps. In other words, this new prototype CT has a unique ability, synchrony, for acquiring images of the pulsating heart. Compared with a conventional 16-slice CT scanner with 0.75 mm slices, with this new 256-slice cone-beam CT, image noise, uniformity, and high contrast detectability are independent of the z-axis.[8] Furthermore, the scanning mechanism can accommo-

date a rotation speed of up to 0.5 s/rotation and ECG-gated acquisition will be possible in the next generation of scanner[8]

In the present MSCT, using retrospective ECG-gating acquisition or respiratory motion-gating acquisition[24,25] which use helical scanning with simultaneous recording of an ECG or respiratory motion signal, following acquisition, it is possible to obtain any volume data of the heart or lung at any cardiac or respiratory phase desired. Furthermore, using this system, it is possible to obtain maximum 100 volumetric data points divided into maximum 100 serial segments of one cardiac or respiratory phase such as 0, 1, 2....97, 98 and 99% of the R-to-R interval of the ECG or respiratory motion. Using serial maximum 100 phase volumetric data, it is also possible to obtain 4-D images on a workstation in which the motion of the heart or thoracic parts can be evaluated. Furthermore, this 256-slice cone-beam CT could represent the dynamics of contrast material in 4-D images; although it is not possible with the present MSCT which so far has been developed as a 64-slice data acquisition system.

This new modality could have applications in the visualization of shunt flow and disorders of blood flow into the LAA and LV aneurysm, which in the latter case may lead to the formation of thrombi. It also may be able to provide visualization of myocardial blood flow when the temporal resolution improves. Gradation of the myocardial blood flow within the myocardium (ie, the difference in the blood flow in the endomyocardium and epicardium) may produce a large amount of information when myocardial ischemia develops.

In the present study, we also demonstrated hepatic perfusion combined with selective hepatic arterial injection and observed clear hepatic enhancement on the 4-D films. Some investigators have reported hepatic perfusion using 3–9 phases of volumetric data of the whole liver, or continuous acquisition for 30 s that covered parts of the liver in 4 slices with the use of time density curves[5–7] However, the former technique does not use a sequential perfusion study, but is an intermittent perfusion study, and the latter technique is not an entirely volumetric only a partial volumetric hepatic perfusion study. To obtain 4-D images using the 256-slice cone-beam CT such as presented in this study, 2 techniques can be envisaged for the future.

One approach is to perform the same procedure as performed in pig 4 in this study using a combination of a selective angiography system with the CT system in which the CT acquisition with selective hepatic artery injection can be achieved without any movement of the patient. In fact, such a system is already in use[26] and it would be possible to obtain 4-D images of the same hepatic enhancement presented in this study. Therefore, if the physician wishes to determine the area of liver supplied by the proper hepatic artery, or needs to obtain quantitative blood flow information in subjects with liver cirrhosis, or intends to evaluate the feeding artery of hepatocellular carcinoma, this technique provides useful information for devising the appropriate treatment strategy. In this study, because we placed the catheter in the proper hepatic artery, we could not evaluate the perfusion of the artery or the portal vein originating from the superior mesenteric artery or the splenic artery.

The other approach is non-invasive image acquisition using the new 256-slice cone-beam CT combined with intravenous injection. Even though with this method segmentation of liver enhancement cannot be performed, we can evaluate the 3-D perfusion of the whole liver non-invasively, which is not possible with 16-slice or even the latest 64-slice MSCT. Using this technique, continuous 25-s acquisitions can be performed, yielding quantitative hepatic perfusion information by using time density curves of the liver on 3-D images.

We describe here a novel prototype CT that has the advantage of whole heart and liver imaging in a single gantry rotation without ECG-gated acquisition. This technique may facilitate cardiovascular and liver diagnosis and may also find application with other organs such as the brain, kidney and peripheral vasculature.

One of the problems encountered with this new 256-slice cone-beam CT scanner is that in order to achieve a detailed 4-D analysis, the number of images that the workstation has to process is very large. For example, 1 volume data set has 256 images, which means that if an image is acquired from 10 phases per s over a total of 25 s, the workstation has to process 64,000 (256×10×25) images at one time in order to achieve a detailed 4-D analysis. At present even the most advanced workstation cannot process such a huge volume of images, but this problem may resolve within a few years as workstations become more sophisticated. Recently, increasing attention has been given to the dose of radiation received during in cardiac CT[7] Specifically, the radiation dose for evaluating blood flow dynamics using the 256-slice cone-beam CT is estimated as 4 mSV/s. Although it is better to keep the radiation dose to a minimum, it may be justifiable to perform such a procedure despite the radiation dose.

There is another type of CT available, a prototype flat-panel CT system (VCT, GE Global Research), with a 200-mm detector panel and a cell pitch factor of 0.2 mm, which also allows an entire organ to be imaged within a single gantry rotation[28] Thus, in the near future, these new imaging modalities will likely become new diagnostic tools.

Conclusion

We successfully demonstrated the cardiovascular circulation and hepatic perfusion in 4-D using 256-slice cone-beam CT. This imaging modality has clinical potential for the visualization and analysis of cardiovascular circulatory problems and hepatic perfusion disorders.

Acknowledgment

This work was supported in part by the 4D-CT research group at the National Institute of Radiological Sciences, Japan.

References

1. Funabashi N, Rubin GD. Qualitative blood flow differentiation: Depiction of a left to right cardiac shunt across a ventricular septal defect using electron-beam computed tomography. *Jpn Circ J* 2000; **64:** 901–903.
2. Nakanishi T, Hamada S, Takayama M, Naito H, Imakita S, Yamada N, et al. A pitfall in ultrafast CT scanning for the detection of left atrial thrombi. *J Comput Assist Tomogr* 1993; **17:** 42–45.
3. Kamiyama N, Koyama Y, Suetsuna R, Saito Y, Kaji S, Akasaka T, et al. Decreased left atrial appendage flow velocity with atrial fibrillation caused by negative inotropic agents. *Circ J* 2003; **67:** 277–278.
4. Beppu S, Izumi S, Miyatake K, Nagata S, Park YD, Sakakibara H, et al. Abnormal blood pathways in left ventricular cavity in acute myocardial infarction: Experimental observations with special reference to regional wall motion abnormality and hemostasis. *Circulation* 1988; **78:** 157–164.

5. Fuentes MA, Keith CJ, Griffiths M, Durbridge G, Miles KA. Hepatic haemodynamics: Interrelationships between contrast enhancement and perfusion on CT and Doppler perfusion indices. *Br J Radiol* 2002; **75:** 17–23.
6. Tsushima Y, Blomley MJ, Kusano S, Endo K. Measuring portal venous perfusion with contrast-enhanced CT: Comparison of direct and indirect methods. *Acad Radiol* 2002; **9:** 276–282.
7. Cuenod CA, Leconte I, Siauve N, Resten A, Dromain C, Poulet B, et al. Early changes in liver perfusion caused by occult metastases in rats: Detection with quantitative CT. *Radiology* 2001; **218:** 556–561.
8. Mori S, Endo M, Tsunoo T, Kandatsu S, Tanada S, Aradate H, et al. Physical performance evaluation of a 256-slice CT scanner for four-dimensional imaging. *Med Phys* 2004; **31:** 1348–1356.
9. Endo M, Tsunoo T, Kandatsu S, Tanada S, Aradate H, Saito Y. Four-dimensional computed tomography (4D CT) concepts and preliminary development. *Radiat Med* 2003; **21:** 17–22.
10. Endo M, Mori S, Tsunoo T, Kandatsu S, Tanada S, Aradate H, et al. Development and performance evaluation of the first model of 4D CT-scanner. *IEEE Trans Nucl Sci* 2003; **50:** 1667–1671.
11. Leitz W, Axelsson B, Szendrö G. Computed tomography dose assessment: A practical approach. *Radiat Protect Dosimetry* 1995; **57:** 377–380.
12. Ito T, Suwa M, Imai M, Hozumi T, Tonari S, Kitaura Y. Acute effects of diltiazem on regional left ventricular diastolic filling dynamics in patients with hypertrophic cardiomyopathy as assessed by color kinesis. *Circ J* 2004; **68:** 1035–1040.
13. Liu J, Murata K, Fujino T, Ueda K, Kimura K, Wada Y, et al. Effect of dobutamine on regional diastolic left ventricular asynchrony in patients with left ventricular hypertrophy. *Circ J* 2003; **67:** 119–124.
14. Inoue T, Watanabe S, Sakurada H, Ono K, Urano M, Hijikata Y, et al. Evaluation of flow volume and flow patterns in the patent false lumen of chronic aortic dissections using velocity-encoded cine magnetic resonance imaging. *Jpn Circ J* 2000; **64:** 760–764.
15. Rumberger JA, Bell MR. Measurement of myocardial perfusion and cardiac output using intravenous injection methods by ultrafast (cine) computed tomography *Invest Radiol* 1992; **27:** 40–46.
16. Ludman PF, Darby M, Tomlinson N, Poole-Wilson PA, Rees S. Cardiac flow measurement by ultrafast CT: Validation of continuous and pulsatile flow. *J Comput Assist Tomogr* 1992; **16:** 795–803.
17. Fujino T, Ishii Y, Takeuchi T, Hirasawa K, Tateda K, Kikuchi K, et al. Recovery of BMIPP uptake and regional wall motion in insulin resistant patients following angioplasty for acute myocardial infarction *Circ J* 2003; **67:** 757–762.
18. Sugimoto K, Ito H, Iwakura K, Ikushima M, Kato A, Kimura R, et al. Intravenous nicorandil in conjunction with coronary reperfusion therapy is associated with better clinical and functional outcomes in patients with acute myocardial infarction. *Circ J* 2003; **67:** 295–300.
19. Funabashi N, Ishida A, Yoshida K, Komuro I. Double aortic arch with a compressed trachea demonstrated by multislice computed tomography. *Circulation* 2004; **110:** e68–e69.
20. Funabashi N, Kobayashi Y, Kudo M, Asano M, Teramoto K, Komuro I, et al. New method for measuring coronary diameter by electron-beam computed tomographic angiography using adjusted thresholds determined by calibration with aortic opacity. *Circ J* 2004; **68:** 769–777.
21. Funabashi N, Misumi K, Ohnishi H, Watanabe M, Suzuki Y, Imai N, et al. Endoluminal perspective volume rendering of coronary arteries using electron-beam computed tomography. *Circ J* 2003; **67:** 1064–1067.
22. Funabashi N, Kobayashi Y, Rubin GD. Utility of three-dimensional volume rendering images using electron-beam computed tomography to evaluate possible causes of ischemia from an anomalous origin of the right coronary artery from the left sinus of Valsalva. *Jpn Circ J* 2001; **65:** 575–578.
23. Funabashi N, Rubin GD. Direct identification of patency achieved by a bi-directional Glenn shunt procedure: Images by volume rendering using electron-beam computed tomography. *Jpn Circ J* 2001; **65:** 457–461.
24. Pan T, Lee TY, Rietzel E, Chen GT. 4D-CT imaging of a volume influenced by respiratory motion on multi-slice CT. *Med Phys* 2004; **31:** 333–340.
25. Nehmeh SA, Erdi YE, Pan T, Yorke E, Mageras GS, Rosenzweig KE, et al. Quantitation of respiratory motion during 4D-PET/CT acquisition. *Med Phys* 2004; **31:** 1333–1338.
26. Hirai T, Korogi Y, Ono K, Uemura S, Yamashita Y. Preoperative embolization for meningeal tumors: Evaluation of vascular supply with angio-CT. *Am J Neuroradiol* 2004; **25:** 74–76.
27. Hunink MG, Gazelle GS. CT screening: A trade-off of risks, benefits, and costs. *J Clin Invest* 2003; **111:** 1612–1619.
28. Knollmann F, Pfoh A. Coronary artery imaging with flat-panel computed tomography. *Circulation* 2003; **107:** 1209.

SCIENTIFIC LETTER

Three dimensional segmented myocardial perfusion images by selective intracoronary injection of contrast using 256 slice cone beam computed tomography

N Funabashi, K Yoshida, H Tadokoro, K Nakagawa, N Komiyama, K Odaka, T Tsunoo, S Mori, M Endo, S Tanada, I Komuro

Heart 2005;**91**:1349–1351. doi: 10.1136/hrt.2004.045997

Information of the segmented left ventricular (LV) area supplied by every coronary artery is potentially useful for strategy and practice of percutaneous coronary intervention, coronary artery bypass surgery, or percutaneous transluminal septal myocardial ablation (PTSMA).[1 2]

Myocardial contrast echocardiography (MCE) with intracoronary contrast injection has been used to evaluate the segmented LV area supplied by a coronary artery but it is invasive and evaluation of myocardial enhancement by ultrasound contrast material may depend upon the skill of the investigator.[1]

With a prototype high speed cone beam computed tomography (CT) apparatus employing 256 detector rows (Athena, Sony-Toshiba), an entire heart can be imaged within a single gantry rotation.[3 4] Using this technique, combined with selective intracoronary injection of contrast, we determined the segmented LV area supplied by every coronary artery selectively.

METHODS

Two domestic pigs (20 kg each) were anaesthetised with isoflurane, and catheters positioned in the left anterior descending branch (LAD) of the coronary artery in pig 1 and the left circumflex branch (LCx) in pig 2, via the femoral arteries. The heart rate of pigs ranged between 70–80 beats per minute.

Scan conditions for the 256 slice cone beam CT were: 120 kV, 200 mA, 1.0 second exposure, 1.0 second gantry rotation time, 0.5 mm slice thickness, and 256×0.5 mm slice collimation. For comparison, those for the 16 slice multislice CT scanner routinely used at our institute (SOMATOM Sensation 16, Siemens) were: 120 kV, 250 mA, 0.42 second exposure, 0.42 second gantry rotation time, 0.75 mm slice thickness, and 16×0.75 mm slice collimation.

To begin, 10 ml of the iodinated contrast material (300 mgI/ml) diluted with 40 ml of saline was injected at a rate of 3 ml/second.

Entire heart scanning and injection of contrast started simultaneously and the scanning was continued for 25 seconds. The radiation dose was 100 mSV for 25 seconds.[5]

Reconstruction parameters were a voxel size of $0.468 \times 0.468 \times 0.500$ mm^3 with 0.500 mm reconstruction increment along the z axis and a matrix size of $512 \times 512 \times 256$. Convolution kernels were standard body kernels; FC10.

The temporal resolution of this new CT is 1 second and spatial resolution was approximately 1.0 mm (transverse) and 1.3 mm (longitudinal).

The reconstruction was performed at every 0.1 second interval.

RESULTS

At 2 seconds, only the coronary arterial trees of LAD (pig 1) or LCx (pig 2) could be observed without myocardial enhancement. At 5 seconds, segmented myocardial enhancement of LAD and LCx could be observed with the coronary arterial trees.

We selected the most static images of the LV at around 5 seconds after contrast injection, so as to avoid any gaps from cardiac motion artefact. Axial source images clearly revealed segmented LV myocardial enhancement of the anterior and apical wall and interventricular septum (IVS) in pig 1 and the lateral and posterior wall in pig 2. Volume rendered images from the anterior and the left anterior views revealed only the anterior and apical wall and IVS portion of the LV myocardium supplied exclusively by the LAD in pig 1 and the lateral and posterior wall of LV myocardium supplied by the LCx in pig 2, together with the coronary artery (fig 1); the segmented LV area could be easily recognised three dimensionally.

DISCUSSION

A prototype 256 slice cone beam CT provides complete volumetric data within a single gantry rotation. In this CT, by combination of reconstruction technique, it is possible to obtain a configuration of the heart without any gaps caused by cardiac motion artefacts. This new prototype CT has a unique character, synchrony, for the acquisition of the pulsating heart. The scanning mechanism can accommodate a rotation speed of up to 0.5 second/rotation and ECG gated acquisition will be possible in the next generation scanner.

In this study using small pigs, we demonstrated segmented LV perfusion combined with selective coronary arterial injection and we successfully observed the segment LV enhancement three dimensionally.

Two plans can be envisaged for the future. Firstly, the combination of a selective angiography system with the CT system in which the CT acquisition with selective coronary artery injection can be achieved without any movement of the patient. In fact, this angiography system with multislice CT is already in use. Using the new system in which an angiography system is combined with a new 256 slice CT, it is possible to obtain the same segmented LV enhancement.

Secondly, acquisition using the new 256 slice CT combined with intravenous injection non-invasively. By this method, even though the segmentation of LV myocardial enhancement cannot be performed, we can evaluate the three

Abbreviations: CT, computed tomography; IVS, interventricular septum; LAD, left anterior descending; LCx, left circumflex; LV, left ventricular; MCE, myocardial contrast echocardiography; PTSMA, percutaneous transluminal septal myocardial ablation

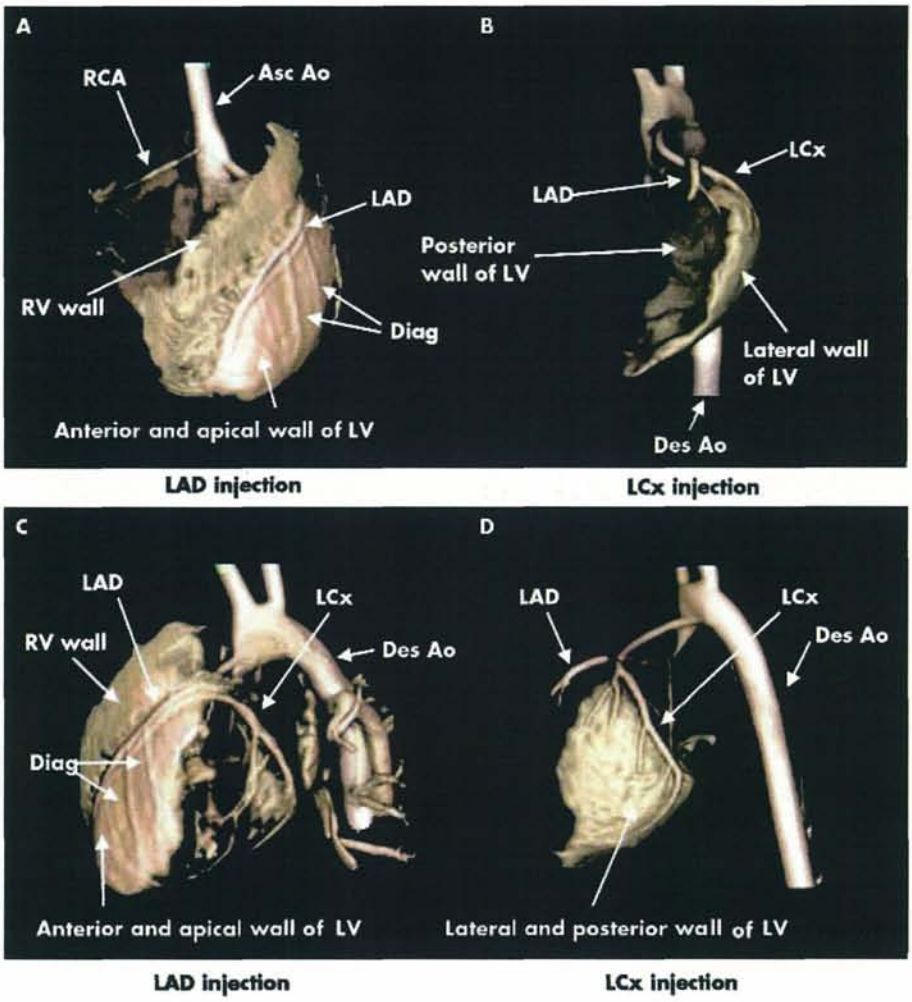

Figure 1 Volume rendered reconstruction images of porcine hearts using enhanced 256 slice high speed cone beam computed tomography (CT) acquired 5 seconds after injection of contrast material from the anterior view (A, B) and the left anterior view (C, D) revealed only the anterior, the apical interventricular septum (IVS) portion of the left ventricle (LV) myocardium, and the anterior wall of right ventricular myocardium supplied exclusively by the left anterior descending coronary artery (LAD) in pig 1 with LAD injection (A, C), and the lateral and posterior portion of LV myocardium by the left circumflex artery (LCx) in pig 2 with LCx injection (B, D). The right coronary artery was visualised from the backflow from the catheter located in the LAD in pig 1(A) as well as the aorta. Asc Ao, ascending aorta; Des Ao, descending aorta; Diag; diagonal branch.

dimensional perfusion of the whole myocardium non-invasively, which is not possible with 16 slice CT. Using this technique, continuous 25 second acquisitions can be performed yielding quantitative myocardial perfusion information by using time density curves of myocardium on three dimensional images.

Especially using the former plan, this technique provides useful information for a physician to arrive at a strategy for percutaneous coronary intervention or coronary artery bypass surgery by combination of this new CT with selective intracoronary contrast injection. Furthermore, during PTSMA in subjects with hypertrophic obstructive cardiomyopathy, information regarding the septal branch of coronary arteries supplying the hypertrophic IVS which occludes the LV outflow tract is required.[2] MCE with intracoronary contrast injection is commonly used during the procedure to guide the selection of the appropriate septal branch that feeds the hypertrophic IVS. As an alternative to MCE, the injection of contrast material from the catheter located in the septal branch followed by 1 second scanning using this CT technique can provide the proper information to select the appropriate septal branch; this technique is less complicated than MCE.

We described here a novel prototype CT that has the advantage of whole heart imaging in a single gantry rotation without ECG gated acquisition.

Of course, further research and technologic developments would be needed to overcome potential problems, such as radiation dose and any technical problems such as using the catheter without complication. Future technological advances in this area should overcome these problems. This technique may facilitate new cardiovascular diagnoses and may also find applications in other organs such as brain, liver, kidney, and vasculature.

ACKNOWLEDGEMENTS

This work was supported in part by the 4D-CT research group at the National Institute of Radiological Sciences, Japan.

Authors' affiliations

N Funabashi, K Yoshida, K Nakagawa, N Komiyama, I Komuro, Department of Cardiovascular Science and Medicine, Chiba University Graduate School of Medicine, Chiba, Japan
H Tadokoro, K Odaka, T Tsunoo, S Mori, M Endo, S Tanada, National Institute of Radiological Sciences, Chiba, Japan

Correspondence to: Nobusada Funabashi, MD, Department of Cardiovascular Science and Medicine, Chiba University Graduate School of Medicine, 1-8-1 Inohana, Chuo-ku, Chiba City, Chiba 260-8670, Japan; nobusada@ma.kcom.ne.jp

Accepted 27 January 2005

REFERENCES

1 **Ito H**, Tomooka T, Sakai N, *et al.* Lack of myocardial perfusion immediately after successful thrombolysis: a predictor of poor recovery of left ventricular function in anterior myocardial infarction. *Circulation* 1992;**85**:1699–705.
2 **van Dockum WG**, ten Cate FJ, ten Berg JM, *et al.* Myocardial infarction after percutaneous transluminal septal myocardial ablation in hypertrophic

obstructive cardiomyopathy: evaluation by contrast-enhanced magnetic resonance imaging. *J Am Coll Cardiol* 2004;**43**:27–34.
3 **Endo M**, Tsunoo T, Kandatsu S, *et al*. Four-dimensional computed tomography (4D CT) concepts and preliminary development. *Radiat Med* 2003;**21**:17–22.
4 **Mori S**, Endo M, Tsunoo T, *et al*. Physical performance evaluation of a 256-slice CT scanner for four-dimensional imaging. *Med Phys* 2004;**31**:1348–56.
5 **Leitz W**, Axelsson B Szendrö G. Computed tomography dose assessment–A practical approach. *Radiat Prot Dosimetry* 1995;**57**:377–80.

IMAGES IN CARDIOLOGY

doi: 10.1136/hrt.2005.064097

Transoesophageal echocardiography showing a thrombosis of the aortic valve mechanical replacement before and after thrombolytic treatment

A 75 year old female patient with a four year history of aortic valve replacement with mechanical prosthesis (Medtronic Hall 20) was admitted to the cardiology department with a one month history of progressing dyspnoea and coughing episodes. She denied having chest pain. Admission ECG showed signs of hypertrophy and overload of the left ventricle and 1 mm ST segment elevations in leads II, III, and aVF. Routine laboratory tests revealed significant increases in cardiospecific enzymes and an international normalised ratio (INR) of 1.71, confirming inadequate anticoagulation treatment with long term administration of warfarin sodium.

Further management was strongly influenced by echocardiography findings. Transoesophageal echocardiography (TOE) on the day of admission revealed a non-dilated hypertrophic left ventricle (LV) with a hypokinetic inferior wall and good global ejection fraction (60%). Mechanical disc prosthesis was present in the aortic position, with severe dysfunction. The whole right coronary sinus was filled with a hyperechogenic mass that hindered the movement of the disc and perfusion of the right coronary artery (panels A, B). Significant aortic stenosis was present with a peak gradient of 95 mm Hg along with grade 2 regurgitation. Because of the high risk of surgery due to the ongoing myocardial infarction we decided to administer a thrombolytic agent. Actilyse 100 mg was given intravenously in a two hour continual infusion, followed by a continuous infusion of unfractioned heparin during the following days.

A follow up TOE on day 5 after admission revealed a completely clear aortic bulb with no pathological masses, good function of the aortic mechanical valve, full motion range of the disc without any limitations, and a significant reduction of the peak grade down to 51–52 mm Hg, which was the patient's pre-morbid value (panels C, D). Global left ventricular function had no significant abnormalities. Anticoagulation treatment with warfarin sodium was resumed and the patient was discharged home on day 11 in satisfactory condition with an INR of 3.30.

P Jelínek
M Vácha
M Šulda
jelinek@nemcb.cz

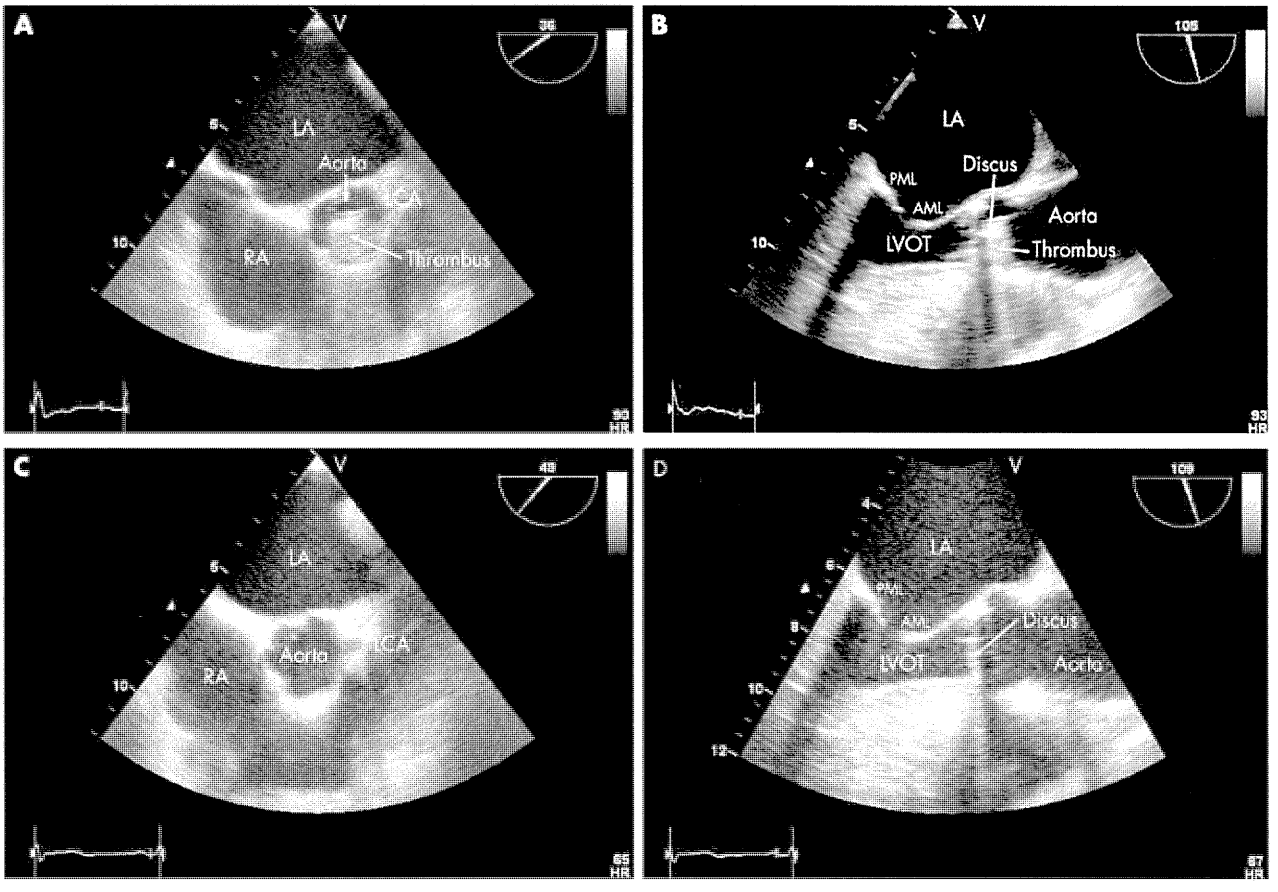

Real-Time Volumetric Imaging of Human Heart Without Electrocardiographic Gating by 256–Detector Row Computed Tomography

Initial Experience

Chisato Kondo, MD, Shinichiro Mori, MS,† Masahiro Endo, PhD,† Kiyoko Kusakabe, MD,* Naoki Suzuki, PhD,‡ Asaki Hattori, PhD,‡ and Masahiro Kusakabe, PhD§*

Objective: The feasibility of human cardiac imaging using a prototype 256–detector row cone-beam computed tomography (256CBCT) scanner without electrocardiographic gating was examined.

Methods: Two healthy male volunteers were examined by contrast-enhanced 256CBCT. The number of detectors was 912 × 256, each measuring approximately 0.5 mm × 0.5 mm at the center of rotation. The craniocaudal coverage was approximately 100 mm after reconstruction by the Feldkamp-Davis-Kress algorithm. The effective time resolution was 500 milliseconds using a half-scan algorithm.

Results: Serial enhancement of the left ventricular myocardium was detected. The right and left coronary arteries at proximal and distal segments were depicted without significant blurring. Although the left ventricular wall motion on cine images was not smooth over time, it was possible to measure ventricular volume and ejection fraction.

Conclusions: Using the 256CBCT, it was possible to visualize the coronary arteries, myocardial perfusion, and ventricular contraction simultaneously during a single acquisition.

Key Words: computed tomography, cone beam, coronary angiography, myocardial perfusion, ventricular function

(*J Comput Assist Tomogr* 2005;29:694–698)

With recent advances in multidetector computed tomography (MDCT), coronary angiography with MDCT has now become a practical method for identifying patients with significant coronary artery stenosis. Because craniocaudal coverage with a conventional MDCT scanner without table movement is typically limited to 20–40 mm, however, electrocardiographic (ECG) gating and a combination of fast gantry rotation, slow table movement, and helical acquisition mode are required for cardiac imaging. Consequently, MDCT images are made by summation of data in the same cardiac phase from multiple cardiac cycles, precluding examination of patients with an irregular heart rhythm.

We have developed a prototype 256–detector row cone-beam computed tomography (256CBCT) scanner to achieve real-time imaging without ECG gating with wider coverage in the craniocaudal direction. This scanner uses a continuously rotating cone-beam x-ray tube and 256 detector rows without table movement to provide volumetric data (3-dimensional data) with the additional dimension of time.[1] Its craniocaudal coverage has a length of approximately 100 mm.[2] Previously, we demonstrated in an in vivo porcine model that 256CBCT was capable of successfully imaging cardiac chambers and vessels according to the passage of contrast media from the right side of the heart to the left side.[3] We also visualized distal coronary arterial branches up to the third generation by intracoronary administration of contrast material and 256CBCT in an excised porcine heart (S. Mori, MS, 2005 unpublished data).

Here, we report the preliminary results of real-time volumetric imaging of the human heart from normal volunteers without the aid of ECG gating.

MATERIALS AND METHODS

Prototype 256–Detector Row Computed Tomography Scanner

Details of the architecture and physical performance of the prototype 256CBCT scanner have been described previously.[3–5] Briefly, this scanner uses a wide-area cylindrical detector design based on new computed tomography (CT) technology and mounted on the gantry (Aquilion; Toshiba Medical Systems, Ohtawara, Japan).[6] The number of elements is 912 channels (transverse) × 256 segments (craniocaudal); the element size is approximately 1.02 mm × 0.90 mm, corresponding to 0.58 mm (transverse) × 0.50 mm (craniocaudal) beam width at the center of rotation. The rotation time of the gantry is 1.0 second. The Feldkamp-Davis-Kress algorithm

Received for publication April 18, 2005; accepted June 2, 2005.

From the *Department of Radiology, Tokyo Women's Medical University School of Medicine, Tokyo, Japan; †Department of Medical Physics, National Institute of Radiological Sciences, Chiba, Japan; ‡Institute for High Dimensional Medical Imaging Research Center for Medical Science, Jikei University School of Medicine, Tokyo, Japan; and §Faculty of Engineering, Fukui University, Fukui, Japan.

Supported in part by the New Energy and Industrial Technology Development Organization of Japan.

Reprints: Chisato Kondo, Division of Nuclear Medicine, Department of Radiology, Tokyo Women's Medical University, 8-1 Kawada-cho, Shinjuku-ku, Tokyo 162-8666, Japan (e-mail: pkondou@rad.twmu.ac.jp).

was used for reconstruction.[7] The craniocaudal coverage was approximately 100 mm, which was less than the value (128 mm) obtained simply from the number of slices (256) × slice collimation (0.5 mm). Its limited coverage is attributable to the geometry of the imaging volume of cone-beam CT when the Feldkamp algorithm was used.[5] Each detector element consisted of a scintillator (Gd_2O_2S ceramic) and photodiode (single-crystal silicon). Reconstruction usually took less than 1 second for volume data of 512 × 512 × 256 voxels with a high-speed image processor with field-programmable gate array–based architecture.

Procedures for Real-Time Volumetric Imaging of the Human Heart

The study procedures were approved by our institutional review board for human research. Written informed consent was obtained from the 2 subjects, both of whom were healthy adult males (weight: 60–70 kg). Each was given 1 mg/kg metoprolol orally (Seloken; AstraZeneca Japan, Osaka, Japan) 2 hours before CT scanning to reduce the heart rate, which was 56–58 bpm at the time of examination. A 20-gauge polyethylene venule was introduced into the anterior cubital vein of the right arm. Oral nitroglycerine was not administered before scanning.

After undergoing an initial scout topogram of the chest, the subjects were scanned without table movement in the cine scan mode with the gantry centered over the heart. Scanning was begun after injecting 70 mL nonionic iodinated contrast material (Iopamiron 370; Nihon Schering, Osaka, Japan) by means of a single-syringe power injector (6.0-mL/s flow rate) without saline flush. The delay between the start of contrast material administration and CT scanning was 10 seconds. Scan parameters were 120 kV, 200 mA, 1.0 second of rotation time, and 256-mm × 0.5-mm beam collimation. The entire scan time was 14 seconds, and the effective radiation dose was 31 mSv. The subjects were instructed to hold their breath in the end-expiration position during scanning. A half-scan algorithm[8] was applied, and the effective temporal acquisition window was 500 milliseconds. The volume elements (voxels) were 0.47 mm × 0.47 mm × 0.47 mm in a 512 × 512 × 216 data matrix covering a volume of 240 mm × 240 mm × 102 mm. The data set was reconstructed every 40 milliseconds. Images were transferred to a dedicated image postprocessing workstation for volume rendering. Images were primarily assessed by visual interpretation in terms of myocardial contrast enhancement, coronary arterial visualization, and left ventricular contraction. We also performed quantitative analyses regarding the following parameters[9]: 1) myocardial density changes between before and peak contrast enhancement, 2) coronary vessel contrast as the difference in mean CT density (Hounsfield units) between the vessel lumen and the perivascular tissue, 3) contrast-to-noise ratio expressed as the quotient of the contrast of the coronary arteries and image noise expressed as the standard deviation value in the aorta, 4) determination of the slope of a CT density curve (ΔHounsfield units per millimeter) over the vessel wall as a measure of its contour sharpness, and 5) end-diastolic and end-systolic left ventricular volumes and ejection fraction determined by Simpson's rule applied to multiple short axial sections skipped every 10 mm.

RESULTS

The 256CBCT satisfactorily demonstrated continuous enhancement of the heart. In the dynamic coronal tomographic planes, contrast enhancement was observed at 1.0 to 12.3 seconds after the start of scanning. The left ventricular chamber was visualized by contrast enhancement 3 seconds after the start of scanning, and the myocardium was enhanced gradually and homogeneously over the left ventricle after 3 seconds and maximally at 10 seconds after the start (Fig. 1a). Postprocessing with a volume-rendered technique was applied to depict the right and left coronary arteries (see Figs. 1b, c). The distal right coronary artery around the crux was visualized without significant blurring. Contrast and contour sharpness of the coronary arteries on 256CBCT were equivalent to or better than those on MDCT.[9] The left ventricular motion was not smooth over time on cine images, because the left ventricular chamber size at end-systole was largely affected by the timing of reconstruction (successively reconstructed every 40 milliseconds, with a time window of 500 milliseconds) at a given cardiac phase. Nevertheless, we found that left ventricular volume and ejection fraction measured by the 256CBCT showed physiologic values for normal male adults (see Fig. 1d).

DISCUSSION

This preliminary study demonstrated that real-time volumetric imaging of the human heart by 256CBCT successfully visualized coronary arteries and myocardial contrast enhancement in a single acquisition. Because the magnitude of contrast enhancement by 256CBCT was similar to previous results of electron beam CT,[10] 256CBCT should be used for evaluation of myocardial perfusion at rest and under pharmacologic vasodilatory stimuli.[10] Myocardial contraction could also be assessed, although with some limitations, during the same acquisition.

This CT scanner was designed to allow volumetric cine imaging over a craniocaudal distance of approximately 100 mm in 1 rotation without table movement. The images created had a slice thickness of less than 0.5 mm in the same time phase, resulting in isotropic voxels that could be used to create images and cine loops in any desired plane, without loss of spatial resolution, with any of several postprocessing techniques. Previously, we demonstrated successful contrast-enhanced cine imaging of ventricles and great vessels in a porcine model.[3] In this model, however, we found that coronary arteries were visualized clearly only at the proximal portion, because the porcine heart is smaller in size and has a higher heart rate than that of a human adult. In the present human study, we could visualize the coronary artery more clearly than that of pigs by controlling the heart rate to <60 bpm after administration of a beta-blocker.

Comparison of 256CBCT with conventional CT methodology would be useful to understand the strengths and limitations of 256CBCT. In electron beam computed tomography (EBCT), a protocol for coronary imaging (volume mode

scanning) uses a slice collimation of 3.0 mm, a table feed of 1.5–2.0 mm per scan, prospective ECG triggering to some predetermined cardiac phase, and multiple scans (>50) to image the entire coronary artery.[11] Because of its relatively thick slices and low signal-to-noise ratio, EBCT is inferior to MDCT with regard to visualization of the coronary arteries.[9] A different protocol of EBCT (cine mode scanning) for ventricular imaging consists of successive acquisitions with a fixed scan

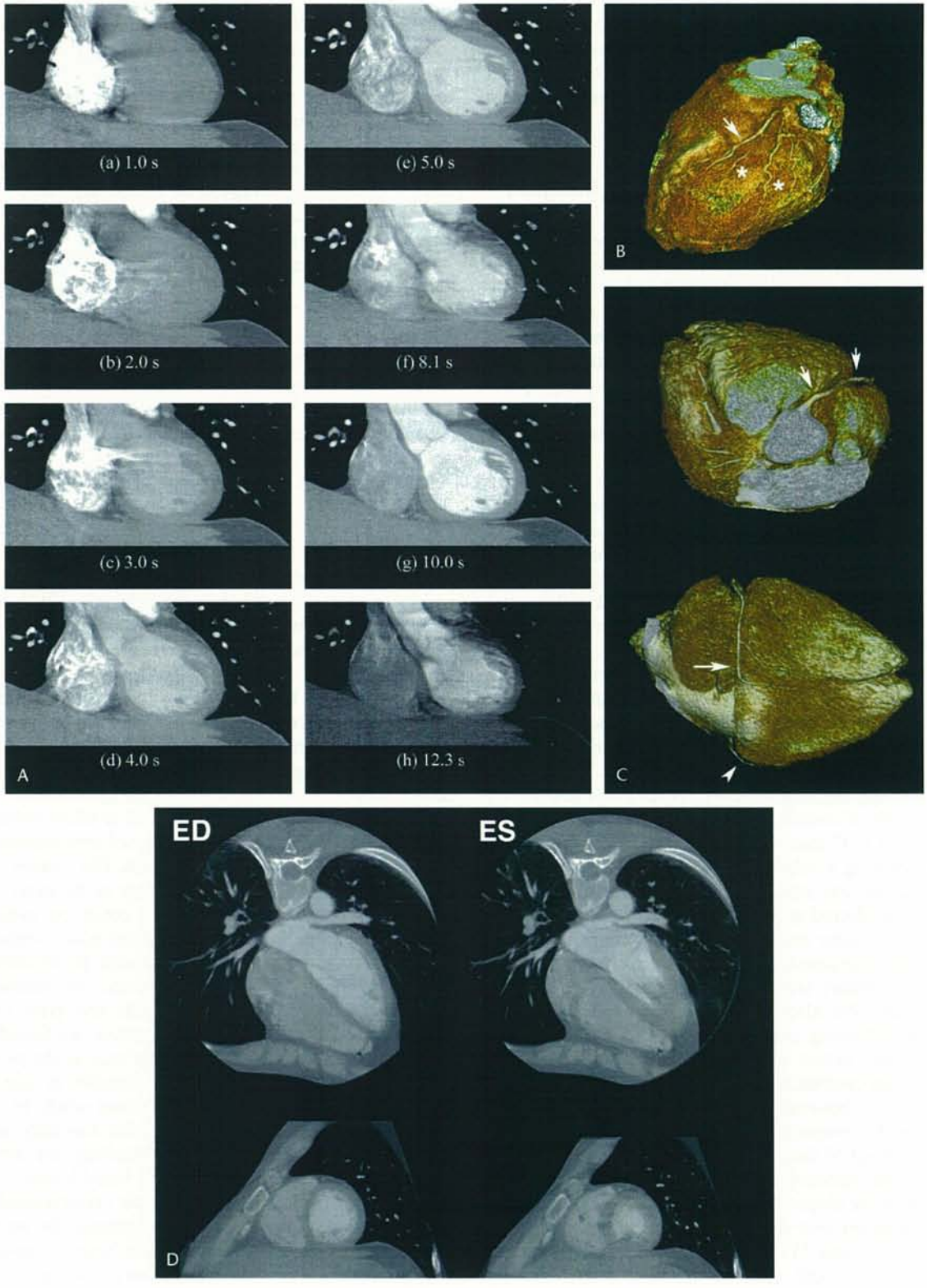

time of 100 milliseconds, a limited number of slices (typically 8–10 slices separated from each other by 10 mm), and orientation of slices determined before acquisition. With the use of high temporal resolution, EBCT is accurate for measuring ventricular volume and ejection fraction.[12] Application of EBCT to assess myocardial perfusion has also been reported.[13] The requirements of a predetermined slice orientation and limited number of slices are likely to limit the capability of EBCT to assess regional myocardial function and perfusion, however. In addition, the volume and cine scanning modes of EBCT cannot be used at the same time, which precludes simultaneous examination of the coronary artery and ventricular perfusion and function. Current ECG-gated 16- or 64-row MDCT scanners perform imaging of coronary arteries, ventricular motion, and myocardial perfusion during the same acquisition with a spatial resolution of ~0.5 mm (isotropic voxel imaging can be attained by 64-row MDCT) and a temporal resolution of ~120–150 milliseconds using a multisegmental reconstruction algorithm, but the acquisition typically takes ~20 seconds (16-row MDCT) or ~10 seconds (64-row MDCT). During this acquisition period, if the heart rhythm is not regular, banding artifacts appear in the final images. In contrast, 256CBCT needs only half of 1 gantry rotation for acquisition of 3-dimensional data sets of the entire heart and coronary arteries with 0.5-mm isotropic voxel resolution without banding artifacts (see Figs. 1b, c).

The major limitation of the prototype 256CBCT used in the present study was the limited time resolution of 500 milliseconds even with the use of a half-scan algorithm, because the time for gantry rotation was 1.0 second. Even with a wide time window, however, we did not find significant blurring of coronary images, including the right coronary artery at the acute margin of the heart (see Fig. 1c). Thus, it is likely that motion artifacts during a single heart beat may only mildly reduce the image quality of coronary arteries on 256CBCT, which is free of ECG gating-related artifacts. Conversely, left ventricular motion was not smooth because of the limited time resolution with artifactual irregular movement of the left ventricular contours. In the design of the prototype, we preferred wide coverage of x-rays in the craniocaudal direction and an x-ray tube tilted at an angle of 5°. The design had several drawbacks, such as the heavy forces on the tube's bearing because of angular momentum conservation and the requirement for a longer time for gantry rotation to protect the tube's bearing (1.0 second per rotation vs. 0.5 second per rotation). We are now constructing a second-generation 256CBCT scanner with a new type of x-ray tube without tilting. The new 256CBCT scanner can rotate in 0.5 second and achieve time resolution close to 250 milliseconds without ECG gating, and it should be able to provide images of coronary arteries and dynamic ventricular contraction more clearly and smoothly. Another limitation of the present study involves the radiation dose (2.21 mSv/s at a tube current of 200 mA for 1.0 second of gantry rotation). Our phantom experiments have indicated that with improvement of detector performance of the second-generation 256CBCT scanner, the radiation dose should be reduced to 60%–70% of that of the first-generation scanner to accomplish the same signal-to-noise ratio (unpublished data). Thus, the new 256CBCT scanner would operate at a tube current of 240 mA (400 mA × 0.6) for 0.5 second of gantry rotation, with an estimated radiation dose of 2.65 mSv/s. In the first-generation scanner, we could not use bolus tracking software (eg, "real-prep" supplied with Aquilion; Toshiba Medical Systems). We also did not use a preliminary minibolus injection to determine the timing of peak contrast enhancement at the ascending aorta, because a dual-syringe injector was not available at the time of the study. Use of such instruments should allow scanning to be limited to only around the peak coronary and myocardial enhancement. Because we noticed that myocardial enhancement followed immediately after coronary visualization, it should be possible to reduce the scan time by ~5 seconds (radiation dose ~15 mSv) for imaging coronary arteries and enhanced myocardium during the same acquisition in normal subjects. Currently, the optimal scan time and required radiation dose for patients with coronary arterial disease are not clear, and further studies are warranted.

The results of the present study with the prototype 256CBCT scanner are promising for future clinical application of CBCT to cardiovascular disease. Although myocardial ischemia can be assessed by repeated scans using 16-row MDCT at rest and under pharmacologic stress the same as in nuclear perfusion studies,[14] the high radiation dose of conventional MDCT restricts repeated scans during the same examination. Conventional MDCT requires a relatively long scan time to image the whole heart, limiting further reduction of the radiation dose. In this respect, 256CBCT may have the potential to reduce the radiation dose. Furthermore, an irregular heart rhythm would not degrade the image quality of 256CBCT. Because coronary morphology, ventricular function, and myocardial perfusion can be assessed simultaneously by 256CBCT,

FIGURE 1. A, A 32-year-old healthy male volunteer. Dynamic coronal sections demonstrated that the left ventricular chamber was visualized by contrast enhancement 3 seconds after the start of scanning (C) and the myocardium was mildly and homogeneously enhanced over the left ventricular wall at 10 seconds after the start (G). The contrast agent increased myocardial density by 33 HU. The delay between the start of contrast material injection and CT scanning was 10 seconds. B, Volume-rendered image of the heart from the same subject as in A. The left anterior descending artery (arrow) and diagonal branches (asterisks) were visualized on the left ventricle. In the proximal left coronary artery, the contrast was 395 HU, the contrast-to-noise ratio was 5.4, and the contour sharpness of the artery was 246 ΔHU/mm. C, Volume-rendered image of the heart from the same subject as in A. The right coronary artery was shown at its origin (arrows in the upper figure) and periphery near the crux (arrow in the lower figure). In the proximal right coronary artery, the contrast was 450 HU, the contrast-to-noise ratio was 6.4, and the contour sharpness of the artery was 200 ΔHU/mm. The peripheral left circumflex artery was also found (arrowhead in the lower figure). D, End-diastolic (ED, left column) and end-systolic (ES, right column) images of the left ventricle in long (upper row) and short (lower row) axial sections from the same subject as in A. ED and ES volumes and the ejection fraction were 113 mL, 39 mL, and 65%, respectively. Changes in the wall motion and wall thickening of the left ventricle during a cardiac cycle were clearly demonstrated.

the 2 separate examinations required currently involving invasive angiography and nuclear perfusion scanning can be replaced by a single examination using 256CBCT in the near future.

In conclusion, this is the first report of the application of 256CBCT for human cardiac imaging by means of real-time volumetric scanning. We considered that the images generated by the prototype scanner were feasible for documenting coronary arterial morphology and myocardial perfusion without ECG gating. It was also possible to assess ventricular function in part during the same acquisition.

ACKNOWLEDGMENTS

The authors express their appreciation to the staff of Toshiba Medical Systems Corporation and Sony Corporation.

REFERENCES

1. Taguchi K. Temporal resolution and the evaluation of candidate algorithms for four-dimensional CT. *Med Phys*. 2003;30:640–650.
2. Endo M, Yoshida K, Kamagata N. Development of a 3D CT-scanner using a cone beam and video-fluoroscopic system. *Radiat Med*. 1998;16:7–12.
3. Mori S, Kondo C, Suzuki N, et al. Volumetric cine imaging for cardiovascular circulation using prototype 256-detector row computed tomography scanner (4-dimensional computed tomography): a preliminary study with a porcine model. *J Comput Assist Tomogr*. 2005;29: 26–30.
4. Mori S, Endo M, Tsunoo T. Physical performance evaluation of a 256-slice CT-scanner for 4-dimensional imaging. *Med Phys*. 2004;31:1348–1356.
5. Mori S, Endo M, Nishizawa K, et al. Enlarged longitudinal dose profiles in cone-beam CT and the need for modified dosimetry. *Med Phys*. 2005;32: 1061–1069.
6. Saito Y, Aradate H, Igarashi K. Large area 2-dimensional detector for real-time 3-dimensional CT (4DCT). *Proc SPIE*. 2001;4320:775–782.
7. Feldkamp L, Davis L, Kress J. Practical cone-beam algorithm. *J Opt Soc Am*. 1984;1:612–661.
8. Parker DL. Optimal short scan convolution reconstruction for fanbeam CT. *Med Phys*. 1982;9:254–257.
9. Lembcke A, Wiese TH, Schnorr J, et al. Image quality of noninvasive coronary angiography using multislice spiral computed tomography and electron-beam computed tomography: intraindividual comparison in an animal model. *Invest Radiol*. 2004;39:357–364.
10. Knollmann FD, Muschick P, Krause W, et al. Detection of myocardial ischemia by electron beam CT. Experimental studies. *Acta Radiol*. 2001; 42:386–392.
11. Lu B, Shavelle DM, Mao S, et al. Improved accuracy of noninvasive electron beam coronary angiography. *Invest Radiol*. 2004;39:73–79.
12. Schmermund A, Rensing BJ, Sheedy PF, et al. Reproducibility of right and left ventricular volume measurements by electron-beam CT in patients with congestive heart failure. *Int J Card Imaging*. 1998;14:201–209.
13. Wolfkiel CJ, Ferguson JL, Chomka EV, et al. Measurement of myocardial blood flow by ultrafast computed tomography. *Circulation*. 1987;76: 1262–1273.
14. Carrascosa P, Capunay C, Merletti P, et al. Usefulness of pharmacological stress multidetector CT studies in the evaluation of myocardial perfusion. *Circulation*. 2004;110:III-446.

AJNR Am J Neuroradiol 26:2536–2541, November/December 2005

Technical Note

Volumetric Perfusion CT Using Prototype 256–Detector Row CT Scanner: Preliminary Study with Healthy Porcine Model[V]

Shinichiro Mori, Takayuki Obata, Naoshi Nakajima, Nobutsune Ichihara, and Masahiro Endo

Summary: This is a preliminary demonstration of volumetric perfusion CT of the brain in domestic pigs by using a prototype 256-detector row CT. Scan range is approximately 100 mm in the craniocaudal direction with 0.5-mm section thickness. The 256–detector row CT is an easily available imaging technique that can provide volumetric cine imaging, CT angiography, and perfusion CT in a wide craniocaudal coverage simultaneously.

A number of methods for the evaluation of acute stroke and brain ischemia have been introduced, including xenon-enhanced CT, positron-emission tomography (PET), single-photon emission CT (SPECT), and MR imaging. These methods, however, are not widely available outside large hospitals. In contrast, the equipment required for dynamic CT perfusion in cerebral perfusion imaging is generally available in most hospitals. The major clinical applications of perfusion CT are in stroke and oncology, including nephrologic and hepatologic oncology. The organ of interest is scanned in cine mode, with the table kept stationary while the contrast medium is injected into the patient and distributed via the circulation. Various image analysis algorithms have been developed during the past 2 decades, and clinical utility has been expanded to include the measurement of cerebral blood flow (CBF), cerebral blood volume (CBV), and mean transit time (MTT) (1).

A principal limitation of CT perfusion by using conventional CT, including multidetector CT (MDCT), however, is its limited sample volume. The latest MDCT now incorporates 64 segments with a segment size of 0.5–0.625 mm at the center of rotation, which represents a substantial improvement from conventional MDCT, especially in cardiac imaging. The maximum axial field of view is <40 mm, however, which makes the location of investigation critical, because only a limited section of the organ of interest can be examined. Although identification of the pathologic area by helical scanning before perfusion CT remains possible, the use of MDCT may result in erroneous perfusion CT mapping of the pathologic area or incomplete coverage of the whole pathologic area.

To increase the coverage of perfusion CT studies in the craniocaudal direction (volumetric perfusion CT), we developed a prototype 256–detector row CT (2). This increase in the number of detector rows allows an isotropic resolution of less <0.5 mm and wide craniocaudal coverage (approximate length 100 mm) in a single rotation. The 256–detector row CT thereby promises to increase the amount of diagnostic information obtainable and solve some of the limitations of present helical CT methods in cardiovascular circulation (3), kinematics, and radiation therapy planning for image-guided radiation therapy (IGRT) and 4D radiation therapy.

Here we describe a preliminary investigation of volumetric perfusion CT by using the 256–detector row CT in the evaluation of 2 healthy domestic pigs.

Materials and Methods

Prototype 256–Detector Row CT

The prototype 256–detector row CT (2, 4) uses a wide-area cylindrical 2D detector designed on the basis of present CT technology and mounted on the gantry frame of a 16–detector row CT (5; Aquilion, Toshiba Medical Systems, Otawara, Japan). It has 912 (transverse) × 256 (craniocaudal) elements, each approximately 0.5 mm × 0.5 mm at the center of rotation. In designing this prototype, we favored wide radiographic coverage in the craniocaudal axis, which required tilting the radiograph tube a few degrees. This approach had several disadvantages, including heavy coriolis forces on the tube's bearing due to angular momentum conservation, which necessitated that the rotation time of the gantry be restricted to 1.0 second to protect the bearing. The 128-mm total beam width allows the continuous use of several collimation sets (eg, 256 × 0.5 mm, 128 × 1.0 mm, 64 × 2.0 mm). Craniocaudal coverage of the 256–detector row CT is approximately 100 mm per rotation. Data sampling rate is 900 views per rotation, and dynamic range of the analogue-digital converter is 16 bits. The detector element consists of a Gd_2O_2S ceramic scintillator and single-crystal silicon photodiode, as used for MDCT.

Reconstruction is done with a Feldkamp-Davis-Kress algorithm (6). Reconstruction of a 512 × 512 × 256-voxel data set by a high-speed image processor in a field programmable gate array–based architecture took <1 second.

Received February 26, 2005; accepted after revision May 13.

From the Departments of Medical Physics (S.M., M.E.) and Medical Imaging (T.O.), National Institute of Radiological Sciences, Chiba, Japan; Shimodate Animal Hospital (N.N.), Ibaraki, Japan; and Laboratory of Anatomy, School of Veterinary Medicine (N.I.), Azabu University, Kanagawa, Japan.

Address correspondence to Shinichiro Mori, MS, 4-9-1 Anagawa, Inage-ku, Chiba-shi, Chiba, 263-8555, Japan.

[V]The online version of this article contains supplemental videos at http://www.ajnr.org.

Data Processing

The theoretical basis for volumetric perfusion CT analysis is the use of CBF, CBV, and MTT for deconvolution analysis. This analysis assumes that the contrast medium is not diffusible, because nondiffusibility is a reasonable assumption in the brain. Here the tissue concentration function $C_t(t)$ was calculated as follows:

$$C_t(t) = F \cdot C_a(t) \otimes R(t),$$

where $\otimes$ is the convolution operator, F is cerebral blood flow, $C_a(t)$ is the measured arterial concentration of contrast media, and $R(t)$ is the time enhancement curve of the tissue obtained by the contrast-injected cine scan. The cine scanning measured $C_t(t)$ and $C_a(t)$ and generated deconvolution between them. CBF and CBV were then calculated from $F\,R(t)$. MTT can be calculated by the central volume principle (7) as follows:

$$MTT = \frac{CBV}{CBF}.$$

CBF, CBV, and MTT maps were generated by using modified commercial deconvolution-based software (CT Perfusion, Toshiba Medical Systems) for volumetric perfusion CT analysis. The analyses were generated by simply extending the conventional 2D analysis (pixel-based) to a 3D analysis (voxel-based). This analysis was used to create time-enhancement curves for each voxel, which were linearly related to the time attenuation curves (TDCs) for the first pass of an iodinated contrast material. Small round regions of interest measuring 4–8 mm^2 were placed manually by a trained research assistant onto the anterior cerebral artery and the superior sagittal sinus to provide arterial and venous TDCs, respectively.

Image quality and accuracy of the perfusion map were evaluated by a board-certified radiologist and 2 veterinarians, each of whom had >10 years of clinical experience. Image quality was assessed by reference to experience-based standards. Reading of the images in multiple planes took about 30 minutes.

Technique for Volumetric Perfusion CT Imaging

All animal procedures were approved by the National Institute of Radiologic Sciences' institutional review board. Two domestic pigs weighing 25 kg were mechanically ventilated under isoflurane anesthesia, and an introducer was positioned in the inferior vena cava via the external carotid artery.

After an initial scout topogram of the head was made, injection of 50 mL of nonionic iodinated contrast material (Iopamiron 370; Nihon Schering, Osaka, Japan) was begun by using a power injector at a flow rate of 9.9 mL/s, followed by scanning in the cine mode with the gantry centered over the head. A 1-second delay between the start of administration and scanning was used, with scan parameters 120 kV, 200 mA, and 128 × 1.0 mm beam collimation. Because continuous scan time was limited by disk storage capacity, 1-second rotation time and 50-second total scan times were selected. Effective dose was 63.0 mSv/50 seconds. The volume elements (voxels) were 0.47 × 0.47 × 0.47 mm in a 512 × 512 × 216 data matrix covering a 240 × 240 × 102 mm volume with a 0.3-second time interval.

Results

The vascular system of a pig brain with and without cranial bones is shown in Figs 1*A* and 1*B*, respectively. Results showed contrast enhancement with 3D volume rendering after the start of injection (pig 1, Fig 1). The carotid arteries were best visualized on images obtained at approximately 5–10 seconds (Fig 1*C*), whereas enhancement of the sagittal venous sinus and infraorbital artery increased gradually from 8 to 16 seconds (Figs 1*D* and 1*E*). Enhancement of the lingual artery was decreased at 25 seconds (Fig 1*F*).

The nonenhanced sagittal section image shows fine structure at the start (0 seconds) of injection (Fig 2*A*). CT angiographs (CTAs; Fig 2*B*) obtained by subtracting nonenhanced images (Fig 2*A*) from the volumetric cine data show contrast enhancement at 14 seconds. Volumetric perfusion analyses for CBF, CBV, and MTT for pig 1 are shown in Fig 2*C–E*. Volumetric perfusion CT maps are superimposed on the sagittal image. In addition to the brain, the lingual arteries are also mapped.

The results of volumetric perfusion CT in an oblique plane at a 40° angle to the horizontal for pig 2 are shown in Fig 3. The CTA (Fig 3*C*) shows contrast enhancement 15 seconds after the start of contrast injection. Volumetric perfusion CT was done in the oblique plane with a maximum intensity projection (MIP) slab thickness of 6.0 mm and MIP slab position and angle parallel to the orbitomeatal line.

Volumetric perfusion CT results were optimized by fixing the position of the pig's head by using the patient belt and the wide coverage of the 256-detector row CT. The thin section thickness (1 mm) facilitated observation of anatomic sites.

Discussion

This study demonstrates a number of advantages of the 256–detector row CT compared with existing systems in terms of both the speed of data acquisition and volume of data provided.

First, the 256–detector row CT was designed to allow cine imaging over a craniocaudal distance of approximately 100 mm with a thin section thickness. The thin section cine image volume data can also be used to create cine loops, CT angiography, and perfusion maps on multiple planes. This is not possible with existing MDCT.

Second, any movement of the patient during repeated MDCT imaging of the same tissue volume for extended periods of time will result in perfusion value errors. Patient motion out of the image plane leads to data loss, though limited tracking of moving tissue from section to section in multisection studies may be possible. Because of its wider imaging area, however, the 256–detector row CT solves this sample volume limitation. This characteristic is of particular importance when the speed of clinical decision making is important, such as in emergency settings in acute stroke, brain ischemia, and intracranial hemorrhage.

Moreover, conventional interventional radiology by using fluoroscopy and CT fluoroscopy to guide interventional procedures constrains radiologists to understanding the relationship between catheter and vascular positions from 2D images alone, with limited information on depth direction. The 256–detector row CT overcomes this problem by providing volumetric cine images during interventional procedures, facilitating interventions and shortening examination times. Although spatial resolution of the 256–detector row CT

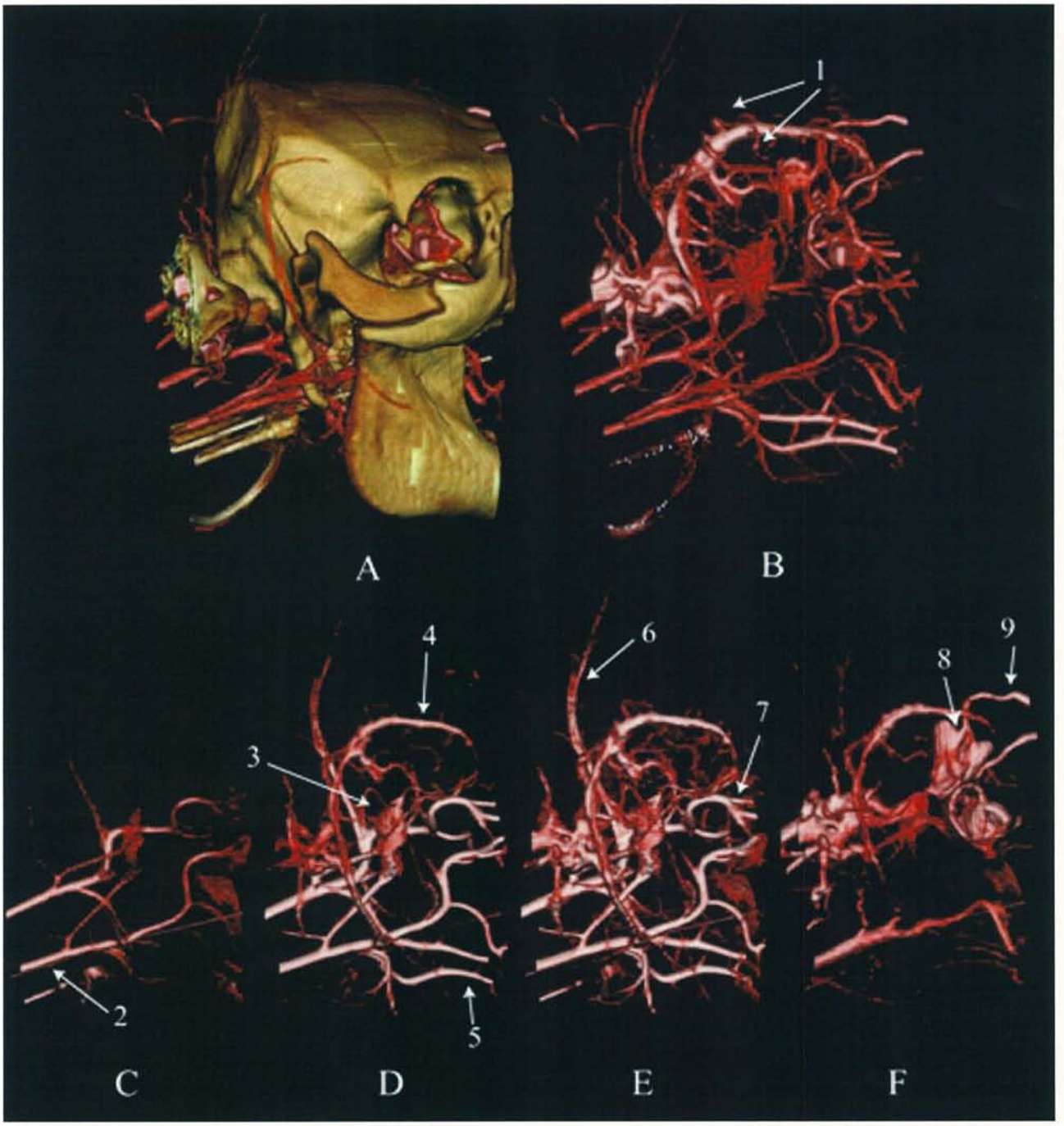

FIG 1. 3D volume rendering beginning 15 seconds after the start of injection (*A*) with and (*B*) without cranial bones. *C*, Shown 7 seconds after the start of injection. *D*, Slightly enhanced visualization of the superior sagittal sinus and inferior sagittal sinus (*arrow*) increasing gradually from 12 seconds after the start of injection. *E*, Optimum visualization of the superior sagittal sinus and inferior sagittal sinus 16 seconds after the start of injection. *F*, Decrease in enhancement of the superior sagittal sinus at 25 seconds after the start of injection. 1, dorsal cerebral veins; 2, carotid artery; 3, transverse facial artery; 4, sagittal venous sinus; 5, lingual artery; 6, caudal auricular artery; 7, infraorbital artery; 8, ophthalmic venous sinus; 9, supraorbital vein.

remains less than that of intra-arterial catheter examination, it is nevertheless a powerful noninvasive method allowing observation of the clear 3D angiogram in multiple planes continuously (Fig 1).

Further, in addition to the head, the 256–detector row CT may also be useful in perfusion studies of the chest and abdominal regions such as the liver and lung. Although voluntary or imposed breath-holding techniques have been proposed to reduce or eliminate the effects of breathing motion during both CT imaging and perfusion studies, many patients cannot tolerate holding their breath. Respiratory gated volumetric perfusion CT may therefore improve examination comfort and reduce misregistration in calculating perfusion maps. Adoption to cardiac gated volumetric perfusion CT should also be feasible.

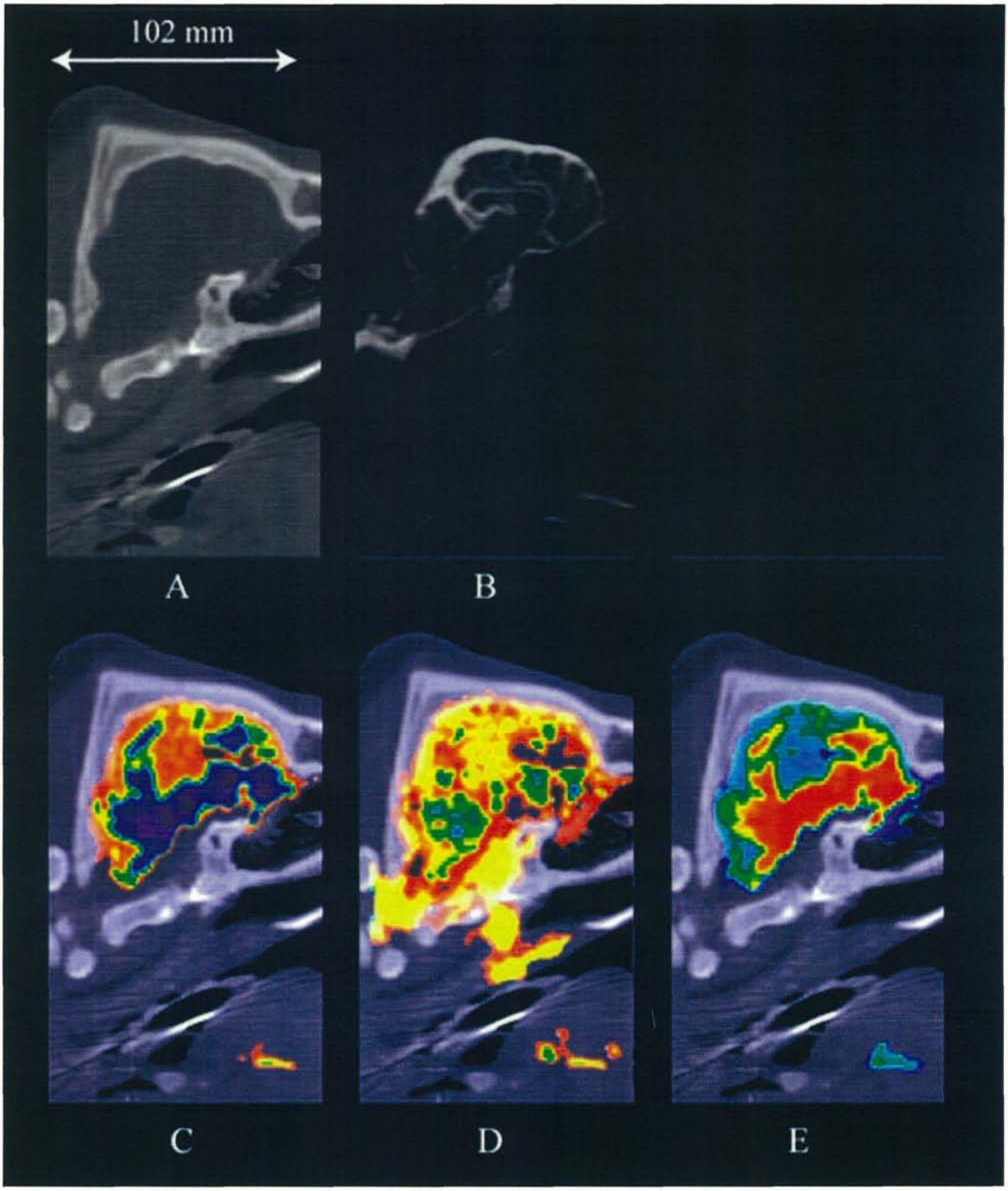

FIG 2. Results for a healthy domestic pig (pig 1). *A*, Nonenhanced sagittal image with a 6-mm section thickness. *B*, CTA in the sagittal plane at 14 seconds after the start of contrast injection. Various color ramps, selected according to user preference, were used to display the sagittal perfusion CT maps of (*C*) CBF, (*D*) CBV, and (*E*) MTT. These perfusion CT maps show enhancement of the lingual artery and vein in addition to the brain.

With regard to contrast media, CT examination requiring contrast medium is generally performed before CT perfusion scanning by helical scanning with a beam collimation of 1.0- or 1.5-mm thickness. This necessitates the administration of more than one contrast medium in the individual patient. In contrast, the 256–detector row CT acquires perfusion CT, CTA, and volumetric cine data simultaneously, thereby minimizing contrast medium dosage, as well as examination and equipment costs.

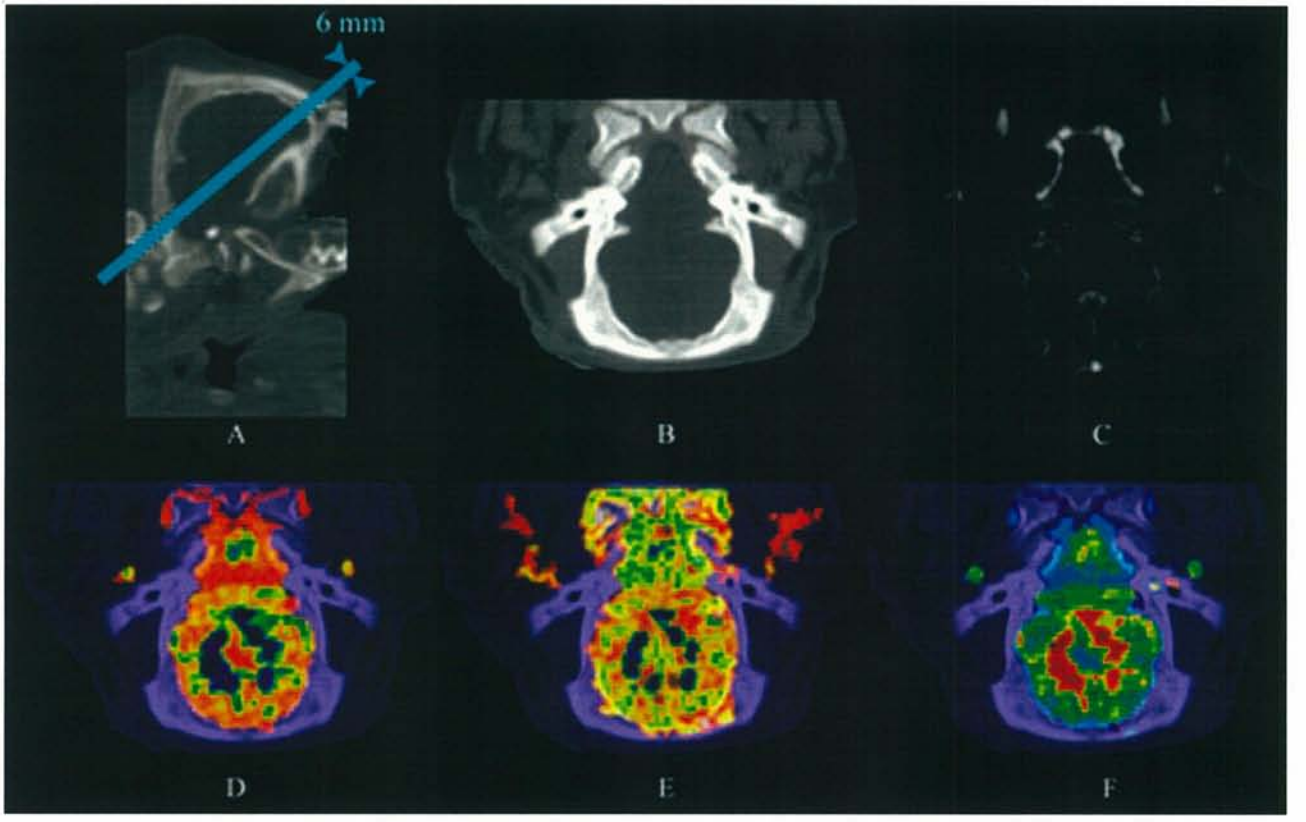

FIG 3. Results for a healthy domestic pig (pig 2). *A*, Nonenhanced sagittal image with a 6-mm section thickness. *B*, Oblique image at a 40° angle to the horizontal line shown in Fig 2*A*. *C*, CTA in an oblique plane at 14 seconds after the start of contrast injection. *D*, CBF. *E*, CBV. *F*, MTT.

With regard to image quality, previous studies have shown that the physical performance (image noise, spatial resolution, contrast detectability, etc) and clinical image quality of 256–detector row CT are closely similar to those of MDCT (4, 8). The relatively low resolution of the present perfusion images is because the pig heads studied were smaller than the human head and because the commercial deconvolution algorithm used is smoother than other algorithms in reducing image noise. Nevertheless, this perfusion algorithm is used commercially in Toshiba CT scanners and has sufficient image quality for diagnosis. Because the volumetric perfusion analysis used deconvolution analysis to simply extend the conventional 2D analysis to a 3D analysis, the accuracy of the perfusion CT map in this study was closely similar to that in MDCT.

One limitation of volumetric perfusion CT is the high patient dose required. Although consideration must be given to dose minimization (9), high doses are presently unavoidable because the beam width of the 256–detector row CT is >3 times that of 64–detector row CT and because radiation scatter increases as beam width widens. Because volumetric perfusion CT imaging results vary widely depending on differences in patient blood circulation (10), minimization of imaging time requires appropriate timing of the scan after the start of contrast injection. As a result of its tremendous reduction in examination time, volumetric perfusion CT can be used in critically ill or uncooperative patients without sedation or intubation. For commercial CT scanners, scanning conditions for cerebral perfusion are generally considered to be approximately 200 mAs and 30–50-second scan time (repeatable scans and intervals), giving total scan times of <25 seconds. In the present study, scan time was set at 50 seconds continuously, because the 256–detector row CT could not perform repeat scans and intervals. Wintermark et al (11) reported that 80-kV increased enhancement, gave better contrast between white and gray material, and lowered the patient dose by a factor of 2.8 compared with 120 kV. The effective dose was reduced by scanning with the gantry tilted to avoid the crystalline lens. When these dose-reduction methods were adopted to the 256–detector row CT, patient dose was reduced to <20 mSv. Although it is presently difficult to reduce patient dose with cone-beam CT to less than that for MDCT, we are now investigating dose reduction methods for volumetric perfusion CT.

In conclusion, the 256–detector row CT is a potentially easily available imaging technique that provides simultaneous cine imaging, CTA and perfusion CT with wide craniocaudal coverage, and in multiple planes. We are now developing a second 256–detector row CT model with a rotation time of .5 seconds and will report the use of this equipment in volumetric perfusion CT in humans.

References

1. Miles KA, Griffiths MR. **Perfusion CT: a worthwhile enhancement?** *Br J Radiol* 2003;76:220–231
2. Endo M, Mori S, Tsunoo T, et al. **Development and performance evaluation of the first model of 4DCT-scanner.** *IEEE Trans Nucl Sci* 2003;50:1667–1671
3. Mori S, Kondo C, Suzuki N, et al. **Volumetric cine imaging for cardiovascular circulation using prototype 256-detector row computed tomography scanner (4-dimensional computed tomography): a preliminary study with a porcine model.** *J Compt Assist Tomog* 2005;29:26–30
4. Mori S, Endo M, S, Tsunoo T, et al. **Physical performance evaluation of a 256-slice CT-scanner for 4-dimensional imaging.** *Med Phys* 2004;31:1348–1356
5. Saito Y, Aradate H, Igarashi K, et al. **Large area 2-dimensional detector for real-time 3-dimensional CT (4DCT).** *Proc SPIE* 2001;4320:775–782
6. Feldkamp LA, Davis LC, and Kress JW. **Practical cone-beam algorithm.** *J Opt Soc Am* 1984;A1:612–61
7. Meier P, Zierler KL. **On the theory of the indicator-dilution method for measurement of blood flow and volume.** *J Appl Physiol* 1954;6:731–744
8. Mori S, Endo M, Obata T, et al. **Clinical potentials of the prototype 256-detector row CT-scanner.** *Acad Radiol* 2005;22: 149–155
9. Hsieh J, Wei Y, Wang G. **Fractional scan algorithms for low-dose perfusion CT.** *Med Phys* 2004;31:1251–1257
10. Silverman PM, Roberts SC, Ducic I, et al. **Assessment of a technology that permits individualized scan delays on helical hepatic CT: a technique to improve efficiency in use of contrast material.** *AJR Am J Roentogenol* 1996;167:79–84
11. Wintermark M, Maeder P, Verdun FR, et al. **Using 80 kVp versus 120 kVp in perfusion CT measurement of regional cerebral blood flow.** *AJNR Am J Neuroradiol* 1991;12:201–213

INSTITUTE OF PHYSICS PUBLISHING PHYSICS IN MEDICINE AND BIOLOGY

Phys. Med. Biol. **50** (2005) N359–N370 doi:10.1088/0031-9155/50/22/N02

NOTE

Prototype heel effect compensation filter for cone-beam CT

Shinichiro Mori[1], Masahiro Endo[1], Kanae Nishizawa[1], Mari Ohno[1], Hiroaki Miyazaki[2], Kazuhiko Tsujita[2] and Yasuo Saito[2]

[1] Department of Medical Physics, National Institute of Radiological Sciences, Chiba 263-8555, Japan
[2] Toshiba Medical Systems, Otawara 324-8550, Japan

Received 7 June 2005, in final form 6 September 2005
Published 2 November 2005
Online at stacks.iop.org/PMB/50/N359

Abstract

The prototype cone-beam CT (CBCT) has a larger beam width than the conventional multi-detector row CT (MDCT). This causes a non-uniform angular distribution of the x-ray beam intensity known as the heel effect. Scan conditions for CBCT tube current are adjusted on the anode side to obtain an acceptable clinical image quality. However, as the dose is greater on the cathode side than on the anode side, the signal-to-noise ratio on the cathode side is excessively high, resulting in an unnecessary dose amount. To compensate for the heel effect, we developed a heel effect compensation (HEC) filter. The HEC filter rendered the dose distribution uniform and reduced the dose by an average of 25% for free air and by 20% for CTDI phantoms compared to doses with the conventional filter. In addition, its effect in rendering the effective energy uniform resulted in an improvement in image quality. This new HEC filter may be useful in cone-beam CT studies.

(Some figures in this article are in colour only in the electronic version)

1. Introduction

Commensurate with higher quality imaging and resulting substantial diagnostic benefits, patient doses in clinical applications of CT have increased steadily over recent decades (IEC 1994). Among new developments in the technology of CT, cone beam CT (CBCT) has attracted particular attention in both the diagnostic and therapeutic fields (Saint *et al* 1994, Endo *et al* 1998, Ning *et al* 2005, Sonke *et al* 2005). Patient dosing with CBCT is of considerable concern, however, because the maximum beam width is greater than that of conventional multi-detector row CTs (MDCT), the latest of which has 64 segments with a segment size of 0.5–0.625 mm at the centre of rotation.

We have developed a prototype 256-detector row CT that has 256 segments with a segment size of 0.5 mm at the centre of rotation (Endo *et al* 2003, Mori *et al* 2004). The wide cone

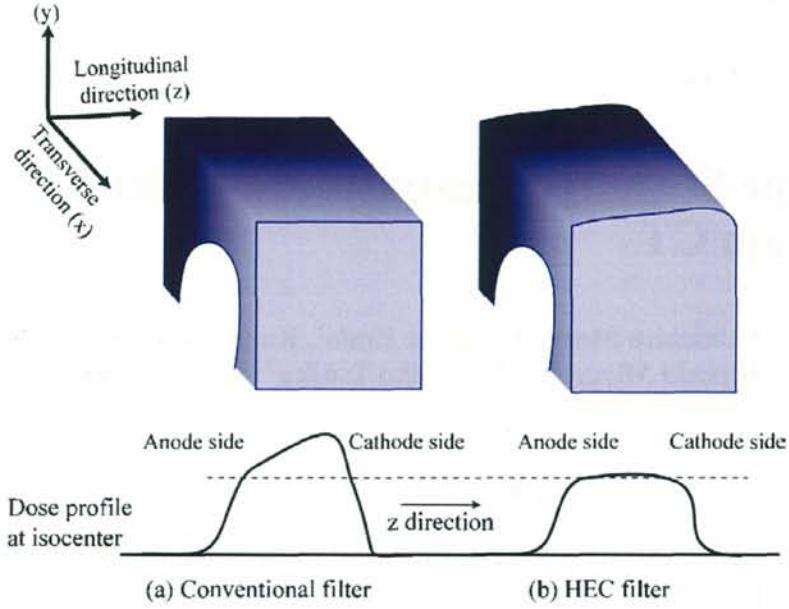

Figure 1. Schematic drawing of the conventional filter (a) and heel effect compensation (HEC) filter (b).

angle of this CT causes a non-uniform angular distribution of the x-ray beam intensity known as the heel effect, which is unavoidable when covering a wide longitudinal direction. Scan conditions of the tube current are adjusted on the anode side to obtain acceptable clinical image quality. The image on the cathode side therefore provides excessive quality, which necessarily produces overdosing (i.e. unnecessary dose). Given fundamental concerns about radiation protection, it is important to minimize unnecessary dosing. To this end, we have developed a heel effect compensation (HEC) filter. Here, we report our physical evaluation of this filter.

2. Materials and methods

2.1. Prototype 256-detector row CT-scanner

The prototype 256-detector row CT (Endo *et al* 2003, Mori *et al* 2004) uses a wide-area cylindrical 2D detector, designed on the basis of present CT technology and mounted on the gantry frame of a 16-detector row CT (Aquilion 16, Toshiba Medical Systems, Otawara, Japan) (Saito *et al* 2001). The number of detectors is 912 (transverse) $\times$ 256 (longitudinal), each of approximately 0.58 mm $\times$ 0.50 mm at the centre of rotation. The rotation time of the gantry is 1.0 s. As with the MDCT, each detector element consists of a scintillator and a photodiode, the scintillator of Gd_2O_2S ceramic and the photodiode of single-crystal silicon. The nominal beam width can be set continuously from 10 to 128 mm at the rotation centre by moving the collimator jaws. Longitudinal coverage of the 256-detector row CT is approximately 100 mm with one rotation (Mori *et al* 2005). The data sampling rate is 900 views/s, and the dynamic range of the A–D converter is 16 bits. A Feldkamp–Davis–Kress (FDK) (Feldkamp *et al* 1984) algorithm is used for reconstruction. It takes 1 s to reconstruct volume data of 512 $\times$ 512 $\times$ 256 voxels using a high-speed image processor with a field programmable gate array (FPGA)-based architecture. Definitions of the coordinate system are shown in figure 1; the

x–y coordinate plane is parallel to the transverse axis, and the z-coordinate axis is parallel to the longitudinal axis.

2.2. *Heel effect compensation (HEC) filter*

The filter used for the 256-detector row CT is a conventional filter fabricated by extending the filter of a MDCT (Aquilion 16, Toshiba Medical Systems) in the longitudinal direction. The conventional filter is shaped to compensate for the variable path length of the patient in the transverse direction. The HEC filter has a thicker aluminium layer on the cathode side than on the anode side (figure 1). Other specifications are the same as for conventional filters. This design allows the HEC filter to compensate for x-ray intensity in the longitudinal as well as in the transverse plane.

2.3. *Dosimeter probe*

A pencil-shaped ionization chamber (CT-30, Oyogiken, Japan) of active length 300 mm was connected to a dosimeter (AE-132, Oyogiken, Japan) to measure the dose profile integral (DPI). This chamber is an extended form of the conventional pencil-shaped ionization chamber (CT-10, Oyogiken, Japan) with an active length of 100 mm. The dosimeter was calibrated at the AIST (National Institute of Advanced Industrial Science and Technology, Japan) for the appropriate radiation qualities. Partial sensitivity of the long chamber was assessed, and variations among the centre part (100–200 mm) and the two sides (0–100 or 200–300 mm), each with an active length of 100 mm, were shown to be less than 0.4% for the effective energy level of 40–60 keV.

An ionization chamber of 0.6 ml volume (C-110, Oyogiken, Japan) was connected to the dosimeter (AE-132, Oyogiken, Japan) and used to measure the effective energy at each point.

Two-pin silicon photodiodes (S2506-04, Hamamatsu, Japan) were used as the x-ray sensor for dose profile measurements (Aoyama *et al* 2002). Each photodiode had a relatively large sensitive area of 2.8 × 2.8 mm^2 and a 2.7 mm thickness. Since the incident side had a larger detection efficiency than the exit side, two photodiodes were glued together back-to-back with epoxy cement and used as a single sensor. This fabricated pin photodiode sensor was connected to a dosimeter (Dual Counter 994, ORTEC, Illinois) and calibrated by mutual comparison with an AIST reference ionization chamber (0.6 ml volume). The minimum detectable dose with 25% uncertainty was estimated to be 0.02 mGy (Aoyama *et al* 2002).

2.4. *Evaluation methods*

The following items were measured with stationary phantoms designed for the 256-detector row scanner using the same method as that for conventional CT: (i) effective energy, (ii) dose profile and DPI, (iii) image noise and uniformity and (iv) low-contrast detectability. Evaluation results with the HEC filter were compared with those of the conventional filter. Scan conditions were 120 kV, 200 mA, 1.0 s acquisition time, 1.0 s gantry rotation time and 256 × 0.5 mm slice collimation. Scan conditions for almost all items were the same for each filter, and were chosen to approximate clinical scan conditions. Reconstruction parameters were a voxel size of 0.47 × 0.47 × 0.50 mm^3 with a 0.50 mm reconstruction increment along the z-axis and a matrix size of 512 × 512 × 256. Convolution kernel was the standard body kernel, which is the default installation in MDCT (Aquilion, Toshiba Medical Systems).

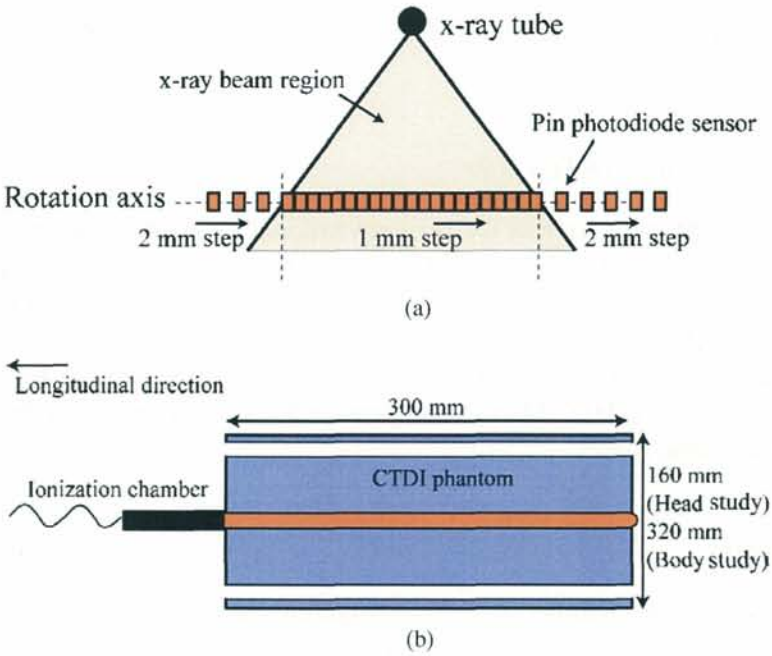

Figure 2. Schematic drawing of measurement methods. (a) Dose profile measurement. Dose profiles were measured with a pin silicon photodiode sensor at 1 mm intervals within the nominal beam width and a 2 mm or greater interval above it at the isocentre in free air. (b) DPI measurement. The ionization chamber was inserted into either the central or one of the peripheral cavities of the phantom.

2.4.1. Effective energy. The effective energy was calculated from the attenuation curve of x-ray intensity. The x-ray tube was fixed at the 6 o'clock position and x-ray irradiation was initiated. The ionization chamber, with a 0.6 ml volume, was positioned at the horizontal plane that passed through the rotation axis centre plane, and the x-ray intensity was measured by setting aluminium attenuators of various thicknesses between the x-ray tube and the ionization chamber (Edyvean *et al* 1997). The effective energy was derived from an attenuation length that gave half of the x-ray intensity produced without aluminium attenuators (half-value layer (HVL)), calculated from the attenuation curve of the beam intensity (Hubbell and Selzer 1996). Effective energy was measured at 0, 50, 100 and 150 mm along the transverse direction and at −40, −20, 0, 20 and 40 mm along the longitudinal direction.

2.4.2. Dose profile and dose profile integral (DPI). A two-dimensional distribution of x-ray beam intensity was measured using film (Kodak X-Omat V non-screen therapy verification film) placed at the centre plane and exposed without gantry rotation. The x-ray tube was fixed at the 12 o'clock position, and the nominal beam width was 128 mm.

Dose profiles were measured with the pin silicon photodiode sensor at 1 mm intervals within the 128 mm nominal beam width and a 2 mm or greater interval above the nominal beam width at the isocentre in free air (figure 2(a)). The pin silicon photodiode sensor was placed at the isocentre facing the anterior and posterior positions, and moved by the mechanical driving system while the phantom remained stationary. A CT scan was done at each measurement point. The DPI was measured with the pencil-shaped ionization chamber in free air and extended CTDI phantoms (Mori *et al* 2005). The standard FDA-recommended CTDI phantoms are at least 140 mm long. These phantoms are made of PMMA (polymethylmethacrylate) cylinders with diameters of 160 mm for head studies and 320 mm for body studies. Holes of

10 mm diameter are located parallel to the central axis of the cylinders, and the centres of the holes are located at the cylinder centre and 10 mm below the cylinder surface at 90° intervals. For cone-beam CT dose measurement, the phantom length should be longer to account for the wider beam width (Mori *et al* 2005). We, therefore, extended the FDA-recommended CTDI phantom to a length of 300 mm (figure 2(b)) on the basis of our group's previous report that the phantom length and integration range for dosimetry needed to be at least 300 mm to represent more than 90% of the line integral dose with a beam width between 20 and 138 mm (Mori *et al* 2005). Since the integration range in the longitudinal direction was 300 mm ($z = \pm 150$ mm), the DPI measurement was made with the ionization chamber while the phantom remained stationary. The DPI (expressed as R cm) was obtained with the ionization chamber dosimeter (figure 2(b)).

At measurement, the phantom was placed on the patient table and its centre was aligned at the isocentre. The ionization chamber was inserted into either the central or one of the peripheral cavities of the phantom (other cavities were filled with PMMA rods). All scans for DPI measurements were made in the axial scan mode. Nominal beam widths were 10, 32, 64, 96 and 128 mm.

We defined DPI for the summation range ±150 mm as follows:

$$\mathrm{DPI}(b) = \mathrm{IC}(b)\ (\mathrm{mGy\ mm}), \tag{1}$$

where IC(b) (mGy mm) was the output of the ionization chamber at the nominal beam width b.

The average of DPI for x, y coordinates is given by

$$\mathrm{DPI_{ave}} = \tfrac{1}{3}\mathrm{DPI_{centre}} + \tfrac{2}{3}\mathrm{DPI_{periphery}}\ (\mathrm{mGy\ mm}), \tag{2}$$

if we assume a linear decrease (or increase) in DPI in the radial direction (Leitz *et al* 1995), where $\mathrm{DPI_{centre}}$ means DPI at the centre and $\mathrm{DPI_{periphery}}$ means average DPI on the peripheries. Note that the volume integral dose in the phantom is given by the product of $\mathrm{DPI_{ave}}$ and the phantom cross section in the transverse plane (x–y plane).

2.4.3. Image noise and uniformity. Image noise was measured with a water-filled acrylic cylinder of 200 mm diameter and 250 mm height. Standard deviations (SDs) of CT-number were calculated in five regions of interest (ROIs) of 25 mm diameter aligned every 38 mm along the diameter of the phantom in the transverse section (figure 2). Calculations were made from $z = -40$ to 40 mm at 10 mm intervals. The same phantom and ROIs were used for uniformity measurement as for noise measurement, and averages of CT-number were calculated in these ROIs. The slice thickness was 1.0 mm (average of two 0.5 mm slices).

2.4.4. Low-contrast detectability. Low-contrast detectability was assessed with commercially available CT phantoms for CT performance evaluation (Catphan 500 with module CTP515). Figure 3 shows schematic drawings of the low-contrast phantom. This phantom included three supra-slice and sub-slice sets of cylinders (figure 4(a)). The sub-slice targets had z-axis lengths of 3, 5 and 7 mm and diameters of 3, 5, 7 and 9 mm (figure 4(b)). These supra-slice sets consisted of cylinders of 2, 3, 4, 5, 6, 7, 8, 9 and 15 mm diameter and 40 mm length, and contrasts of three sets of cylinders from the background were 0.3%, 0.5% and 1.0%. A 1.0% contrast meant that the mean CT-number of the object differed from its background by 10 HU. To facilitate understanding of the differences of these filters, the slice thickness was selected as a relatively thick 20.0 mm for both filters, because the dynamic range of the prototype 256-detector row CT was 16 bits, the LCD of the 256-detector row CT may be significantly lower than MDCT using conventional detector. Detectability was given by the

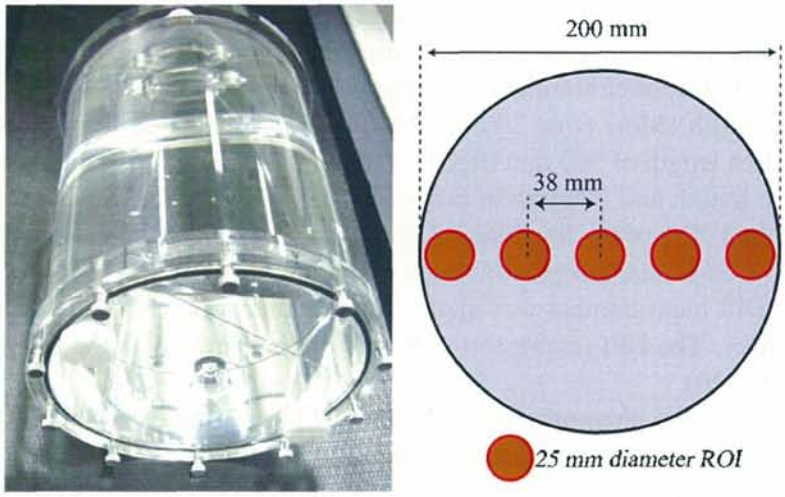

Figure 3. Water phantom used for the evaluation of image noise and uniformity. Five ROIs of 25 mm diameter were aligned every 38 mm along the diameter of the phantom.

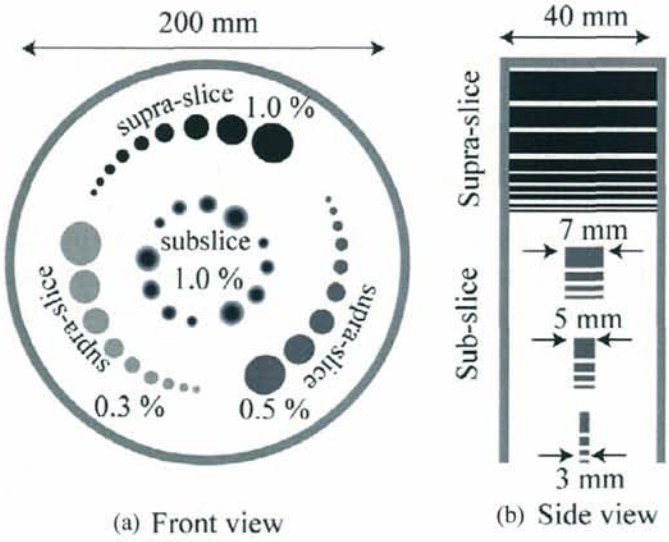

Figure 4. Schematic drawing of the phantom for low-contrast detectability. The contrasts of three sets of cylinders, excluding sub-slice sets from the background, were 0.3%, 0.5% and 1.0%. The phantom included sets of cylinders of 2, 3, 4, 5, 6, 7, 8, 9 and 15 mm diameter. (a) Front view. (b) Side view.

average of twenty 1.0 mm slices. Two medical physicists (ME and SM) evaluated the results by observing images with supra-slice rather than sub-slice targets to avoid volume-averaging errors at $z = -40$, 0 and 40 mm.

3. Results

3.1. Effective energy

2D distributions of the effective energy for the conventional and HEC filters are shown in figure 5, in which the effective energy is symmetrically drawn with respect to the x-axis. The effective energy of the conventional filter showed a non-uniform distribution in

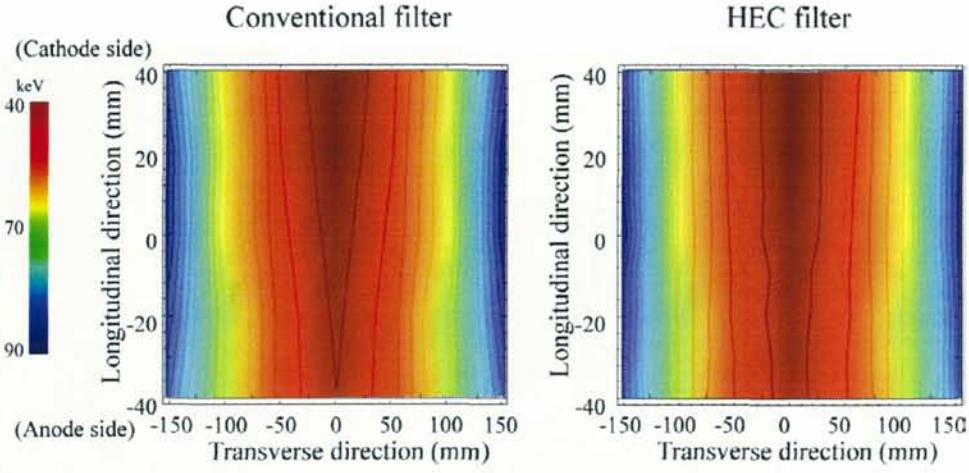

Figure 5. 2D images of effective energy with the conventional and HEC filters.

Table 1. Effective energy (keV) of the longitudinal average at transverse positions of $x = 0$, 50, 100 and 150 mm from the isocentre.

		Transverse position (mm)			
Filter		$x = 0$	$x = 50$	$x = 100$	$x = 150$
HEC	Small	48.8	52.2	58.3	93.9
	Large	50.2	56.5	61.4	74.9
Conventional	Small	42.9	48.4	55.5	77.5
	Large	47.4	51.5	59.8	70.6

the longitudinal direction. In contrast, that of the HEC filter showed an almost uniform distribution, demonstrating the advantage of this filter. Longitudinal average effective energy is summarized in table 1. Effective energy for the HEC filter is on average 6 keV higher than that for the conventional filter.

3.2. Dose profile and dose profile integral (DPI)

Film images of dose distribution at the centre in free air are shown in figure 6, and dose profiles measured with the pin silicon photodiode at the isocentre in free air are plotted in figure 7. The dose profile with the conventional filter shows the heel effect, whereas that with the HEC filter shows an approximately uniform distribution of x-ray beam intensity.

DPI_{ave} in the CTDI phantoms is shown in figure 8. DPI_{ave} increases with increases in the nominal beam width. DPI_{ave} values for the HEC filter are an average 20% (=612 (mGy mm/100 mAs)/764 (mGy mm/100 mAs) × 100%) for the phantoms and 25% (=1359 (mGy mm/100 mAs) mm/1804 (mGy mm/100 mAs) × 100%) for free air less than those for the conventional filter, with these values calculated as:

$$\sum_{b\in\{10,32,64,96,128\}} \frac{DPI_{ave}^{HEC}(b)}{DPI_{ave}^{Conv}(b)} \times 100\ (\%), \tag{3}$$

where $DPI_{ave}^{HEC}(b)$ and $DPI_{ave}^{Conv}(b)$ mean DPI_{ave} (mGy mm/100 mAs) with HEC and conventional filters, respectively, for the nominal beam width b (mm).

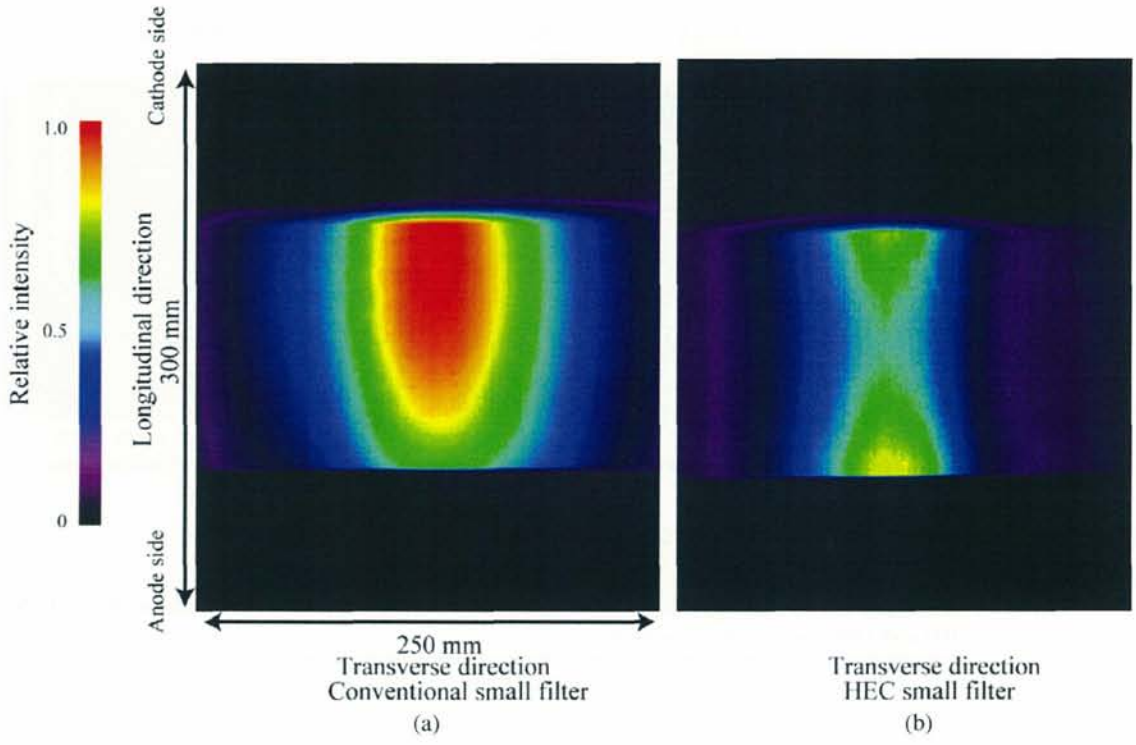

Figure 6. Film image of the dose distribution at the centre in free air with a fixed tube position. The nominal beam width was 128 mm. (a) Conventional filter. (b) HEC filter.

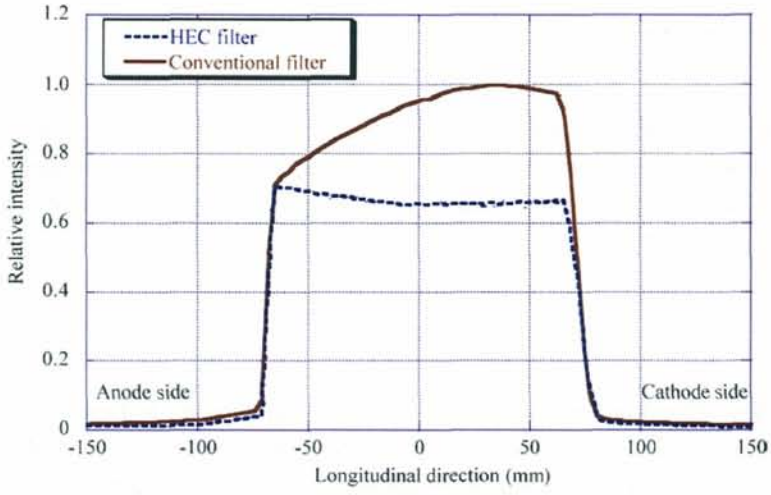

Figure 7. Longitudinal dose profiles using a pin photodiode sensor with a 128 mm nominal beam width in free air.

3.3. Image noise and uniformity

The magnitude of image noise was obtained from the standard deviations of CT-number in the five ROIs in a transverse section (see figure 3). Figure 9(a) shows the relationship between the average standard deviation of the five ROIs and the position along the longitudinal direction for both filters. As the average image noise for the conventional filter was 10.6 HU at $z = 40$ mm (cathode side), 10.8 HU at $z = 0$ mm (midplane) and 11.1 HU at $z = -40$ mm (anode side), the magnitude of image noise slightly increased from the cathode to the anode

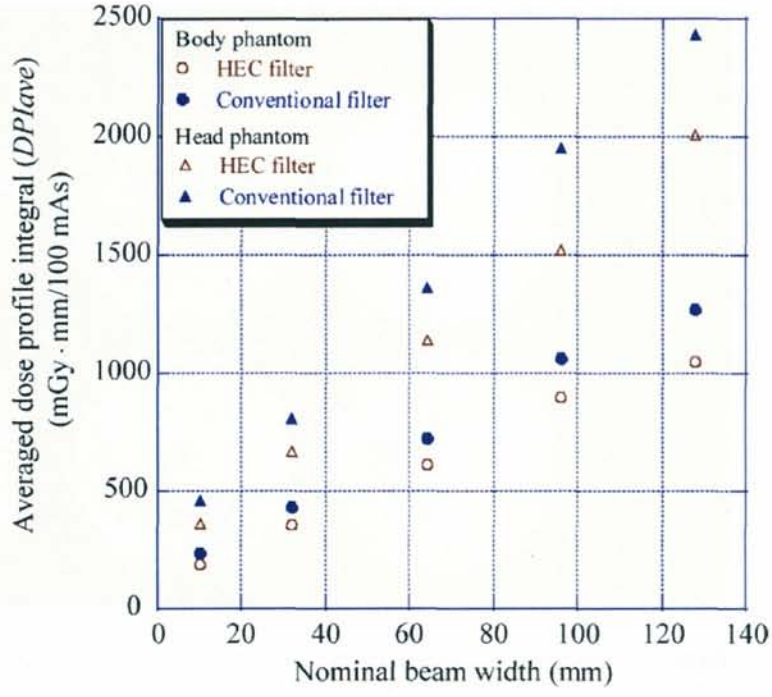

Figure 8. DPI measured with the pencil-shaped ionization chamber for 10–128 mm beam widths.

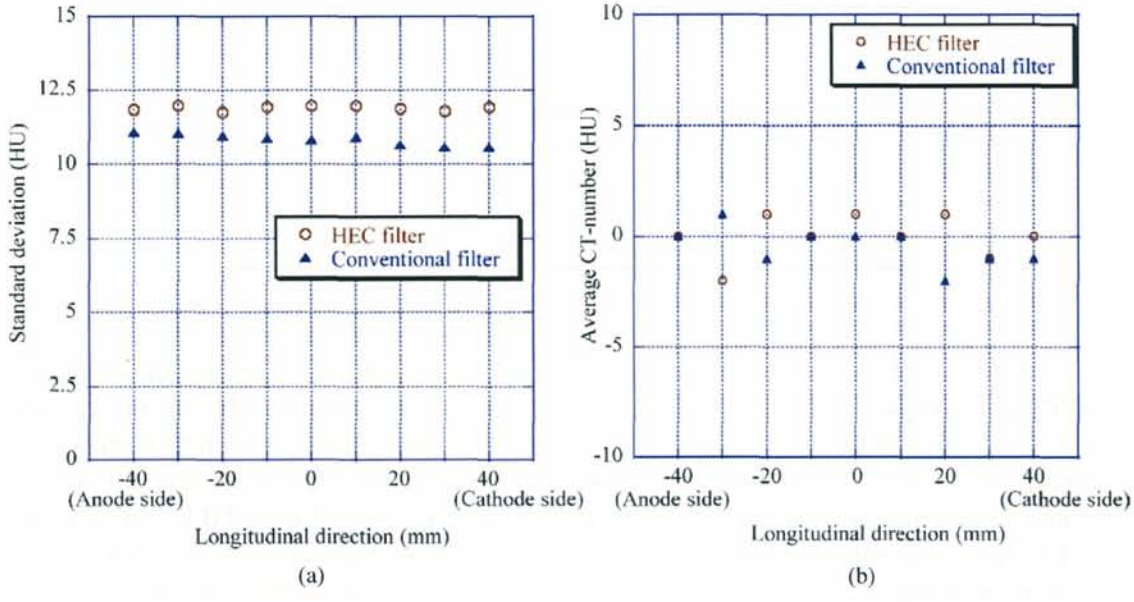

Figure 9. (a) Average standard deviation of five ROIs in the longitudinal direction. (b) Average CT-number of five ROIs along the longitudinal direction.

side. Average standard deviations for the HEC filter were 11.6 HU at $z = -40$ mm (cathode side), 12.1 HU at $z = 0$ mm (midplane) and 11.9 HU at $z = 40$ mm (anode side), and the magnitude of image noise was approximately uniform. Image noise for the HEC filter was 9.7% (= (11.8 HU − 10.6 HU)/11.8 HU × 100% at $z = 40$ mm) higher than that for the conventional filter in the longitudinal average, but approximately 4.0% (= (11.6 HU − 11.1 HU)/11.6 HU × 100% at $z = -40$ mm) higher than that for the conventional filter at the anode side.

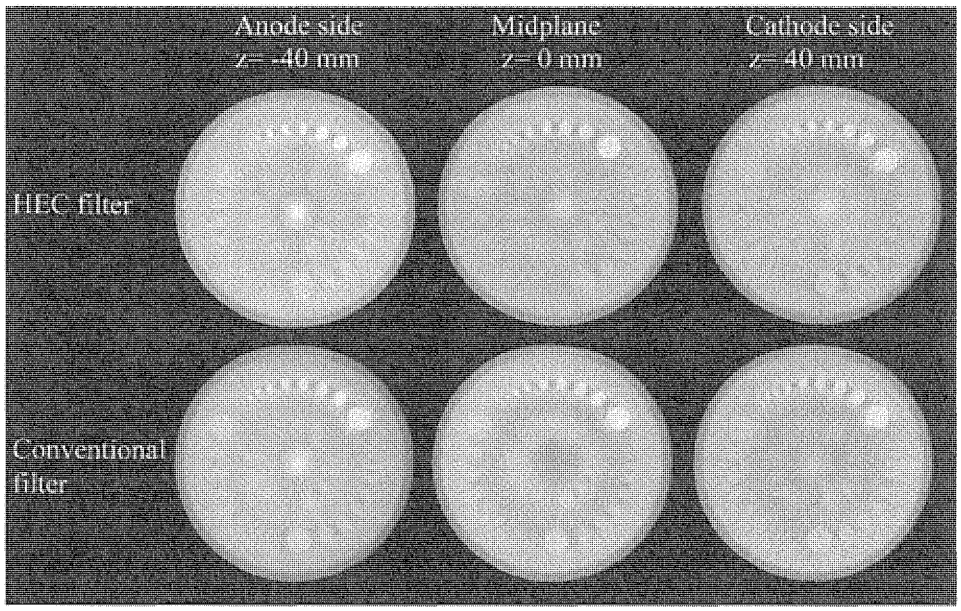

Figure 10. Low-contrast phantom images in the transverse section for the conventional and HEC filters at $z = -40$ mm, 0 mm and 40 mm.

Table 2. Minimum diameter of detected cylinders (mm).

		Contrast (%)		
Wedge	Position	1.0%	0.5%	0.3%
HEC	Cathode side ($z = 40$ mm)	2	4–5	7
	Midplace ($z = 0$ mm)	2	4–5	7
	Anode side ($z = -40$ mm)	2–3	4–5	7
Conventional	Cathode side ($z = 40$ mm)	2	3–4	6
	Midplace ($z = 0$ mm)	2	3–4	6
	Anode side ($z = -40$ mm)	2	4–5	7

With regard to uniformity measurement, we calculated the averages of CT-number in ROIs in the transverse plane (see figure 3). Figure 9(b) shows the relationship between the average for five ROIs and the position along the longitudinal direction for both filters. Standard deviations of the CT-number averages were 1.0 HU for the HEC filter and 0.9 HU for the conventional filter, owing to the fact that the larger image noise for the HEC filter affected the CT-number uniformity. Further, CT-number of the HEC filter showed an almost symmetric pattern, whereas the conventional filter at the anode side was slightly higher than that at the cathode side and showed an asymmetric pattern, because the CT-number shift was due to the FDK reconstruction algorithm rather than the CT-number shift caused by heel effect.

From these uniformity measurements, we note that the HEC filter has nearly the same performance as the conventional filter, and is independent of the longitudinal direction.

3.4. Low-contrast detectability

Figure 10 shows images of the low-contrast phantom made using the conventional and HEC filters. Table 2 lists the minimum diameters of detected cylinders, and shows that the performance of the HEC filter was slightly worse than that of the conventional filter when

the dose was adjusted to the anode side. Because use of the HEC filter decreased dose at the cathode side to that at the anode side, decreasing the dose at the cathode side and midplane increased image noise and prevented the detection of the low-contrast phantom.

Although the performance of the conventional filter at the anode side ($z = -40$ mm) was worse than that at the cathode side ($z = 40$ mm), performance of the HEC filter at all positions was closely similar. Circular band-like artefacts were more strongly suppressed with the HEC filter than with the conventional filter at $z = 0$ mm and 40 mm.

4. Discussion

We have developed an HEC filter to reduce unnecessary dosing in CBCT. Here, we investigated the physical performance of this filter, and identified two advantages over conventional filters in CBCT.

First, because it compensates for the heel effect in the longitudinal direction, the HEC filter reduced doses by an average of 20% for CTDI phantoms and by 25% for free air compared to the conventional filter. From these results, we conclude that the HEC filter reduced excessive dosing.

The second advantage of the HEC filter is that it provided a uniform effective energy distribution along the longitudinal direction. As a result of this, the circular band-like artefacts seen in figure 10 due to inadequate artefact correction processing by the conventional filter were significantly improved by the HEC filter via its reduction of the beam hardening effect. The effective energy for the conventional filter at the cathode side was lower than that at the anode side, and the magnitude of artefacts decreased in this order as well. The x-ray path with lower effective energy tended to induce more beam hardening than that with higher effective energy.

In figure 10, although the results for the HEC filter improved band-like artefacts, the results for the HEC filter were slightly worse than those for the conventional filter because adoption of the HEC filter resulted in a decrease in dosage at the cathode side. This decrease in dose at the cathode side and midplane increased image noise and prevented us from detecting the low-contrast phantom. Image noise was increased by an average of 10%. In particular, the difference in image noise between the filters at the cathode side was approximately 4%, and image noise for the HEC filter was uniformly distributed. Diagnostic accuracy is highly dependent on the maintenance of uniform image quality in the longitudinal direction via decreases in the beam hardening effect.

A current limitation of this prototype HEC filter is that, owing to the difficulty in designing it to provide x-ray attenuation in both the transverse and longitudinal directions, mechanical vibration due to the fast gantry rotation and x-ray focal spot movement due to thermal and mechanical flexing mean that x-ray intensity distribution in the longitudinal direction is not completely uniform. Further investigation is required to overcome these problems.

With regard to the reconstruction zone in axial scanning, the longitudinal coverage of the 256-detector row CT (=approximately 100 mm) was less than the total beam width (=128 mm) with one rotation, because its limited coverage is attributable to the geometry of the imaging volume of cone-beam CT when the original Feldkamp algorithm was used. Recently, axial cone-beam reconstruction algorithms that can reconstruct the image proximal to the longitudinal boundaries of the detector were reported (Grass *et al* 2001, Tang *et al* 2005); the longitudinal coverage of the 64-detector row CT (64 × 0.625 mm) was extended to 40 mm as an example. Therefore, the reconstruction coverage of the 256-detector row CT can be extended to 128 mm with one rotation by these reconstruction algorithms.

In conclusion, angular distributions of dose and effective energy are unfortunately inevitable in CBCT which covers a wide longitudinal direction. The new HEC filter tested here reduced unnecessary dosing and provided good image quality for a wide longitudinal direction. This HEC filter may be useful in CBCT studies.

References

Aoyama T, Koyama S and Kawamura C 2002 An in-phantom dosimetry system using pin silicon photodiode radiation sensors for measuring organ doses in x-ray CT and other diagnostic radiology *Med. Phys.* **29** 1504–10

Edyvean S, Lewis M A and Britten A J 1997 CT scanner dose survey: measurement protocol Ver. 5 *ImPACT Report*

Endo M *et al* 2003 Development and performance evaluation of the first model of cone-beam CT-scanner *IEEE Trans. Nucl. Sci.* **50** 1667–71

Endo M, Yoshida K, Kamagata N, Satoh K, Okazaki T, Hattori Y, Kobayashi S, Jimbo M, Kusakabe M and Tateno Y 1998 Development of a 3D CT-scanner using a cone beam and video-fluoroscopic system *Radiat. Med.* **16** 7–12

Feldkamp L A, Davis L C and Kress J W 1984 Practical cone-beam algorithm *J. Opt. Soc. Am.* A **1** 612–9

Grass M, Khler T and Proksa R 2001 Angular weighted hybrid cone-beam CT reconstruction for circular trajectories *Phys. Med. Biol.* **46** 1595–610

Hubbell J H and Selzer S M 1996 Tables of x-ray mass attenuation coefficients and mass energy-absorption coefficients *National Institute of Standard and Technology (NIST) Physical Reference Data*

International Electrotechnical Commission (IEC) 1994 Evaluation and routine testing in medical imaging departments constancy tests—x-ray equipment for computed tomography *Publication IEC 1994* 1223-2-6

Leitz W, Axelsson B and Szendro G 1995 Computed tomography dose assessment—a practical approach *Radiat. Prot. Dosim.* **57** 377–80

Mori S *et al* 2004 Physical performance evaluation of a 256-slice CT-scanner for 4-dimensional imaging *Med. Phys.* **31** 1348–56

Mori S, Endo M, Nishizawa K, Tsunoo T, Aoyama T, Fujiwara H and Kenya M 2005 Enlarged longitudinal dose profiles in cone-beam CT and the need for modified dosimetry *Med. Phys.* **32** 1061–9

Ning R, Tang X and Conover D 2005 X-ray scatter correction algorithm for cone beam CT imaging *Med. Phys.* **31** 1195–202

Saito Y, Aradate H, Igarashi K and Ide H 2001 Large area 2-dimensional detector for real-time 3-dimensional CT (cone-beam CT) *Proc. SPIE* **4320** 775–82

Saint F D, Trousset Y, Picard C, Ponchut C, Romeas R and Rougee A 1994 *In vivo* evaluation of a new system for 3D computerized angiography *Phys. Med. Biol.* **39** 583–95

Sonke J, Zijp L, Remeijer P and Herk M 2005 Respiratory correlated cone beam CT *Med. Phys.* **32** 1176–86

Tang X, Hsieh J, Hagiwara A, Nilsen R A, Thibault J B and Drapkin E 2005 A three-dimensional weighted cone beam filtered backprojection (CB-FBP) algorithm for image reconstruction in volumetric CT under a circular source trajectory *Phys. Med. Biol.* **50** 3889–905

US FDA Code of Federal Regulations 1984 Diagnostic x-ray systems and their major components *21CFR* 1020.23 (Govt. Printing Office)

The British Journal of Radiology, 78 (2005), 1–6 © 2005 The British Institute of Radiology
DOI: 10.1259/bjr/39775216

Comparison of patient doses in 256-slice CT and 16-slice CT scanners

[1,2]S MORI, [1]M ENDO, [1]K NISHIZAWA, [2]K MURASE, [2]H FUJIWARA and [3]S TANADA

[1]*Department of Medical Physics, National Institute of Radiological Sciences, Chiba 263-8555, Japan,* [2]*School of Allied Health Sciences, Faculty of Medicine, Osaka University, Osaka 565-0871, Japan and* [3]*Department of Medical Imaging, National Institute of Radiological Sciences, Chiba 263-8555, Japan*

Abstract. The 256-slice CT-scanner has been developed at National Institute of Radiological Sciences. Nominal beam width was 128 mm in the longitudinal direction. When scanning continuously at the same position to obtain four-dimensional (4D) images, the effective dose is increased in proportion to the scan time. Our purpose in this work was to measure the dose for the 256-slice CT, to compare it with that of the 16-slice CT-scanner, and to make a preliminary assessment of dose for dynamic 3D imaging (volumetric cine imaging). Our group reported previously that the phantom length and integration range for dosimetry needed to be at least 300 mm to represent more than 90% of the line integral dose with the beam width between 20 mm and 138 mm. In order to obtain good estimates of the dose, we measured the line-integral dose over a 300 mm range in PMMA (polymethylmethacrylate) phantoms of 160 mm or 320 mm diameter and 300 mm length. Doses for both CT systems were compared for a clinical protocol. The results showed that the 256-slice CT generates a smaller dose than the 16-slice CT in all examinations. For volumetric cine imaging, we found an acceptable scan time would be 6 s to 11 s, depending on examinations, if dose must be limited to the same values as routine examinations with a conventional multidetector CT. Finally, we discussed the studies necessary to make full use of volumetric cine imaging.

In 2001 the introduction of a 16-slice CT-scanner raised some new topics in CT technology development. 16-slice CT allows applications of three-dimensional (3D) images in clinical fields such as diagnosis, surgical simulation, planning of radiation therapy and monitoring of interventional therapy. However, it is still difficult to take dynamic 3D images of moving organs such as the heart or lung to enlarge the application fields. In order to take these images, we have developed a prototype 256-slice CT at NIRS (National Institute of Radiological Sciences) which employs continuous rotations of a cone-beam [1].

Clinical applications of CT techniques have continued to increase the dose to patients during recent decades, as CT examinations have come to provide higher quality X-ray imaging with substantial benefits in clinical diagnosis [2]. Notwithstanding the potential benefits to the healthcare of patients using CT, the fundamental concern in radiological protection is the optimization of radiation exposure.

The maximum nominal beam width of the 256-slice CT is 128 mm and is four times larger than the third-generation 16-slice CT-scanner (Toshiba Aquilion, Toshiba Medical Systems, Japan). A wider beam width is more efficient for imaging in a wider coverage. However, doses to patients with 256-slice CT are of considerable concern if it is to be used for obtaining dynamic 3D images (volumetric cine images). When scanning continuously at the same position, the effective dose is increased in proportion to the scan time and a wider coverage brings larger doses to patients. Therefore, it is very important to assess the dose of the 256-slice CT before volumetric cine imaging for patients.

This work was carried out to compare doses, including scattered radiation, of the 256-slice CT and 16-slice CT and to make a preliminary assessment of dose for volumetric cine imaging.

Received 6 August 2004 and in revised form 8 April 2005, accepted 13 June 2005.

Address correspondence to: Shinichiro Mori, 4-9-1 Anagawa, Inage-ku, Chiba-shi, Chiba, 263-8555, Japan.

Materials and methods

Acquisition systems of 256-slice CT and 16-slice CT scanners

The prototype 256-slice CT-scanner uses a wide-area 2D detector designed on the basis of the present CT technology and is mounted on the gantry frame of a state-of-the-art CT-scanner (Figure 1) [3]. The number of elements is 912 channels × 256 segments; element size is approximately 1 mm × 1 mm, corresponding to a 0.5 mm (transverse) × 0.5 mm (longitudinal) beam width at the centre of rotation. Gantry rotation time is 1.0 s. Data sampling rate is 900 views/s, and the dynamic range of the A/D converter is 16 bits. As shown in Appendix 1, the reconstructed regions are cylinders of 240 mm diameter and 102.4 mm length for the head scan and 320 mm diameter and 93.9 mm length for the body scan. The detector element consists of a scintillator and photodiode, which are the same as for the scintillator of multidetector CT (MDCT) (Toshiba Aquilion). Three wedge designs (large, small, and flat) on the 256-slice CT are intended to extend the conventional wedge designs of the third-generation 16-slice CT-scanner (Toshiba Aquilion) in the longitudinal direction. The large and small wedges are shaped to compensate for the variable path length of the patient across the scan field of view (FOV). The small

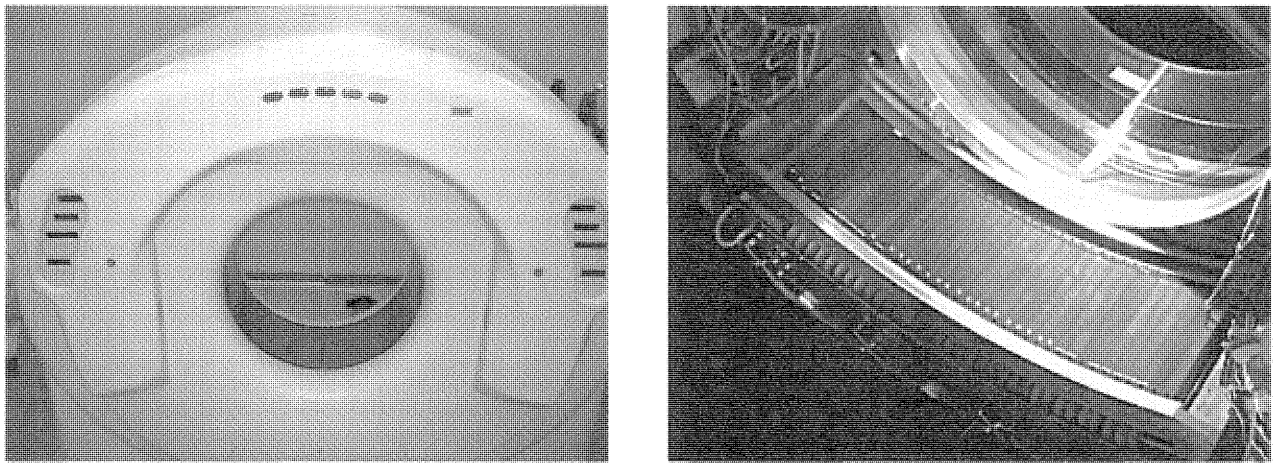

(a) (b)

Figure 1. (a) Front view of 256-slice CT-scanner. (b) A wide-area 2D detector is designed on the basis of the present CT technology and mounted on the gantry frame of the state-of-the-art CT-scanner.

wedge is used for an object under 240 mm FOV, and the large wedge is used for over 240 mm FOV (*e.g.* chest and abdomen). The flat wedge is thicker at the centre than the other wedges.

A Feldkamp-Davis-Kress (FDK) algorithm [4] is used for reconstruction. All further data processing and interpretation are done with a high-speed image processor with field programmable gate-array based-(FPGA) architecture. It takes less than 1 s to reconstruct volume data of a $512 \times 512 \times 256$ matrix.

The 16-slice CT detector consists of 40 segments, which can be electronically grouped to provide different image slice configurations. The longitudinal FOV is 32 mm at the maximum. Other major components are the same as those of the 256-slice CT. In addition to the axial scan, the helical scan mode can be selected to cover volumes beyond the detector width.

Phantoms

The length of the IEC-recommended dosimetry phantom [5] is at least 140 mm. This conventional phantom contains holes just large enough to accept the pencil-shaped ionization chamber. For dose measurement in cone-beam CT, the length of the phantom should be longer, because of the wider scatter distribution. According to our previous results [6], the phantom length and integration range for dosimetry needed to be at least 300 mm to represent more than 90% of line integral dose with the beam width between 20 mm and 138 mm. Therefore, in the present study we used 300 mm long phantoms of PMMA (polymethylmethacrylate). The diameters of the phantoms are 160 mm for head and 320 mm for body examination. These phantoms were provided by joining unit cylinders 150 mm long. The details of the phantoms were described by Mari et al [6].

Detectors

A pencil-shaped ionization chamber (CT-30; Oyogiken, Japan) of active length 300 mm was connected to a dosemeter (AE-132; Oyogiken, Japan) and used to measure dose. The dosemeter was calibrated the (National Institute of Advanced Industrial Science and Technology, Japan for the appropriate radiation qualities.

Clinical scan conditions

We compared the doses of the 256-slice CT and the 16-slice CT for clinical scan conditions. These conditions were mainly derived from those recommended by the manufacture for the 16-slice CT. The X-ray tube current was set that the effective mAs should be the same for both CTs, as given by (current) × (rotation time)/(helical pitch) for the 16-slice CT and by (current) × (rotation time) for the 256-slice CT. For the 256-slice CT, slice collimation was 224 mm × 0.5 mm for the head, 128 mm × 1.0 mm for the pelvis, and 256 mm × 0.5 mm for others. For the 16-slice CT, the slice collimation was set to 16 mm × 1.0 mm for pelvis and 16 mm × 0.5 mm for others, helical pitch was 0.69 for the head, and 0.94 for others, because the scan conditions were chosen to obtain the same spatial resolution as for the 256-slice CT.

The whole scan ranges were 93.9 mm for chest, 187.8 mm for abdomen, and 281.7 mm for pelvis. These scan ranges, except chest examination, were beyond the detector width of the 256-slice CT in the longitudinal direction, therefore they were set as multiples of 93.9 mm, the maximum longitudinal FOV of the 256-slice CT (Appendix 1). For the head examination, because the recommended value for the 16-slice CT was shorter than the maximum FOV of 256-slice CT, the FOV was adjusted to narrow the collimator width for the 256-slice CT. The clinical scan conditions thus obtained are summarized in Table 1.

Dose measurements

The dose for both CT systems was measured with the 300 mm long pencil-shaped ionization chamber and 300 mm long phantoms (160 mm and 320 mm diameter) in one rotation scan. The measurement range in the

Table 1. Scan conditions for 256-slice CT and 16-slice CT-scanners

Examination	Scanner	Voltage (kV)	Current (mA)	Rotation time (s)	Scan time (s)	Beam collimation	FOV	Scan range (mm)	Scan mode	Helical pitch
Head	256-slice CT	120	326	1.0	1.0	224 × 0.5 mm	240	90.0	Axial	N/A
	16-slice CT		300	0.75	17.0	16 × 0.5 mm			Helical	0.69
Chest	256-slice CT	120	160	1.0	1.0	256 × 0.5 mm	320	93.9	Axial	N/A
	16-slice CT		300	0.5	8.3	16 × 0.5 mm			Helical	0.94
Abdomen	256-slice CT	120	213	1.0	1s × 2	256 × 0.5 mm	320	187.8	Axial	N/A
	16-slice CT		400	0.5	14.5	16 × 0.5 mm			Helical	0.94
Pelvis	256-slice CT	120	213	1.0	1s × 3	128 × 1.0 mm	320	281.7	Axial	N/A
	16-slice CT		400	0.5	11.4	16 × 1.0 mm			Helical	0.94

FOV, field of view.

longitudinal direction was 300 mm ($z = \pm 150$ mm). The phantom was placed on the patient table and its centre was aligned at the isocentre. The ionization chamber was inserted into either the central or one of the peripheral cavities of the phantom (other cavities were filled with PMMA rods). The exposure (expressed as roentgens) was obtained with the ionization chamber dosemeter and converted to the values of absorbed dose to air measured in PMMA with the f-factor 0.898 cGy R^{-1}.

Dose assessment

The dose was assessed using the dose profile integral (DPI) over 300 mm ($z = \pm 150$ mm) (Appendix 2), which was given by the output of the pencil ionization chamber of 300 mm length [6].

The weighted average of DPI for at the centre and peripheries of the phantoms is given by

$$DPI_w = \frac{1}{3}DPI_c + \frac{2}{3}DPI_p \quad (1)$$

if we assume a linear decrease (or increase) of DPI in the radial direction, where DPI_c is the DPI at the center and DPI_p the average DPI on the peripheries.

Clinical image quality

We imaged four healthy male volunteers (mean age 30.0 years ± 7.6 (standard deviation) (SD); age range 23–53 years) using the 256-slice CT. The study was approved by the Institutional Review Board, and written informed consent was obtained from all subjects before starting. A non-enhanced examination with a step-and-shoot approval was carried out as follows: (i) head, (ii) chest, (iii) abdomen, and (iv) pelvis for one subject at each anatomical site. The subjects held their breath at end-inhale for the chest examination and end-exhale for the abdomen and pelvis examinations during scanning. Scan conditions were the same as the clinical conditions (Table 1) except the scan ranges, which were 102.4 mm for head (one scan), 375.6 mm for chest (four contiguous scans), 93.9 mm for abdomen and pelvis (one scan). The matrix size was 512 × 512 × 111 − 512 × 512 × 205, and the convolution kernel was the standard head kernel (FC43) for the head examination and the standard body kernel (FC10) for the others.

Image quality was evaluated by three board-certified radiologists who had more than 10 years experience in clinical diagnosis. They compared quality of the images taken with the prototype scanner to their quality standard formed by experience. It took about 1.5 h to read the images obtained in multiple planes in all four cases.

Results

For both CTs, DPI_c, DPI_p, and DPI_w in axial scan are summarized in Table 2. These values are normalized to 100 mAs. For the 256-slice CT, DPI_w is 1966 mGy·mm/100 mAs for the head phantom and 1109 mGy·mm/100 mAs for the body phantom. For the 16-slice CT, DPI_w is 181.6 mGy·mm/100 mAs with 8 mm beam width for the head phantom, 88.4 mGy·mm/100 mAs with 8 mm beam width and 155.9 mGy·mm/100 mAs with 16 mm beam width for the body phantom.

In Table 3 DPI_w values are calculated for the clinical protocols. Values for the 256-slice CT are smaller than those for the 16-slice CT in all examinations. We note that

Table 3. Dose profile integral weighted average (DPI_w) for clinical protocols for 256-slice CT and 16-slice CT

Examination	DPI_w (mGy·mm)		DPI_w percentage (%)
	256-slice CT	16-slice CT	
Head	6410	12127	52.9
Chest	1775	2462	72.1
Abdomen	4725	5773	81.9
Pelvis	7088	7981	88.8

Table 2. Dose profile integral (DPI) for the 256-slice CT and 16-slice CT

CT scanner	Phantom	Beam width (mm)	DPI_c (mGy mm/100 mAs)	DPI_p (mGy mm/100 mAs)	DPI_w (mGy mm/100 mAs)
256-slice CT	Head	112	1829	2034	1966
	Body	128	781	1273	1109
16-slice CT	Head	8	174.2	185.3	181.6
	Body	8	67.7	98.7	88.4
	Body	16	117.6	175.0	155.9

especially in the head examination, the DPI_w for the 256-slice CT is approximately 47% smaller than that for the 16-slice CT.

With regard to the clinical image quality, Figure 2 shows normal anatomical images from the 256-slice CT. Auditory ossicles are observed clearly in the sagittal section with the same image quality as the state-of-the-art CT-scanner (Figure 2a). For the chest examination, 3D visualization of the lung from four contiguous axial scans is shown in Figure 2b. For the abdomen examination, the coronal image has an image quality as good as that of conventional CT (Figure 2c). For the pelvis examination, three contiguous coronal images are shown in Figure 2d. These images also show the same image quality as conventional CT.

Discussion

In the present study, we compared doses in the 256-slice CT and the 16-slice CT for clinical conditions. The results showed that the dose for the 256-slice CT was smaller than that of the 16-slice CT in all examinations (Table 3). The percentages of DPI_w for the 256-slice CT to that for the 16-slice CT were 52.9%, 72.1%, 81.9% and 88.8% in the examinations of head, chest, abdomen and pelvis, respectively.

The dose for the 256-slice CT was less than that of the 16-slice CT in all examinations for the following reason. In a MDCT-scanner the actual beam width is set as the nominal beam width (slice thickness × slice number) plus a certain margin, where the margin is added to cover penumbra and mechanical errors. X-ray photons incident on a to a marginal portion do not contribute to image formation, but they do contribute to increased dose. If the nominal beam width becomes large, the contribution of this portion becomes smaller. Thus, the 256-slice CT with larger beam width provides smaller DPI_w values than the 16-slice CT. For the 16-slice CT the pelvis examination with 16 mm nominal beam width is more effective than the others with 8 mm beam width. In general, helical scans with pitch less than one caused overlap regions. Therefore in the present study, we set the effective mAs value to be the same to obtain the same signal-to-noise ratio in both CT systems.

Not with standing the dose for the 256-slice CT being smaller than that of the 16-slice CT, the 256-slice CT provides sufficient image quality for diagnosis (Figure 2) [7]. In these clinical conditions, the 256-slice CT achieved a 0.5–0.8 mm isotropic resolution and large volumes of data were taken in a one-rotation scan [8]. Therefore coronal and sagittal images were obtained at sufficient spatial resolution without secondary reconstruction.

Regarding the limit of dose, the effective dose [9] for the [2] MDCT was approximately 15 mSv for routine chest examinations and 30 mSv for routine abdomen or pelvis examinations [10]. If these values are taken as upper limits

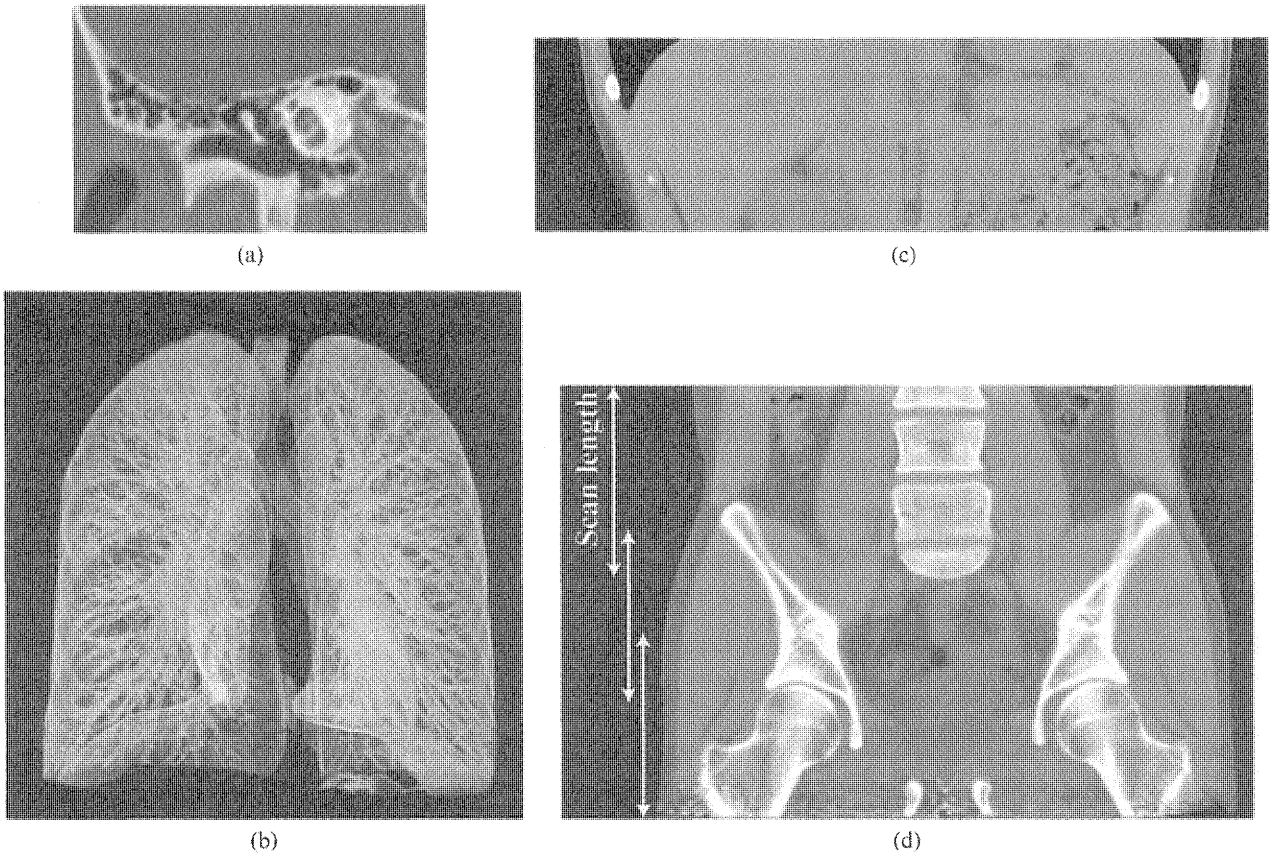

(a) (c) (b) (d)

Figure 2. Clinical images. (a) The 0.5 mm isotropic normal anatomy images of auditory ossicles in sagittal section. (b) 3D visualization of the chest with four contiguous scans. (c) Normal anatomy images of abdomen (0.63 mm reconstruction increment). (d) Coronal image (0.63 mm reconstruction increment) of pelvis with three contiguous scans.

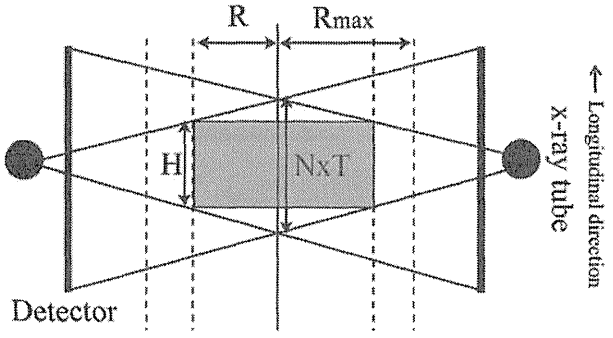

Figure A1. Reconstruction geometry of cone-beam CT. An X-ray source and a 2D detector rotate around the z-axis. The volume that can be reconstructed with the Feldkamp algorithm is shown by the shaded region and is a double conical region within a cylinder of radius R_{max}, which is determined by the detector size in the x-direction and shows the maximum field of view in the transverse plane. R and H show diameter and height, respectively, of a cylindrical reconstructed volume as it varied with an object. $N \times T$ show the nominal beam width where N is the number of slice and T is the slice collimation.

Table A1. Calculated weighted CT dose index ($CTDI_w$), dose–length product (DLP) and effective dose E for the 256-slice CT

	DPI_w (mGy·mm)	$CTDI_w$ (mGy)	DLP (mGy·cm)	E (mSv)
Chest	1775	13.87	130.2	2.21
Abdomen	2363	18.46	173.3	2.60
Pelvis	2363	18.46	173.3	3.29

and X-ray conditions are the same as those in Table 1, the acceptable scan time in volumetric cine imaging might be estimated in the following way. From Appendix 2, the estimated effective dose for a 1 s scan was 2.21 mSv, 2.60 mSv and 3.29 mSv for chest, abdomen and pelvis, respectively. Therefore, the acceptable scan time should be 6 s (= 15 [mSv]/2.21 [mSv]), 11 s (=30 [mSv]/2.60 [mSv]) and 9 s (= 30 [mSv]/3.20 [mSv]) for chest, abdomen, and pelvis, respectively. As these scan times may not be sufficient for a dynamic study in some cases, further efforts are necessary to develop dose reduction methods such as automatic dose control [11–13], as well as to justify increasing the dose in dynamic studies consistent with risk-benefit. Resolution of these issues, will allow full use of volumetric cine images which will significantly increase the amount of diagnostic information available to radiologists. In particular, we expect new applications such as computed tomographic angiography (CTA) of coronary arteries or perfusion studies of the whole brain.

Appendix 1. Field of view for the 256-slice CT

In the 256-slice CT, the reconstructed images with the Feldkamp algorithm is the region that is passed through during scanning by the tetra-angular pyramid whose apex and base are the X-ray source and the 2D detector, respectively (Figure A1). The reconstructed region is a double conical shape within a maximum FOV (R_{max}) in the transverse plane that is determined by the detector size in the transverse direction. Reconstruction is not made in the entire R_{max} except at the midplane and depends on a reconstructed FOV (R). In the case of the 256 mm × 0.5 mm (= $N \times T$) beam collimation, the length of the reconstruction region (H) is 102.4 mm for R= 240 mm and 93.9 mm for R= 320 mm. As seen in this example, the reconstructed region is generally smaller than the nominal beam width in cone beam CT.

Appendix 2. Effective dose estimation

CT dose index (CTDI), dose–length product (DLP), and effective dose (E) are usually used for CT dosimetry [2], and they are derived from DPI described in the present report.

CTDI is given as follows.

$$CTDI = \frac{1}{NT}\int_{-l/2}^{l/2} d(z)dz \ [\text{mGy}] \qquad (A1)$$

where N is the number of slices, T (mm) is the nominal slice thickness, and $d(z)$ is the dose profile for an axial scan, l indicates the integration range. The International Electrotechnical Comission (IEC) recommended an integration range of 100 mm. However we used the integration range of 300 mm for the reason described.

DPI is given with these notations as follows.

$$DPI = \int_{-l/2}^{l/2} d(z)dz \ [\text{mGy mm}] \qquad (A2)$$

From Equations (A1) and (A2),

$$CTDI = \frac{1}{NT}DPI \qquad (A3)$$

Weighted CTDI ($CTDI_w$) is defined with CTDIs measured at the centre and peripheries of the phantoms as follows.

$$CTDI_w = \frac{1}{3}CTDI_C + \frac{2}{3}CTDI_P \ [\text{mGy}] \qquad (A4)$$

$CTDI_c$ and $CTDI_p$ represent the CTDI measured at the centre and the average CTDIs measured on the periphery of the phantom, respectively. $CTDI_w$ is given by DPI_w as follows.

$$CTDI_w = \frac{1}{NT}DPI_w \ [\text{mGy}] \qquad (A5)$$

Dose–length product (DLP) for a complete examination is given as:

$$DLP = CTDI_w \times L \ [\text{mGy cm}] \qquad (A6)$$

where L (cm) is the scan range in the longitudinal direction.

Estimation of effective dose (E) may be derived from values of DLP for an examination using appropriately normalized coefficients:

$$E = E_{DLP} \cdot DLP \ [\text{mSv}] \qquad (A7)$$

E_{DLP} is the region-specific normalized effective dose (mSv mGy^{-1} cm^{-1}) [9].

From these equations $CTDI_w$, DLP and E can be calculated from measured DPI_w. Table A1 gives calculated DPI_w, $CTDI_w$, DLP and E with one second scan of the 256-slice CT in the clinical conditions for chest, abdomen and pelvis examinations, respectively.

References

1. Endo M, Mori S, Tsunoo T, Kandatsu S, Tanada S, Aradate H, et al. Development and performance evaluation of the first model of 256-slice CT-scanner. IEEE Trans Nuc Sci 2003;50:1667–71.
2. International Commission on Radiological Protection. Managing patient dose in computed tomography. ICRP Publication 87. Annals of the ICRP 30 (4), Pergamon Press, Oxford, 2000.
3. Saito Y, Aradate H, Igarashi K, Ide H. "Large area 2-dimensional detector for real-time 3-dimensional CT (256-slice CT)," Proc SPIE 2001;4320:775–82.
4. Feldkamp LA, Davis LC, Kress JW. Practical cone-beam algorithm. J Opt Soc Am 1984;A 1:612–9.
5. International Electrotechnical Commission. Evaluation and routine testing in medical imaging departments constancy tests – X-ray equipment for computed tomography. Publication IEC 1994:1223-2-6.
6. Mori S, Endo M, Nishizawa K, Tsunoo T, Aoyama T, Fujiwara H, et al. Enlarged longitudinal dose profiles in cone-beam CT and the need for modified dosimetry. Med Phys in press. [3]
7. Mori S, Endo M, Obata T, Murase K, Fujiwara H, Kandatsu S, et al. Clinical potentials of the prototype 256-detector roe CT-scanner. Acad Radiol 2005;22:149–55.
8. Mori S, Endo M, Tsunoo T, Kandatsu S, Tanada S, Aradate H, et al. Physical performance evaluation of a 256-slice CT-scanner for 4-dimensional imaging. Med Phys 2004;31:1348–56.
9. European Guidelines. Quality Criteria for Computed Tomography. EUR 16262, CEC Luxembourg, 1997.
10. Aoki C, Nishizawa K, Tonari A, Hachiya J. Effective dosing for multi-detector CT scanning. Jpn J Med Imaging 2001;20:101–9.
11. Nagel HS, Galanski M, Hidajat N, Maier W, Schmidt T. Radiation exposure in computed tomography-fundamentals, influencing parameters, dose assessment, optimization, scanner data, terminology. Hamburg: CTB Publications. [4]
12. Thomas LT, Neil BB, Tin-Su P, Jerry R, Steven JW, Jianying Li, et al. A dose reduction X-ray beam positioning system for high-speed multislice CT scanners. Med Phys 2000;27:2659–68.
13. Kachelrieß M, Kalender WA. Dose reduction by generalized 3D adaptive filtering for conventional and spiral single-, multirow and conebeam CT. Radiology 1999;213:283–4.

付　　録

付　録

【4次元CT研究班】

班長

遠藤真広（放射線医学総合研究所研究推進部）

班員（基礎系）

日下部正宏（福井大学工学部知能システム工学科）

工藤博幸（筑波大学電子・情報工学系）

鈴木直樹（東京慈恵会医科大学）

中森伸行（京都工芸繊維大学工芸学部電子情報工学科）

松本政雄（大阪大学医学部保健学科）

仁木　登（徳島大学工学部光応用工学科）

班員（臨床系）

片田和廣（藤田保健衛生大学医学部放射線医学教室）

日下部きよ子（東京女子医科大学放射線医学教室）

中土幸男（国立長野病院整形外科）

森井浩世（大阪市立大学）

森山紀之（国立がんセンター中央病院放射線診断部）

望月輝一（愛媛大学医学部放射線医学教室）

吉田勝哉（千葉大学大学院循環病態医科学）2004年3月まで

船橋信禎（千葉大学大学院循環病態医科学）2004年4月から

棚田修二（放射線医学総合研究所重粒子医科学センター画像医学部）

神立　進（放射線医学総合研究所重粒子医科学センター病院）

オブザーバー

宍戸文男（福島医科大学医学部放射線医学講座）：ネットワーク会議委員

【共同研究者】

近藤千里（東京女子医科大学放射線医学教室）

鈴木昌彦（千葉大学病院整形外科）

滝口裕一（千葉大学大学院呼吸器内科）

荒舘　博（東芝メディカルシステムズ（株））

杉原直樹（東芝メディカルシステムズ（株））

斎藤泰男（東芝メディカルシステムズ（株））

宮崎博明（東芝メディカルシステムズ（株））

佐藤一雅（ソニー（株）コーポレートテクノロジー部）

松下　聡（ソニー（株）コーポレートテクノロジー部）

馬場雅行（放射線医学総合研究所重粒子医科学センター病院）

小松秀平（放射線医学総合研究所重粒子医科学センター病院）

小幡隆行（放射線医学総合研究所重粒子医科学センター画像医学部）

角尾卓紀（放射線医学総合研究所重粒子医科学センター医学物理部）

森　慎一郎（放射線医学総合研究所重粒子医科学センター医学物理部）

「４次元 CT の研究開発」報告集

2006 年 2 月発行

編集　遠藤真広

発行者　佐々木康人

発行　放射線医学総合研究所

〒263-8555 千葉市稲毛区穴川４－９－１

TEL 043(251)2111

印刷・製本　有限会社 B.D.S